Advanced Calibration of Electrochemical NO$_2$ Sensors for Air Quality Monitoring

Sheng Ye

München 2026

Advanced Calibration of Electrochemical NO_2 Sensors for Air Quality Monitoring

Sheng Ye

Dissertation
der Fakultät für Physik
der Ludwig-Maximilians-Universität
München

vorgelegt von
Sheng Ye
aus Xuzhou, China

München, den 13.01.2026

Erstgutachter: Prof. Mark Wenig
Zweitgutachter: Prof. Christoph Haisch
Tag der mündlichen Prüfung: 23.03.2026

Contents

Zusammenfassung

Luftverschmutzung, insbesondere durch Stickstoffdioxid (NO_2), stellt weltweit eine bedeutende Herausforderung für Umwelt und öffentliche Gesundheit dar. Konventionelle Überwachungsnetzwerke mit Referenzinstrumenten sind aufgrund hoher Kosten und betrieblicher Anforderungen in ihrer räumlichen Abdeckung begrenzt. Kostengünstige elektrochemische Sensoren bieten Möglichkeiten für dichte Überwachungsnetzwerke, jedoch wird ihr Einsatz durch Probleme bei der Messgenauigkeit, Umweltabhängigkeiten und Langzeitstabilität erschwert.

Diese Arbeit untersucht die Kalibrierung kostengünstiger elektrochemischer NO_2-Sensoren und entwickelt eine tragbare Plattform zur Luftqualitätsüberwachung, die AIR Quality Inspection boX (AIRQUIX). Die Forschung beleuchtet Herausforderungen der Sensorkalibrierung, einschließlich Temperatur- und Feuchtigkeitsabhängigkeiten, Querempfindlichkeiten gegenüber Störgasen und zeitlichem Driftverhalten.

Ein neuartiger Kalibrierungsalgorithmus, basierend auf einem White-Box-Modell, wurde entwickelt, um diese Herausforderungen zu adressieren. Im Gegensatz zu Black-Box-Modellen des maschinellen Lernens bewahrt dieser Ansatz die Interpretierbarkeit und korrigiert effektiv Umweltabhängigkeiten. Die Leistungsbewertung erfolgt über einen Multi-Metrik-Rahmen, der Korrelationskoeffizient (r), den quadratischen Mittelwertfehler (RMSE), die mittlere normalisierte Abweichung (MNB) und die relative erweiterte Unsicherheit (REU) umfasst und sich an regulatorischen Richtlinien orientiert. Die Ergebnisse zeigen, dass diese Kalibrierungsmethodik die Messunsicherheiten signifikant reduziert und die Langzeitstabilität im Vergleich zu Herstellerkalibrierungen und Standardalgorithmen verbessert.

Das AIRQUIX-Gerät integriert elektrochemische Sensoren (NO_2, NO, O_3), einen optischen Partikelzähler (PM) und einen NDIR-Sensor (CO_2) in einer kompakten, batteriebetriebenen Einheit mit Wi-Fi-Konnektivität. Ein umfassendes Backend-System wurde für Datenmanagement, automatisierte Qualitätskontrolle und Visualisierung entwickelt.

Feldeinsätze evaluierten das Gerät in drei Bereichen: mobile Überwachung, persönliche Expositionsabschätzung und stationäre Überwachung. Mobile Anwendungen umfassten die stadtweite NO_2-Kartierung mit Elektrobussen (AIRQMORE), Studien zur Exposition in Fahrzeugen (AIRIDE) und städteübergreifende Untersuchungen (METROUNO2). Die persönliche Exposition wurde mittels tragbarer Technologien bewertet (PEARL). Stationäre Anwendungen evaluierten die Auswirkungen häuslicher Holzverbrennung (WOODY) und die Wirksamkeit von straßennahen Luftfiltersystemen (CLEANROAD).

Zu den methodischen Beiträgen gehören Datenfusionstechniken von Sensor- und Referenzdaten sowie Qualitätssicherungsverfahren für verschiedene Überwachungsszenarien. Validierungsstudien zeigen, dass kalibrierte kostengünstige Sensoren eine Datenqualität erreichen, die für ergänzende Überwachungsanwendungen geeignet ist, wenngleich Einschränkungen in der Präzision im Vergleich zu Referenzinstrumenten bestehen bleiben. Diese Arbeit liefert robuste Kalibrierungsmethodiken und Einsatzstrategien, die die Integration kostengünstiger Sensoren in Luftqualitätsüberwachungsprogramme als ergänzende Werkzeuge zu Referenznetzwerken unterstützen.

Abstract

Air pollution, particularly nitrogen dioxide (NO_2), poses significant environmental and public health challenges globally. Conventional monitoring networks utilizing reference-grade instruments are constrained by limited spatial coverage due to their substantial costs and operational requirements. While low-cost electrochemical sensors present opportunities for dense monitoring networks, their deployment is hindered by issues of measurement accuracy, environmental dependencies, and long-term stability.

This thesis investigates the calibration of low-cost NO_2 electrochemical sensors and develops a portable air quality monitoring platform, the AIR Quality Inspection boX (AIRQUIX). The research examines sensor calibration challenges including temperature and humidity dependencies, cross-sensitivity to interfering gases, and temporal drift characteristics.

A new calibration algorithm based on a white-box model was developed to address these challenges. Unlike black-box machine learning models, this approach maintains interpretability while effectively correcting for environmental dependencies. Performance assessment employs a multi-metric evaluation framework, including correlation coefficient (r), Root Mean Square Error (RMSE), Mean Normalized Bias (MNB), and Relative Expanded Uncertainty (REU), aligning with regulatory guidelines for sensor performance classification. Results demonstrate that this calibration methodology significantly reduces measurement uncertainties and improves long-term stability compared to manufacturer calibrations and standard algorithms.

The AIRQUIX device integrates electrochemical sensors (NO_2, NO, O_3), an optical particle counter (PM), and an NDIR sensor (CO_2) into a compact, battery-powered unit with Wi-Fi connectivity. A comprehensive backend system was developed for data management, automated quality control, and visualization.

Field deployments evaluated the device across three domains: mobile monitoring, personal exposure assessment, and stationary monitoring. Mobile applications included city-wide NO_2 mapping using an electric bus (AIRQMORE), in-vehicle exposure studies (AIRIDE), and multi-city investigations (METROUNO2). Personal exposure was assessed using wearable technologies (PEARL). Stationary applications evaluated residential wood burning impacts (WOODY) and the effectiveness of roadside air filtration (CLEANROAD).

Methodological contributions include sensor-reference data fusion techniques and quality assurance procedures for diverse monitoring scenarios. Validation studies indicate that calibrated low-cost sensors achieve data quality suitable for supplementary monitoring applications, though limitations in precision relative to reference instruments persist. This work provides robust calibration methodologies and deployment strategies, supporting the integration of low-cost sensors into air quality monitoring programs as complementary tools to reference networks.

Chapter 1

Introduction

Air pollution has emerged as one of the most critical environmental challenges of the 21st century, with far-reaching impacts on public health, ecosystem integrity, and climate change. Traditional air pollutants include particulate matter (PM), nitrogen oxides (NO and NO_2), ozone (O_3), sulfur dioxide (SO_2), and carbon monoxide (CO). These pollutants originate predominantly from anthropogenic activities like traffic, industrial processes, and residential heating, and continue to exceed the thresholds recommended by the World Health Organization (WHO) in many urban and industrial regions worldwide. When WHO updated its global air quality guidelines in 2021, 99 % of the population worldwide was exposed to air quality levels exceeding these guidelines (World Health Organization, a, 2021). The dense clustering of emission sources in cities, combined with meteorological conditions such as temperature inversions and low wind speeds, exacerbates pollution levels, trapping pollutants near ground level and increasing exposure risks for urban populations. Meanwhile, indoor air quality (IAQ) further complicates the pollution landscape. IAQ is influenced by complex interactions between outdoor air infiltration, ventilation, and indoor emission sources (e.g., building materials, cleaning products). As a result, residents face health issues such as heightened susceptibility to respiratory and cardiovascular diseases, which are associated with long-term exposure to poor air quality. WHO attributes 6.7 million premature deaths annually to ambient and household air pollution exposure (World Health Organization, 2024), while global health costs related to air pollution reach 8.1 trillion USD (World Health Organization, b). Consequently, accurate and dense monitoring of these pollutants has become an essential component of environmental management and public health protection strategies, underscoring the need for a high-resolution spatial and temporal air quality monitoring system. Such a system enables precise tracking of pollution variations across different locations and time scales, facilitating more effective air quality management and policy interventions.

Traditional air pollution monitoring relies primarily on high-end, expensive instruments deployed in designated monitoring stations. These high-end measurement instruments utilize complex methodologies and auxiliary tools including temperature controllers, air filters, and built-in calibration systems with additional dilution systems and standard gas cylinders to ensure data accuracy and quality. While these systems provide reliable measurements, they come with unavoidable limitations. The extraordinary cost of acquisition, installation, and maintenance results in sparse deployment of monitoring stations, creating gaps in spatial coverage. The bulky size and weight of these instruments further restrict their application options, making it expensive and difficult to establish monitoring stations in critical pollution hotspots or areas undergoing rapid urban development, and nearly impossible to set up reliable air quality monitors for indoor applications.

Low-cost air quality sensors represent a potential approach to address limitations in spatial coverage of conventional monitoring networks, enabling higher density deployments that may capture pollutant variability at finer spatial and temporal resolutions. However, the performance of these sensors, particularly for trace gases such as NO_2, requires rigorous calibration and validation against reference instruments. This thesis investigates the development of calibration algorithms for low-cost NO_2 electrochemical sensors and examines their performance characteristics in outdoor and indoor environments.

1.1 Research Motivation

The spatial heterogeneity of air pollutants, particularly in urban environments, necessitates monitoring networks with high spatial and temporal resolution. Conventional monitoring stations, while providing accurate measurements, are limited in number due to their high cost of acquisition, installation, and maintenance. This limitation results in inadequate spatial coverage, particularly in areas with complex emission patterns and topography. Low-cost sensor technologies present an alternative approach to achieving higher spatial resolution in air quality monitoring networks. However, significant technical challenges remain regarding sensor accuracy, stability, and calibration, particularly for reactive trace gases such as NO_2. These challenges must be systematically addressed to evaluate the utility of low-cost sensors for scientific and regulatory applications.

1.2 Scope and Objectives

This thesis addresses specific technical challenges in the evaluation and application of low-cost air quality sensors through systematic investigation of their performance characteristics, calibration methodologies, and deployment strategies. The research objectives are defined to advance understanding of low-cost sensor capabilities and limitations for air quality monitoring applications.

The primary research questions addressed in this thesis concern the effective evaluation of accuracy, precision, and reliability of low-cost air quality sensors compared to reference instruments, the identification of calibration methods that can optimize the performance of low-cost sensors under varying environmental conditions, and the exploration of potential applications of low-cost air quality sensors in urban and indoor environments along with the insights these measurements can provide for understanding air quality dynamics and human exposure patterns.

The development of a comprehensive evaluation framework for low-cost air quality sensors constitutes a primary objective of this research. While commonly employed metrics such as correlation coefficient (r) and Root Mean Square Error (RMSE) provide useful performance indicators, additional statistical methods are required to fully characterize sensor behavior across varying operating conditions. This thesis examines complementary evaluation approaches to assess sensor stability, environmental interferences, and long-term performance. A second objective involves the development of calibration procedures to improve the measurement accuracy of low-cost sensors. This approach incorporates corrections for cross-sensitivities and environmental dependencies, with the goal of reducing systematic biases and improving agreement with reference instruments.

This research also examines practical considerations for sensor network deployment, including data transmission protocols, power management strategies, and maintenance procedures. These investigations aim to identify operational requirements for sustained sensor network performance in urban environments and to provide empirical evidence regarding the applicability of low-cost sensors for air quality monitoring under realistic deployment conditions.

1.3 Atmospheric ground-level gas species

Atmospheric pollutants are compounds or particles introduced into the air that negatively impact human health, ecosystems, and climate. These pollutants originate from both natural sources, such as wildfires and volcanic eruptions, and anthropogenic sources, including industrial activities, motor vehicles, and agriculture. Pollutants are generally categorized into two groups: primary pollutants, which are directly emitted into the atmosphere (e.g., NO, CO, and primary PM), and secondary pollutants, which form in the atmosphere through chemical reactions involving primary pollutants (e.g., NO_2, O_3, and secondary PM). A comprehensive understanding of the nature and behavior of these pollutants is critical for air quality management, especially as pollution levels can differ significantly between outdoor and indoor environments, with significant consequences for public health and the environment. This thesis mainly focuses on nitrogen dioxide (NO_2), which is prevalent in both outdoor and indoor environments and has significant health implications. It is necessary to briefly introduce other atmospheric pollutants and gas species such as nitric oxide (NO), ozone (O_3), particulate matter (PM_x), and carbon dioxide (CO_2), which, although not the primary focus here, play essential roles in determining overall environmental and human health outcomes.

1.3.1 Nitrogen Oxides (NO_x)

Nitrogen oxides (NO_x) refer to a group of gases that includes nitric oxide (NO) and nitrogen dioxide (NO_2), both of which are harmful pollutants that contribute to the formation of ground-level ozone and fine particulate matter. NO_x plays a critical role in atmospheric chemistry, particularly in urban environments where vehicular traffic and industrial activities are prevalent. These gases are produced from the combustion of fossil fuels. Other human activities, such as fertilizer application and the cattle industry, also contribute to NO_x emissions, particularly in rural areas.

Natural processes, such as soil microbial activity, lightning, and the oxidation of ammonia (NH_3), also release NO_x into the atmosphere. While these sources are less significant on a global scale compared to human activities, they can contribute to localized increases in NO_x levels, especially in agricultural areas. Once released into the atmosphere, NO is quickly oxidized to NO_2, and the balance between NO and NO_2—known as the photostationary state—is influenced by factors such as ozone (O_3) levels, sunlight, and atmospheric reactions. This relationship is described by the Leighton relationship (Leighton, 2012), which states that under typical daytime conditions, the ratio of NO_2 to NO is determined by the photolysis of NO_2 and the oxidation of NO by O_3. NO_x contributes to the formation of several other nitrogen-containing compounds, collectively referred to as odd nitrogen species (NO_y), which include nitric acid (HNO_3), nitrate radical (NO_3), dinitrogen pentoxide (N_2O_5), and peroxyacetyl nitrate (PAN). These compounds further contribute to air pollution and can have detrimental effects on human health and the environment.

NO_x is a precursor to ground-level ozone, a major air pollutant that is harmful to both human health and ecosystems. In the presence of volatile organic compounds (VOCs) and sunlight, NO_x reacts to form ozone, which is particularly problematic in urban areas during the summer months. Managing NO_x emissions is essential for improving air quality and reducing the formation of ozone and secondary particulate matter, both of which have severe health implications.

Beyond its role in atmospheric chemistry, direct exposure to nitrogen oxides (NO_x), especially nitrogen dioxide (NO_2), can irritate mucous membranes and exacerbate respiratory diseases such as asthma, colds, and pneumonia.Long-term exposure increases the risk of respiratory infections and reduces lung function (Chauhan et al., 1998; Kagawa, 1985). NO_2 also heightens susceptibility to respiratory infections, particularly in children and the elderly, making it a critical pollutant for air quality control.

1.3.1.1 Nitrogen Dioxide (NO_2)

Nitrogen dioxide (NO_2) is a reddish-brown, toxic gas with a characteristic pungent odor. It is known for its harmful effects on both human health and the environment. Prolonged exposure to elevated NO_2 levels can cause respiratory problems, exacerbate asthma, and increase the risk of infections and cardiovascular diseases. Due to its impact on public health, NO_2 is heavily regulated by environmental agencies worldwide (European Parliament and Council of the European Union, 2008, 2024).

NO_2 also plays a role in the formation of ground-level ozone and fine particulate matter, both of which are associated with serious health impacts. Efforts to reduce NO_2 levels are central to air quality management strategies, particularly in urban areas where the levels tend to be the highest due to vehicle emissions and industrial activities.

1.3.1.2 Nitric Oxide (NO)

While nitrogen dioxide receives significant regulatory attention, nitric oxide (NO) also plays a crucial role in atmospheric chemistry. NO is a colorless, odorless gas that, while less harmful than nitrogen dioxide, is an important precursor in the formation of NO_2 and ozone.NO is emitted primarily from combustion processes, including motor vehicles and power plants, and is often found in varying ratios with NO_2 depending on local atmospheric conditions. Although NO is not directly regulated for human health in the European Union or by the WHO, it plays a significant role in atmospheric reactions that lead to the production of harmful pollutants like NO_2 and ozone.

In addition to its contributions to air pollution, NO also participates in reactions that form secondary pollutants, such as nitric acid (HNO_3), which can contribute to acid rain. The EU has established a critical level for NO_x ($NO + NO_2$) to protect vegetation, setting a limit of 30 μg m^{-3} annually to minimize damage to sensitive ecosystems.

1.3.2 Ground-Level Ozone (O_3)

Ground-level ozone (O_3) is an irritating gas with a distinctive odor and pale blue color. It is a toxic, explosive, and extremely powerful oxidant. On Earth, 90% of O_3 exists in the stratosphere, where it plays an important role in protecting life by reducing the intensity of damaging ultraviolet radiation from the sun. In the troposphere, however, much of the ozone is generated indirectly through in-situ gas-phase reactions involving the oxidation of VOCs, CO, and CH_4 in the presence of NO_x, catalyzed by sunlight and heat (Wallace and Hobbs, 2006). In many countries, an increasing O_3 trend has been observed over the past decades (Massagué et al., 2019; Xu et al., 2019; Yan et al., 2018).

Ground-level O_3 poses a significant health risk, affecting large populations with mild symptoms and smaller populations with more severe conditions. The health impacts of O_3 range from reversible reductions in lung function to more serious outcomes like airway hyperreactivity and chronic inflammation (Uysal and Schapira, 2003). Long-term exposure to high O_3 levels can lead to the development of asthma and is associated with increased mortality from cardiovascular disease (Bell et al., 2004; McConnell et al., 2002; McDonnell et al., 1999; Tager et al., 2005).

1.3.3 Particulate Matters (PM_x)

Particulate matter (PM) pollution refers to a mixture of tiny solid and liquid particles suspended in the air. These particles vary in size, with PM10 representing particles less than 10 μm in diameter, PM2.5 representing fine particles smaller than 2.5 μm, PM1 representing particles smaller than 1 μm, and PM0.1 representing ultrafine particles smaller than 0.1 μm. PM pollution originates from a wide range of sources, including vehicle emissions, industrial activities, domestic fuel burning, and natural sources like dust storms and sea salt. In urban areas, traffic is a major contributor to PM levels, particularly from diesel engines. Secondary particles can also form in the atmosphere through chemical reactions involving primary pollutants like NO_x and VOCs (Karagulian et al., 2015). Exposure to high levels of PM is associated with respiratory and cardiovascular diseases, and it can lead to premature death, particularly in vulnerable populations such as children, the elderly, and individuals with pre-existing health conditions.

Smaller the particles show more harmful to human health, as they can penetrate deep into the lungs and even enter the bloodstream. PM exposure has been linked to respiratory diseases such as asthma, lung inflammation, and chronic conditions like cardiovascular disease and lung cancer (Ghio and Huang, 2004; Künzli and Tager, 2005; Li et al., 2003; Sullivan et al., 2005).

Inhalation of fine particles (PM2.5) has also been associated with increased heart rate variability (HRV), ectopic heartbeats, and markers of inflammation and coagulation in the blood (Riediker et al., 2004).

Historically, the Great Smog of London in 1952 was a severe pollution event that caused thousands of deaths, primarily due to coal burning and adverse weather conditions. The event provided critical insights into the dangers of PM, with studies revealing high concentrations of small particles and metals in lung tissue samples from the victims (Wallace and Hobbs, 2006).

1.3.4 Carbon Dioxide (CO_2)

Carbon dioxide (CO_2) is a naturally occurring gas that is essential for life on Earth. It plays a critical role in the Earth's carbon cycle and is a key greenhouse gas, contributing to global warming and climate change when present in excess. Atmospheric CO_2 mixing ratios have been rising steadily with anthropogenic emissions since the industrial revolution. The rate of increase has accelerated in recent decades, from approximately 0.8 ± 0.1 ppm per year in the 1960s to 3.75 ppm per year in 2024 (Lindsey and Miller, 2025; Stein, 2024).

While CO_2 is not toxic at typical ambient mixing ratios, elevated levels indoors can indicate poor ventilation and lead to drowsiness and reduced cognitive function, particularly above 1000-2500 ppm (Satish et al., 2012). In confined environments, such as offices, classrooms, and vehicle cabins, CO_2 mixing ratio is often used as a proxy for air quality and ventilation efficiency. According to the American Society of Heating, Refrigerating, and Air-Conditioning Engineers (ASHRAE), permissible exposure levels for CO_2 are set at 5000 ppm in most standards, with Canadian guidelines recommending a lower threshold of 3500 ppm (ASHRAE Standards Committee, 2013). Monitoring CO_2 levels can help ensure adequate air circulation and prevent indoor air quality issues.

1.4 Importance of NO_2 Monitoring

NO_2 poses a direct threat to human health and also serves as a key precursor to secondary pollutants. Its levels vary significantly between indoor and outdoor environments and are highly sensitive to local emission sources. Given its substantial health and environmental impacts, NO_2 stands out as a priority target for the development of innovative monitoring strategies. A thorough understanding of its fundamental properties, emission sources, and environmental behavior is essential for accurate air quality assessment and for evaluating its broader effects on human health and ecosystems.

Chapter 2

Overview of in-situ NO_2 Monitoring Techniques

Air quality monitoring plays a crucial role in assessing and managing the impact of pollutants on health, the environment, and policymaking. Key air quality parameters include Nitrogen Oxides (NO_2, NO), ground-level Ozone (O_3), carbon dioxide (CO_2), and Particulate Matter (PM_x). These pollutants significantly influence both outdoor and indoor air quality, making their real-time monitoring essential for informed decision-making and effective mitigation strategies.

This chapter provides an overview of the current state of air quality monitoring techniques, with a focus on in-situ NO_2 measurement methods.

There are two fundamental categories of in-situ air quality measurement methods: remote sensing techniques and in-situ measurement techniques. Remote sensing involves detecting information about the area under investigation at a distance without direct contact, which allows for extensive spatial coverage and can provide valuable data on the distribution and transport of pollutants across large areas.

In contrast, in-situ measurement techniques refer to point measurements where the instrument is in contact with the sampled air. There are various techniques available. Classified by measurement principle, traditional techniques include methods such as mass spectrometry and optical methods. Mass spectrometry allows for the precise identification and quantification of different pollutants based on their mass-to-charge ratio, while optical methods, such as laser-based sensors, detect pollutants through their interaction with light. When classified by sampling methods, in-situ techniques can be divided into active and passive sampling. Active sampling involves drawing air through a sensor or filter using a pump, providing real-time data and enabling the measurement of a wide range of pollutants at varying levels. Passive sampling, on the other hand, relies on the natural diffusion of air pollutants onto a sorbent material over a longer period, offering a cost-effective and low-maintenance option for monitoring air quality in remote or less accessible areas.

The integration of both remote sensing and in-situ measurements offers a complete picture of air quality. Remote sensing provides a broad overview of atmospheric conditions, identifying trends and large-scale patterns, while in-situ measurements offer detailed, site-specific data which is necessary for understanding local air quality dynamics. Together, these methods enhance our ability to monitor and manage air quality, contributing to more effective environmental protection and public health strategies.

Traditionally, in-situ techniques are commonly employed by official air quality monitoring stations, which use high-precision instruments to monitor pollutants in urban and rural areas. These stations are essential for satisfying domestic air quality directives, providing accurate and localized data that inform public health decisions and regulatory policies.

2.1 Traditional air quality measurement instruments

2.1.1 Chemiluminescence NO/NO_x detector

Currently, the state of the art in NO_2 measurements is the gas phase chemiluminescence method. A chemiluminescence NO/NO_x detector is a device used to measure levels of nitrogen oxides (NO and NO_x) in air. NO_2 monitors employing this technique provide in-situ values and have been used for decades by most environmental protection departments, making it the most widespread detection method for NO_2.

The principle of operation is based on the chemiluminescent reaction between nitric oxide (NO) and ozone (O_3). When nitric oxide (NO) reacts with ozone, it forms nitrogen dioxide (NO_2) in an excited state (Reaction 1). This reaction produces light, or chemiluminescence, which can be detected. The nitrogen dioxide in the excited state (NO_2^*) releases light as it returns to its ground state (Reaction 2). The light emitted by the excited nitrogen dioxide molecules is measured by a photodetector. The intensity of the light is directly proportional to the level of NO in the sample.

$$NO + O_3 \longrightarrow NO_2^* + O_2 \tag{1}$$

$$NO_2^* \longrightarrow NO_2 + \text{light} \tag{2}$$

To measure the total mixing ratio of nitrogen oxides, a converter is used to convert all the nitrogen dioxide (NO_2) in the sampled air to nitric oxide (NO). This is usually done by passing the air sample through a heated catalytic converter, where NO_2 is reduced to NO. The total NO mixing ratio, including both the original NO and the converted NO_2, is measured using the same chemiluminescence process. The mixing ratio of NO_2 is then determined by subtracting the NO measurement before the converter from the total NO_x measurement after the converter.

Nevertheless, this method has its drawbacks as it suffers from interferences by other unstable nitrogen compounds, leading to errors in polluted urban atmospheres when combined with commonly used catalytic conversion methods (Dunlea et al., 2007; Villena et al., 2012).

2.1.2 The Cavity-Enhanced DOAS (CE-DOAS) instrument

Given the limitations of chemiluminescence methods, alternative measurement techniques have been developed. The DOAS technique (Platt and Stutz, 2008) is a widely used approach for measuring stratospheric and tropospheric trace gases. Based on the modified Beer-Lambert Law, it measures the absorptions of multiple trace gases simultaneously.

$$I(\lambda) = I_0(\lambda)e^{\sum_i \sigma_i(\lambda)SCD_i}g(\lambda) \tag{2.1}$$

With the sum in the exponential term running over all trace gases i, the Slant Column Density (SCD_i) is the concentration of trace gas i integrated along the light path, and g(λ) describes additional attenuation by the optical system, as well as by Rayleigh and Mie scattering in the atmosphere and all other broadband structured influences, such as reflection from the ground.

The equation is linearized with respect to the SCDs, and ln(g(λ)) is modeled by a polynomial, allowing linear retrieval of the SCDs of the involved gases. However, for uncertain wavelength mapping, the optimization becomes non-linear, which may introduce error sources such as the so-called I_0 or undersampling effect (Wenig et al., 2005), which must be corrected.

Cavity-enhanced spectroscopy has been developed to provide long absorption paths necessary for the detection of ambient atmospheric trace gases by multiple reflections in a small optical resonator (Ball et al., 2004; Brown, 2003; Zalicki and Zare, 1995). Using this technique in combination with a continuous light source allowed the application of the DOAS method to in-situ measurements (Horbanski et al., 2019; Meinen et al., 2010; Platt and Stutz, 2008; Zhu, 2018). In this thesis, a cavity enhanced DOAS (CE-DOAS) instrument is used for calibration and validation of low-cost sensors.

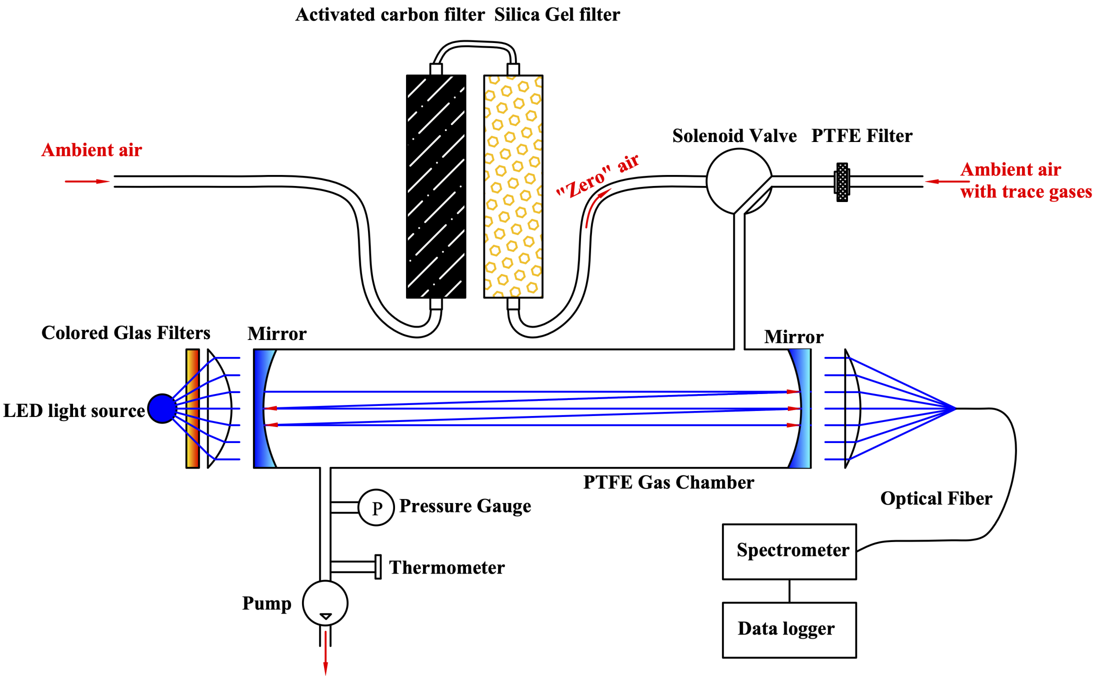

Figure 2.1: Schematic of CE-DOAS instrument.

A schematic of the CE-DOAS instrument is shown in Fig. 2.1. The instrument includes a blue LED light source, an optical resonator with two high-reflectivity dielectric mirrors, a spectrometer, and an air sampling system. The optical resonator is formed by placing dielectric-coated mirrors at both ends of the gas chamber. Light from the blue LED is introduced into the resonator. Light exiting the resonator is coupled into an optical fiber. The transmitted light is then guided through the optical fiber to a spectrometer. A direct current (DC) vacuum pump, located at the outlet of the sampling chamber, ensures sample flow. A Teflon filter is placed at the inlet to prevent aerosols from entering the cell, thereby reducing scattering effects and mirror contamination (Horbanski et al., 2019). During mobile measurements and calibration campaigns, the instrument operated with a time resolution of 4 seconds.

2.2 Low-cost sensors and the classification

There is a growing interest in a group of low-cost measurement techniques that have emerged in recent years, particularly for measuring NO_2 and other air pollutants. These techniques are based on low-cost sensors, which are small, lightweight, and easy to deploy, making them ideal for mobile monitoring applications. These sensors can improve air quality monitoring and public health by providing high-resolution data at a lower cost, and offer a promising solution for establishing dense monitoring networks especially in urban areas where traditional monitoring stations are limited due to high costs and maintenance requirements. They can fill gaps in existing monitoring networks, are particularly beneficial for low- and middle-income countries, and represent an important additional tool that can be utilized at the community level to support data-driven policy actions towards air pollution management. This is especially critical given that the effects of air pollution lead to an estimated 7 million deaths every year. However, these sensors have limitations in terms of accuracy, precision, and cross-sensitivity to other gases. To address these challenges, researchers are developing novel sensor technologies and calibration techniques to enhance the performance of low-cost air quality sensors.

2.2.1 MO_x sensors

Metal Oxide (MO_x) semiconductor sensors represent a prominent class of low-cost gas sensing devices, favored for their compact size, high sensitivity, and ease of integration into mobile monitoring setups. The specific sensor utilized in this thesis is the MICS-6814 manufactured by SGX Sensortech. This compact unit comprises three independent sensing elements on a single chip, designed to detect nitrogen dioxide (NO_2), carbon monoxide (CO), and hydrocarbons (measured as CH_4) respectively. To facilitate the necessary chemical reactions, the sensor element is heated to a specific operating temperature, typically ranging from 200°C to 400°C, by an integrated resistive heater.

The fundamental working principle of the MO_x sensor relies on the chemiresistive effect, where the electrical resistance of the semiconductor material changes in response to the composition of the surrounding gas atmosphere. When the sensor is heated in clean air, oxygen molecules from the atmosphere adsorb onto the surface of the metal oxide grains. These ad-

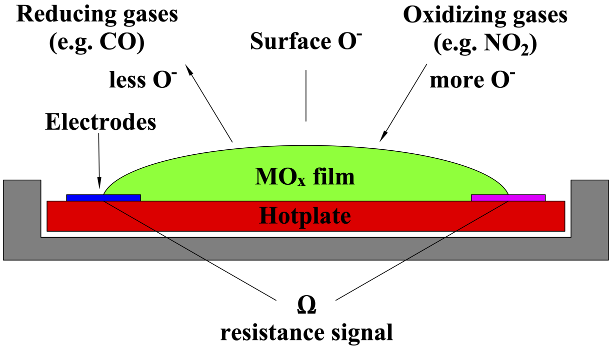

Figure 2.2: Metal Oxide (MO_x) semiconductor sensor working principle.

sorbed oxygen species trap free electrons from the semiconductor's conduction band, creating negatively charged oxygen ions (such as O^- or O^{2-}). This electron trapping leads to the formation of an electron-depleted region, known as the space-charge layer, at the grain boundaries. Consequently, a potential barrier is established that impedes the flow of current, resulting in a high baseline electrical resistance.

When the sensor is exposed to a target gas, the gas molecules interact with the adsorbed oxygen species or directly with the oxide surface, altering the density of trapped electrons. For an oxidizing gas like NO_2, the gas molecules act as electron acceptors. Upon adsorption, NO_2 molecules trap additional electrons from the conduction band, further widening the depletion layer and increasing the potential barrier. This process results in a significant increase in the electrical resistance of the sensor, which is directly correlated to the concentration of NO_2 in the air. Conversely, for reducing gases such as CO, the gas molecules react with the surface oxygen ions, releasing the trapped electrons back into the conduction band. This lowers the potential barrier and decreases the electrical resistance. By monitoring these resistance changes (Fig. 2.2), the concentration of the target pollutants can be determined.

2.2.2 Electrochemical sensors

The other type of low-cost sensor is electrochemical sensors (ECSs). ECSs are widely used for measuring various gases, including NO_2, due to their high sensitivity and selectivity. ECSs are based on the principle of electrochemical reactions, where the target gas interacts with an electrode surface, resulting in a measurable electrical signal. This principle allows for direct and sensitive detection of the target gas in the environment.

The ECSs can detect reactive trace gas species such as NO, NO_2, and O_3. The sensors used in this thesis are four-electrode electrochemical sensors from Alphasense Limited, which consist of a working electrode (WE), auxiliary electrode (AE), counter electrode, and reference electrode (Fig. 2.3). A small current is generated from the oxidation and reduction reactions within the sensor cell. The reaction of the measured target gas occurs on the working electrode to generate a level-correlated current. The selectivity of this reaction is achieved through the specific catalyst material coating the working electrode and the precise electrical potential applied to it, which are

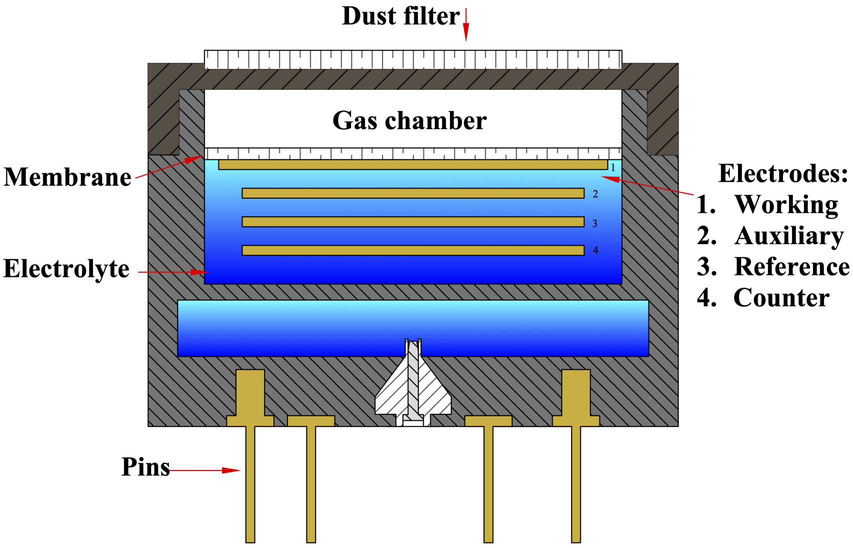

Figure 2.3: Electrochemical sensor working principle.

tuned to facilitate the oxidation or reduction of the target gas while minimizing reactions with other species. The counter electrode balances the current generated at the working electrode by performing the opposite oxidation or reduction chemical reaction. The reference electrode helps to stabilize the working electrode potential by connecting with the WE through a potentiostat to ensure the WE works at a stable potential. The auxiliary electrode has a similar design and material to the WE but is not in contact with the target gas. Hence, the AE can represent the environmental conditions and is suggested to be used for temperature correction (suggested by the manufacturer Alphasense Limited (c)).

Although the AE can provide some environmental correction, in practice, it is normally found that the calibration methods recommended by manufacturers do not provide conversion methods with the accuracy required for environmental air analysis. The response of ECSs is further affected by other environmental factors, such as relative humidity (the sensor itself can gain or lose water according to ambient humidity, which leads to a change in the sensor's performance (Alphasense Limited, a)) and cross-sensitivity in the presence of other gases (O_3 sensors are additionally sensitive to NO_2, and NO_2 sensors are additionally slightly sensitive to O_3). A comprehensive characterization of interference responses is critical for obtaining reliable measurements under different atmospheric conditions.

Chapter 3

Low-cost sensor calibration techniques

Calibration is essential for qualifying the output of ECSs. It is typically conducted in laboratory settings, where sensors are exposed to known levels of the target gas. The sensor response is recorded to generate a calibration curve that correlates the sensor output with gas mixing ratio. However, this process is time-consuming and requires specialized equipment, making it impractical for real-time or field-based applications. To overcome these limitations, researchers are developing individual calibration methods that can be implemented in the field to provide accurate and reliable data.

3.1 Review of Previous Studies on Low-cost air quality sensors

Advanced data processing techniques, including traditional statistical algorithms, and machine learning models, are widely used to improve sensor calibration and performance. These approaches enable the correction of sensor errors and enhance data reliability. Previous studies have demonstrated the effectiveness of algorithms in addressing challenges such as sensor drift, cross-sensitivity, and environmental variability. A comprehensive review of these works provides insights into best practices for improving sensor accuracy and reliability.

3.1.1 Classification of Calibration methods for Low-cost Sensors

The algorithms provided by manufacturers are ready-to-use and easy to implement. However, these algorithms are often found to be insufficient for accurate calibration, especially in complex environments with varying atmospheric conditions, which has been reported in the research community (Ayvaz et al., 2025; Liang et al., 2021). As a result, researchers have explored more advanced calibration techniques to improve sensor performance. Low-cost sensor calibration methods can be classified into two main categories based on their interpretability and underlying mathematical principles: white-box models and black-box models. Each category offers distinct advantages and limitations for sensor calibration applications.

White-box models provide transparent and interpretable relationships between input variables and sensor responses, allowing researchers to understand how each input factor influences the output. In contrast, black-box models utilize complex algorithms that can capture non-linear relationships without explicitly defining the mathematical relationships, often providing superior performance but with reduced interpretability.

A growing trend in the statistical community involves utilizing over-parameterized models for sensor calibration (Ionascu et al., 2021; van Zoest et al., 2019). For example, some studies have incorporated additional parameters such as wind speed and direction into their calibration models, sometimes achieving improved performance. However, this trend raises concerns that it may undermine the fundamental principle of in-situ sensing by shifting the focus from direct measurement toward atmospheric modeling (Hagler et al., 2018).

Air pollutants and meteorological conditions typically exhibit complex interactions with each other. In such cases, these algorithms may be able to predict target gas mixing ratios without directly utilizing signals from the monitoring devices (as discussed in Section 6.3). While these approaches might be useful for ambient air quality monitoring in environments with well-understood atmospheric chemistry, they may not be suitable for personal exposure monitoring or urban roadside air quality monitoring at different locations where local conditions vary significantly.

3.1.1.1 White-box Model

White-box models are characterized by their transparency and interpretability, allowing researchers to understand the relationship between input variables and sensor responses. These models provide clear insights into how environmental factors and sensor characteristics influence measurements, making them valuable for scientific understanding and validation.

3.1.1.1.1 Simple Ordinary Least Squares (OLS) Regression

Although some studies occasionally rely on simple OLS using only raw sensor outputs or manufacturer settings, most use it primarily as a baseline for comparison with more advanced calibration methods. This approach assumes a single predictor variable and provides a straightforward benchmark for evaluating other techniques. OLS regression establishes a direct linear relationship between sensor readings and reference measurements but lacks the capability to account for environmental influences.

3.1.1.1.2 Multiple Linear Regression (MLR)

MLR is the most widely used calibration technique in the literature, incorporating multiple predictor variables alongside the primary sensor signal (Cordero et al., 2018; Jiao et al., 2016; Karagulian et al., 2019a; Maag et al., 2016, 2018; Piedrahita et al., 2014; Spinelle et al., 2015). The key challenge in MLR implementation is identifying reasonable input variables that improve calibration accuracy without compromising the measurement principle. The most commonly used variables include raw sensor output and environmental parameters such as temperature, relative humidity, and pressure. Additionally, interference sensor outputs from co-located sensors measuring gases like ozone (O_3) and carbon monoxide (CO) are sometimes incorporated to address cross-sensitivity issues.

3.1.1.2 Black-box Model

Black-box models utilize complex algorithms that can capture non-linear relationships and interactions between variables without explicitly defining the mathematical relationships. While these models often provide superior performance, their internal workings are less transparent. The interpretation and validation of these models are challenging and themselves a subject of ongoing research.

3.1.1.2.1 Convolutional Neural Networks (CNN)

Convolutional Neural Networks (CNN) are a class of deep learning algorithms primarily known for their success in image processing but increasingly applied to time-series data and sensor calibration (LeCun et al., 1989). CNNs are designed to automatically and adaptively learn spatial hierarchies of features from input data through the use of convolutional layers, pooling layers, and fully connected layers.

For sensor calibration, 1D-CNNs are particularly useful as they can extract temporal features and patterns from sequential sensor readings and environmental parameters. By applying sliding filters over the time-series input, the network can capture local dependencies and trends, such as the delayed response of sensors to rapid concentration changes or transient environmental effects. This capability allows CNNs to model complex, non-linear dynamic relationships that simpler static models might miss.

The main advantage of using CNNs for low-cost sensor calibration lies in their ability to learn feature representations directly from raw data without extensive manual feature engineering. They are robust in handling noise and can effectively model the temporal dynamics inherent in atmospheric processes. However, CNNs have disadvantages as they typically require larger datasets and more time for training compared to other methods (Ali et al., 2023; Bagkis et al., 2025; Liang et al., 2023).

3.1.1.2.2 Random Forest (RF)

Random Forest (Breiman, 2001) is recognized as the most accurate machine learning method for low-cost sensor calibration in the literatures (Apostolopoulos et al., 2023, 2024; Kim et al., 2022; Margaritis et al., 2021; Zhao and Lai, 2021). RF is an ensemble learning method that combines multiple decision trees to improve prediction accuracy and reduce over-fitting. RF models are robust against outliers and can handle missing data effectively, while providing variable importance rankings that offer some interpretability despite their black-box nature.

3.1.1.3 Performance Comparison and Selection Criteria

The choice between white-box and black-box models depends on several factors, including data availability, environmental conditions, and application requirements. Each approach offers distinct advantages for low-cost NO_2 sensor calibration.

White-box models, particularly MLR, provide transparency and interpretability, allowing researchers to understand how environmental factors influence sensor performance. MLR is straightforward to implement and offers clear insights into the calibration process. However, these models may have limited ability to capture complex non-linear relationships and interactions between multiple variables.

Black-box models, such as RF and CNN, are excellent at capturing complex patterns and non-linear relationships in sensor data. RF has been consistently identified as the most accurate machine learning method for low-cost sensor calibration across multiple studies, demonstrating superior performance in handling environmental variability and cross-sensitivity issues. CNN offers the advantage of modeling temporal dynamics but may require substantial computational resources for training.

The selection between these methods should consider the specific requirements of the monitoring application. For applications requiring interpretability and scientific understanding, white-box models are preferred. When maximum accuracy is the primary concern and computational resources are available, RF typically provides the best performance. The choice should also consider factors such as available training data, deployment environment complexity, and long-term maintenance requirements.

In this thesis, we utilize MLR and RF as the comparison with our calibration method. MLR serves as a baseline for evaluating the effectiveness of the approach, while RF is used to demonstrate the potential of machine learning techniques in enhancing sensor calibration accuracy.

3.2 Research Gaps and Challenges

Despite significant advances in low-cost sensor technology and calibration methods, several important challenges remain in the field of NO_2 monitoring. Low-cost NO_2 sensors are increasingly deployed in urban environments and indoor spaces, where they provide useful data on pollutant levels. However, their performance in these settings depends on factors such as sensor placement, environmental conditions, and data accuracy (Carl Malings et al., 2024).

Current calibration methods often provide inadequate correction for environmental factors such as temperature fluctuations, humidity changes, and atmospheric pressure variations, leading to sensor drift and reduced measurement accuracy over time. Most studies focus on specific environments, with insufficient validation across diverse real-world conditions including urban areas, rural settings, and indoor environments, limiting the generalizability of calibration approaches.

Another significant limitation concerns temporal resolution. Many field studies report only hourly or daily averaged data. According to Karagulian et al. (2019b), among 34 studies of low-cost sensors co-located at urban sites, 7 at rural sites, and 10 at traffic sites, most laboratory and field tests reported hourly data (610 records for 86 sensor models), with 248 records for 42 sensors using daily data. This limits the ability to capture short-term pollution events and rapid level changes.

Furthermore, there is insufficient integration between high-precision reference instruments and low-cost sensors, making it difficult to establish reliable calibration standards and validate sensor performance in operational conditions.

3.3 Sensor Selection and Configuration

As discussed in Section 2.2, both Electrochemical sensors (ECS) and Metal Oxide (MO_x) sensors are widely utilized in the scientific community. While MO_x sensors offer advantages in terms of compact size and lower cost, they generally exhibit lower selectivity compared to ECSs, making them more susceptible to cross-sensitivity from other atmospheric gases. Furthermore, they are characterized at the initial evaluation by slower response times to fluctuations in pollutant levels and often require more frequent calibration (Described in Fig.6.48 and Fig.6.49). Consequently, this thesis focuses on the performance evaluation of NO_2 ECSs from Alphasense Limited, which feature a four-electrode configuration. Although MO_x sensors are not the primary subject of this study, a comparative evaluation with ECSs is presented in Section 6.4.1.1.2.

ECSs represent the current state of the art for low-cost sensors. They measure reactive trace gas species such as NO, NO_2, O_3, etc. These sensors operate in an amperometric mode with four electrodes as described in Sec. 2.2.2. These sensors require frequent calibration, which is why they can not be used for longer periods without reference instruments or calibration gases. The combination of precise high-end instruments and low-cost portable sensors is ideal for such applications.

3.4 Current Challenges and Future Directions

While low-cost sensor networks have significantly advanced air quality monitoring capabilities, several challenges persist that require continued research and development efforts.

Key technical challenges in low-cost NO_2 sensor deployment include sensor drift, which affects long-term stability and measurement accuracy over extended deployment periods. Cross-sensitivity from other atmospheric species can lead to measurement errors, while environmental effects such as temperature, humidity, and pressure variations influence sensor response characteristics. Additionally, the need for periodic recalibration to maintain measurement quality in field conditions remains a practical challenge.

Future developments in low-cost air quality monitoring are expected to focus on several key areas. Advanced calibration algorithms incorporating machine learning techniques for real-time adaptive calibration can automatically adjust to changing environmental conditions. Multi-pollutant sensor platforms capable of simultaneously monitoring multiple air quality parameters with improved accuracy and reliability are being developed. Enhanced data fusion approaches between low-cost sensor networks and reference monitoring stations can leverage the strengths of both measurement approaches. Finally, standardized quality assurance protocols for sensor validation, calibration, and data quality control are essential to ensure reliable measurements across different applications.

Chapter 4

Evaluation Methodology

This chapter describes the methodology used to evaluate the performance of electrochemical sensors (ECSs) for NO_2 monitoring. The evaluation process includes data collection, preprocessing, feature selection, model selection, and statistical analysis. The goal is to develop the best calibration algorithm and assess the accuracy, precision, and reliability of ECSs in measuring NO_2 mixing ratio under various environmental conditions.

4.1 Setup of the calibration station

With the support of JCDecaux and SWM/MVG, a reference air quality monitoring station has been set up at the bus stop "Maxvorstadt", which can be used as the calibration station. It is a typical urban environment with high traffic density. The ECSs are located together with the inlet of CE-DOAS in a calibration station. As shown in Fig. 4.1a, the calibration station is equipped with a calibration box including CE-DOAS (Recall Sec. 2.1.2), 2BModel205 for O_3 measurements (2B Technologies), and Licor840A for CO_2 measurements (LI-COR Environmental). The calibration is done by comparing the sensor readings with the CE-DOAS measurements.

Data were collected from stationary CE-DOAS instruments and ECSs installed at the calibration station. The ECSs were connected to a Raspberry Pi, which recorded the voltage signals (Recall Sec. 2.2.2). These data were stored locally on an SD card and simultaneously transmitted to a cloud server for further analysis and visualization. Environmental parameters, including temperature, relative humidity, and pressure, were measured using a BME280 sensor (Bosch Sensortec, 2024). The data were initially collected at a frequency of approximately 8 Hz and subsequently resampled to 1-second intervals for upload to the server and storage in the database. During the calibration process, the data were further resampled to match the CE-DOAS measurement frequency (approximately every 5 seconds), resulting in a high-resolution dataset suitable for a wide range of applications.

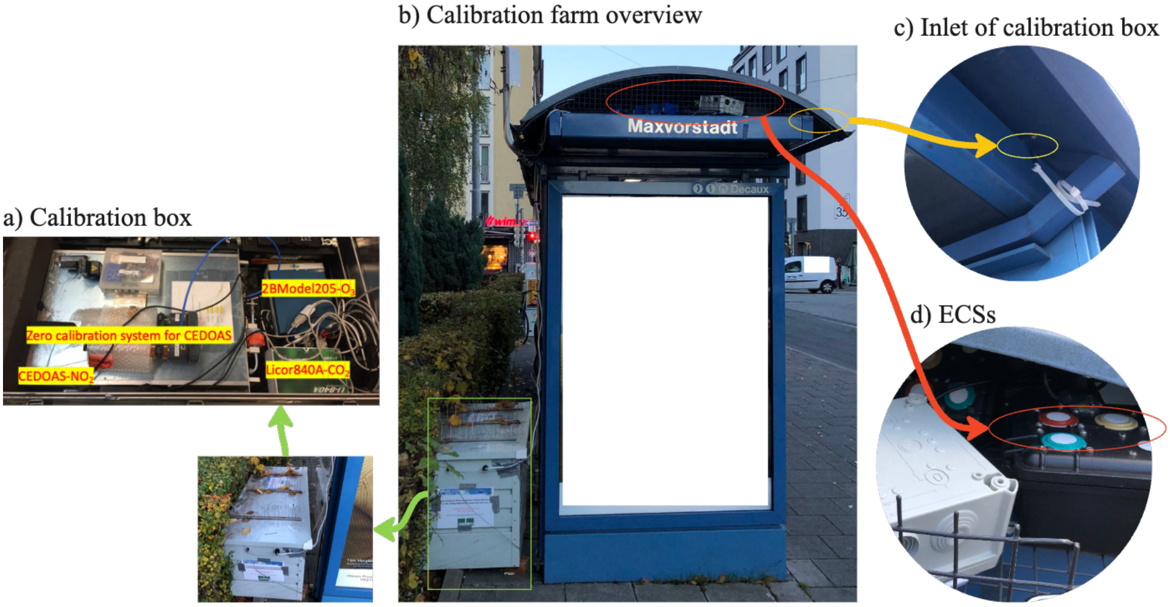

a) Calibration box

b) Calibration farm overview

c) Inlet of calibration box

d) ECSs

Figure 4.1: Reference air quality monitoring station as calibration station with ECSs and CE-DOAS instrument

4.2 Statistical Metrics for Validation

To comprehensively evaluate sensor performance, multiple statistical metrics are employed including fundamental metrics as well as those recommended by regulatory guidelines.

The correlation coefficient (r) is the most commonly used metric to assess the linear relationship between predicted and observed values, providing insight into how well the sensor tracks reference measurements. The Root Mean Square Error (RMSE) quantifies the magnitude of differences between predicted and observed values, offering a measure of overall prediction accuracy.

Beyond these fundamental metrics, regulatory guidelines emphasize the importance of additional performance indicators. According to EPA guidelines, the Mean Normalized Bias (MNB) and Coefficient of Variation (CV) should be calculated when evaluating the performance of at least three sensors (Clements et al., 2022). These metrics are particularly valuable for assessing sensor precision and bias across multiple devices. There are five tiers of performance criteria defined, ranging from Tier I (Education and Information) to Tier V (Regulatory Monitoring). Each tier has specific MNB and CV thresholds that sensors must meet to be considered suitable for different applications. These criteria help ensure that sensors are reliable and accurate enough for their intended use.

Furthermore, European standards provide data quality objectives (DQO) for air quality monitoring devices. European Parliament and Council of the European Union (2024) defines performance thresholds for fixed measurement methods and indicative measurement methods. These standards provide important benchmarks for evaluating whether low-cost sensors meet regulatory requirements for different applications. They are evaluated based on the uncertainty analysis of the sensor measurements. Uncertainty analysis provides a comprehensive framework for evaluating sensor reliability and measurement quality. This analysis follows the methodology outlined in regulatory guidelines to quantify the various sources of uncertainty in sensor measurements (Diez et al., 2022, 2024; European Commission, 2010). The uncertainty metrics enable comparison of sensor performance against regulatory requirements and provide guidance for appropriate applications based on measurement uncertainty levels.

Correlation coefficient (r)

$$r = \frac{\sum_{i=1}^{N}(y_i - \bar{y})(\hat{y}_i - \bar{\hat{y}})}{\sqrt{\sum_{i=1}^{N}(y_i - \bar{y})^2 \sum_{i=1}^{N}(\hat{y}_i - \bar{\hat{y}})^2}} \tag{4.1}$$

where:

- y_i is the reference measurement (from CE-DOAS),
- $\hat{y}_i$ is the sensor measurement (from ECS),
- $\bar{y}$ is the mean of reference measurements,
- $\bar{\hat{y}}$ is the mean of sensor measurements, and
- N is the total number of measurements.

Root Mean Square Error (RMSE):

The RMSE is a measure of the differences between values predicted by a model or an estimator and the values observed. It is defined as:

$$\text{RMSE} = \sqrt{\frac{1}{N}\sum_{i=1}^{N}(y_i - \hat{y}_i)^2}. \tag{4.2}$$

where:

- y_i is the observed value at time (or index) i,
- $\hat{y}_i$ is the predicted value at time (or index) i, and
- N is the total number of measurements.

Mean Normalized Bias (MNB) and Coefficient of Variation (CV):

Tier criteria from EPA for MNB and CV values are defined as follows:

- Tier I: Education and Information (-0.5 < MNB < 0.5 and CV < 0.5 for all pollutants).

- Tier II: Hotspot Identification and Characterisation ($-0.3 < \text{MNB} < 0.3$ and $\text{CV} < 0.3$ for all pollutants).
- Tier III: Supplemental Monitoring ($-0.2 < \text{MNB} < 0.2$ and $\text{CV} < 0.2$ for O_3, PM, CO, NO_2, SO_2 and TVOCs).
- Tier IV: Personal Exposure ($-0.3 < \text{MNB} < 0.3$ and $\text{CV} < 0.3$ for all pollutants).
- Tier V: Regulatory Monitoring ($-0.07 < \text{MNB} < 0.07$ and $\text{CV} < 0.07$ for O_3, $-0.10 < \text{MNB} < 0.10$ and $\text{CV} < 0.10$ for CO, SO_2, PM2.5 and PM10, and $-0.15 < \text{MNB} < 0.15$ and $\text{CV} < 0.15$ for NO_2).

Mean Normalized Bias (MNB) Calculation

The Mean Normalized Bias (MNB) is defined for multiple sensors compared against a single reference measurement. The formula is given by:

$$\text{MNB} = \frac{1}{M}\sum_{j=1}^{M}\left(\frac{1}{N}\sum_{i=1}^{N}\frac{s_{ij}-r_i}{r_i}\right). \tag{4.3}$$

where:

- s_{ij} is the measurement from sensor j at time (or index) i,
- r_i is the reference measurement at time (or index) i,
- M is the number of sensors, and
- N is the total number of measurements.

Coefficient of Variation (CV)

The Coefficient of Variation (CV) is a normalized measure of dispersion of sensor measurements. It is defined as the ratio of the standard deviation to the mean of the measurements. In the context of multiple concurrently recording sensors, let:

- s_{ij} denote the measurement from sensor j at time i,
- $\bar{s}_i$ denote the mean of the sensor measurements at time i,
- M be the number of sensors,
- N be the number of timestamps (concurrent measurements),
- $n = M \times N$ be the total number of measurements.

The pooled standard deviation is computed as:

$$\sigma = \sqrt{\frac{\sum_{i=1}^{N} \sum_{j=1}^{M} \left(s_{ij} - \bar{s}_i\right)^2}{n-1}}. \tag{4.4}$$

The overall mean (average pollutant value) is given by:

$$\mu = \frac{1}{n} \sum_{i=1}^{N} \sum_{j=1}^{M} s_{ij}. \tag{4.5}$$

Thus, the Coefficient of Variation (CV) is:

$$\mathrm{CV} = \frac{\sigma}{\mu} = \frac{\sqrt{\frac{\sum_{i=1}^{N} \sum_{j=1}^{M} \left(s_{ij} - \bar{s}_i\right)^2}{n-1}}}{\frac{1}{n} \sum_{i=1}^{N} \sum_{j=1}^{M} s_{ij}}. \tag{4.6}$$

The calculation of the Mean Normalized Bias (MNB) and Coefficient of Variation (CV) requires data from at least three sensors, evaluated at hourly time intervals. The MNB is used to assess sensor bias, while the CV measures sensor precision. These metrics are particularly useful for evaluating the performance of concurrently operating sensors, as they provide insights into how well the sensors agree with one another and with reference measurements.

Uncertainties (REU and AU)

Classification criteria for NO_2 sensors are defined based on hourly time intervals as follows:

- For fixed measurement methods (Defined as Class 1 in this thesis): 30 μg m^{-3} (16 ppb) or 15 % (whichever is larger).
- For indicative measurement methods (Defined as Class 2 in this thesis, less strict): 50 μg m^{-3} (26.6 ppb) or 25 % (whichever is larger).

The uncertainty analysis begins with establishing the relationship between sensor measurements and reference values using an ordinary least squares (OLS) model:

$$y_i = \beta_0 + \beta_1 x_i + \varepsilon_i \tag{4.7}$$

where:

- y_i represents the ith reference measurement,
- x_i is the ith sensor measurement,
- β_0 and β_1 are the regression coefficients, and
- ε_i is the residual error term.

The residual sum of squares (RSS) quantifies the total unexplained variance in the model:

$$\text{RSS} = \sum_{i=1}^{n} \left[y_i - \left(\beta_0 + \beta_1 x_i \right) \right]^2 \tag{4.8}$$

From this, the error variance is calculated to estimate the random uncertainty component:

$$\sigma^2 = \frac{\text{RSS}}{n-2} \tag{4.9}$$

The systematic deviation from the ideal 1:1 relationship between sensor and reference measurements is captured by:

$$e_{c,i} = \left(\beta_0 + \beta_1 x_i - x_i \right)^2 \tag{4.10}$$

This term accounts for both bias (intercept deviation from zero) and scaling errors (slope deviation from unity).

Finally, the relative expanded uncertainty (REU) provides a comprehensive measure that combines both random and systematic uncertainty components:

$$u_{REU,i} = k \times \frac{\sqrt{\sigma^2 - u_\xi^2 + e_{c,i}}}{y_i} \times 100 \tag{4.11}$$

where:

- $u_{REU,i}$ is the relative expanded uncertainty (in %) at ith measurement,
- k is the coverage factor ($k = 1.96$ is used for 95 % confidence interval),
- u_ξ^2 represents the uncertainty of the reference measurement (e.g., CE-DOAS)

The relative expanded uncertainty provides a normalized measure of measurement quality, while the Absolute Uncertainty (AU) gives the actual magnitude of uncertainty in the same units as the measurement. The absolute uncertainty is calculated as:

$$u_{AU,i} = \frac{u_{REU,i}}{100} \times y_i \tag{4.12}$$

where:

- $u_{AU,i}$ is the absolute uncertainty at ith measurement,
- y_i is the reference measurement value at ith measurement.

4.3 Statistical Analysis

4.3.1 Feature Selection

The selection of relevant features is crucial for accurate sensor calibration. Factors such as WE, AE, environmental factors, and environmental transients have the potential to influence NO_2 sensor readings. These features are evaluated for their impact on sensor performance. Factors that influence the precision and accuracy of ECSs include temperature, relative humidity, pressure, cross-sensitivity, and environmental transients. These factors are considered in the calibration algorithm to improve sensor performance.

4.3.1.1 Working Electrode (WE) and Auxiliary Electrode (AE) Signals

Recall the introduction of ECSs in Sec. 2.2.2, the ECSs are equipped with four electrodes and have two voltage outputs: WE and AE. The WE is proportional to the mixing ratio of the target gas, while the AE is used to correct for environmental factors. Their ratio ($\frac{WE}{AE}$) is used to calculate the NO_2 mixing ratio, which is then compared to the reference value from the CE-DOAS instrument.

4.3.1.2 Cross-sensitivity

Cross-sensitivity refers to the response of a sensor to gases other than the target gas. For NO_2 sensors, cross-sensitivity to O_3 is particularly significant due to the chemical relationship between these two pollutants and the similar electrochemical properties that affect sensor response. The correlation between NO_2 and O_3 sensors is evident in field measurements, where changes in O_3 mixing ratios can influence NO_2 sensor readings even when actual NO_2 levels remain constant.

This cross-sensitivity occurs because both gases can undergo similar electrochemical reactions at the sensor electrodes, leading to interference in the measurement signal. The magnitude of this interference varies with environmental conditions, particularly temperature and humidity, making it essential to account for O_3 mixing ratios when calibrating NO_2 sensors.

To address this cross-sensitivity, both NO_2 and O_3 sensors are deployed together in the calibration setup. The ratio of WE and AE signals for both NO_2 and O_3 sensors ($\frac{WE_{NO_2}}{AE_{NO_2}}$ and $\frac{WE_{O_3}}{AE_{O_3}}$) is incorporated into the calibration models to correct for the interference effects. This approach allows the calibration algorithms to distinguish between genuine NO_2 signals and those caused by O_3 interference, significantly improving measurement accuracy.

4.3.1.3 Environmental Factors: Temperature, Relative Humidity, Pressure

Environmental factors such as temperature, relative humidity, and pressure can influence sensor readings. These factors are measured by the BME280 sensor (Bosch Sensortec, 2024) and are used to correct the sensor output for environmental conditions.

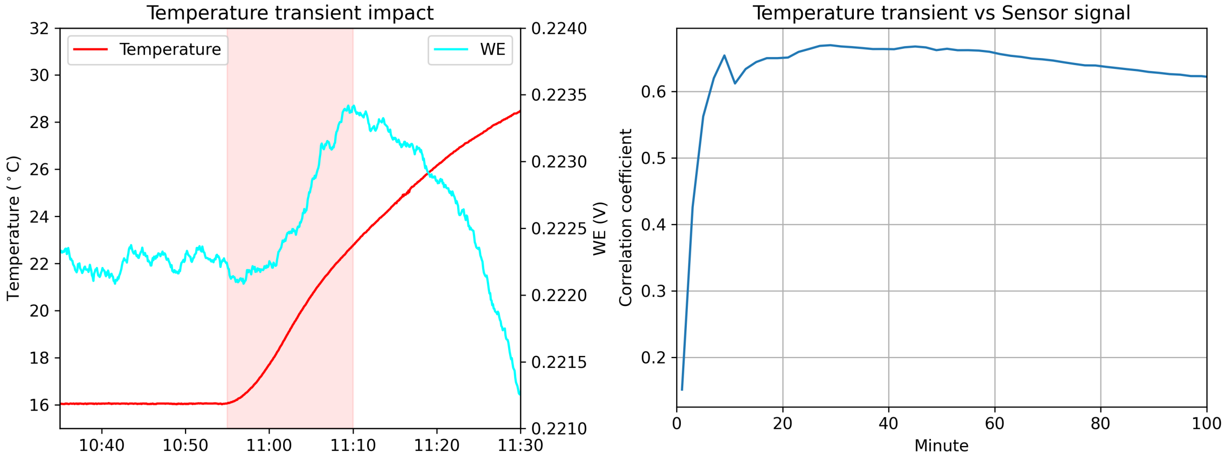

Figure 4.2: Time series illustrating the impact of temperature transients on sensor readings. The shaded region highlights the 15-minute interval where rapid temperature changes cause significant deviations in sensor output, identified as the optimal window for applying transient correction.

4.3.1.4 Environmental Transients

Environmental transients significantly affect sensor readings, particularly for electrochemical sensors used in mobile and portable applications. These transient effects occur when environmental conditions change rapidly, causing temporary fluctuations in sensor output that can lead to measurement errors.

According to Alphasense Limited (d), environmental transients can cause measurement errors even after applying basic correction algorithms. Additionally, real-world environments differ significantly from controlled laboratory conditions where correction factors are typically determined. These current spikes caused by transients typically decay over time, and their direction and magnitude depend on whether environmental factors are increasing or decreasing. This creates characteristic positive and negative current patterns that must be accounted for in calibration algorithms. This information is incorporated into calibration algorithms to identify and correct for transient-induced measurement errors. The correction approach involves detecting rapid environmental changes and applying appropriate compensation factors during periods when sensors may exhibit unstable behavior due to environmental transitions (Alphasense Limited, b; Buck et al., 2013).

Take temperature as an example. Rapid changes in temperature can lead to significant measurement errors in sensor readings. These errors arise from the sensor's temperature-dependent electrochemical reaction kinetics and electrode response characteristics, which respond differently during transient versus steady-state temperature conditions.

To mitigate these effects, the calibration algorithm incorporates a transient correction factor that adjusts sensor output based on the rate of environmental transients. This approach helps stabilize sensor readings during periods of rapid environmental transitions, ensuring more accurate and reliable measurements. It is particularly useful for applications where sensors operate under dynamic environmental conditions, such as mobile or portable monitoring systems. As illustrated in Fig. 4.2, the optimal time range for transient correction is set to 15 minutes, where the correlation between temperature transients and sensor readings reaches its maximum. The time series of temperature transients and their effects on sensor readings is shown in Fig. 4.2. The shaded area indicates the period during which transient correction is applied. When temperature started increasing, sensor readings initially exhibited an unusual increase for 15 minutes, followed by a gradual decline along with the raising temperature, demonstrating the direct impact of temperature transients on sensor performance. This time range is sufficient to capture the transient effects of environmental changes on sensor readings and is chosen based on the typical response time of the sensor and the expected duration of transient effects when other parameters are held relatively constant.

4.3.2 Model Selection

The choice of regression model is another critical factor for achieving robust calibration. Generalized Additive Model (GAM) is selected for their flexibility in capturing non-linear relationships. GAMs are particularly well-suited for handling complex interactions and cyclic variables, making them ideal for calibrating air quality sensors. For comparison, the Generalized Linear Model (GLM) is also evaluated, assuming linear relationships among covariates. As discussed in Sec. 3.1.1, Multiple Linear Regression (MLR), the most commonly used regression method, and Random Forest (RF) regression, a high-performing machine learning model, are also included in the evaluation. Furthermore, raw manufactory methods using only sensor outputs and Convolutional Neural Networks (CNN) are evaluated for comparison. These models' performance are assessed using the same validation metrics including r, RMSE, MNB, CV, REU, and AU to compare the effectiveness of different calibration approaches.

4.3.2.1 Raw Calibration method from sensor outputs (Raw)

The "raw" method constitutes the most fundamental approach for determining gas concentrations, relying exclusively on the sensor's raw voltage outputs without incorporating environmental parameters or complex algorithmic corrections. This method derives the pollutant mixing ratio by applying a simple linear regression model directly to the working electrode (V_{WE}) and auxiliary electrode (V_{AE}) signals. The calculation is expressed as:

$$y_{NO_2} = \beta_0 + \beta_1 V_{WE} + \beta_2 V_{AE} + \varepsilon \tag{4.13}$$

where y_{NO_2} is the NO_2 mixing ratio from CE-DOAS; β_0 is the intercept term; β_n is the coefficient of V_{WE} and V_{AE}; and ε is the residual error term.This linear relationship assumes that the sensor response depends primarily on the target gas concentration, with the auxiliary electrode providing a baseline correction. While computationally efficient and straightforward to implement, this method fails to account for complex environmental dependencies or cross-sensitivities, frequently resulting in substantial measurement errors under field conditions. Consequently, it serves primarily as a comparison for evaluating the enhancements achieved by advanced calibration algorithms.

4.3.2.2 Convolutional Neural Networks (CNN)

Convolutional Neural Networks (CNN) are employed as a representative deep learning approach for sensor calibration. While primarily known for image processing, 1D-CNNs are particularly effective for time-series data regression. Even without including explicit time information as a feature, the model could capture temporal dependencies and local patterns by processing sequences of input data. In this study, a 1D-CNN architecture is used to model the non-linear mapping between input features and NO_2 mixing ratio:

$$y_{NO_2} = f_{\mathrm{CNN}}\left(x_{t-L+1}, \ldots, x_t\,; \boldsymbol{\theta}\right) + \varepsilon \tag{4.14}$$

where y_{NO_2} is the predicted NO_2 mixing ratio at time t; $x_{t-L+1}, \ldots, x_t$ denote the sequence of input vectors over a sliding window of length L (including sensor signals, environmental variables, and transients); $f_{\mathrm{CNN}}(\cdot)$ is the convolutional neural network with trainable parameters $\boldsymbol{\theta}$; and ε is the residual error term.

The 1D-CNN extracts temporal features and patterns from the sequential inputs by applying convolutional filters and pooling operations. These filters capture local dependencies and trends, such as the delayed response of sensors to rapid concentration changes or transient environmental effects. The final fully connected layers then perform the regression from learned feature representations to NO_2 mixing ratio. This structure allows the model to learn complex, non-linear dynamic relationships directly from raw data without extensive manual feature engineering. The CNN model therefore serves to demonstrate the potential of deep learning techniques in enhancing calibration accuracy compared to traditional statistical methods.

4.3.2.3 Random Forest (RF)

Random Forest (RF) is essentially an ensemble learning method that combines multiple decision trees to create a robust predictive model based on the bagging (bootstrap aggregating) approach. Bagging is a technique that reduces model variance and improves generalization by training multiple models on different subsets of the training data and averaging their predictions (Breiman, 1996). The RF algorithm extends this concept by introducing additional randomness through feature selection at each split. It operates by creating each tree using a bootstrap sample of the original training data, with approximately 63 % of observations used for training each tree and the remaining 37 % serving as out-of-bag (OOB) samples for internal validation. At each node split, a random subset of features is considered, which reduces overfitting, decreases sensitivity to individual covariates, and improves generalization. The final prediction is the average of all individual tree predictions, providing built-in uncertainty quantification through the variance of tree predictions.

RF offers several advantages including automatic feature selection, handling of non-linear relationships, robustness to outliers, and built-in variable importance measures. The model can capture complex interactions between environmental factors without explicit specification of interaction terms. However, RF models are less interpretable than parametric approaches and may still suffer from overfitting to the calibration dataset, particularly when deployed over extended periods with changing environmental conditions.

The model is implemented using the sklearn library (Pedregosa et al., 2011) in Python, which provides efficient and scalable implementations of the RF algorithm.

The RF model for this study is configured as follows:

$$y_{NO_2} = \frac{1}{B}\sum_{b=1}^{B} T_b(x_1, x_2, ..., x_{12}) + \varepsilon \tag{4.15}$$

where y_{NO_2} is the NO_2 mixing ratio from CE-DOAS; B is the number of trees; T_b represents the b-th decision tree; and the input features x_1 through x_{12} include the same covariates as other models.

The hyperparameters of the RF model are optimized using grid search with cross-validation to find the best combination of parameters such as the number of trees, maximum depth, and minimum samples per leaf. The model is trained on the calibration dataset and evaluated on the application dataset to assess its performance.

4.3.2.4 Multiple Linear Regression (MLR)

Multiple Linear Regression (MLR), as introduced in Sec. 3.1.1.1.2, is included in this evaluation for comparison. The model formulation for this study is:

$$y_{NO_2} = \beta_0 + \sum_{n=1}^{12} \beta_n x_n + \varepsilon \tag{4.16}$$

where y_{NO_2} is the NO_2 mixing ratio from CE-DOAS; β_0 is the intercept term; β_n is the coefficient of the nth covariate; x_n represents the nth covariate including $\frac{WE_{NO_2}}{AE_{NO_2}}$, $\frac{WE_{O_3}}{AE_{O_3}}$, $\frac{WE}{AE} \times t$, $\frac{WE}{AE} \times \frac{1}{rh}$, temperature, relative humidity, pressure, and environmental transients; and ε is the residual error term.

4.3.2.5 Generalized linear model (GLM) regression

GLM is a generalization of the linear regression model, which allows the response variable to have an error distribution other than a normal distribution. The model in this study is shown in Equation (4.17).

$$g(y_{NO_2}) = \beta + \sum_{n=1}^{12} \beta_n x_n + \varepsilon \tag{4.17}$$

where g(·) is the link function; y_{NO_2} is the NO_2 mixing ratio from CE-DOAS; β is the intercept term; β_n is the coefficient of the nth covariate; x_n is the nth covariate including $\frac{WE_{NO_2}}{AE_{NO_2}}$, $\frac{WE_{O_3}}{AE_{O_3}}$, $\frac{WE}{AE} \times t$, $\frac{WE}{AE} \times \frac{1}{rh}$, temperature, relative humidity, pressure, and environmental transients in the past minutes; ε is the residual. A gamma distribution has been employed because the NO_2 mixing ratio is strictly positive. The link function is the log-link function, which introduces a multiplicative effect. In the case of limited data points, Y may not be Gamma distributed. In this case, the model is fitted with the Gaussian distribution.

4.3.2.6 Generalized additive model (GAM) regression

Generalized Additive Model (GAM) is a white-box regression technique, which applies the flexible smooth functions for the covariates (Hastie, 1990; Hastie and Tibshirani, 1986). GAM is particularly useful for capturing non-linear relationships and interactions between covariates, making it suitable for complex trends. The model in this study is shown in Equation (4.18).

$$g(y_{NO_2}) = \beta + \sum_{n=1}^{12} s(x_n) + \varepsilon \tag{4.18}$$

where $g(\cdot)$ is the link function; y_{NO_2} is the NO_2 mixing ratio from CE-DOAS; β is the intercept term; $s(\cdot)$ denotes the smooth spline function applied to each covariate; x_n is the nth covariate including $\frac{WE_{NO_2}}{AE_{NO_2}}$, $\frac{WE_{O_3}}{AE_{O_3}}$, $\frac{WE}{AE} \times t$, $\frac{WE}{AE} \times \frac{1}{rh}$, temperature, relative humidity, pressure, and environmental transients in the past minutes; ε is the residual. A gamma distribution has been employed because the NO_2 mixing ratio is strictly positive. The link function is the log-link function, which introduces a multiplicative effect. Same as GLM, the model is fitted with log-link function and the gamma distribution if applicable.

4.3.3 Regression Model Evaluation

The performance of each regression model was evaluated using multiple metrics including r, RMSE, MNB, CV, REU, and AU. The r and RMSE were computed on the high-frequency (5-second) data, whereas MNB, CV, REU, and AU were assessed using hourly values to comply with EPA and EU standards. Together, these metrics offer a comprehensive view of each model's accuracy, precision, and overall reliability.

Table 4.1: Performance metrics for all models (r and RMSE evaluated on 5-second data, AU, MNB and CV evaluated on hourly data).

Type	Metrics	Raw	CNN	RF	MLR	GLM	GAM
Calibration (60 days)	r	0.79	0.90	0.90	0.87	0.85	0.87
	RMSE	2.06	1.01	0.95	1.22	1.23	1.06
	AU	3.50	1.72	1.72	2.37	2.45	2.04
Application (55 days)	r	0.56	0.65	0.58	0.67	0.45	0.61
	RMSE	2.90	2.09	3.00	2.32	2.19	2.04
	AU	7.47	3.56	4.67	4.14	4.36	3.38
Calibration (15 days)	MNB	0.355	0.136	0.054	0.059	0.102	0.083
	CV	0.061	0.101	0.031	0.102	0.117	0.095
Application (15 days)	MNB	0.661	0.243	0.488	0.213	0.143	0.073
	CV	0.024	0.126	0.069	0.130	0.103	0.080

The performance metrics summarized in Table 4.1 provide a comprehensive overview of model performance across calibration and application periods. Figure 4.3 and Figure 4.4 show

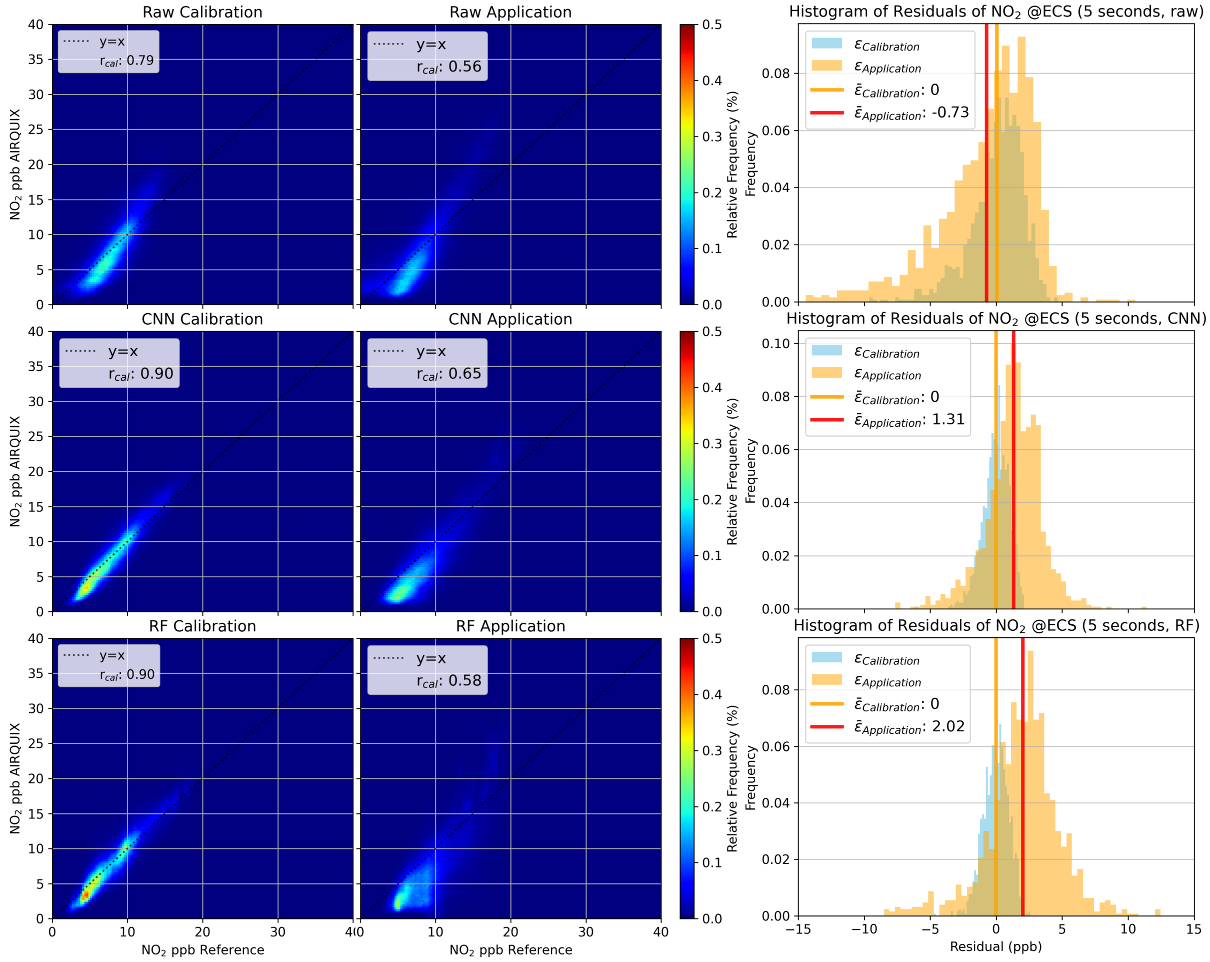

Figure 4.3: Comparison of model performance during calibration (left column) and application (middle column) periods. The 2D histograms display the density of predicted vs. reference NO_2 mixing ratios. The dashed black line indicates the ideal 1:1 relationship. The right column shows the distribution of residuals for both periods, illustrating the shift in error distribution over time for Raw, CNN, and RF models.

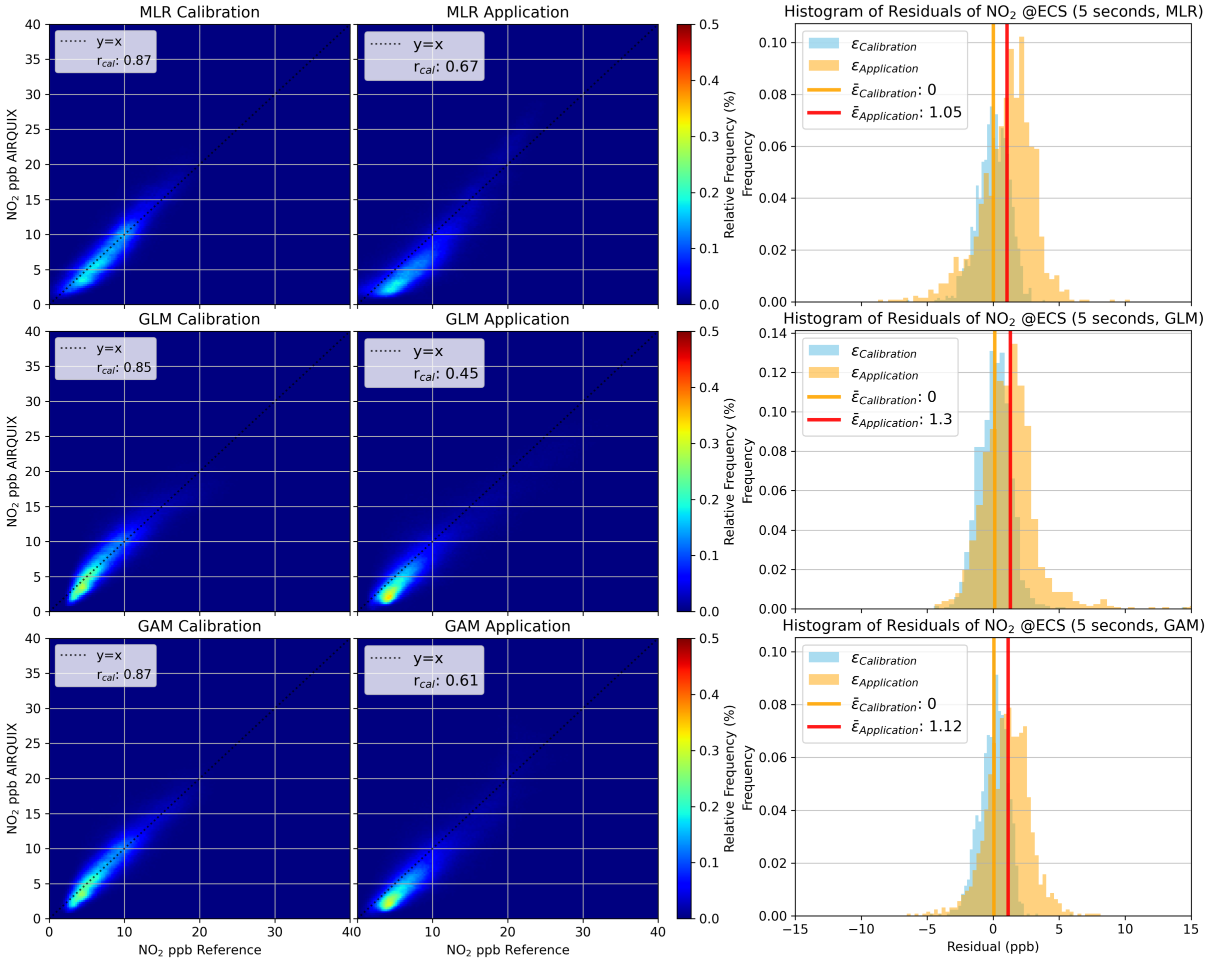

Figure 4.4: Comparison of model performance for MLR, GLM, and GAM models. All others are the same as in Fig. 4.3.

the 2D histogram plots and residuals histogram plots comparing calibration and application data for Raw, CNN, RF, MLR, GLM, and GAM regressions using the 5-second time interval data. The calibration data spanning 60 days was used to train the models, while the application data from 55 days after calibration was used to evaluate model performance. The 2D histogram plots illustrate the distribution of predicted NO_2 mixing ratios against reference NO_2 mixing ratios, with the color intensity indicating the density of points in each bin. The histogram plots on the right side show the distribution of residuals for each model during both calibration and application periods.

During the calibration period, the RF and CNN models demonstrated the strongest correlations ($r = 0.90$) with reference NO_2 mixing ratios, achieving low RMSEs of 0.95 ppb and 1.01 ppb, respectively. The GAM regression showed a slightly lower correlation ($r = 0.87$) with an RMSE of 1.06 ppb. The MLR model exhibited an equivalent correlation of $r = 0.87$ but a higher RMSE of 1.22 ppb, while the GLM regression showed a correlation of $r = 0.85$ with an RMSE of 1.23 ppb. The raw regression yielded the lowest correlation ($r = 0.79$) and the highest RMSE of 2.06 ppb.

The application period revealed different performance patterns. The performances of RF and CNN model degraded significantly, showing correlations of $r = 0.58$ and $r = 0.65$ respectively. The MLR model demonstrated improved stability with correlation of $r = 0.67$. The GAM regression maintained reasonable performance with correlation of $r = 0.61$. The GLM regression showed correlation of $r = 0.45$, while the raw model exhibited a correlation of $r = 0.56$ during the application period.

A trend analysis for stability was conducted using daily RMSE. Fig. 4.5 presents the RMSE values increasing trend for all models during application periods except the GAM regression. It can be observed that the GAM regression maintained the most stable performance with consistent RMSE. The MLR and GLM regression showed gradually increasing RMSE. Although the RF model achieved the lowest initial RMSE of 0.94 ppb at calibration period, it exhibited the steepest increasing trend throughout the application period. This rapid degradation in the RF model suggests significant overfitting to the training data, causing it to struggle with new environmental conditions or pollutant levels encountered during the application phase. Consequently, more attention should be paid to the overfitting issue inherent in the RF model, which makes it difficult to use and potentially inapplicable for long-term monitoring. In contrast, the GAM's ability to maintain a flat RMSE profile highlights its robustness and superior generalization capabilities, effectively handling temporal shifts without the substantial drift observed in the other models.

The Mean Normalized Bias (MNB) and Coefficient of Variation (CV) are also calculated to assess model performance. Three sensors were concurrently deployed in the calibration station to evaluate the MNB and CV metrics. The dataset is divided into two parts for calibration and application. The first half (15 days) of the dataset is used for calibration, while the second half (15 days) is used for prediction. The MNB and CV are calculated for both calibration and application periods to evaluate model performance over time.

Figure 4.6 shows the MNB and CV for all models. The Raw model yielded unacceptable results and is therefore excluded from this discussion. It can be observed that all other models achieved MNB and CV values within Tier V during the calibration period, indicating top-tier performance according to EPA criteria. However, the RF model showed significant increases in

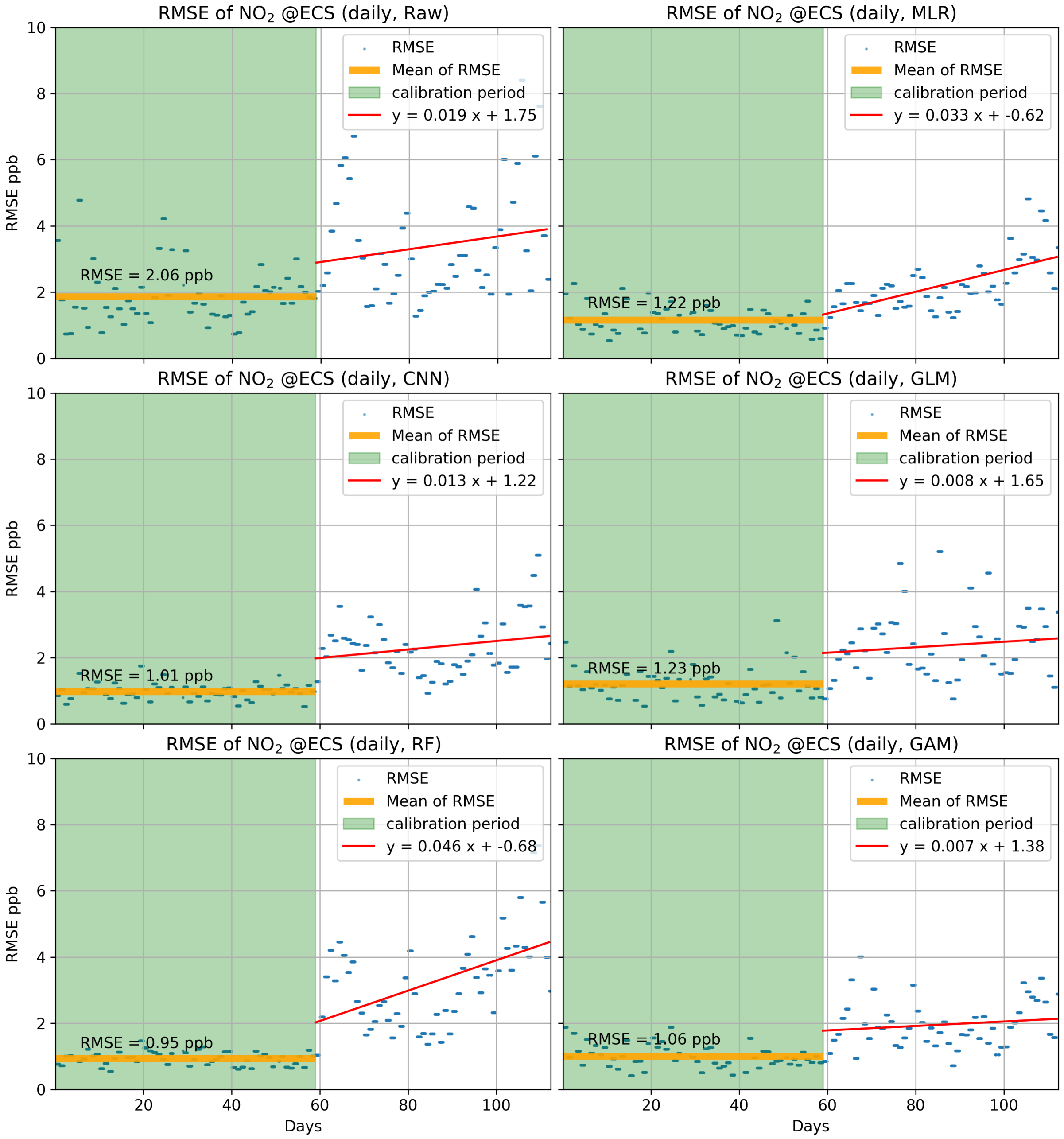

Figure 4.5: Daily RMSE trends for Raw, CNN, RF, MLR, GLM, and GAM models over the entire study period. The vertical dashed line separates the calibration period (first 60 days) from the application period (subsequent 55 days), illustrating the stability and degradation of model performance over time.

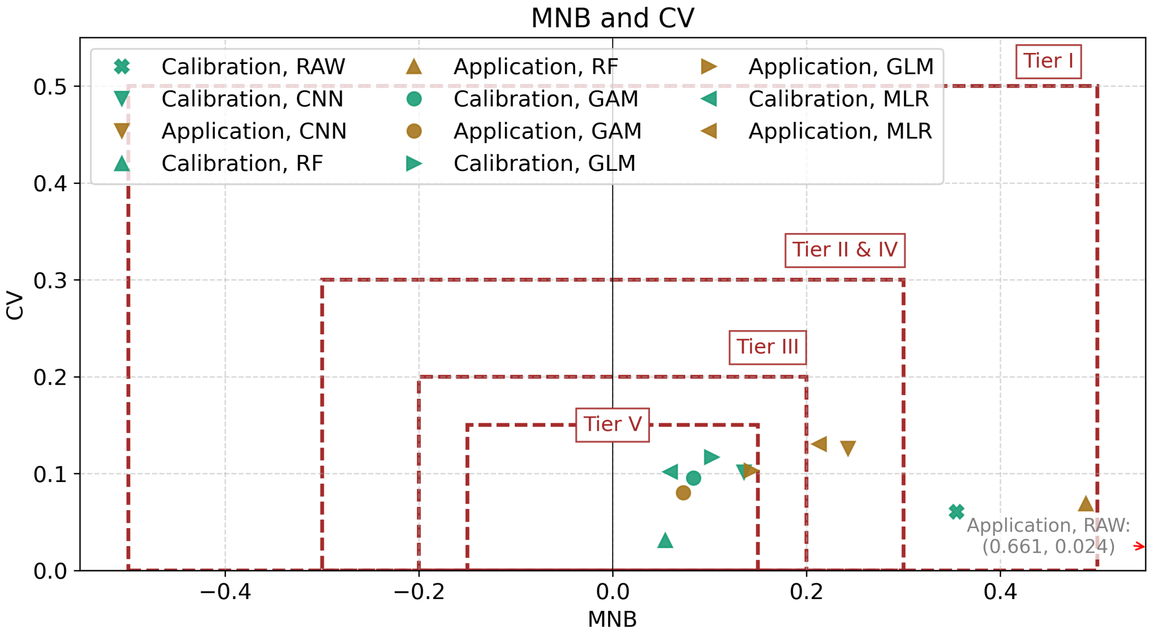

Figure 4.6: Mean Normalized Bias (MNB) and Coefficient of Variation (CV) for Raw, CNN, RF, MLR, GLM, and GAM models. The plot compares performance during the calibration period (first 15 days) and the application period (subsequent 15 days). The shaded regions represent different EPA performance tiers, with the innermost box (Tier V) indicating the strictest regulatory monitoring standards.

MNB and CV during the application period, indicating a degradation in performance (dropping to Tier I). Both the MLR and CNN models also exhibited increases in MNB and CV, placing them in Tiers II and IV during the application period. The GLM showed a modest increase (remaining in Tier V), while the GAM regression maintained the most stable MNB and CV values (remaining in Tier V). This demonstrates that GAM regression achieves reliable calibration results that meet regulatory standards for air quality monitoring applications.

The uncertainty analysis reveals additional insights into model performance characteristics. While distinguishing clear performance differences between models based solely on REU plots is challenging due to the low NO_2 mixing ratios, the absolute uncertainty analysis provides more definitive conclusions regarding model stability and reliability. This analysis highlights significant differences in model performance and long-term stability. During the calibration period (Figs. 4.7 and 4.8), the RF and CNN models achieved the lowest absolute uncertainty of 1.72 ppb, followed by GAM (2.04 ppb), MLR (2.37 ppb), GLM (2.45 ppb), and Raw (3.50 ppb). However, the application period (Figs. 4.9 and 4.10) revealed a markedly different pattern that highlights the limitations of complex methods. The absolute uncertainties of the RF and CNN models increased substantially to 4.67 ppb and 3.56 ppb, respectively, during the application period. This represents an increase to 271.5 % and 207 % of their calibration phase values. In contrast, the other models demonstrated better long-term stability, with GAM achieving 3.38 ppb, MLR reaching 4.14 ppb, and GLM exhibiting 4.36 ppb. The Raw model showed the highest absolute uncertainty of 7.47 ppb during the application period since it lacks any calibration adjustments.

Notably, the MLR model displayed anomalous behavior at low mixing ratios during both calibration and application periods, with these anomalies becoming more pronounced and leading to model failure at low mixing ratios during the application phase. The RF model showed anomalies at higher mixing ratios, indicating its sensitivity to mixing ratio ranges outside the training data. This performance degradation demonstrates the limitation of RF models. They excel at capturing complex patterns during calibration, but suffer from overfitting and poor generalization while exceeding the mixing ratio range covered by the training data (Kim et al., 2022; Margaritis et al., 2021). This constraint becomes particularly problematic in real-world deployments where sensors encounter conditions outside the original calibration range. In contrast, white-box models such as MLR, GAM, and GLM maintain more consistent performance over time, with GAM demonstrating the best long-term stability and reliability.

These findings highlight that RF models, despite their initial superior performance, are not always the optimal choice for sensor calibration. The rapid performance degradation over time, combined with their black-box nature that provides limited interpretability, makes them less suitable for long-term environmental monitoring applications. Sometimes the white-box model performance is equivalent to or even better than black-box models (Kim et al., 2022; Margaritis et al., 2021), particularly when considering long-term stability and reliability.

GAM emerges as the most suitable choice for NO_2 sensor calibration due to several key advantages. First, GAM maintains more consistent performance over time, as evidenced by its smaller uncertainty increase between calibration and application periods. Second, GAM provides better interpretability compared to RF models through its smooth functions, allowing researchers to understand how individual features influence sensor responses. Third, GAM offers an optimal balance between model complexity and generalization capability, avoiding the overfitting issues

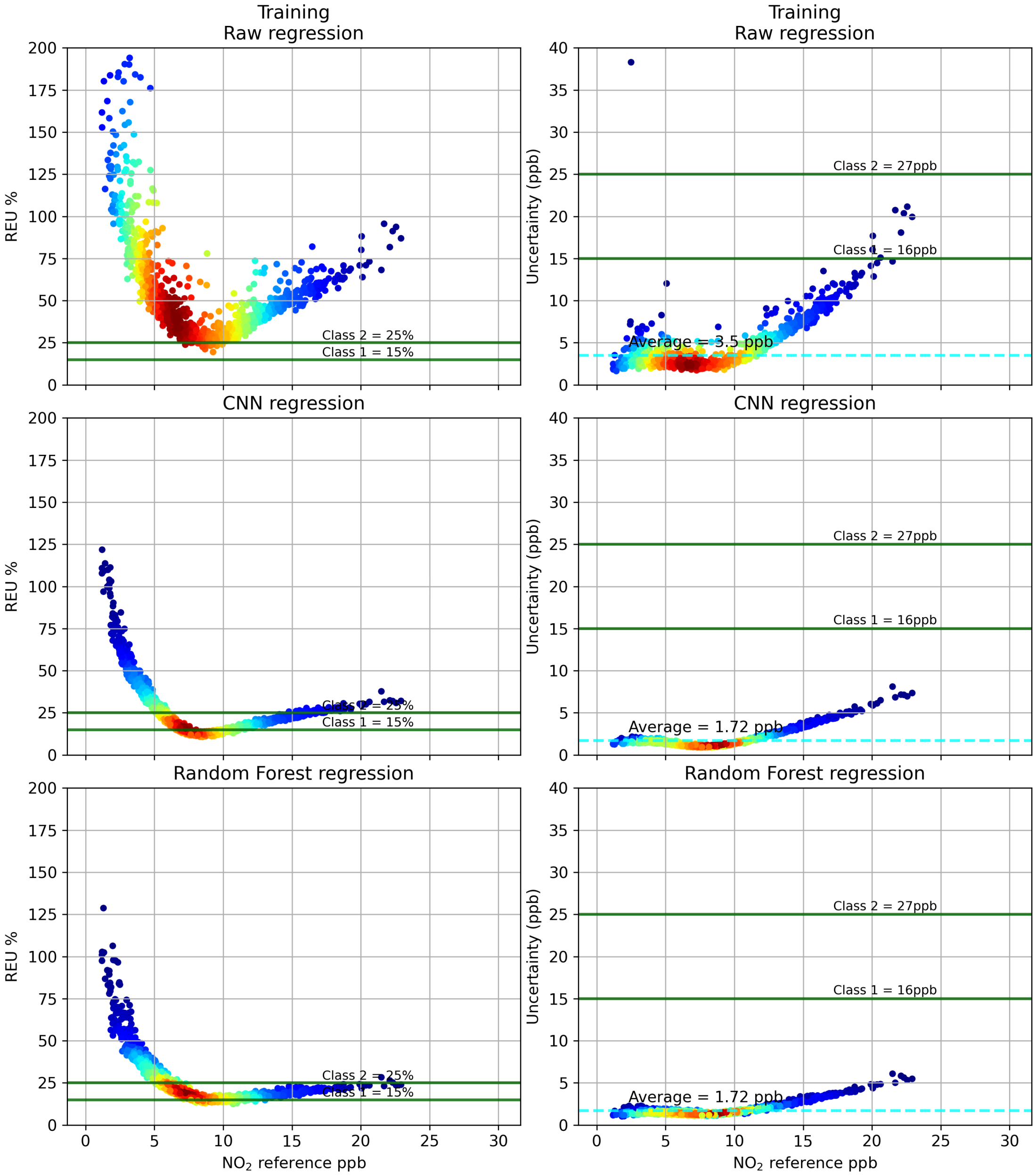

Figure 4.7: Relative Expanded Uncertainty (REU) (left column) and Absolute uncertainty (right column) for Raw, CNN, and RF models during the calibration period. The color of the points is a representation of a Kernel Density Estimate (KDE) using Gaussian kernels calculated from SciPy python package (Virtanen et al., 2020), ranging from low (blue) to high (red). The green lines represent the uncertainty limits for Class 1 (fixed measurement methods) and Class 2 (indicative measurement methods) as defined by European standards.

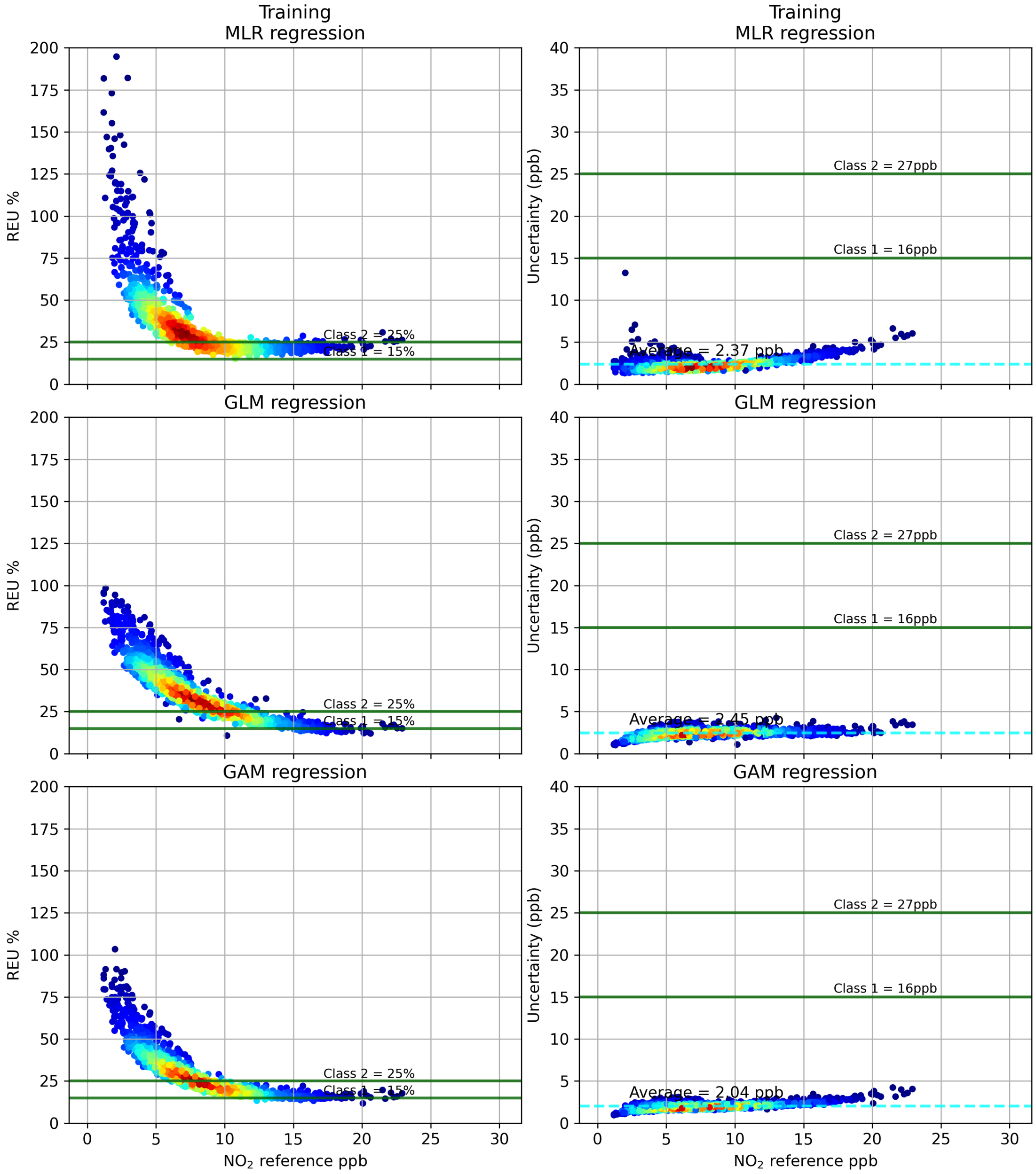

Figure 4.8: Relative Expanded Uncertainty (REU) and Absolute uncertainty (AU) for MLR, GLM, and GAM models. All others are the same as in Fig. 4.7.

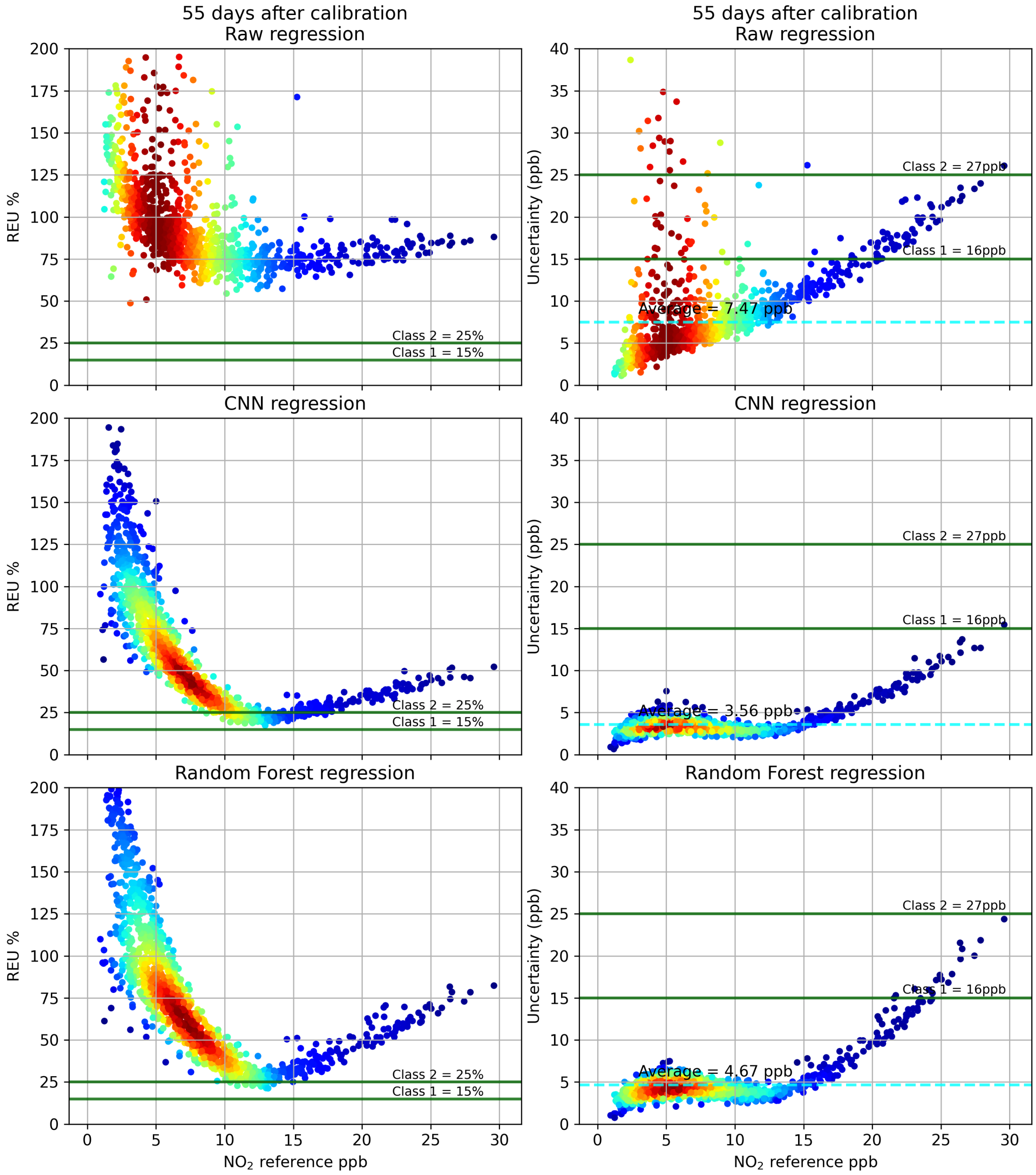

Figure 4.9: Relative Expanded Uncertainty (REU) (left column) and Absolute uncertainty (right column) for Raw, CNN, and RF models during the application period (55 days after calibration). All others are the same as in Fig. 4.7.

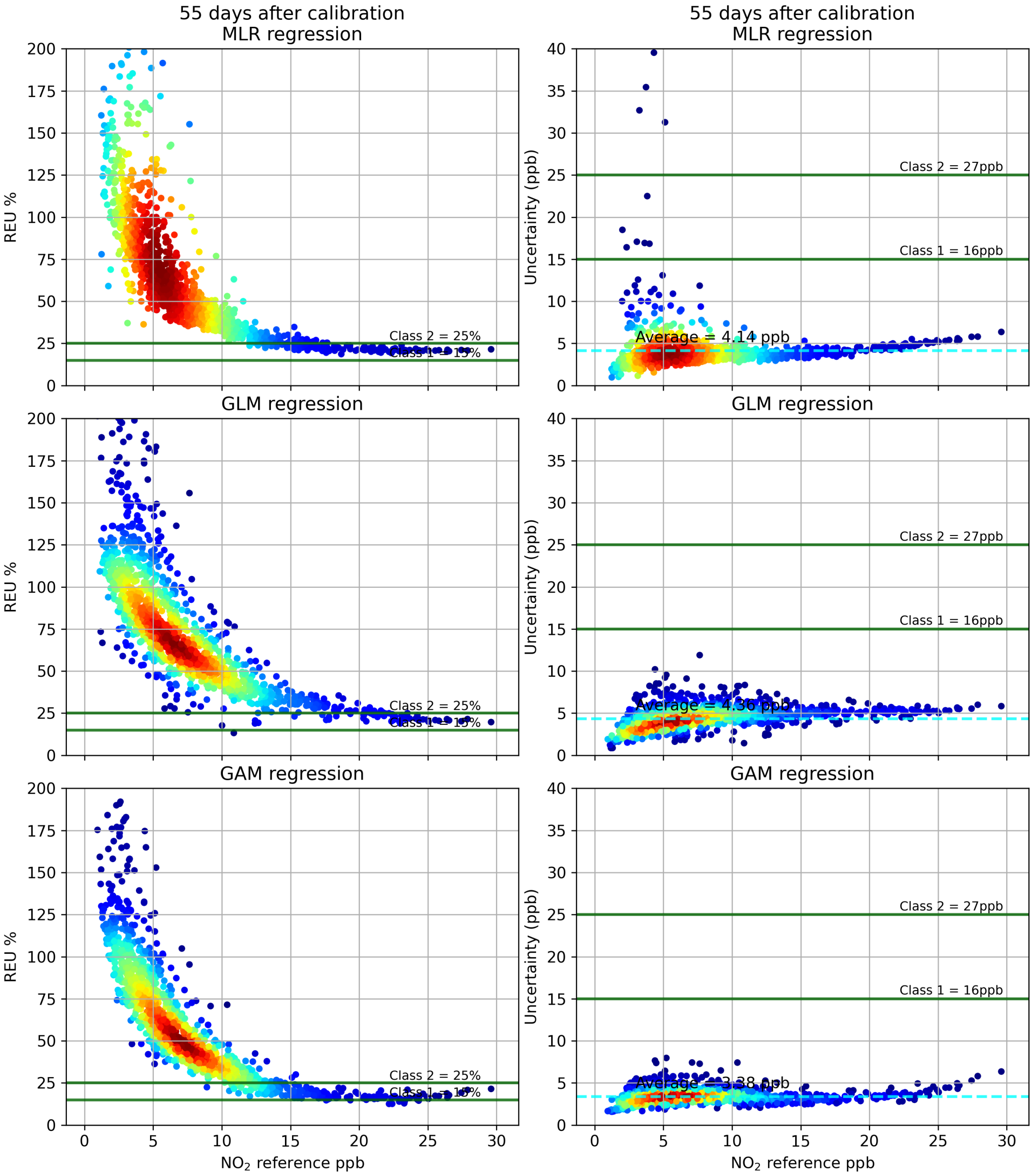

Figure 4.10: Relative Expanded Uncertainty (REU) (left column) and Absolute uncertainty (right column) for MLR, GLM, and GAM models during the application period (55 days after calibration). All others are the same as in Fig. 4.8.

commonly associated with ensemble methods while still capturing non-linear relationships effectively. These make GAM the optimal choice for this study. While RF models may appear attractive due to their excellent initial performance, their rapid degradation over time and lack of interpretability limit their practical utility in environmental monitoring applications where consistent long-term performance is crucial.

4.4 Conclusion

This chapter highlights the critical role of covariates and introduces a comprehensive evaluation methodology for calibrating low-cost NO_2 ECSs. The methodology addresses key challenges in sensor calibration including environmental interference, temporal drift, and model selection for reliable long-term performance.

The evaluation framework establishes clear performance criteria based on regulatory standards, with uncertainty thresholds defined for different measurement classes. The comprehensive statistical analysis incorporates *r*, RMSE, MNB, CV, REU, and AU to thoroughly assess sensor reliability against regulatory requirements.

A major advancement in this approach is the use of high-frequency (5-second) data for both calibration and evaluation, except where ho, whereas the evaluation is performed using hourly data to comply with EU and EPA regulationsly data are required to comply with EU and EPA regulations. This fine temporal resolution captures rapid environmental changes and transient effects that would be lost in time-averaged measurements. It also allows for a more precise assessment of sensor response characteristics and the patterns of environmental interference. By producing a much larger dataset, high-frequency sampling supports robust statistical analyses and more effective model training. Furthermore, it improves the detection and correction of short-lived measurement artifacts. Such temporal resolution is especially important for electrochemical sensors, which often exhibit swift responses to sudden changes in humidity, temperature, or co-existing gases.

Feature selection analysis confirms that working electrode and auxiliary electrode signals, along with environmental factors and environmental transients, significantly influence sensor performance. The incorporation of environmental corrections proves essential for addressing sensor instability caused by rapid environmental changes, which can only be properly captured and corrected with high-frequency data sampling.

Model comparison reveals that while Random Forest models achieve excellent initial performance, they suffer from significant performance degradation over time due to overfitting. Multiple Linear Regression and Generalized Linear Models show reasonable performance but with limitations in capturing complex relationships.

Generalized Additive Models (GAM) emerge as the optimal choice for NO_2 sensor calibration. GAM demonstrates superior long-term stability, maintains consistent performance over time, and provides the best balance between capturing non-linear relationships and ensuring reliable generalization. The model shows the smallest increase in AU, REU, MNB, and CV between calibration and application periods, making it the most suitable approach for practical sensor calibration applications.

This evaluation methodology, with its high temporal resolution data processing and comprehensive model assessment, establishes a robust foundation for assessing low-cost sensor performance and will be applied throughout subsequent chapters to evaluate sensor deployment under various conditions.

Chapter 5

Prototype Development of the AIR QUality Inspection boX (AIRQUIX)

Air quality monitoring using low-cost sensors has demonstrated great potential across various applications, ranging from personal exposure studies and mobile measurements to long-term stationary monitoring. Building upon the sensor evaluation presented in Chapter 4, a portable monitoring device, the Air Quality Inspection boX (AIRQUIX), was developed (Fig. 5.1). The device was designed to be lightweight and cost-effective, enabling versatile deployment across diverse monitoring scenarios. This chapter outlines the development of the AIRQUIX prototype, detailing its hardware and software architecture, system specifications, and current limitations.

5.1 Hardware Architecture

The AIRQUIX prototype is designed as an integrated platform for portable air quality monitoring, combining a diverse sensor suite with a robust hardware architecture. The device incorporates electrochemical sensors for detecting NO_2, NO, and O_3; an optical particle counter (OPC) for measuring PM1, PM2.5, and PM10; and a nondispersive infrared (NDIR) sensor for CO_2. Additionally, the system records environmental parameters, including temperature, relative humidity, and pressure, which are essential for calibrating sensor outputs and converting raw data into accurate pollutant concentrations. An integrated GPS module, with an option for an external antenna, ensures precise location tracking.

Central processing is performed by a Raspberry Pi, a compact and cost-effective single-board computer. Power is supplied by a 3.7 V, 4800 mAh lithium polymer battery pack connected to an uninterruptible power supply (UPS). This configuration maintains continuous power to the electrochemical sensors even when the device is powered off, effectively eliminating the sensor warm-up period (see Fig. 5.2).

The custom printed circuit board (PCB) for the AIRQUIX was designed using Fritzing software. Appendix B presents the layout of both the main board and the battery management board. The main board is engineered to accommodate all sensors and the microcontroller, while the battery management board ensures reliable power delivery. The compact and lightweight design

Figure 5.1: AIRQUIX prototype

of the PCBs facilitates easy assembly, disassembly, and maintenance.

5.2 Software and Data Infrastructure

The AIRQUIX relies on both onboard firmware for data acquisition, and cloud-based backend for data processing and visualization.

5.2.1 Onboard Firmware

The device's onboard software, written in Python, integrates several core capabilities to support continuous and reliable monitoring. It manages uninterrupted data acquisition from each sensor, locally archiving all measurements before uploading them via Wi-Fi to a central database. A built-in watchdog monitors system health and automatically restarts any stalled processes, ensuring uninterrupted operation. The software's modular design enables the seamless addition of new sensors or features. Furthermore, a remote-calibration functionality allows for the over-the-air update of calibration parameters based on regular reference measurements.

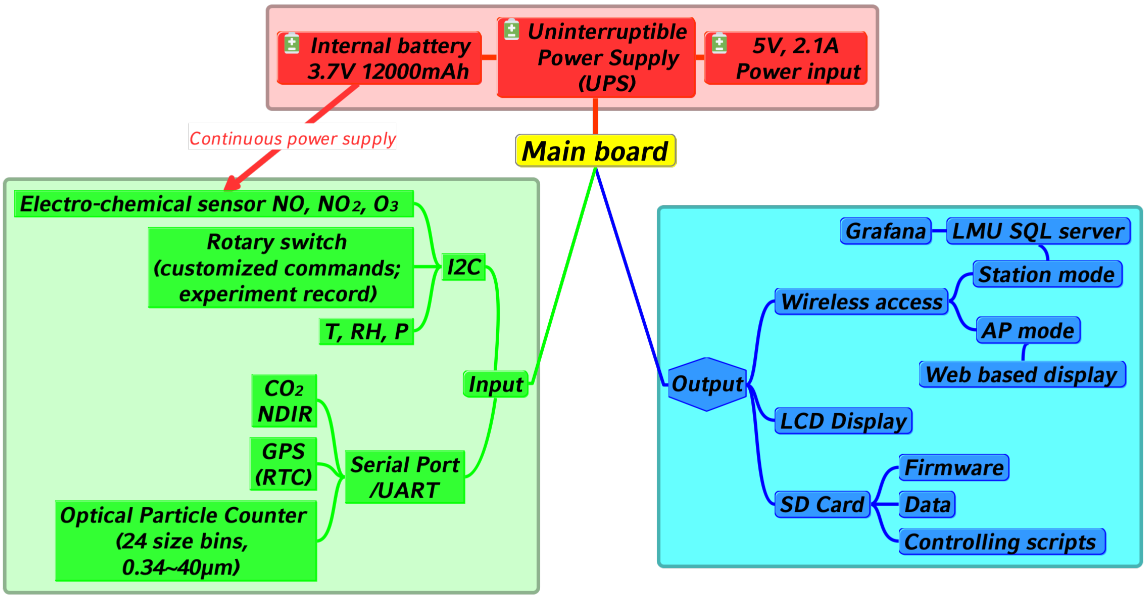

Figure 5.2: Schematic diagram of the AIRQUIX hardware architecture, illustrating the integration of the processing unit, sensor array, the uninterruptible power supply system and the visualization modules.

5.2.2 Backend and Visualization

Complementing the hardware, a comprehensive cloud solution was developed using the Python-Flask framework to support robust, bidirectional, near-real-time data communication. Sensor measurements are transmitted to the server every 5 seconds and simultaneously stored in an indexed SQL database, ensuring secure archiving and immediate availability. The data transfer protocol is optimized for low bandwidth, requiring only a 5 KB/s connection.

Data retrieval is enabled through a set of custom query commands, allowing for flexible analysis. All transmitted data are encrypted, and system access is managed centrally via unique credentials. To improve scalability, the API functions were structured for modular compatibility. A Grafana dashboard visualizes the collected data, offering time-series plots and pollutant level maps to explore air quality trends and spatial patterns. All server-side scripts are containerized using Docker, simplifying maintenance and deployment. The server, hosted on a secure cloud platform, includes a robust backup system. With support from LMU's IT department, the API and Grafana ports are exposed on a public server, where direct SQL access is restricted to administrators (see Appendix C for a detailed server/client diagram).

5.3 System Characteristics

The AIRQUIX design prioritizes portability and usability to support diverse field applications.

Portability

With a weight of less than 2 kg and a compact form factor (210 x 167 x 90 mm), the device can be carried by hand, mounted on a bicycle or vehicle, or deployed for stationary monitoring. The internal battery provides up to 7.5 hours of operation, supports recharging within 5 hours (10 W input), and allows operation via an external 5 V USB power supply.

User Interface

A 2.4-inch LCD displays real-time pollutant levels, GPS coordinates, and environmental data. A 10-position rotary switch allows the user to tag measurements with specific conditions (e.g., outdoor, indoor, street canyon). Position 10 is currently defined as a sleep mode, while positions 1-9 are reserved for future applications.

Connectivity

Data are accessible via Wi-Fi, allowing near-real-time uploads to the central server. This connectivity supports the API-driven visualization and analysis pipeline described in Section 5.2.

5.4 Technical Specifications

The AIRQUIX prototype has demonstrated robust performance under field conditions. Table 5.1 summarizes the comprehensive performance specifications of the sensor suite, including measurement ranges, sampling rates, and absolute uncertainty values (see Chapter 4 for details).

Table 5.1: Performance Specifications of the AIRQUIX

Sensors		Range	Sampling Rate	Uncertainty
Air pollutants	NO_2	0-2000 ppb	from 1 second	5 ppb
	NO	0-2000 ppb		-
	O_3	0-1000 ppb		5 ppb
	PM1	24 size bins 0.35-40 μm	from 1.2 seconds	-
	PM2.5			-
	PM10			-
Greenhouse Gas	CO_2	0-5000 ppm	from 1 second	10 ppm
Environmental Parameters	T	-40-85 °C	from 1 second	1 °C
	RH	0-100 %		3 %
	P	300-1100 hPa		1 hPa

5.5 Discussion, Limitations, and Future Improvements

The AIRQUIX prototype successfully demonstrates the feasibility of integrating multiple low-cost sensor technologies into a portable monitoring platform. The NO_2 measurements show acceptable agreement with reference instrumentation under controlled calibration conditions. However, several limitations constrain its current operational range and measurement reliability.

Performance under extreme meteorological conditions remains incompletely characterized, as the calibration dataset does not encompass the full range of ambient temperature and humidity conditions encountered in all field deployments. The passive diffusion sampling approach, while cost-effective, exposes sensor components directly to atmospheric conditions without adequate protection against precipitation or condensation, potentially compromising measurement integrity. Furthermore, system reliability is occasionally affected by intermittent data transmission interruptions due to wireless connectivity limitations, which can impede near-real-time analysis.

Future development will prioritize two key areas: physical design and calibration methodology. Regarding the physical design, efforts will focus on implementing protective housing to shield sensors from adverse weather conditions, such as precipitation and condensation, while ensuring representative air sampling. In terms of calibration, work will shift towards developing more intelligent, automatic calibration functions. These advanced algorithms will aim to dynamically adjust sensor parameters based on environmental context and reference data, reducing the need for frequent manual intervention. Additionally, efforts will be made to optimize connectivity for cloud-based data processing to reduce transmission delays. While individual exposure assessment represents a potential application, the primary objective of the AIRQUIX development remains establishing a technical foundation for high-spatial-resolution air quality monitoring networks. Addressing these limitations is essential for achieving the reliability required for scientific research and regulatory compliance assessment.

Chapter 6

Applications of the AIRQUIX

The applications described in this chapter showcase the transition from laboratory validation to real-world deployment, demonstrating the AIRQUIX's performance across three distinct monitoring domains: mobile monitoring, personal exposure assessment, and stationary monitoring. These case studies illustrate specific implementation strategies, technical challenges, and the practical integration of low-cost sensors with established air quality monitoring infrastructure. Collectively, they evaluate the AIRQUIX's capability to capture air quality dynamics that are typically missed by conventional monitoring approaches, while providing quantitative validation of the calibration methodologies developed in previous chapters.

This chapter begins with **mobile applications**: the AIRQMORE project demonstrates city-wide NO_2 mapping using an electric bus, AIRIDE investigates in-vehicle exposure dynamics, and METROUNO2 expands the analysis to a multi-city study of traffic-related NO_2 across Germany. We then transition to **personal exposure monitoring** with the PEARL project, which develops wearable sensing technologies and characterizes individual exposure patterns. Finally, **stationary applications** are presented: the WOODY study assesses residential wood burning impacts, and CLEANROAD evaluates roadside air filtration effectiveness. Table 6.1 summarizes the main AIRQUIX application case studies, the dominant deployment configurations, key sensors, and the primary monitoring objectives to provide an overview.

6.1 Case I: Pilot study of Air Quality Mobile Observation and Research with an Electric bus in Munich (AIRQMORE)

The AIRQMORE project introduces an air quality monitoring strategy in Munich by equipping an electric bus (EBUS) with mobile sensor units. This approach creates a dynamic complement to the existing official static monitoring network, which is often limited in spatial coverage. By leveraging the mobility of public transport, the pilot study demonstrates how mobile monitoring can significantly expand spatial resolution, facilitate near-real-time data visualization, and identify localized pollution hotspots across the urban landscape. Through the integration of low-cost sensors with cloud connectivity and the development of real-time calibration techniques, AIRQMORE addresses inherent challenges such as the correction of sensor drift. The result is a set of

Table 6.1: Overview of AIRQUIX application case studies, deployment setups, sensors and objectives.

Case study	Full name	Deployment configuration & key sensors / instruments	Deployment objective / summary
		Mobile Applications	
AIRQMORE	Pilot study of Air Quality Mobile Observation and Research with an Electric bus in Munich (AIRQMORE)	Electric bus rooftop rack; dual AIRQUIX units; UPS; GPS; communication module	Citywide NO_2 mapping with passing-by calibration and diurnal cycle normalization.
AIRIDE	Assessment of In-vehicle Reactive gases and Indoor air during Driving Environments (AIRIDE)	Two passenger vehicles; AIRQUIX; Pandas (low-cost sensor package developed by AISIN company); CE-DOAS; Chemiluminescence Detector; 2B O_3; LI-COR 840A CO_2 monitor	In-vehicle vs. outdoor pollutant levels; effects of cabin filters and ventilation.
METROUNO2	Multi-city Evaluation of Traffic Related Urban NO_2 levels in Germany (METROUNO2)	Fixed AQMS; LP-DOAS; mobile AIRQUIX; ICAD	Multi-city modelling of traffic and meteorology effects on NO_2, including COVID-19 anomalies.
		Portable Applications	
PEARL	VADER - Development of a fan-assisted respiratory protection mask APPLE - Air Pollution Personal Lifestyle Exposure	Fan-assisted mask; MICS-6814 MO_x; PMSA003 OPC; SCD30 CO_2; T/RH/p sensors Portable AIRQUIX	Development of a respiratory mask that measures pollutants and warns on exceedances. Lifestyle exposure study quantifying real-life NO_2 and PM levels across daily activities.
		Stationary Applications	
WOODY	WOod-burning stOve impact on Domestic air qualitY (WOODY)	Residential house; multiple AIRQUIX units (PM, NO_2)	Indoor/outdoor PM and NO_2 during residential wood-stove use.
CLEANROAD	Carbon-based Localized Evaluation of Air purification Near ROADsides (CLEANROAD)	Roadside installation; AIRQUIX array	Evaluation of an activated-carbon roadside filter on near-road NO_2.

comprehensive pollution maps that reveal the complex dynamics of urban air quality with high spatial fidelity.

Munich's current air quality monitoring infrastructure consists of only five official active monitoring stations providing hourly data, supplemented by dozens of passive samplers that collect monthly NO_2 measurements. This limited network includes two general background monitoring stations and three roadside monitoring stations, creating substantial gaps in spatial coverage and real-time monitoring capability across the urban area.

The limitation in the existing monitoring system presents significant challenges for comprehensive air quality assessment and management. The distribution of existing monitoring stations is not sufficient to capture the complex spatial variations in air pollutant levels across urban environments, particularly in areas with varying traffic patterns, building densities, and localized emission sources (see Sec. 6.3.2). Additionally, the passive samplers, while useful for long-term trend analysis, cannot provide sufficient temporal resolution necessary for understanding dynamic pollution events or daily fluctuations.

To address these issues, the AIRQMORE pilot study proposes a supplementary mobile monitoring approach that leverages the city's EBUS network as a platform for continuous, widespread air quality data collection. This solution aims to expand monitoring coverage while providing higher temporal and spatial resolution data compared to the existing static network. By integrating innovative low-cost monitoring devices onto vehicles that regularly travel in diverse urban environments, the study creates possibilities for identifying pollution hotspots, understanding pollutant dispersion patterns, and evaluating the effectiveness of air quality improvement measures across Munich.

6.1.1 Design of Mobile Monitoring System

The mobile monitoring system in this study has been designed with consideration of both technical requirements and practical constraints of deployment on public transportation vehicles. Safety and reliability were primary concerns in the system design. It is important to use fire-resistant and weather-resistant materials throughout the installation. The monitoring device was therefore mounted on a TÜV-certified vehicle rooftop rack (Fig.6.1), ensuring secure attachment and compliance with vehicle safety standards.

The core monitoring system integrates several essential hardware components to collect, process, and transmit measured data. Two AIRQUIXs serve as the primary air quality monitoring instruments, each equipped with individual inlet fans to ensure consistent air sampling regardless of vehicle movement or static conditions. These sensors continuously collect air quality parameters as the bus travels along its route, providing high-resolution spatial data across diverse urban environments.

To address the power requirements of continuous monitoring, the system incorporates a power management solution. A transformer converts the 24V power supply from the EBUS to the 5V required by the AIRQUIX, while an uninterruptible power supply (UPS) system with an integrated battery farm built on lead-acid batteries provides backup power during periods when the bus is stationary or the engine is off to avoid the long warm-up period of the sensor. This ensures uninterrupted data collection throughout the bus's operational schedule.

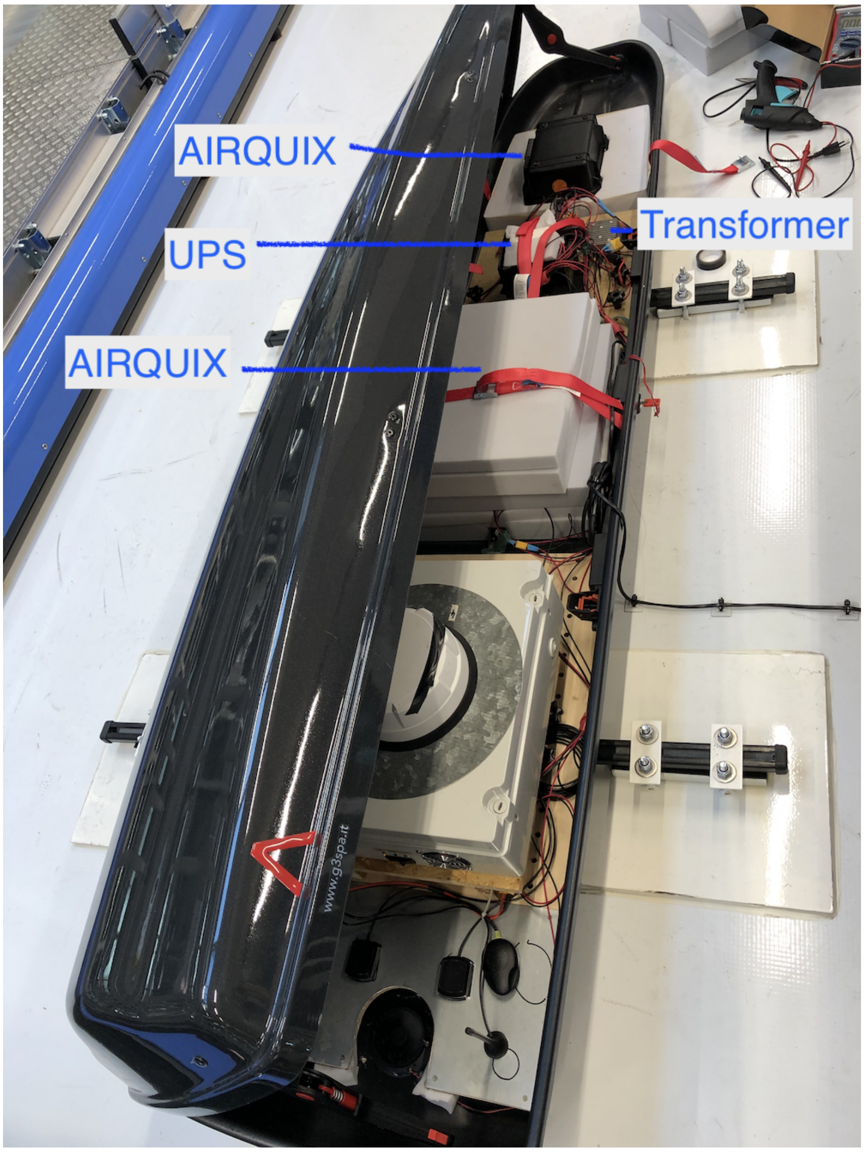

Figure 6.1: Schematic of the AIRQMORE mobile monitoring system installed on the rooftop rack of an electric bus (EBUS) in Munich. The system includes dual AIRQUIX units, a UPS with battery farm, a power transformer, an intelligent ventilation/cooling system, and an internet access point for real-time data transmission.

Another critical aspect of the system design is the intelligent ventilation and cooling system. It maintains optimal operating conditions for the sensitive measurement device. This system activates automatically when ambient temperatures exceed 50 °C, ensuring continuous air circulation while preventing overheating that could compromise data quality or system longevity.

Data connectivity is established through an integrated internet access point, enabling near-real-time transmission of collected measurements to a cloud platform. This connectivity solution supports the transmission of data at 5-second intervals, allowing for immediate visualization and analysis.

The entire system is designed with portability and adaptability in mind, facilitating easy deployment across different vehicles or relocation to different routes as required. This flexibility represents a significant advantage over traditional fixed monitoring stations, allowing the system to be strategically deployed to address specific air quality concerns or fill gaps in the existing monitoring network.

6.1.2 Calibration Methodology and Data Processing

One of the primary challenges in mobile air quality monitoring, particularly when using low-cost sensors, is maintaining measurement accuracy and precision under varying environmental conditions and over time. The AIRQMORE project addresses this challenge through innovative calibration approaches that leverage both reference stations and advanced data processing techniques.

A key innovation in the project is the development of a periodic real-time recalibration method that maintains sensor accuracy throughout deployment. The cloud-based solution integrates advanced connectivity features, enabling not only real-time data transmission and visualization at 5-second intervals but also supporting automated maintenance tasks and calibration procedures. This connectivity creates a dynamic monitoring system that can continuously adjust to changing conditions and maintain data quality.

The project has implemented a preliminary “passing-by” calibration technique that leverages the mobile nature of the monitoring platform. This approach compares measurements from the mobile unit with those from reference stations whenever the EBUS passes in proximity to these stations during its normal route. The GPS capabilities of the AIRQUIX automatically trigger the recalibration process, allowing for real-time adjustments to the mobile measurements without requiring manual intervention or specialized routes.

A practical demonstration of this calibration approach occurred on 16 February 2024, when the EBUS equipped with the monitoring system passed by a reference station between 10:09:44 and 10:10:01. During this brief window, a server-side recalibration was conducted, resulting in NO_2 measurements that more closely aligned with the reference values (Fig. 6.3). This real-world validation demonstrates the effectiveness of the passing-by calibration approach in improving data accuracy while maintaining the operational efficiency of the mobile monitoring system.

To disentangle spatial and temporal variability and derive a representative spatial distribution of NO_2 across Munich, we applied a normalization algorithm based on long-term LP-DOAS measurements (Zhu et al., 2020). While the LP-DOAS path integrates over a significant urban fetch, local influences can still affect specific measurements. Therefore, we utilized a normalized long-term average of the diurnal NO_2 cycle for each day of the week to correct for temporal variations.

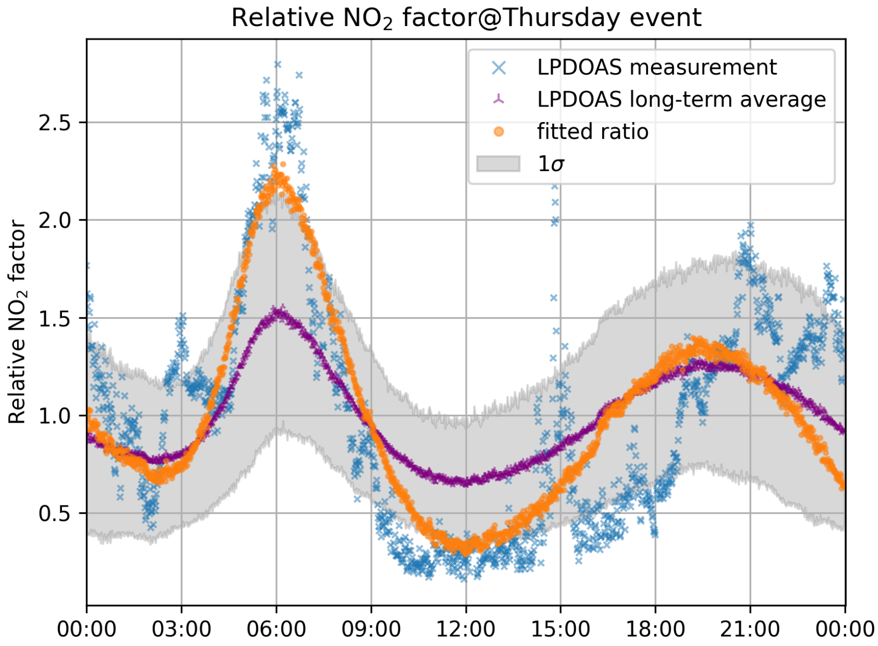

Figure 6.2: Example of the diurnal NO_2 normalization process for a specific Thursday. Blue dots indicate the measured LP-DOAS mixing ratios for that day. The purple curve represents the long-term averaged diurnal pattern for Thursdays, with the shaded area denoting ±1 standard deviation. The orange dots show the calculated time-dependent correction factors used to normalize mobile measurements.

The normalization process involves several steps. First, the atmospheric NO_2 mixing ratios measured by the LP-DOAS for each day are normalized by dividing them by that day's mean NO_2 level. These normalized values are then averaged for each day of the week over a multi-year period to establish a representative diurnal NO_2 variation pattern. For any specific day during the mobile measurement campaign, this long-term averaged diurnal pattern (corresponding to the specific weekday) is scaled and shifted to fit the normalized LP-DOAS measurements of that day. A least-squares regression is used for this fitting. The resulting fitted diurnal pattern provides a time-dependent correction factor. Finally, the mobile measurements are divided by the inverse of this factor to remove the temporal influence of the diurnal cycle, yielding values that are more representative of the spatial differences in the measurement areas (Fig. 6.2).

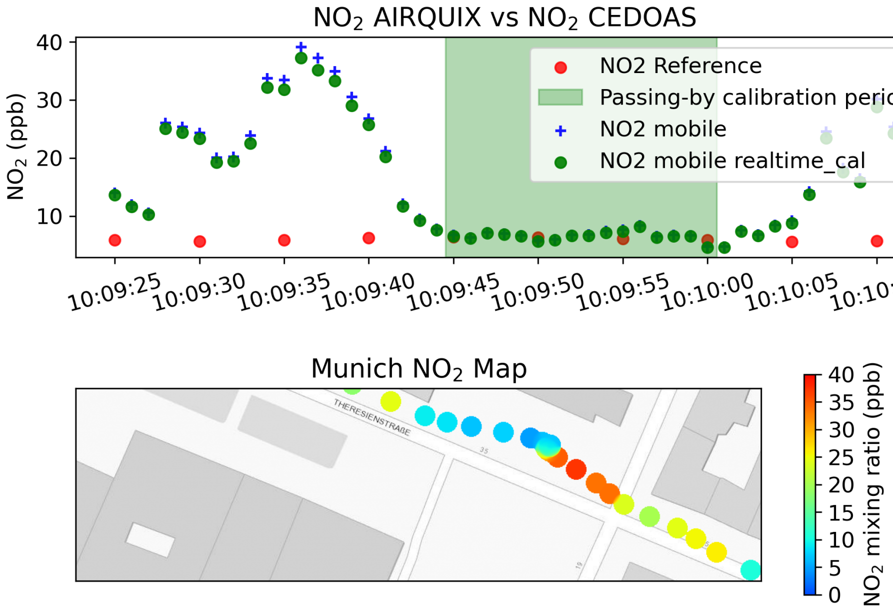

Figure 6.3: Demonstration of the real-time passing-by calibration on 16 February 2024. The green dots show the raw NO$_2$ measurements from the mobile sensor, while the blue dots represent the recalibrated data after passing the reference station (red dots).

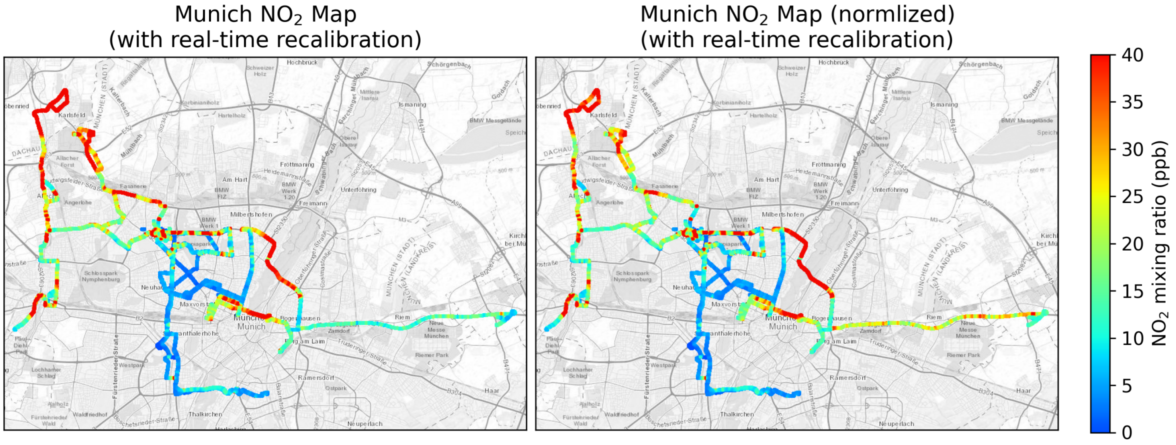

Figure 6.4: Combined NO$_2$ map generated with raw (left panel) and normalized (right panel) NO$_2$ mixing ratios.

6.1.3 Results and Discussion

The initial pilot results from the AIRQMORE project demonstrate the potential of mobile monitoring to provide detailed spatial insights into urban air pollution patterns. The primary output of the pilot phase was a comprehensive NO_2 pollutant map generated from data collected by the AIRQUIXs mounted on the EBUS. As the bus traveled along its routes during both rush and non-rush hours, it captured a complex pollution landscape that reflects both spatial distribution and temporal variations across Munich.

In Fig. 6.4, the raw pollution map provides initial insights into areas with elevated NO_2 mixing ratios, potentially identifying pollution hotspots that might be missed by the limited existing static monitoring network. However, it is recognized that the raw data incorporates both spatial and temporal influences, potentially obscuring the true spatial patterns of pollution across the city. The normalized map provides urban planners and environmental managers with a more reliable tool for identifying areas consistently experiencing elevated pollution levels, independent of the time of measurement. On the map, the eastern part of Munich is clearly underestimated in the raw data due to the temporal influence, and the northwestern part is overestimated. After normalization, these biases while relying on temporal variations are effectively mitigated, revealing a more accurate spatial distribution of NO_2 pollution.

The success of this mapping approach demonstrates the value of combining mobile monitoring with advanced data processing techniques. By leveraging the mobility of the EBUS network along with advanced normalization algorithms, the AIRQMORE project achieves monitoring coverage and resolution that would be economically and logistically impossible with traditional static monitoring approaches.

Despite these promising results, the pilot study faced several important limitations that must be considered when interpreting the findings. The passing-by calibration period was relatively short (less than 1 minute), potentially limiting the robustness of the calibration model. Additionally, the current deployment includes only two mobile units on a single EBUS, which may not provide sufficient coverage for comprehensive city-wide air quality assessment.

The calibration frequency represents another significant limitation, as the mobile units can only pass by the calibration station once every few weeks based on the EBUS route schedule. This infrequent calibration may not adequately account for sensor drift or changing response characteristics over time. Furthermore, the current calibration approach does not fully address factors such as height differences between the mobile units and reference stations, the influence of varying distances during passing-by events, or the impact of local weather conditions like wind direction on pollutant transportation and distribution.

These limitations highlight areas for future refinement in the AIRQMORE project. The mobile approach expands monitoring coverage and provides high spatial resolution, creating opportunities for targeted air quality management interventions.

6.2 Case II: Assessment of In-vehicle Reactive gases and Indoor air during Driving Environments (AIRIDE)

While AIRQMORE focuses on city-wide mapping using public transport, understanding the air quality inside vehicles is also crucial for mobile populations. A pilot study AIRIDE is presented which utilizes low-cost sensor systems, including the AIRQUIXs and Pandas sensor boxes, to evaluate in-vehicle air quality and compare it with ambient pollution levels. This work illustrates how localized measurements within vehicle cabins can refine mobile sampling data and enhance our understanding of pollutant dynamics in real-world driving conditions.

6.2.1 Current Research on In-Vehicle Air Pollutants

Many studies have investigated pollutant exposures in various in-vehicle and roadside microenvironments, revealing significant differences in exposure levels based on the measurement location and vehicle conditions.

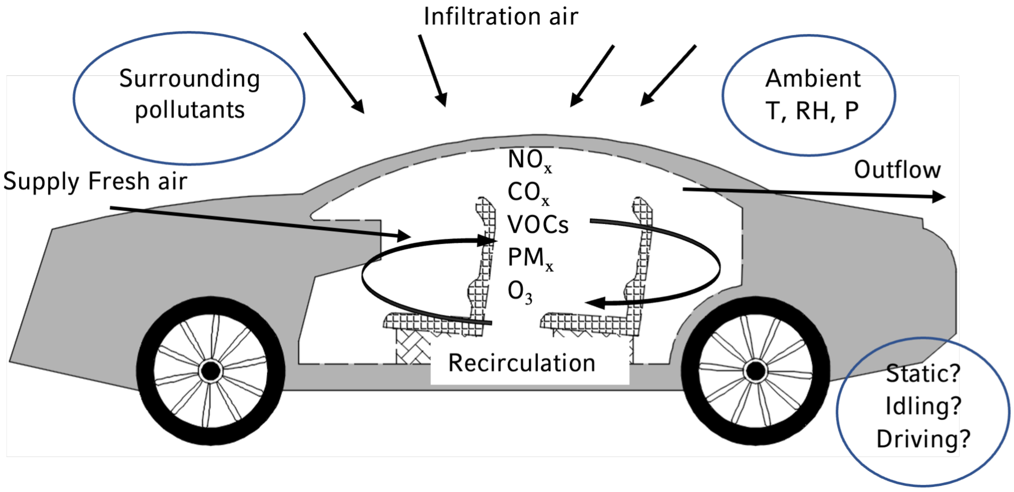

Figure 6.5: Impact factors for in-vehicle air quality

The factors influencing in-vehicle air quality can be broadly categorized into three groups: vehicle-related factors, including vehicle type, age, and interior materials; environmental factors, such as ambient temperature, humidity, and surrounding air quality; and driving conditions, including speed, traffic density, and ventilation modes. These factors interact in complex ways to determine the overall in-vehicle air quality. A comprehensive summary of all potential impact factors on in-vehicle air quality is concluded by Chen et al. (2014); Fedoruk and Kerger (2003); Xu et al. (2018); Yoshida and Matsunaga (2006); Yoshida et al. (2006); You et al. (2007) and shown in Fig. 6.5. The most relevant pollutants for in-vehicle air quality include nitrogen oxides (NO_x), carbon monoxide (CO), volatile organic compounds (VOCs), particulate matter (PM), and ozone (O_3). The following sections summarize the studies on these pollutants.

6.2.1.1 Nitrogen Oxides (NO_x)

A study conducted by Żak et al. (2017) reported that pedestrians along residential roads experience lower median NO_2 mixing ratios (approximately 12 ppb) compared to drivers and passengers in urban traffic, where median levels can reach around 57 ppb (see Fig. 6.6). Moreover, Chan (2003) examined the in/out ratios of NO, NO_2, and CO under varying ventilation modes and driving conditions, demonstrating that meteorological factors, such as wind and sunlight, play a critical role in in-vehicle pollutant levels (Fig. 6.7).

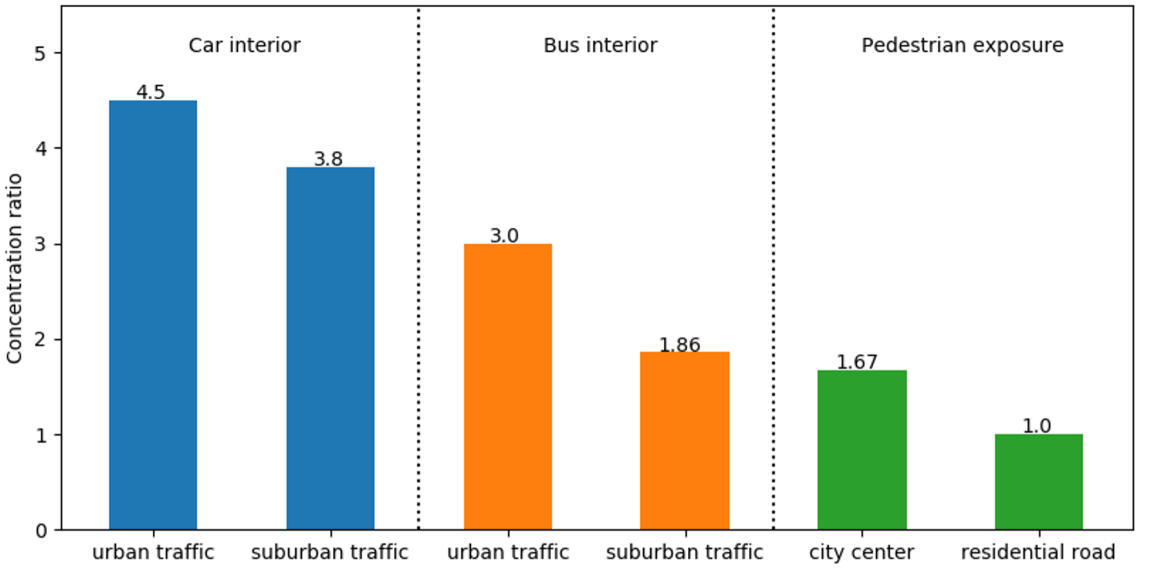

Figure 6.6: NO_2 exposure in different traffic microenvironment relative to pedestrian exposure at a residential road (Żak et al., 2017)

6.2.1.2 Carbon Monoxide (CO)

Studies by Barnes et al. (2018) in Hong Kong found that while CO mixing ratios in vehicles generally met established indoor air quality standards, elevated CO_2 levels in many vehicles highlighted potential issues with cabin ventilation. Alameddine et al. (2016) further noted that in-vehicle CO exposure is largely governed by ambient conditions, with wind influencing the diffusion of pollutants into the vehicle.

6.2.1.3 Volatile Organic Compounds (VOCs)

Research on VOCs has revealed complex patterns of in-vehicle exposure. Brodzik et al. (2014) identified over 260 VOC species in new vehicles, with higher levels observed in static conditions compared to driving conditions (Fedoruk and Kerger, 2003). Variations in VOC mixing ratios have also been linked to factors such as vehicle age, interior materials, temperature, and humidity

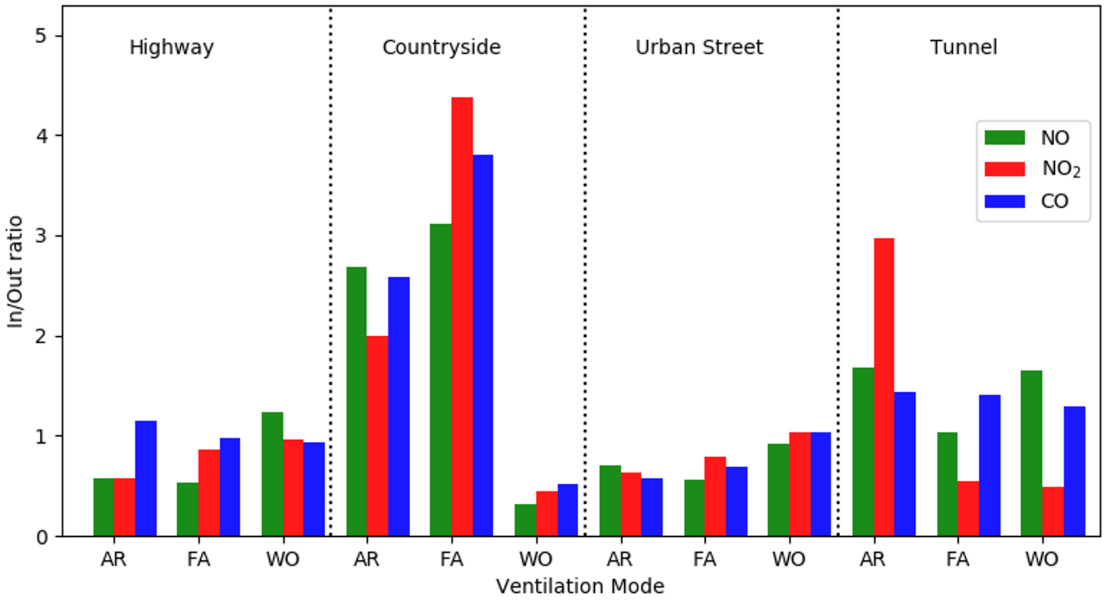

Figure 6.7: The In/Out ratios of NO, NO_2 and CO in different ventilation modes and environments (AR-Air recirculation; FA-Fresh Air intake; WO-Window Open) (Chan, 2003)

(Chan et al., 1991; Faber et al., 2012, 2013; Grabbs et al., 2000; Yoshida and Matsunaga, 2006; You et al., 2007).

6.2.1.4 Particulate Matter (PMx)

Measurements of particulate matter (PM2.5 and PM0.3) inside vehicles indicate that pollutant levels are subject to substantial variability. Barnes et al. (2018) observed higher PM2.5 concentrations during driving compared to idling, while studies by Alameddine et al. (2016) and Chan et al. (2002) showed that recirculation modes can effectively lower in-vehicle PM levels. Additional research suggests that vehicles following those with stricter emission standards or equipped with integrated filters tend to have reduced in-vehicle PM concentrations (Campagnolo et al., 2019; Vande Hey et al., 2018).

6.2.1.5 Ozone

According to Chan et al. (1991), in-vehicle ozone levels are generally lower than ambient values, with reported mean mixing ratios around 15.4 ppb versus 52.8 ppb at fixed monitoring stations. However, the limited availability of on-road ozone measurements leaves the in/out ratio less well defined.

6.2.2 Health Impacts and Filter Technologies

The in-vehicle air quality is a growing concern due to the average time people spend commuting (FAZ, 2019; Johnson, 1995). Poor in-vehicle air quality has been associated with a range of adverse health effects, including mucous membrane irritation, respiratory and cardiovascular problems, and potential impacts on the liver, spleen, nervous, and reproductive systems (Brunekreef and Holgate, 2002; Komulainen, 2008). Vulnerable populations, such as children, pregnant women, and the elderly, are particularly susceptible. Comprehensive assessments that consider pollutant toxicity, exposure duration, and synergistic effects are essential for understanding these health impacts.

To protect drivers and passengers from exposure to harmful pollutants, automotive manufacturers have widely adopted in-vehicle air filters. Currently, most in-vehicle air purifiers consist of filters integrated into the air conditioning system, typically constructed from fibrous or porous materials. In addition, high efficiency particulate air (HEPA) filters and standalone purification units, despite their higher costs, have been introduced in certain applications. Several studies have evaluated the effectiveness of these in-vehicle air filters in reducing pollutant levels (Othman et al., 2018; Qi et al., 2008; Yu et al., 2017). For example, Ao and Lee (2003) demonstrated that immobilizing TiO_2 on activated carbon filters significantly enhanced the removal of nitrogen oxide (NO) and volatile organic compounds, such as benzene, toluene, ethylbenzene, and o-xylene (BTEX), while also suppressing the formation of NO_2 from NO photodegradation. Additional research on in-vehicle air purifiers (Tartakovsky et al., 2013) and High Efficiency Cabin Air (HECA) systems (Lee and Zhu, 2014; Lee et al., 2015) has reported reductions in particulate matter concentrations exceeding 90 %.

Although specific standards for in-vehicle air quality levels have yet to be established, standardized testing procedures are available (ISO, 2021). Many automotive manufacturers regulate in-vehicle air quality according to their own proprietary testing protocols. Xu et al. (2018) recommended that future developments in in-vehicle air purification technology should strive for high removal efficiencies for both particulate matter and gaseous pollutants. Furthermore, given the considerable influence of ambient air quality on in-vehicle conditions, the development of integrated air quality detection systems is essential. Such systems can provide critical data to optimize the operation of air purifiers and filters, balancing energy efficiency with effective pollutant removal.

6.2.3 Experimental Setup

To assess in-vehicle air quality, we conducted a measurement campaign using two vehicles equipped with low-cost sensor technology as well as multiple high-end instruments:

- Vehicle 1 (Fig. 6.8) is an Audi A4 equipped with an activated carbon filter at the air conditioner inlet. The instrumentation in Vehicle 1 includes:
    - A two-chamber CE-DOAS for simultaneous measurement of in-vehicle and ambient NO_2. This system utilizes a blue LED (wavelength range 440–455 nm) combined with high-reflectivity mirrors.
    - Two portable Pandas sensor boxes, integrating a NO_2 MO_x sensor, a Honeywell PM sensor, a BME680 air quality sensor to measure volatile organic compounds (VOCs)

Figure 6.8: Inlet setup of Vehicle 1 used in the AIRIDE campaign.

(without calibration), a CO_2 sensor, as well as temperature, relative humidity, and pressure sensors.

Figure 6.9: Inlet setup of Vehicle 2 used in the AIRIDE campaign.

- Vehicle 2 (Fig. 6.9) is a 10-year-old Mercedes Sprinter with a simple paper filter. The instrumentation in Vehicle 2 includes:
    - A 2B Model205 Dual Beam Ozone Monitor for O_3 monitoring.
    - A single-chamber CE-DOAS for NO_2 monitoring.
    - A ChemiLuminescence Detector (CLD) APNA-370 NO_x monitor, employing dual cross-flow modulation for measuring NO and NO_2.
    - A Licor-840A NDIR CO_2 monitor.
    - Two portable Pandas sensor boxes (identical to those in Vehicle 1).
    - Two portable AIRQUIXs (Fig. 5.1), equipped with ECSs for NO_2, NO, and O_3 measurement, in addition to sensors for temperature, relative humidity, pressure, and an optical particle counter.

In Vehicle 1, the dual-chamber CE-DOAS enabled concurrent measurements inside and outside the cabin, with additional Pandas sensors placed at both locations. In Vehicle 2, one Pandas sensor and one AIRQUIX were mounted externally, while their counterparts were installed within the breathing zone of the middle back seat. Other instruments, with inlet tubing positioned outside the window, captured ambient conditions. Notably, the sunroof and side window in Vehicle 2 were kept slightly open during the campaign, allowing for enhanced air infiltration.

In addition to the in-vehicle measurements, bicycle-based AIRQUIX campaigns were conducted in Munich to characterize the typical diurnal cycle of urban NO_2 at street level. These mobile transects were combined with long-term LP-DOAS measurements at 30 m height (see Case METROUNO2, Sec. 6.3) to derive time-of-day normalization factors. These factors are used to correct for daily-cycle effects when comparing mobile measurements taken at different times of day or seasons, and they provide the basis for the temporal normalization applied later to the EBUS-based AIRQMORE (Sec. 6.1) maps.

6.2.4 Results and Discussion

6.2.4.1 Nitrogen Oxides (NO_x)

Figure 6.10 displays the time series of NO_2 mixing ratios measured inside and outside Vehicle 1, showing that in-vehicle levels were generally lower than ambient levels. The NO_2 in/out (I/O) ratios, illustrated in Fig. 6.11, had an average value of 0.37 ± 0.63 and a median of 0.15. This reduction is likely attributable to the activated carbon filter. Elevated I/O ratios observed during parking (as indicated by the grey and black shaded areas in the figures) suggest that air exchange, such as when the car door is opened, temporarily increases in-vehicle pollutant levels.

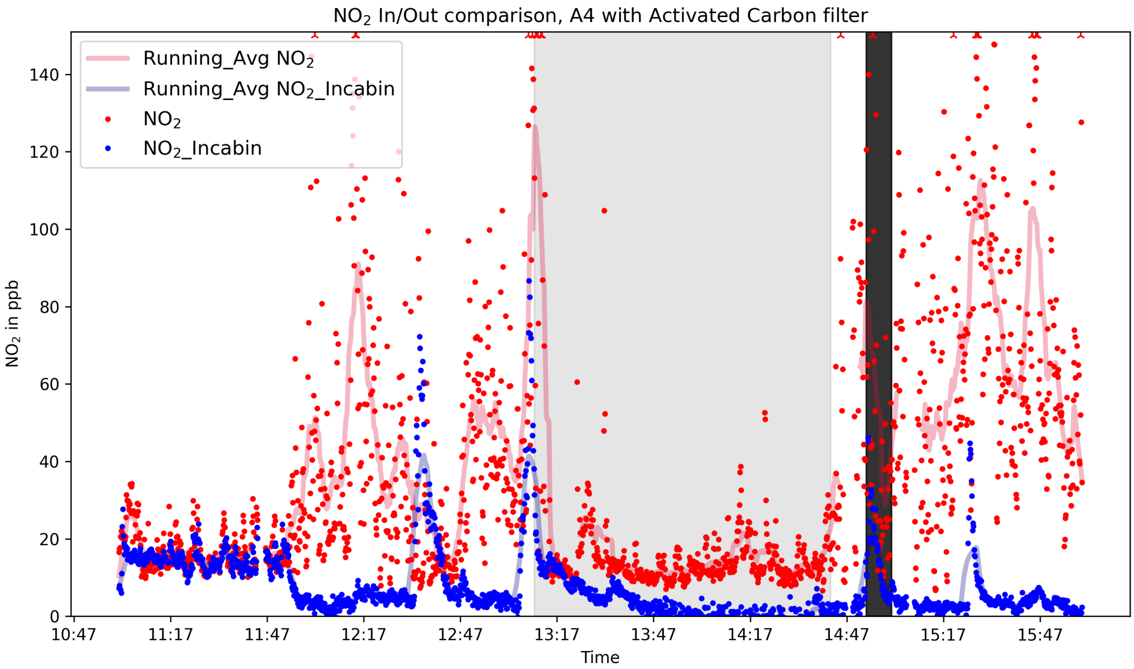

Figure 6.10: The NO_2 inside / outside mixing ratio of vehicle 1 measured by CEDOAS on 29 July 2019 (Grey area: Static status in the parking lot. Black area: Idling parking on roadside

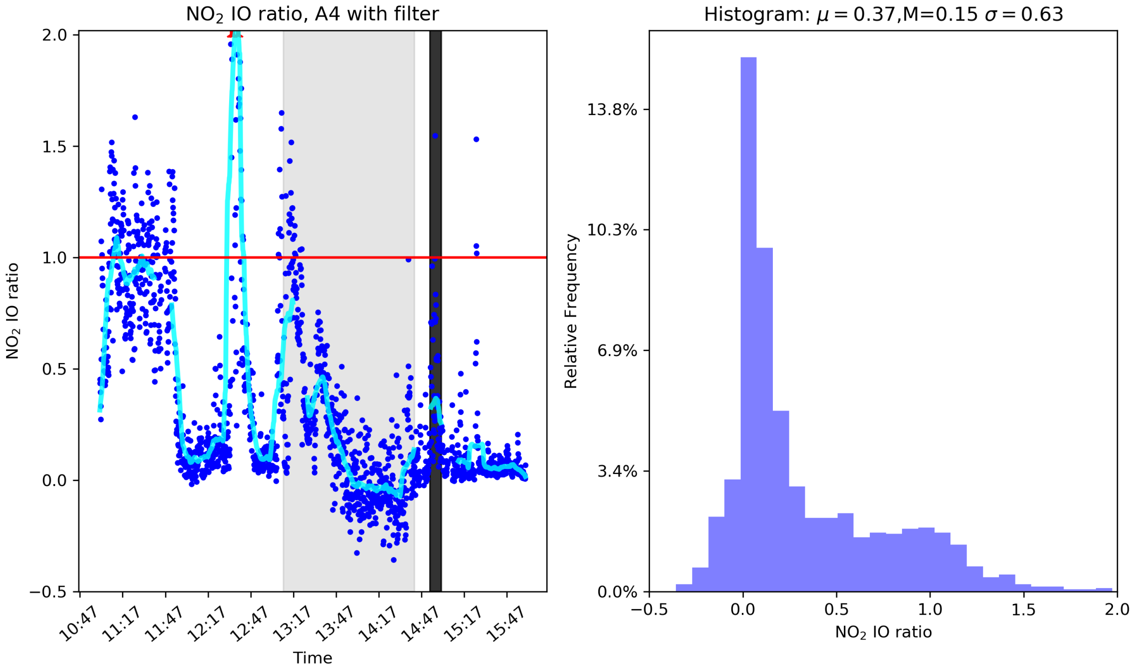

Figure 6.11: The NO_2 In / Out ratio time series and histogram plot of vehicle 1 measured by CEDOAS on 29 July 2019 (Grey area: Static status in the parking lot)

For Vehicle 2, which did not have an air filter, Figures 6.12 and 6.13 show an average NO_2 I/O ratio of 0.76 ± 1.05 (median 0.46), reflecting higher in-vehicle pollutant levels, likely due to the absence of filtration and the effect of non-enclosed environment.

Figures 6.14 and 6.15 present NO measurements for Vehicle 2 over the period 22 July 2019 to 25 July 2019. The average NO I/O ratio was 4.67 ± 9.56 (median 1.71), with large variability that may be explained by the diffusion of pollutants back into the cabin through the open sunroof and fluctuating traffic conditions.

In a chasing study (Figs. 6.16–6.18), the CE-DOAS was used to monitor NO_2 emissions directly from the exhaust of Vehicle 2, while a second CE-DOAS on Vehicle 1 measured the resulting NO_2 mixing ratios in the following vehicle. Although a clear correlation was not established, likely due to interference from other vehicles in busy urban traffic, previous highway studies suggest that NO_2 mixing ratios depend on the distance to the preceding vehicle and the composition of the traffic stream.

6.2.4.2 Ozone

Figures 6.19 and 6.20 show the ozone I/O ratios for Vehicle 2 from 22 July 2019 to 25 July 2019. The average ratio was 1.33 ± 2.35 (median 0.92). Ambient ozone levels peaked during periods of strong sunlight, and while in-vehicle ozone also increased, it did so at a reduced rate. Consequently, higher I/O ratios were observed in the morning, which gradually decreased later in the day—likely a result of strong sunlight combined with the open sunroof.

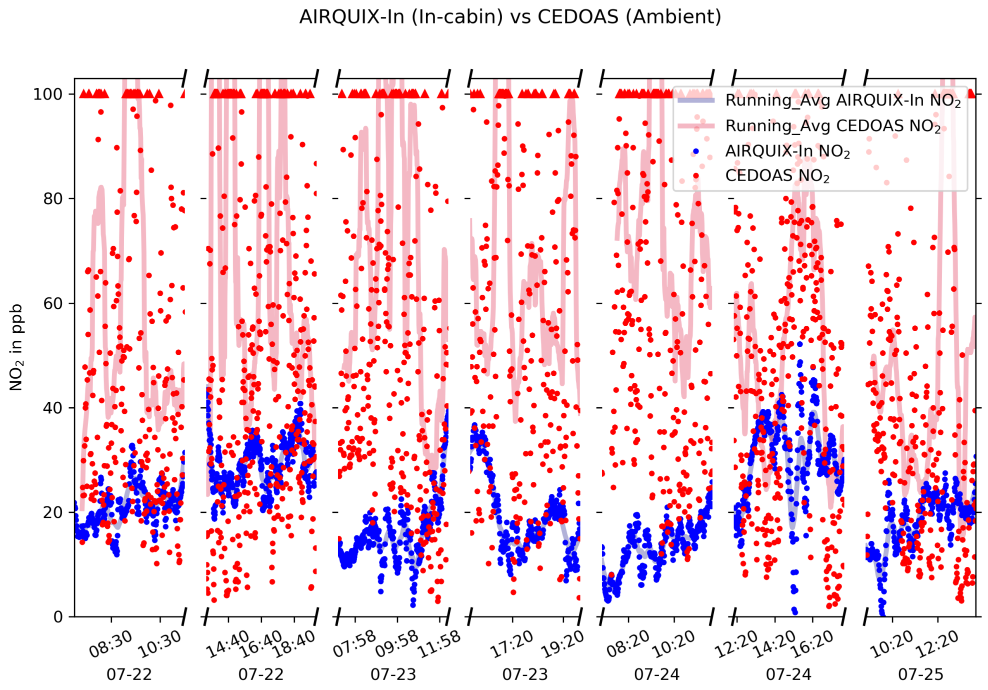

Figure 6.12: The NO$_2$ inside / outside mixing ratio of vehicle 2 measured by AIRQUIX (in-vehicle) and CEDOAS (Ambient) and 30 minutes running average plot

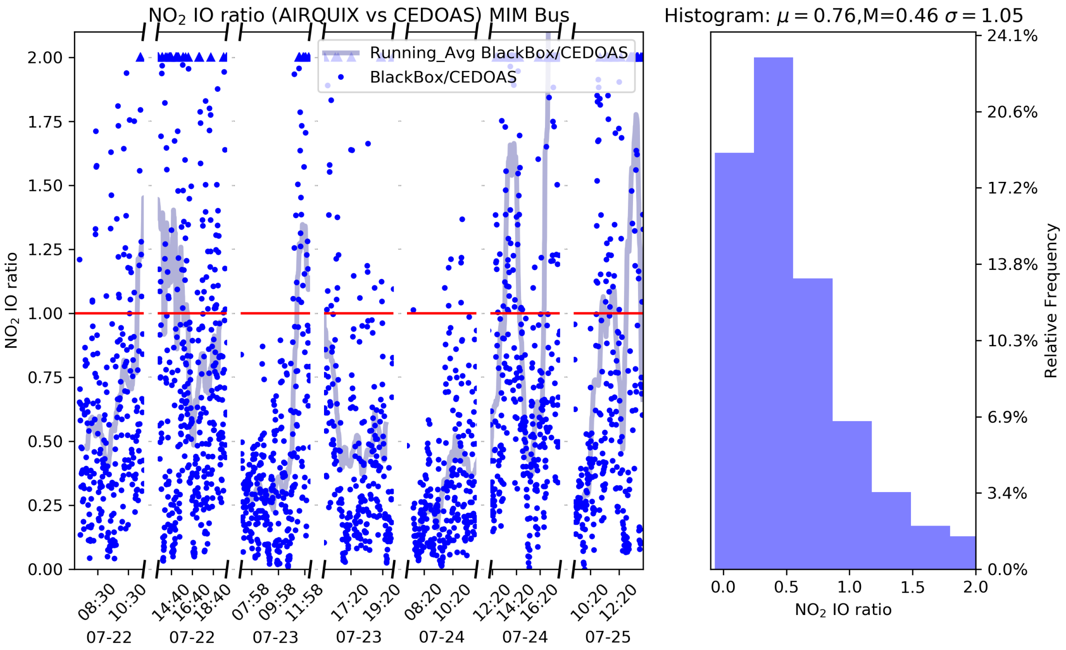

Figure 6.13: The NO$_2$ In / Out ratio time series and histogram plot of vehicle 2 measured by AIRQUIX (in-vehicle) and CEDOAS (Out) with 1 hour running average

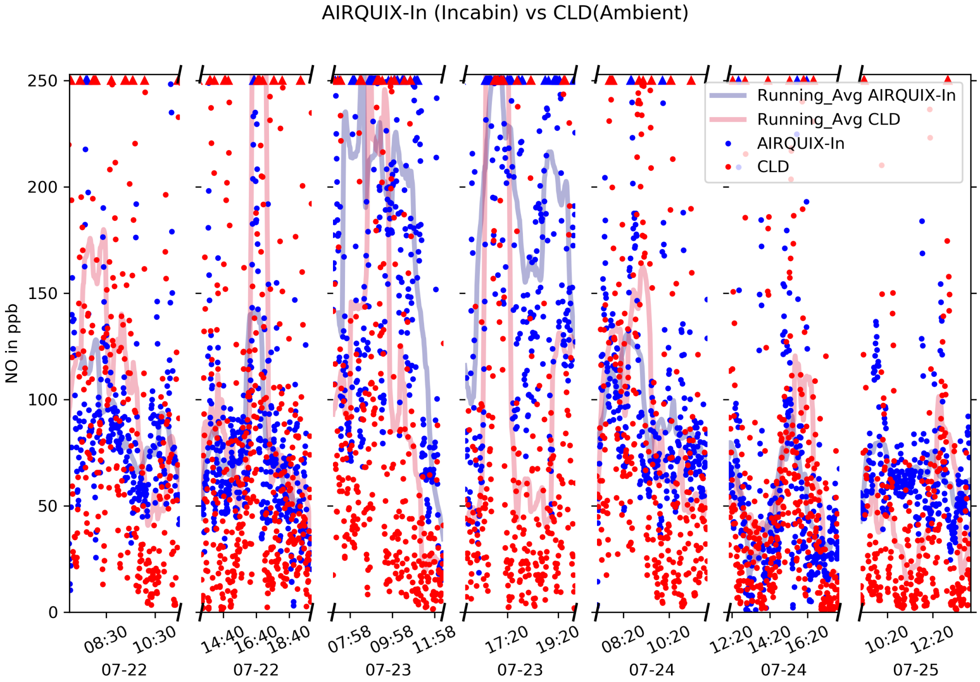

Figure 6.14: The NO inside / outside mixing ratio of vehicle 2 measured by AIRQUIX (in-vehicle) and CLD (Ambient) and 30 minutes running average plot

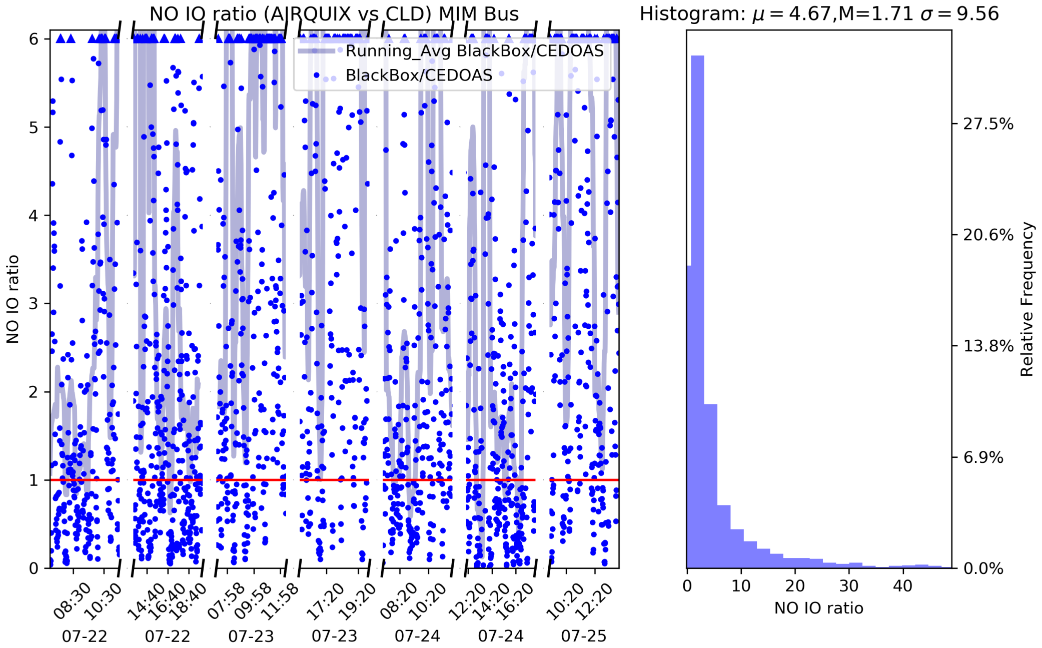

Figure 6.15: AIRQUIX (in-vehicle) vs NO (CLD ambient) of vehicle 2 measured by AIRQUIX (in-vehicle) and CLD (Ambient)

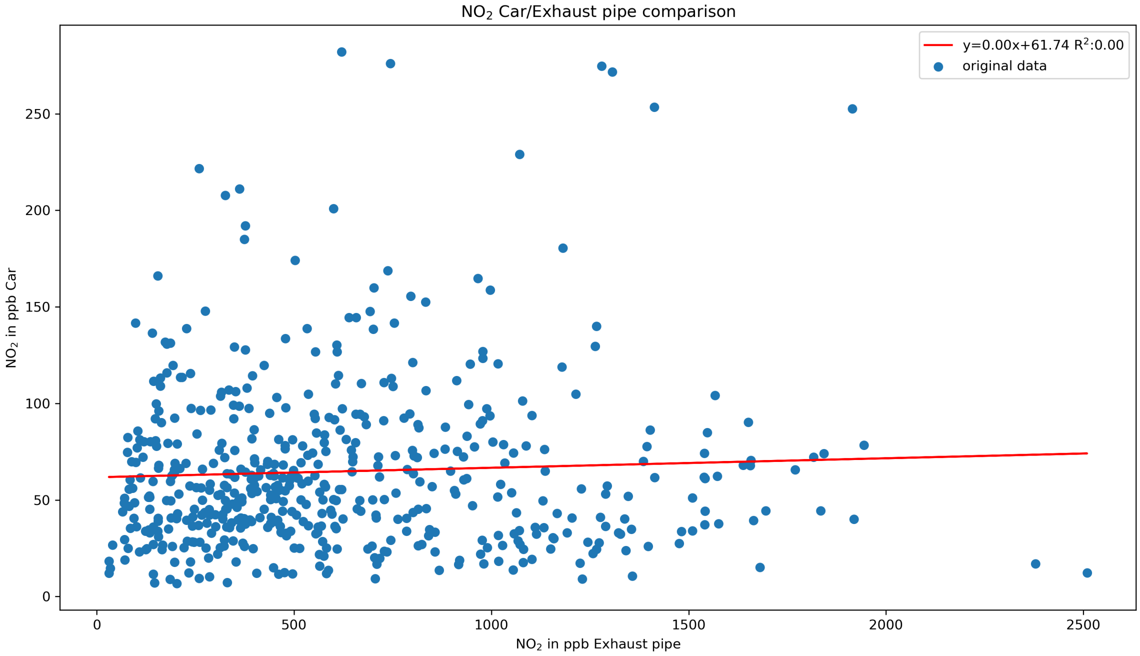

Figure 6.16: The correlation of NO$_2$ mixing ratio between the emission from vehicle 2 exhaust and the following vehicle 1 ambient measurement.

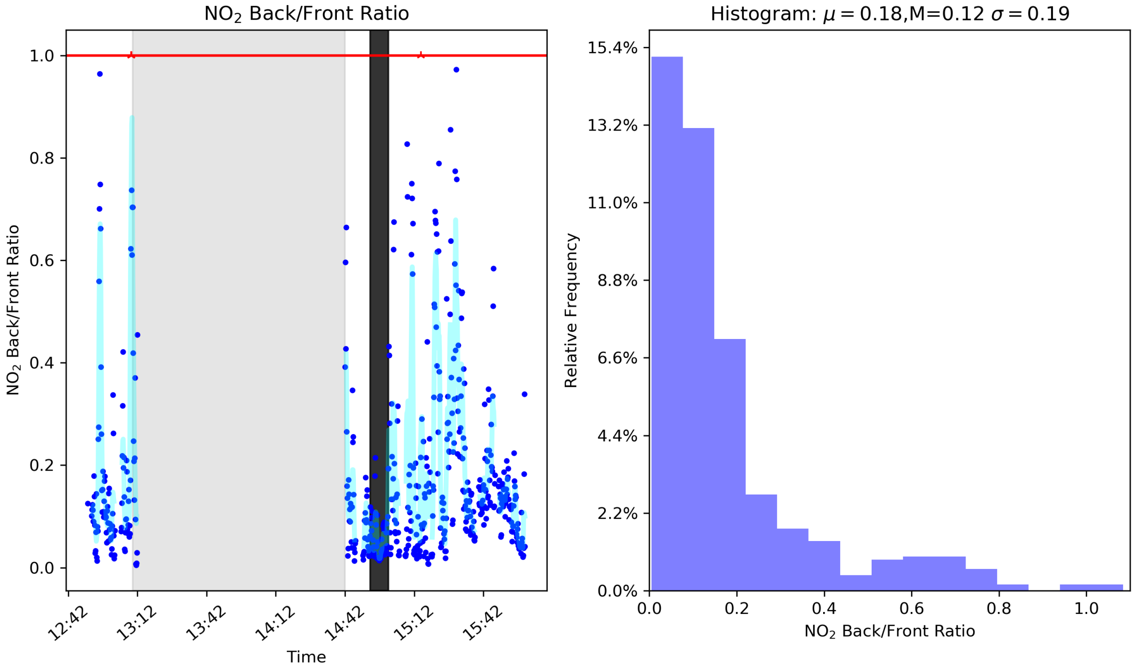

Figure 6.17: NO$_2$ ratio $c_{followingvehicle}/c_{Exhaustoffrontvehicle}$

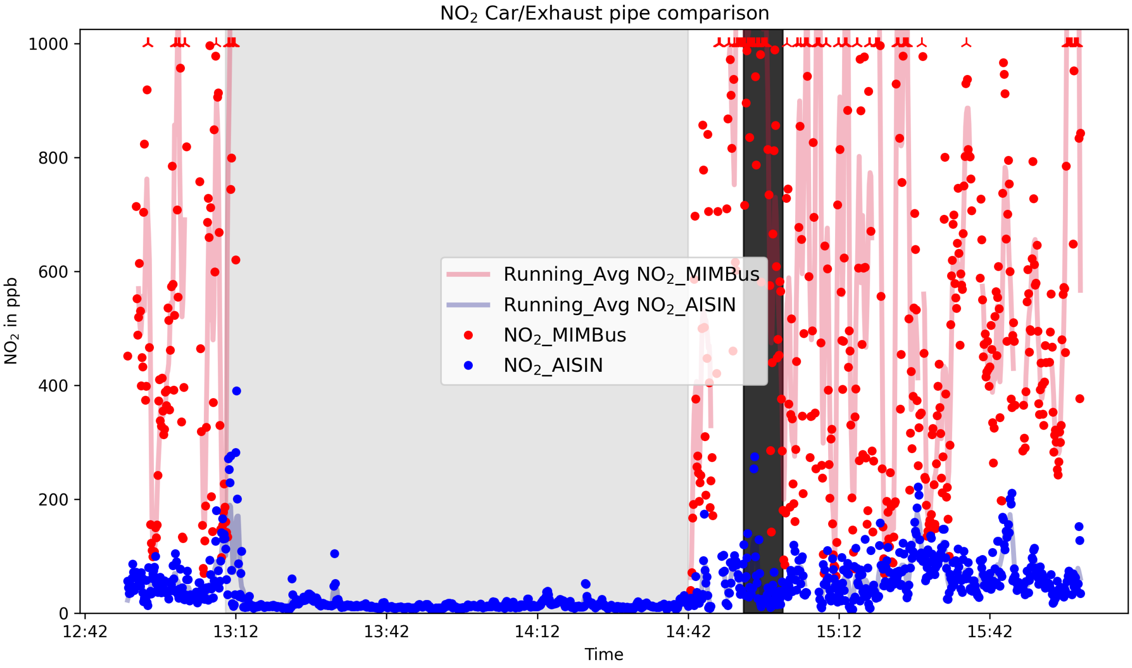

Figure 6.18: The NO$_2$ mixing ratios measured by CEDOAS

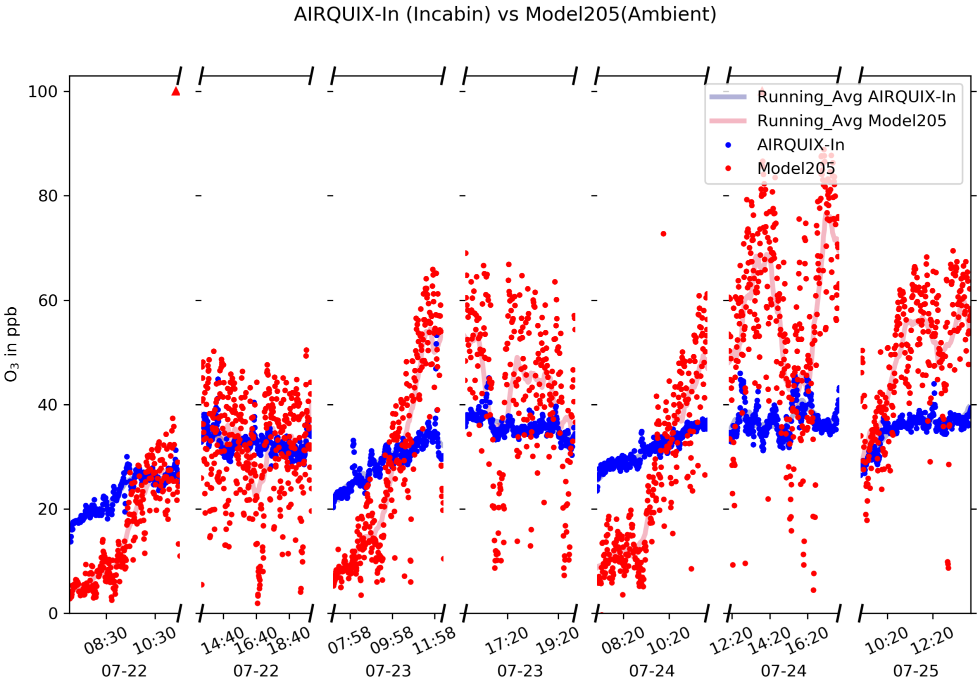

Figure 6.19: The O$_3$ inside / outside mixing ratio of vehicle 2 measured by AIRQUIX (in-vehicle) and 2B Model205 (Ambient) and 30 minutes running average plot

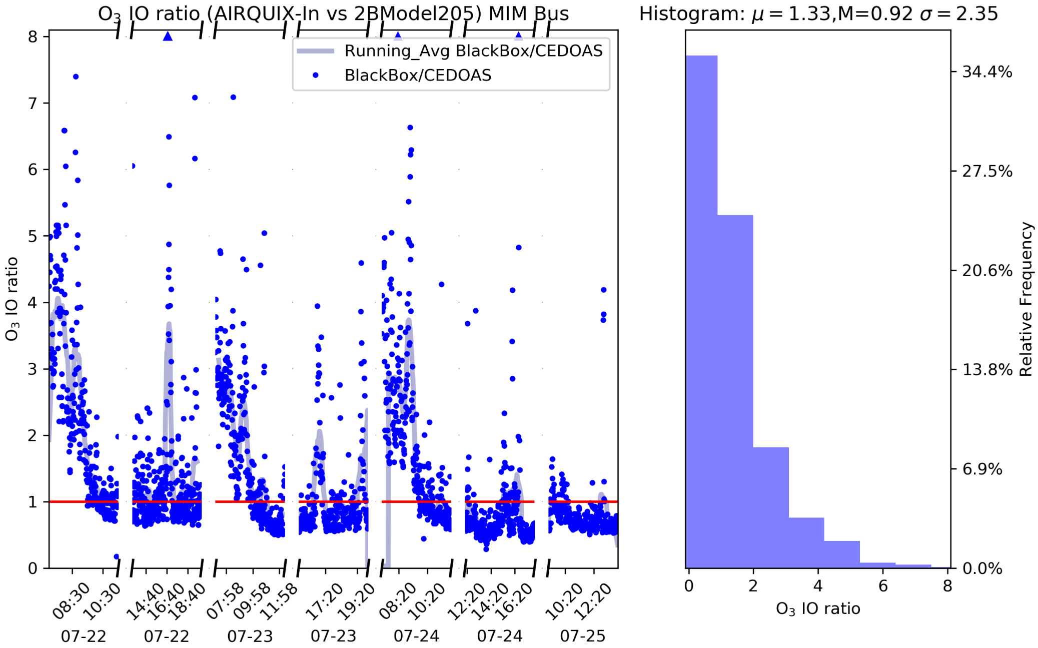

Figure 6.20: AIRQUIX (in-vehicle) vs O_3 (ambient) measured by AIRQUIX (in-vehicle) and 2BModel205 (Ambient)

6.2.4.3 Particulate Matter (PM)

In Vehicle 1, the average PM2.5 I/O ratio was 1.47 ± 0.71 (median 1.43) and the PM10 I/O ratio was 1.30 ± 0.49 (median 1.29), as shown in Figs. 6.21 and 6.23. In Vehicle 2, PM2.5 ratios varied between parking and driving conditions, with an average of 1.45 ± 0.55 (median 1.39), while PM10 ratios averaged 1.25 ± 0.32 (median 1.24) (Figs. 6.25 and 6.27). Overall, in-vehicle PM concentrations were slightly higher than ambient levels, and no significant filtering effect was observed for particulate matter. Future investigations under diverse driving conditions are necessary to better characterize PM removal dynamics.

6.2.4.4 VOCs

The VOC I/O ratios in Vehicle 1 averaged 1.85 with a standard deviation of 1.64 (Fig. 6.30), while Vehicle 2 exhibited a lower average ratio of 1.09 ± 0.35 (Fig. 6.32). Time series data (Figs. 6.29 and 6.31) indicate that VOC levels significantly increased during parking when the vehicles were heated up, and dropped sharply when the car door was opened, likely due to rapid air exchange. Similar fluctuations were observed in external measurements for Vehicle 2, which may be attributed to insufficient air conditioning and rising in-vehicle temperatures that promote VOC emissions from interior materials. In contrast, the more robust air conditioning in Vehicle 1 resulted in lower VOC levels while driving.

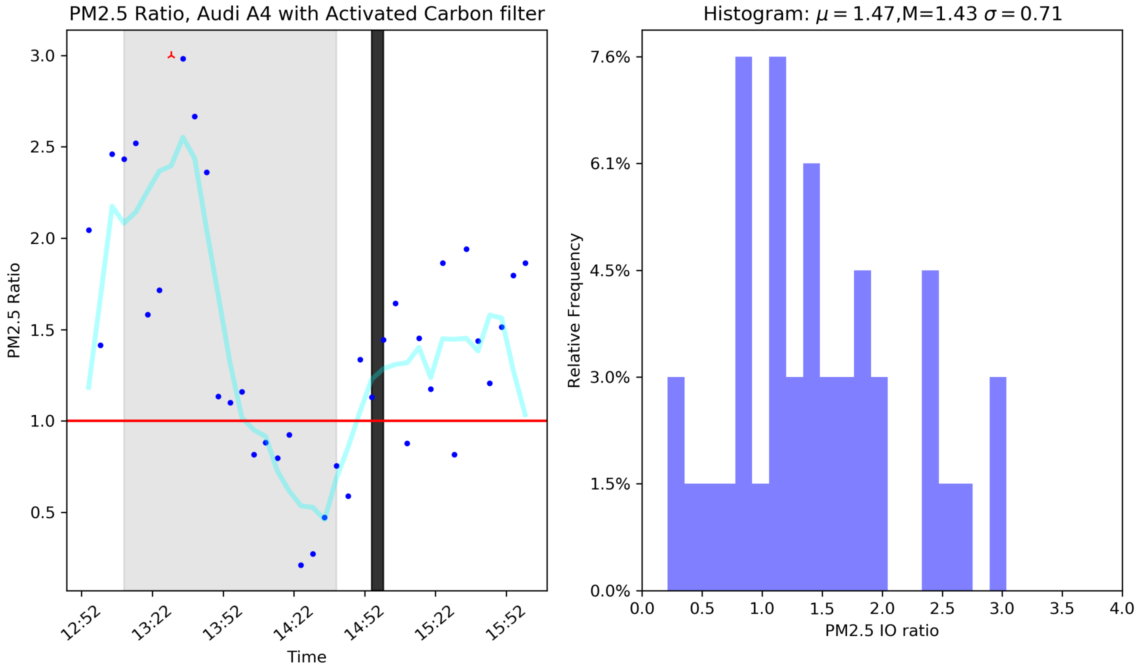

Figure 6.21: The PM2.5 inside / outside ratio on 29 July 2019 of vehicle 1 measured by Pandas Honeywell sensor

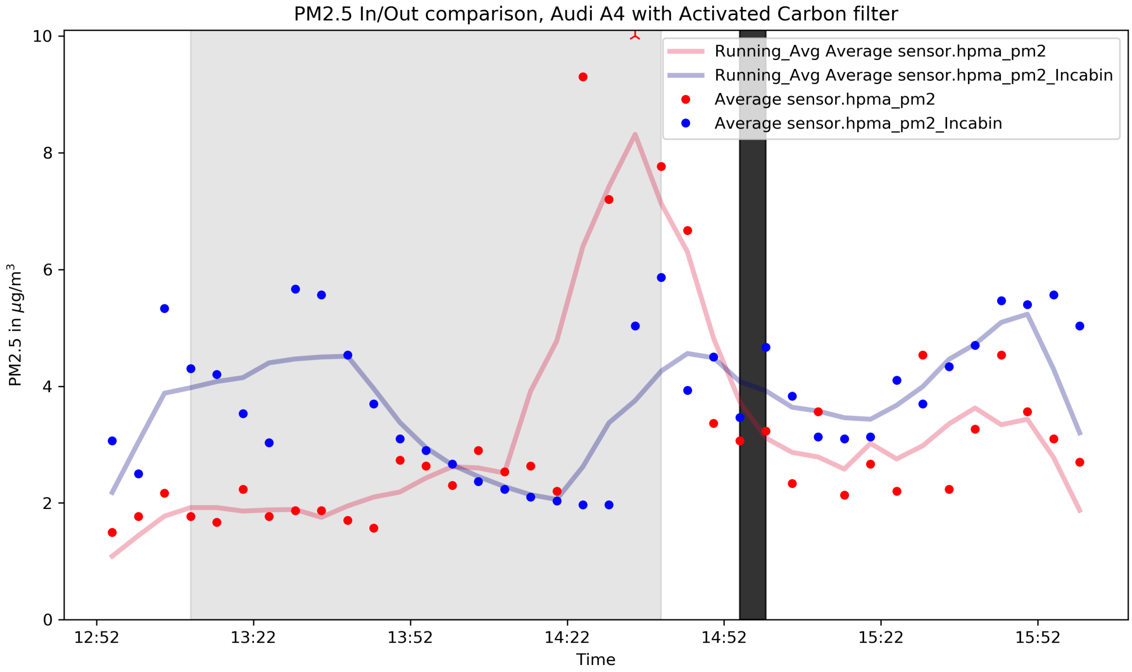

Figure 6.22: PM2.5 concentration on 29 July 2019 of vehicle 1 measured by Pandas Honeywell sensor

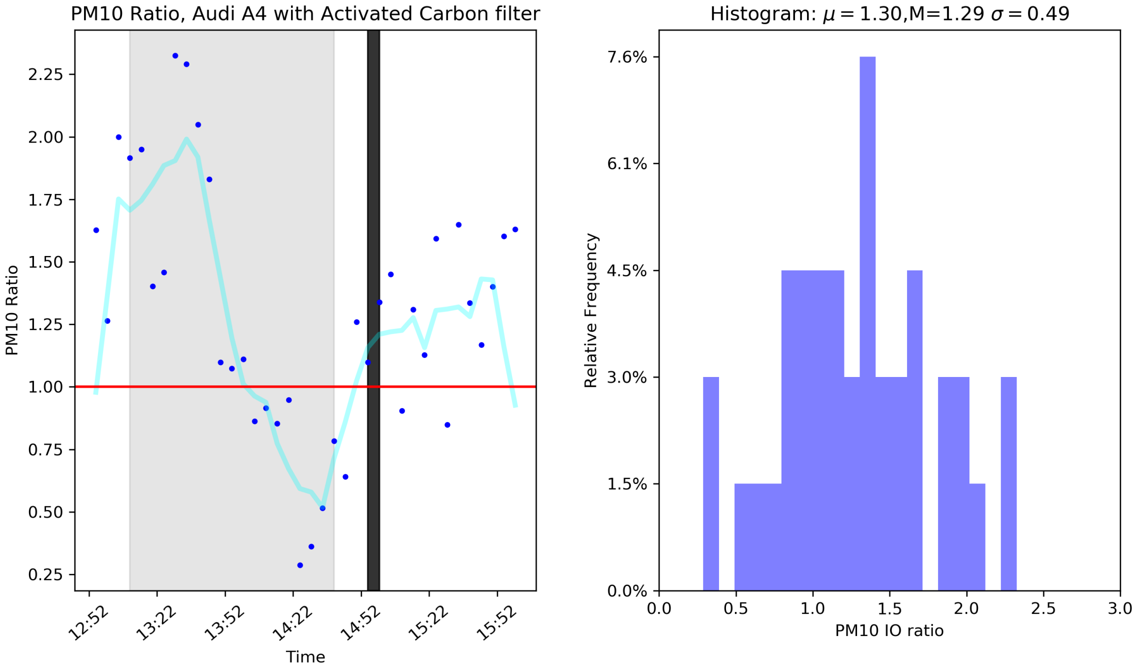

Figure 6.23: The PM10 inside / outside ratio on 29 July 2019 of vehicle 1 measured by Pandas Honeywell sensor

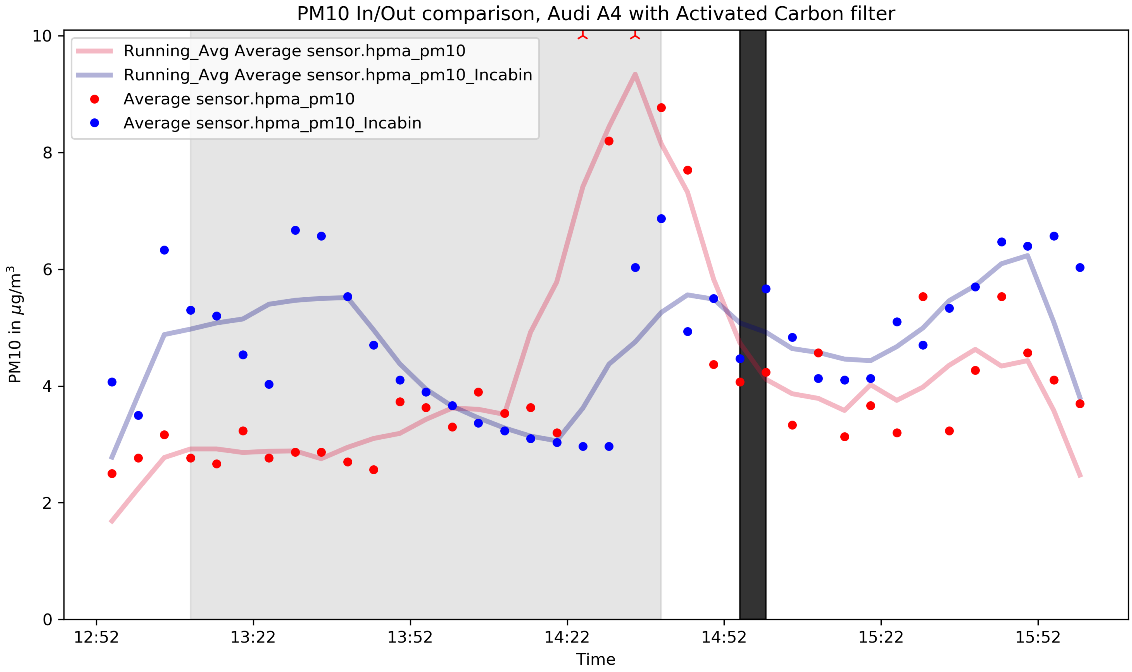

Figure 6.24: PM10 concentration on 29 July 2019 of vehicle 1 measured by Pandas Honeywell sensor

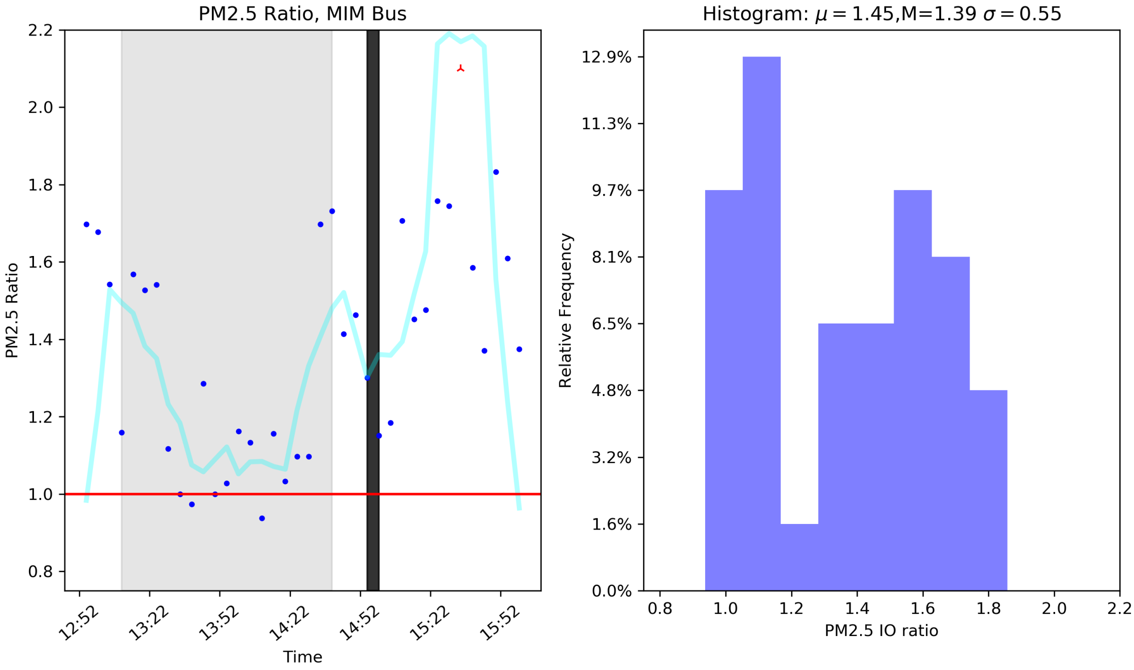

Figure 6.25: The PM2.5 inside / outside ratio on 20190729 of vehicle 2 measured by Pandas Honeywell sensor

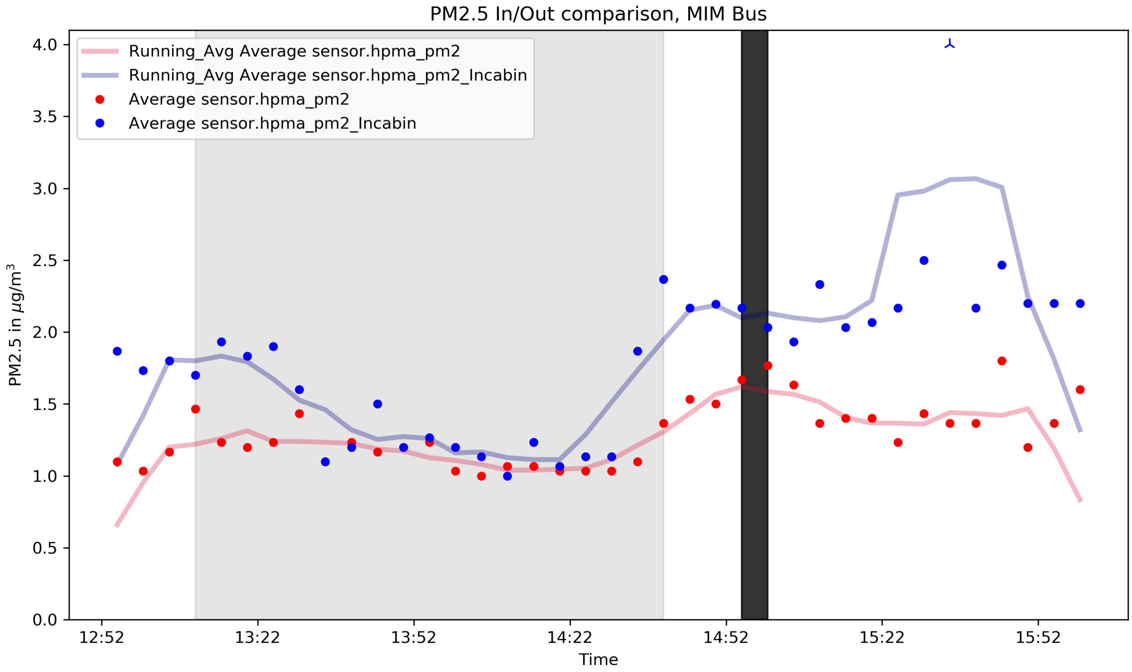

Figure 6.26: PM2.5 concentration on 29 July 2019 of vehicle 2 measured by Pandas Honeywell sensor

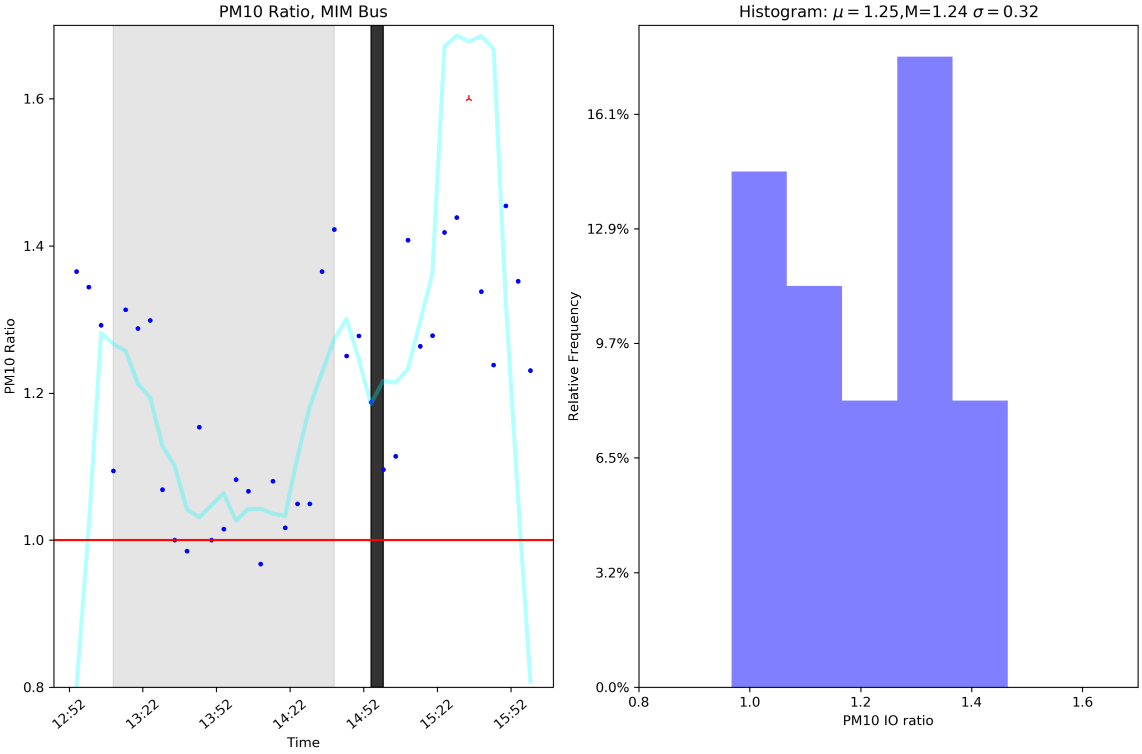

Figure 6.27: The PM10 inside / outside ratio on 29 July 2019 of vehicle 2 measured by Pandas Honeywell sensor

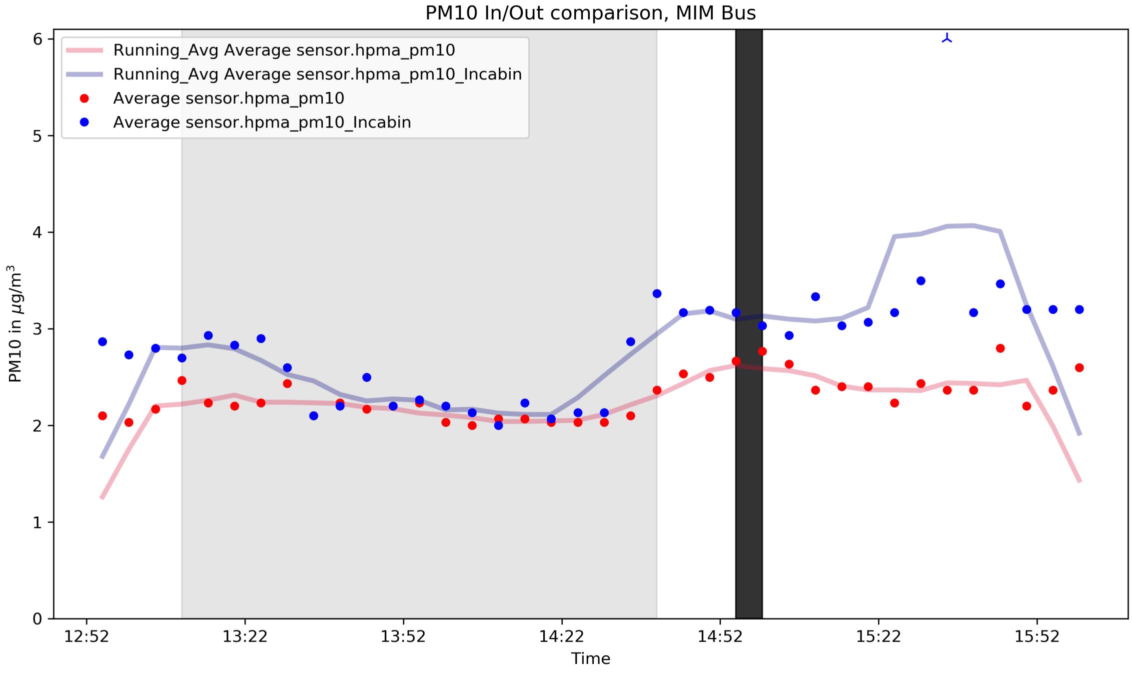

Figure 6.28: PM10 concentration on 29 July 2019 of vehicle 2 measured by Pandas Honeywell sensor

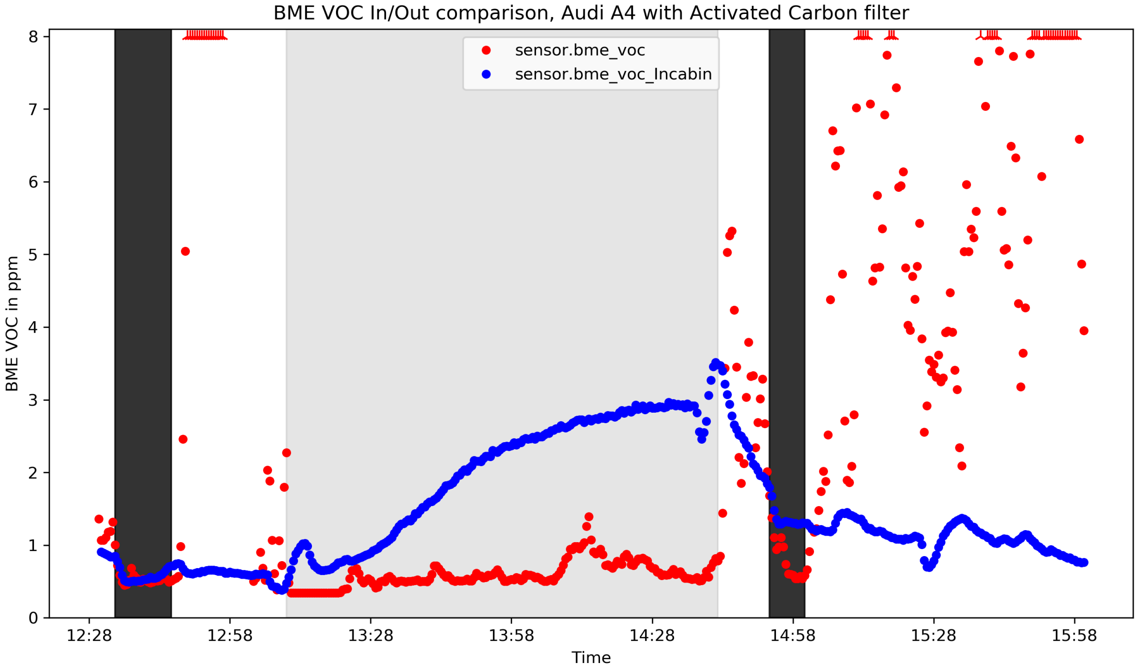

Figure 6.29: The VOC mixing ratio on 29 July 2019 of vehicle 1 measured by Pandas BME sensor

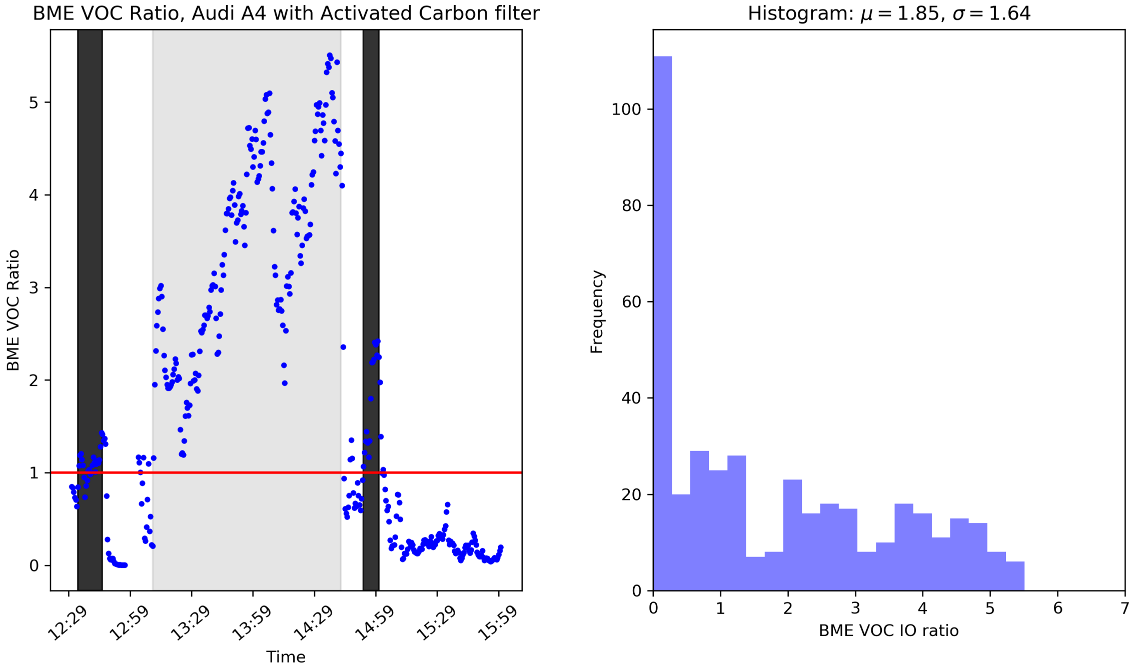

Figure 6.30: The VOC inside / outside ratio on 29 July 2019 of vehicle 1 measured by Pandas BME sensor

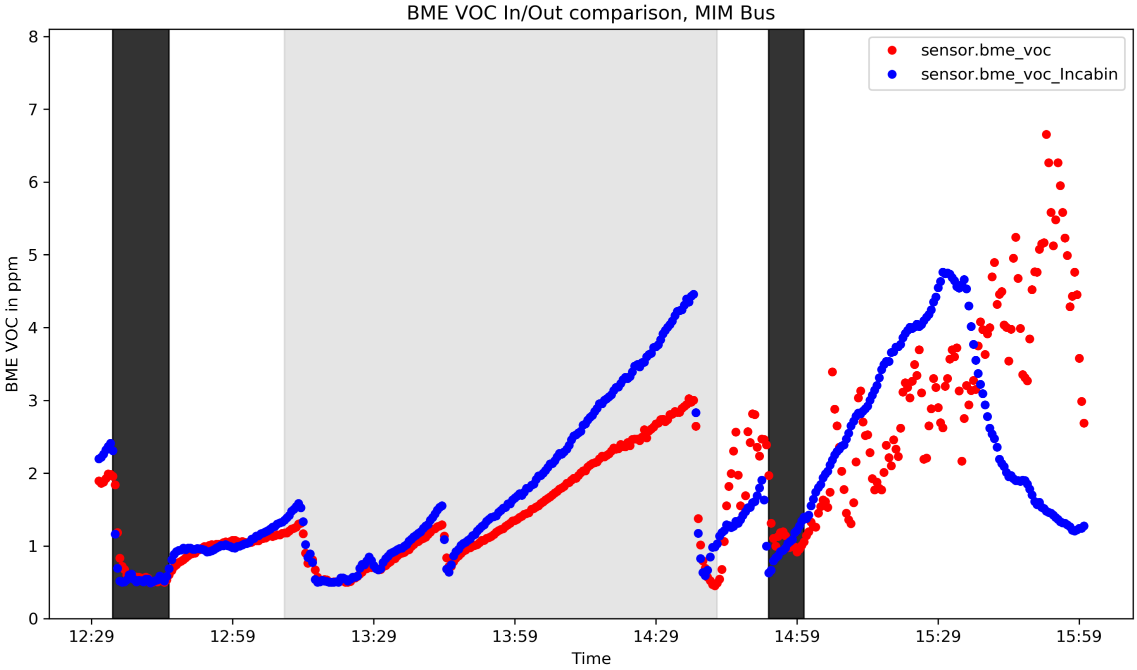

Figure 6.31: The VOC mixing ratio on 29 July 2019 of vehicle 2 measured by Pandas BME sensor

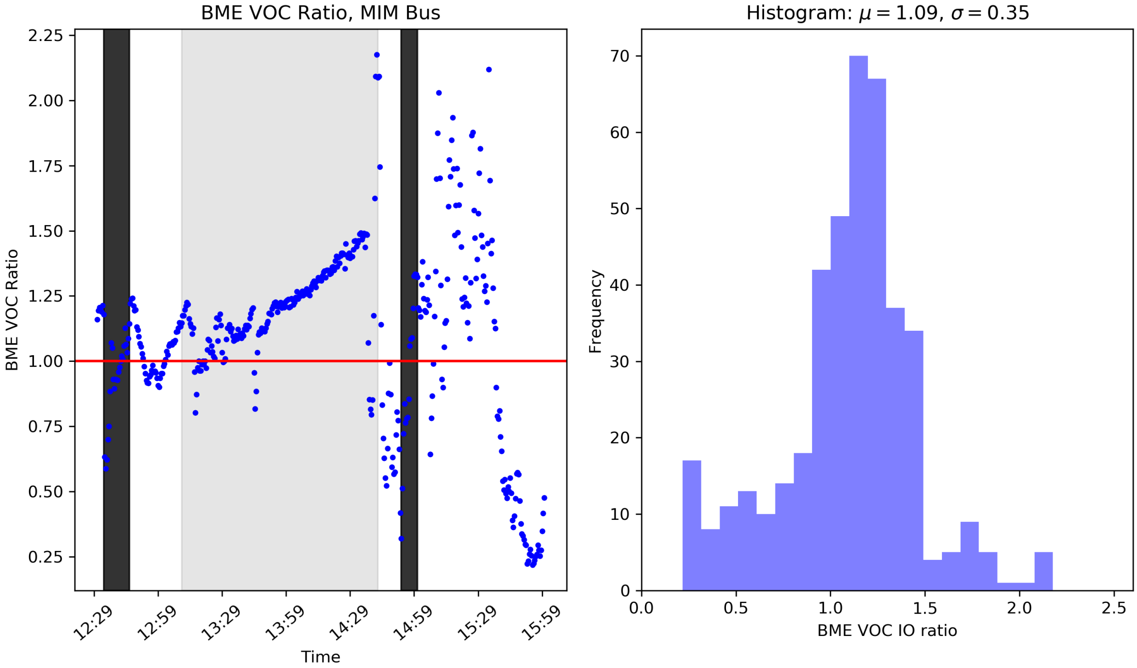

Figure 6.32: The VOC inside / outside ratio on 29 July 2019 of vehicle 2 measured by Pandas BME sensor

6.3 Case III: Multi-city Evaluation of Traffic Related Urban NO_2 levels in Germany (METROUNO2)

Complementing the mobile measurements in Munich, the METROUNO2 study expands the scope to a multi-city analysis across Berlin, Hamburg, Stuttgart, and Munich. In German cities, traffic emissions are a primary source of NO_2, prompting measures such as low-emission zones and diesel bans.

The COVID-19 pandemic provided a unique natural experiment to disentangle the effects of emission reductions from meteorological variability. While global studies reported substantial NO_2 decreases due to mobility restrictions (Cooper et al., 2022; Lian et al., 2020), local meteorological conditions often complicated these assessments (Kerr et al., 2022; von Schneidemesser et al., 2021). In this study, we employ a Generalized Additive Model (GAM) to quantify the distinct impacts of traffic volume and meteorology on urban NO_2 variability. An additional analysis in Munich combines stationary measurements at a height of 30 meters with mobile on-road data to validate the findings during the lockdown periods.

6.3.1 Methodology

6.3.1.1 Experiment setup and data collection

Our primary objective was to characterize the temporal and spatial variability of NO_2 mixing ratios, alongside key meteorological parameters. The following sections detail the data sources and measurement techniques employed in this study.

6.3.1.1.1 Stationary NO_2 data from air quality monitoring stations in Berlin, Hamburg, Stuttgart and Munich

We collected NO_2 data from urban Air Quality Monitoring Stations (AQMS) in Berlin, Hamburg, Stuttgart and Munich, operated by their respective environmental agencies (Bayerischen Landesamtes für Umwelt; Behörde für Umwelt, Klima, Energie und Agrarwirtschaft; Landesanstalt für Umwelt Baden-Württemberg; Senatsverwaltung für Mobilität, Verkehr, Klimaschutz und Umwelt). Stations were chosen for their proximity to major roadways and traffic density, ensuring that the measurements reflect vehicle-related NO_2 emissions.

6.3.1.1.2 Stationary NO_2 measurement from LP-DOAS at 30 meters height in Munich

We deployed three Long-Path Differential Optical Absorption Spectroscopy (LP-DOAS) instruments on the rooftop of the Meteorological Institute of Ludwig-Maximilians-Universität (LMU) at approximately 30 meters height. DOAS is a well-established remote sensing technique widely used in various configurations that can measure trace gases with high sensitivity and specificity (Platt and Stutz, 2008). Our instruments detect trace gases along light paths ranging from a few hundred meters to a few kilometers between the instrument and retro reflectors, utilizing the pollutant's absorption structure from an emitted LED light signal. The three LP-DOAS are aimed at different directions to simultaneously capture city-wide NO_2 mixing ratios across Munich (Zhu et al., 2020).

6.3.1.1.3 Additional analysis in Munich: Mobile measurements for on-road NO_2 study of the COVID-19 influence analysis

Mobile measurements campaigns were conducted to achieve extensive coverage of on-road NO_2 emission. An Iterative Cavity-Enhanced DOAS (ICAD) NO_2 instrument developed by Airyx GmbH and several portable measurement boxes we developed which we call Air Quality Inspection boXes (AIRQUIX) were used to perform ground-based mobile measurements.

In the ICAD instrument, an optical cavity, equipped with two reflective mirrors, folds the light path to achieve a sufficient path length (approximate 1 km). The degree of spectral absorption by NO_2 gas is analyzed to retrieve NO_2 mixing ratio with very high accuracy due to the long absorption path length (Horbanski et al., 2019). This instrument was used for the mobile measurement campaign (19-25 July 2019) to access the NO_2 pollutant distribution in Munich.

During the lockdown period starting from 21 March 2020, multi-person cooperative experiments were difficult to implement due to government regulations in Munich. Therefore, a newly developed low-cost portable air quality monitoring device, AIRQUIX, was used for mobile measurements via bicycle and private car from 24 March 2020 to 29 March 2020, and from 15 December 2020 to 16 December 2020. AIRQUIX is equipped with several sensors, which can measure NO_2, NO, O_3, CO_2, PM1, PM2.5, PM10, environmental parameters (temperature, relative humidity, pressure) for sensor data correction, and GPS for location tracking. It detects NO_2 pollutant with a low-cost electrochemical sensor. A novel algorithm was developed and applied to the sensor raw output to improve the accuracy and precision of NO_2 measurements. In this study, pre- and post-calibrations were performed through side-by-side comparisons with ICAD to achieve the highest data accuracy. AIRQUIX shows a good coefficient of determination (R^2) of 0.90 with a Root mean square error of 2.73 ppb.

6.3.1.1.4 Meteorological information

Air pollution is closely associated with various meteorological factors, such as wind direction (WD) and wind speed (WS), absolute humidity (AH), daily sum diffuse radiation (DDR) (Aldrin and Haff, 2005; Cichowicz et al., 2017; Jones et al., 2010). Absolute humidity affects chemical reaction rates and the formation of pollutants. DDR represents the amount of solar radiation that reaches the Earth's surface after being scattered or diffused by the atmosphere, which influences photochemical processes and atmospheric mixing. The meteorological data, continuously measured at approximately 30 meters in height at the Meteorological Institute of LMU, were obtained for data analysis in Munich. For Berlin, Hamburg, and Stuttgart, we obtained these meteorological data from Deutscher Wetterdienst (DWD) climate stations (Deutscher Wetterdienst), which provide a wide range of meteorological parameters.

6.3.1.1.5 Mixing layer height (MLH)

NO_2 ground concentration in the atmosphere has been found to possibly be inversely correlated with the MLH (Geiß et al., 2017; Yassin et al., 2018). However, this correlation is only applicable to a well mixed layer, which might not be the case for roadside measurements and LP-DOAS measurements at 30 meters height. Therefore, a detailed analysis of the mixing layer height influence is crucial.

We use the boundary layer height data from ERA5 reanalysis provided by the Copernicus Climate Change Service (C3S) Climate Data Store (CDS) (Copernicus Climate Change Service, 2024) for Berlin, Hamburg, Stuttgart, and Munich roadside measurements. ERA5 calculates MLH using the bulk Richardson number method (European Centre for Medium-Range Weather Forecasts), which incorporates wind profile information (Yang and Pan, 2025), potentially creating collinearity. Therefore, for Munich's LP-DOAS analyses, we utilized ceilometer derived MLH due to co-location and superior data availability. These MLH values were derived using the automatic MLH retrieval algorithm COBOLT (Continuous Boundary Layer Tracing, Geiß, 2016) applied to measurements from a Lufft CHM15kx ceilometer at LMU Munich. The algorithm employs a time-height tracking procedure that combines gradient analysis, variance statistics, and wavelet covariance transforms, accounting for varying solar angles to trace MLHs.

6.3.1.1.6 Traffic data

Traffic emissions are considered as one of the primary urban sources of NO_2. Therefore, traffic volume data have been collected to assess variations in NO_2 emission. This data were obtained from transportation authorities of each city (Behörde für Verkehr und Mobilitätswende Hamburg; Landeshauptstadt München Mobilitätsreferat; Ministerium für Verkehr Baden-Württemberg; Verkehrsinformationszentrale Berlin). To simplify the analysis, we assume same emission factors for different vehicle types in this study.

6.3.1.2 Model setup for impact factors analysis

To quantify how meteorological and traffic drivers influence NO_2 mixing ratios, we employed a Generalized Additive Model (GAM) to perform regression fitting between NO_2 mixing ratios and various impact factors. GAM extends the generalized linear model by incorporating flexible smooth functions for the covariates (Hastie, 1990; Hastie and Tibshirani, 1986). This model has been widely applied in many areas, particularly in air pollution studies. The fitting was conducted utilizing the Mixed GAM Computation Vehicle with Automatic Smoothness Estimation ('mgcv', Wood, 2023, 2017).

We chose GAM for our analysis because meteorological factors generally show non-linear relationships with NO_2 levels. The semiparametric GAM regression allows for more flexible modeling with its smooth functions (Diao et al., 2021; Orak, 2022; Xiao et al., 2021; Yan et al., 2024). Additionally, as a white box model, GAM offers clear and interpretable results by enabling the separate examination of individual predictor effects. This capability is valuable for understanding how various factors impact the response variable. Our study is focusing on ground-based, traffic-related NO_2 emissions in an urban, traffic dominated environment. Therefore, other activities, such as industrial emissions, were assumed to be negligible within our study area.

After testing various candidate factors, we retained those with clear physical relevance, low collinearity, and significant explanatory power, which are wind direction and wind speed, absolute humidity, mixing layer height, daily sum diffuse radiation and traffic volume. Other variables such as temperature, pressure, and relative humidity were excluded due to either high collinearity with the retained factors or lower explanatory contribution. The model used in this study is described in Equation (6.1).

$$g(\hat{c}_{NO_2}) = \beta + \sum_{n=1}^{6} s_n(x_n) \tag{6.1}$$

where g is the link function, $\hat{c}_{NO_2}$ is the predicted NO_2 mixing ratio, β is the intercept term, s_n are the smooth functions describing the dependence of the $\hat{c}_{NO_2}$ on x_n. The x_n represent the covariates (wind direction and wind speed, traffic volume, absolute humidity, daily sum diffuse radiation and mixing layer height). We picked a cyclic cubic regression spline for the factor wind direction due to the inherent periodic nature of it. Thin-plate smoothing splines were selected for the other smooth functions s_n because they can model complex, non-linear relationships between covariates and response. These splines allow for flexible curves that can adapt to various data patterns without the need to specify knot locations. A Gamma distribution was assumed for the response variable c_{NO_2} to account for the positive and right-skewed nature of the data. A log-link function $g(\cdot) = \ln(\cdot)$ was used to relate the expected NO_2 mixing ratio to the linear predictor, ensuring positive predictions and resulting in a multiplicative effect of the covariates. So the model can be transformed as shown in Equation (6.2).

$$\hat{c}_{NO_2} = exp(\beta + \sum_{n=1}^{6} s(x_n)) \tag{6.2}$$

A modified Generalized Cross-Validation (GCV) score is calculated for smoothing parameter determination with γ=1.4 to reduce the chance of overfitting, as shown in Equation (6.3) (Kim and Gu, 2004).

$$GCV(\lambda) = \frac{m^{-1}\sum_{i=1}^{m}(c_{NO_2,i} - \hat{c}_{NO_2,i})^2}{(1 - \gamma tr(A)/m)^2} \tag{6.3}$$

where c_{NO_2} is the measured NO_2 mixing ratio, $\hat{c}_{NO_2}$ is the predicted NO_2 mixing ratio, m is the number of observation, and A is the influence matrix that maps the measured data c_{NO_2} to the predicted data $\hat{c}_{NO_2}$ in the fitting process ($\hat{c}_{NO_2} = Ac_{NO_2}$).

Relative importance reflects individual variable's contribution. Collinearity among factors redistributes their explanatory power in models, which makes relative importance into more robust measure in complex systems. A leave-one-out measure developed by Aldrin and Haff (2005) has been applied to analyze the relative importance of covariates. This method modifies the model by replacing individual covariates with constants (the mean of each covariate) to omit the impact of each covariate. First, the progress calculates the Mean Squared Errors (MSE) of the original model on the log-scale, followed by calculating $\sigma_{(-i)}$ for each model iteration where one covariate is omitted. The relative importance (R_i) of the different factors can be determined by:

$$R_i = \frac{\sigma_{(-i)} - \sigma}{\sum_{i=1}^{p}\sigma_{(-i)} - p\cdot\sigma} \tag{6.4}$$

where σ is the MSE of the original model, $\sigma_{(-i)}$ is the MSE while omitting the impact of the ith covariate, and p is the number of covariates.

6.3.2 Results and discussion

6.3.2.1 Comparison of the GAM regression results with stationary measurements in different cities

We trained the GAM on NO_2 mixing ratios from January 2020 to December 2021, then used it to predict values for the other periods. The fitting results are shown in Fig. 6.33-6.37. The 2D histogram in these figures demonstrates a strong correlation (0.81 for Berlin, 0.78 for Hamburg, 0.75 for Stuttgart, 0.47 for Munich-AQMS, and 0.75 for Munich-LPDOAS) between the measured NO_2 mixing ratio and the overall fitted values. Time-series plots in respective figures(c) show the training, predicted, and measured NO_2 mixing ratios, showing that the model effectively captured the overall NO_2 trends. The residuals were fitted with a linear regression line, which showed a negative trend in respective figures(d), revealing a gradual overestimation by the model over time. This temporal bias corresponds to the distribution shift observed in figures(b) between

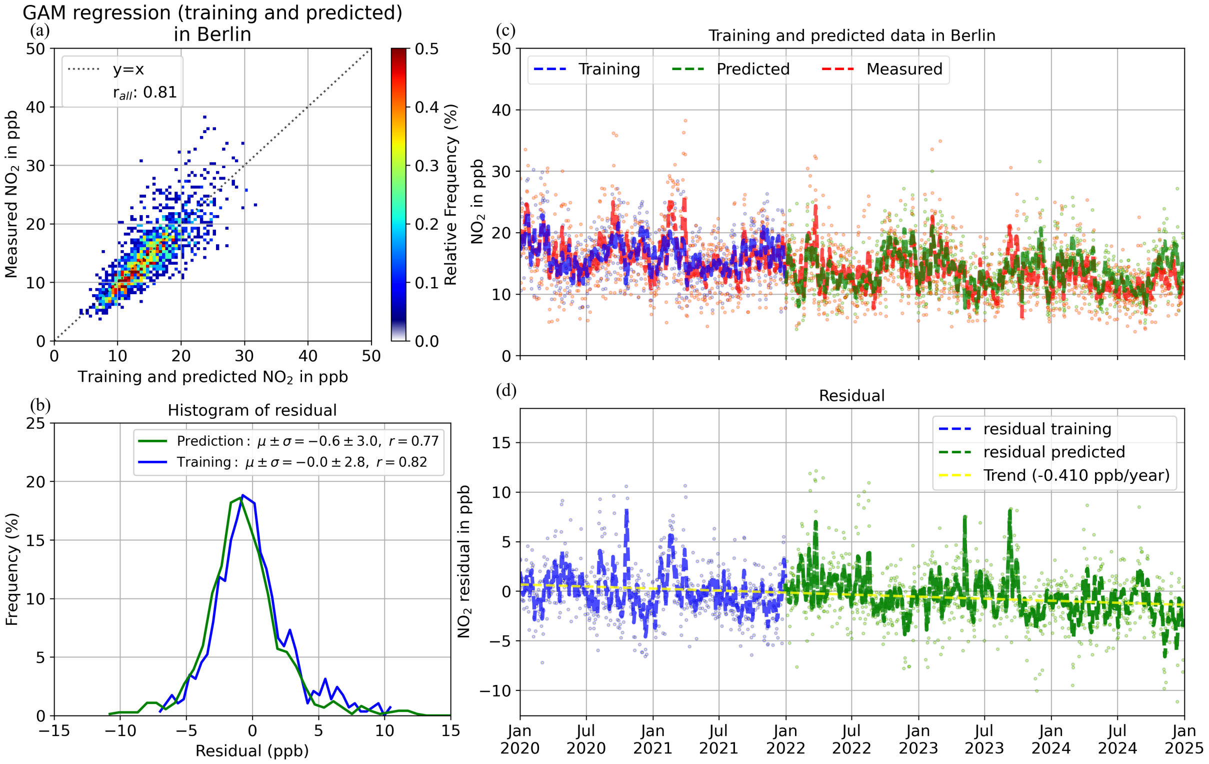

Figure 6.33: GAM regression for Berlin between NO_2 mixing ratio and the key factors. (a) 2D histogram plot showing the correlation between measured and fitted NO_2 mixing ratios (including both training and predicted data). (b) Distribution of residuals for training (blue) and predicted (green) data. (c) Time series of NO_2 mixing ratios with 7-day moving averages: training period (blue, from January 2020 to December 2021), predicted period (green, periods outside the training period), and measured values (red). (d) Residual analysis of predicted NO_2 mixing ratios with linear trend line (dashed yellow) indicating the temporal bias as NO_2 trend in model predictions.

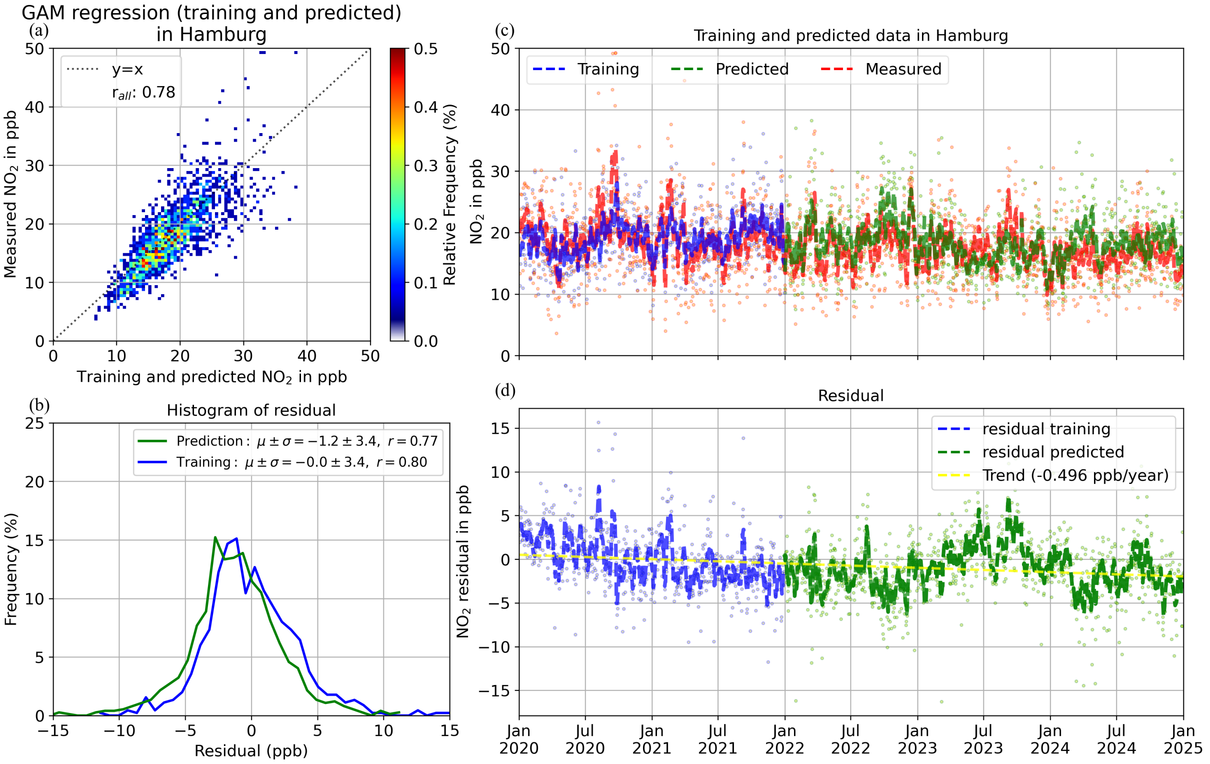

Figure 6.34: GAM regression for Hamburg between NO_2 mixing ratio and the key factors. (same analysis as in Fig. 6.33)

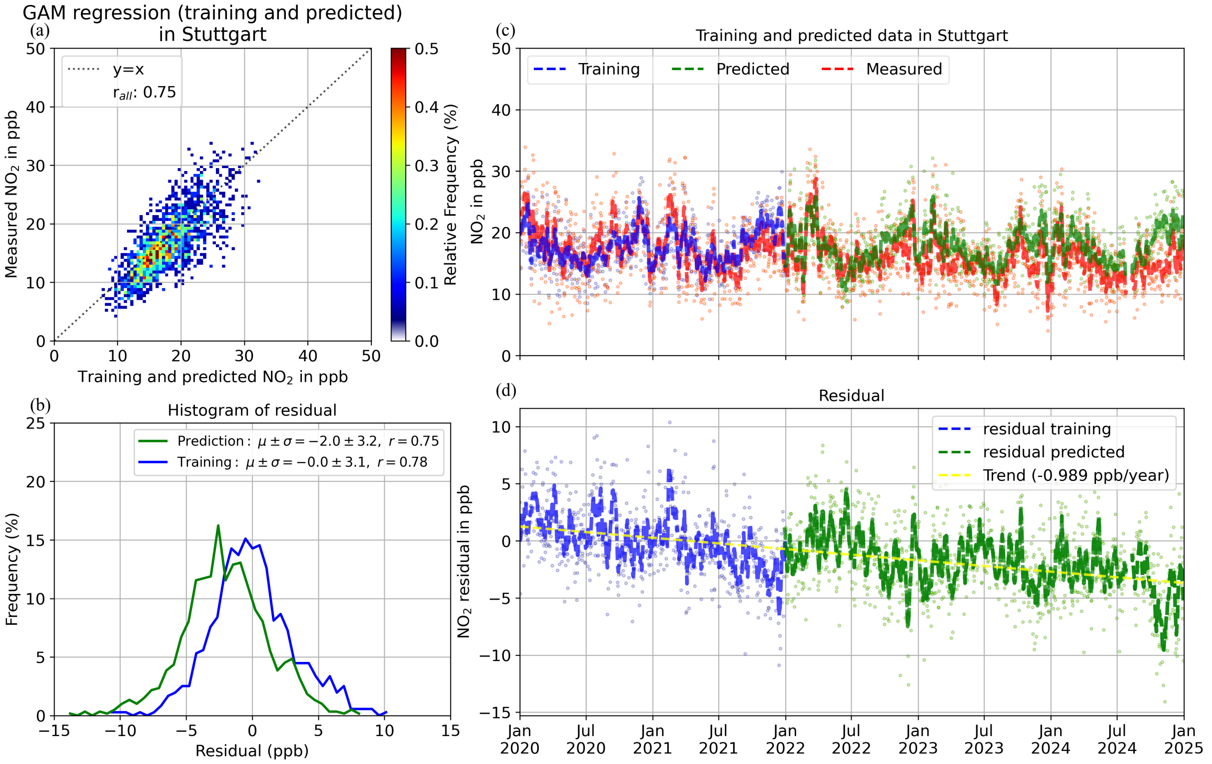

Figure 6.35: GAM regression for Stuttgart between NO$_2$ mixing ratio and the key factors. (same analysis as in Fig. 6.33)

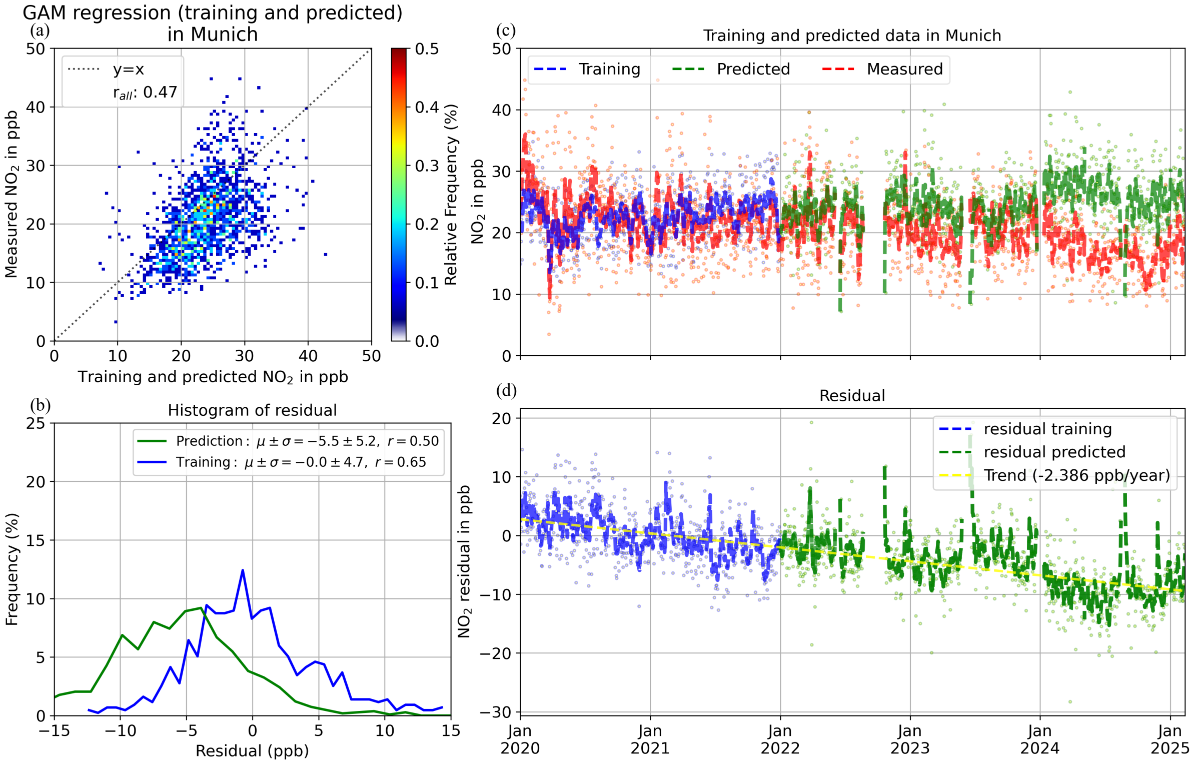

Figure 6.36: GAM regression for Munich between NO_2 mixing ratio from Munich's Air Quality Monitoring Station (Munich-AQMS) and the key factors. (same analysis as in Fig. 6.33)

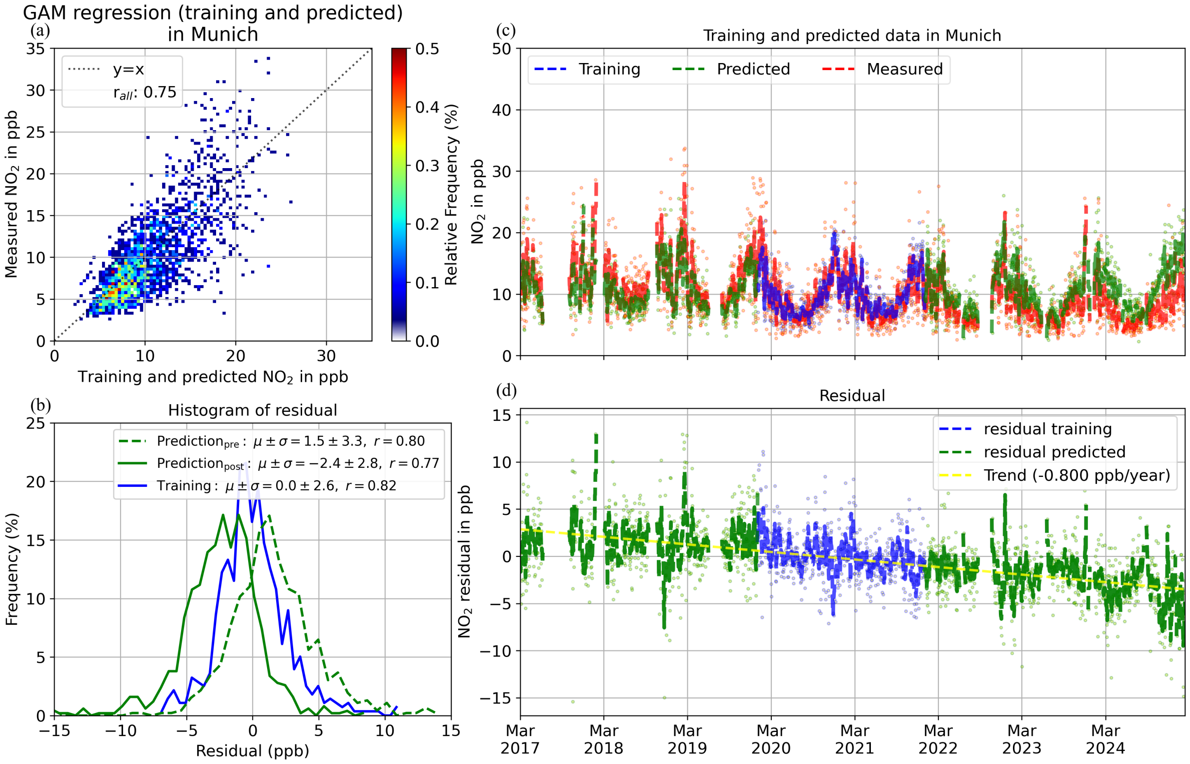

Figure 6.37: GAM regression for Munich between NO_2 mixing ratio measured by LP-DOAS (Munich-LPDOAS) and the key factors, where the MLH was retrieved with COBOLT. (b) shows the distribution of residuals for periods before (dashed green line, Prediction$_{pre}$), within (blue, Training), and after (green, Prediction$_{post}$) the training period. (All other analyses are the same as in Fig. 6.33)

training and prediction periods. This bias decline likely reflects the cumulative effects of the implementation of various clean air policies and plans (including the introduction of low-emission zones, plan of phasing out combustion engine), strategies of numerous car manufacturers and the promotion of electric vehicles (German Institute of Development and Sustainability (IDOS); Landeshauptstadt München; Leibinger et al., 2024). Munich-AQMS shows the highest residual decline (-2.386 ppb per year) compared to the other cities (from -0.410 to -0.989 ppb per year), which is likely the reason for its lowest overall correlation. This pattern aligns with findings by Gu et al. (2022), and corresponds to Munich's phased diesel ban implementation from February 2023 (Landeshauptstadt München; Leibinger et al., 2024). Munich-LPDOAS site shows a modest decline (-0.800 ppb per year), likely due to its elevated, less traffic influenced location.

6.3.2.1.1 Partial dependence and relative importance of the impact factors

To interpret the GAM, we examined covariates' influence using Partial Dependence Plots (PDP) and relative importance metrics (Fig. 6.38-6.42). The left panels display each factor's relative importance computed by the leave-one-out approach (Eq. 6.4), while the right panels show PDPs with 95 % confidence intervals (dashed red lines) and stripes at bottom to indicate data density. The PDPs reveal that NO_2 mixing ratios rise with increasing traffic volume, vary with wind direction according to source sectors, and decline non-linearly with the other factors.

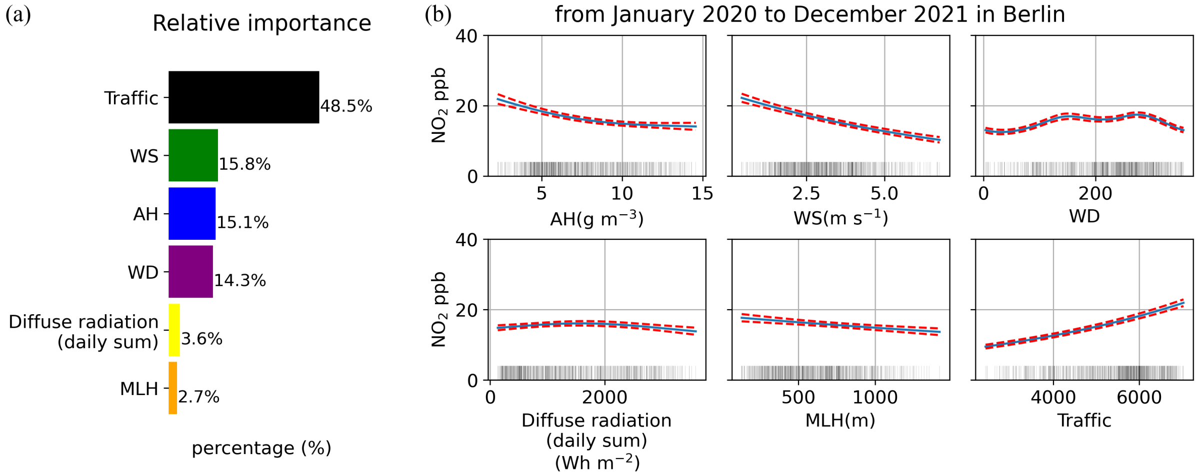

Figure 6.38: Partial dependence plots and relative importance plots of GAM regression for Berlin (a) Relative importance of all fitted covariates. (b) Partial dependence plots with 95 % confidence interval (dashed red curves) for GAM regression (training data). Stripes show the data distribution.

Across all air quality monitoring stations, traffic volume is the dominant driver of NO_2 (48.5 % in Berlin, 43.7 % in Hamburg, 37.6 % in Stuttgart, 35.6 % in Munich-AQMS), reflecting the roadside high traffic density locations of these measurements. The order of relative importance for other factors is different for different cities. In Berlin, wind speed (15.8 %),

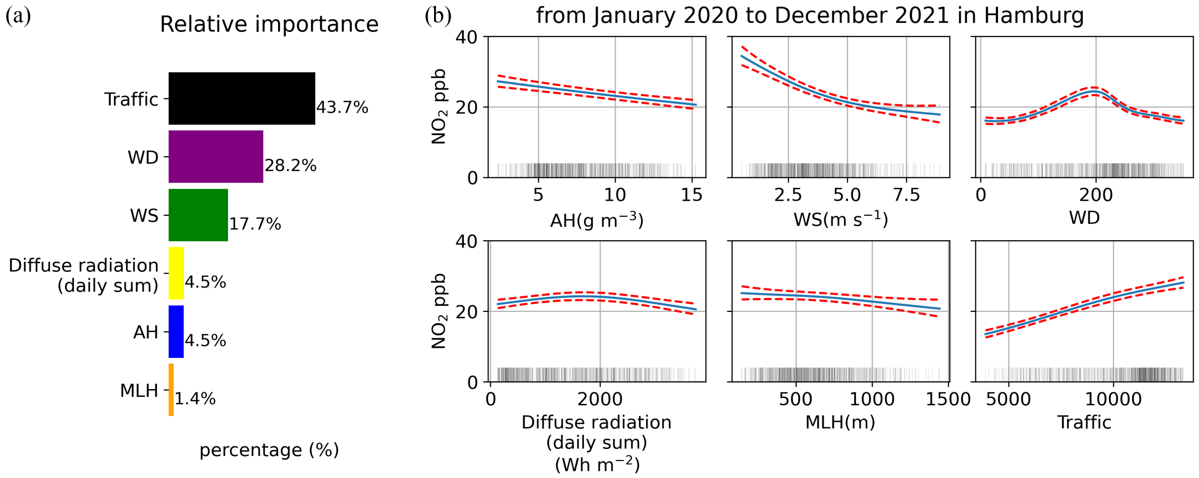

Figure 6.39: Partial dependence plots and relative importance plots of GAM regression for Hamburg. (same analysis as in Fig. 6.38)

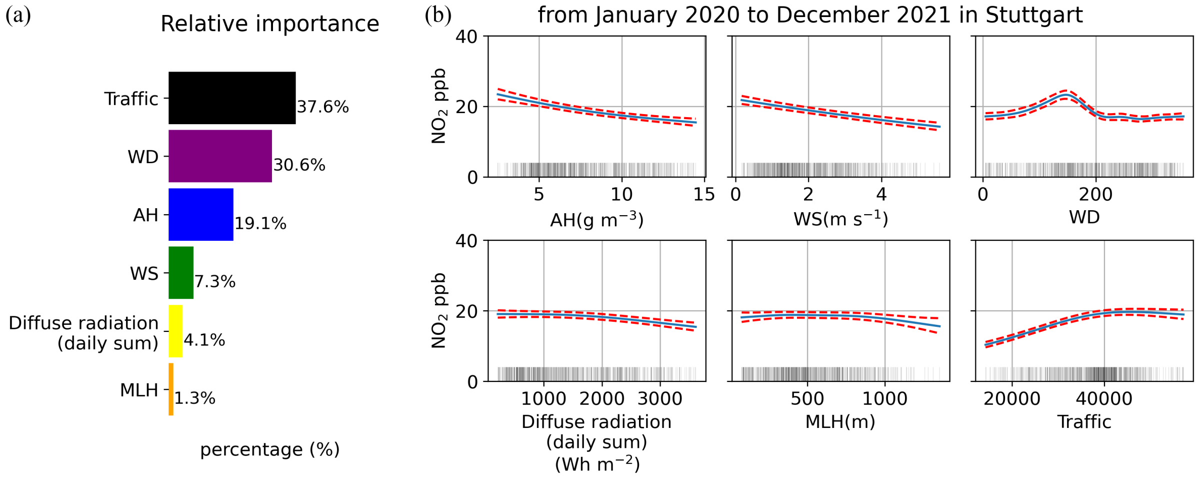

Figure 6.40: Partial dependence plots and relative importance plots of GAM regression for Stuttgart. (same analysis as in Fig. 6.38)

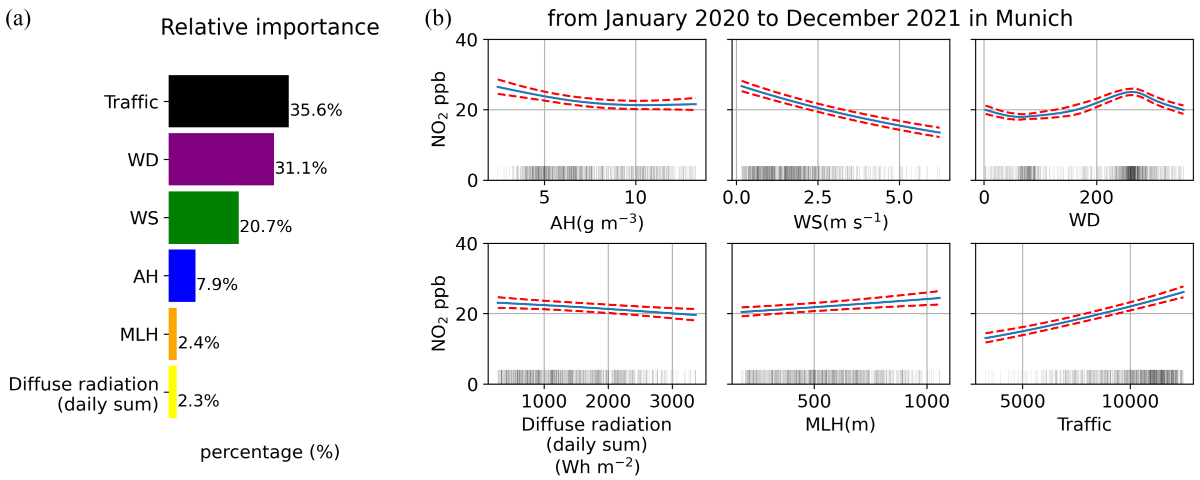

Figure 6.41: Partial dependence plots and relative importance plots of GAM regression for Munich-AQMS. (same analysis as in Fig. 6.38)

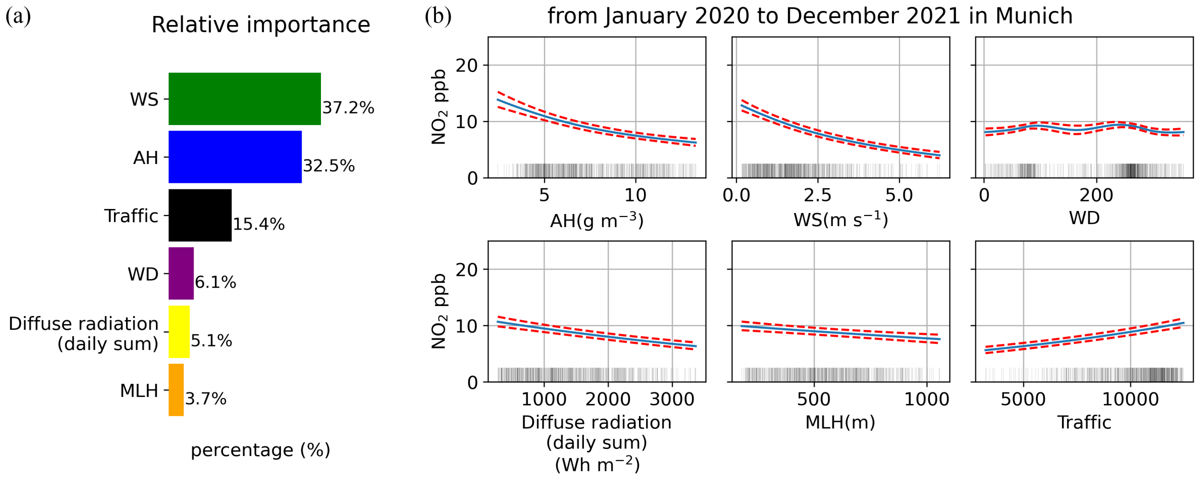

Figure 6.42: Partial dependence plots and relative importance plots of GAM regression for Munich-LPDOA and using MLH retrieved with COBOLT. (same analysis as in Fig. 6.38)

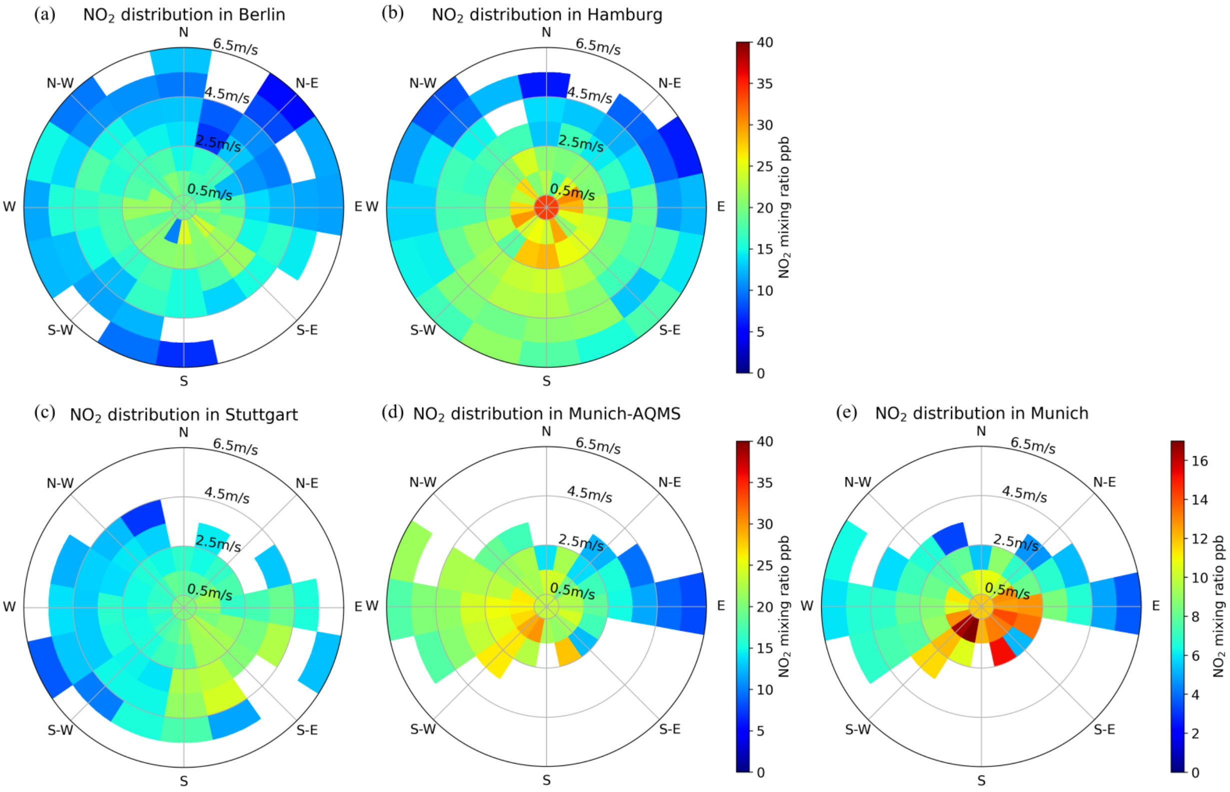

Figure 6.43: Wind rose plot for NO$_2$ mixing ratio in different cities. (a) Berlin, (b) Hamburg, (c) Stuttgart, (d) Munich-AQMS, (e) Munich-LPDOAS. The wind direction is shown in the polar coordinate system, where the radius represents the wind speed. Low wind speed condition is defined as speeds below 0.5 m s^{-1} where assuming wind speed has no influence on NO$_2$ mixing ratio. Wind direction is classified into 16 sectors, and wind speed is divided with a step of 1 m s^{-1}. Wind speed higher than 6.5 m s^{-1} is not shown in the plot due to the low data density. The color indicates the NO$_2$ mixing ratio.

absolute humidity (15.1 %) and wind direction (14.3 %) show comparable secondary impacts. Daily sum diffuse radiation (3.6 %) and mixing layer height (2.7 %) show less impacts on NO_2 levels. The data in Hamburg highlight wind direction (28.2 %) as the second important factor, followed by wind speed (17.7 %), daily sum diffuse radiation (4.5 %), absolute humidity (4.5 %), and mixing layer height (1.4 %). Similarly, wind direction play the secondary important role in Stuttgart (23.4 %), followed by absolute humidity (19.1 %), wind speed (7.3 %). Daily sum diffuse radiation (4.1 %) and mixing layer height (1.3 %) show minimal impacts. In Munich-AQMS, wind direction emerged as the most influential meteorological driver (31.1 %), followed by wind speed (20.7 %), absolute humidity (7.9 %), mixing layer height (2.4 %) and daily diffuse radiation (2.3 %).

For the case in Munich-LPDOAS (Fig. 6.42) with the NO_2 measured at 30 meters height, the order of importance shifts: wind speed (37.2 %), absolute humidity (32.5 %), traffic volume (15.4 %), wind direction (6.1 %), daily sum diffuse radiation (5.1 %), and mixing layer height (3.7 %). These differences are attributed to the height and location of the measurement.

The differing factor rankings reflect each city's unique meteorology and geography. In coastal Hamburg, for example, NO_2 levels are highly sensitive to wind direction and speed, whereas absolute humidity plays a minor role. Wind speed plays a key role in all cities except Stuttgart, there, the basin topography and surrounding hills restrict airflow, causing pollutant accumulation and reducing the apparent influence of wind.

Wind direction critically shapes the spatial distribution of NO_2, especially in Hamburg, Stuttgart, and at the Munich-AQMS site. The wind-rose plots in Fig. 6.43 display NO_2 mixing ratios by wind sector (radial axis) and speed (radius), with color indicating NO_2 mixing ratio. In Munich-LPDOAS, (Fig. 6.43e), the color scale is normalized to the one in Munich-AQMS for clarity. Across Berlin, Hamburg, and Stuttgart, southerly winds coincide with elevated NO_2 levels. In Hamburg, this pattern may be related to its coastal location. Air quality monitoring stations are positioned in the northern/northeastern part of the harbor, and are influenced by southerly winds carrying emissions from the port activities. This finding is consistent with research by Pültz et al. (2025), who reported significant contributions from international shipping at German coasts, particularly in Hamburg. In Stuttgart, the observed wind-related pattern may be influenced by the complex arrangement of multiple low-emission zones: the Stuttgart area features one large, continuous low-emission zone connecting with Ludwigsburg to the north and the Leonberg/Hemmingen area to the northwest. where the low emission zones were abolished on 1 January 2024 due to significant air quality improvements (Baden-Württemberg), but valid during the training period (from January 2020 to December 2021). Additionally, Stuttgart maintains two distinct low-emission zones, with air quality monitoring stations primarily located within the northern, more restrictive zone, creating asymmetric pollution patterns depending on wind direction. A simulated NO_2 distribution in Stuttgart by Schwitalla et al. (2021) using the Weather Research and Forecasting model coupled with its chemistry component (WRF-Chem) highlights NO_2 hotspots on the highway in the southern and southeastern parts of Stuttgart, which is consistent with our observed patterns.

At the Munich-AQMS site, the prevailing wind direction is generally west to east. The most polluted location in Germany, Landshuter Allee, is located along a north-south-oriented street with heavy traffic. Higher NO_2 mixing ratios are observed when wind comes from the west, primarily due to the street canyon effect: westerly winds hit the buildings on the eastern side, creating turbulence and recirculation zones that trap and redirect pollutants toward the monitoring station on the western side of the street. In contrast, easterly winds tend to introduce relatively cleaner air from above, thereby reducing NO_2 levels. At the Munich-LPDOAS site, NO_2 levels exhibit a more uniform distribution across wind directions, likely because the measurements are taken at a height of 30 meters, where local surface effects such as traffic emissions and street canyon effect are less pronounced.

Diffuse radiation and daily mean mixing layer height consistently show the weakest but still significant influence on NO_2 in all cities. We used daily averages of MLH to avoid collinearity with diurnally varying factors (e.g., wind speed, temperature, traffic), though this may understate MLH's true impact on NO_2. Overall, the GAM regression model effectively captures these complex relationships, providing a detailed understanding of the factors influencing NO_2 variability in urban environments.

Our findings based on GAM are consistent with previous research emphasizing the importance of meteorological factors in urban air quality modeling. Kerr et al. (2022) employed eXtreme Gradient Boosting (XGBoost) with the NASA GEOS Composition Forecast Modeling System (GEOS-CF) data to show that wind information (u and v wind components) contributed most significantly to model performance when analyzing the impacts of diesel vehicle emissions and meteorological conditions on NO_2. Although their methodology and input variables differ from ours, their results complement our GAM regression findings, reinforcing the critical role of meteorological factors in explaining urban NO_2 variability.

6.3.2.2 Public discussion about NO_2 anomalies during COVID-19 lockdown period

During the first lockdown period in Germany, some cities unexpectedly reported little to no NO_2 decrease, or even slight increases, when comparing levels before and after the lockdown, particularly in Stuttgart. These observations raised discussions about diesel-ban policies (Deutscher Bundestag, 2020; Kunkel, 2020; Viehmann, 2020; Westfälische Nachrichten, 2020). To address these concerns, we analyzed NO_2 levels in these cities, focusing on a potentially anomalous lockdown period t_{post} (5-11 April 2020). This period was selected based on findings by Burns et al. (2021), who demonstrated that NO_2 reductions reached their maximum magnitude during the two weeks immediately following first lockdown implementation. We excluded the days immediately preceding the lockdown to avoid potential confounding effects from panic-driven behavior and selected a representative pre-lockdown week t_{pre} (8-14 March 2020) for comparison. This approach meanwhile ensured that full weekly cycles were included, thereby minimizing the influence of weekly variability while avoiding the confounding effects of meteorological factors.

Using results from GAM regression, we calculated percentage changes ($\frac{t_{post}-t_{pre}}{t_{pre}}$) for all relevant factors by comparing t_{pre} and t_{post}. In Munich, despite an overall -11.0 % change in NO_2 levels, the individual factor contributions revealed complex interactions: traffic volume provided the largest negative influence at -26.97 %, followed by wind direction at -11.62 % and daily diffuse radiation at -2.57 %. However, these reductions were partially overwhelmed by positive meteorological influences, with wind speed contributing the strongest increase at +33.06 %, followed by absolute humidity at +1.97 % and mixing layer height at +1.63 %. In Stuttgart, an overall 6.3 % increase in NO_2 levels occurred despite substantial traffic reduction. The traffic volume decrease provided the dominant negative influence at -25.37 %, which was completely compensated by adverse meteorological conditions. Among these contributors, wind speed had the strongest effect at +18.57 %, followed by wind direction at +10.46 %, mixing layer height at +2.63 %, daily diffuse radiation at +1.39 %, and absolute humidity at +0.34 %.

These discrepancies demonstrate that meteorological conditions can mask traffic-related improvements in air quality, which has been confirmed by numerous studies (Morillas et al., 2024; Urbansky, 2020; Varga et al., 2024; von Schneidemesser et al., 2021; Yu et al., 2025). Therefore, conclusions drawn from NO_2 levels alone can be misleading. Comprehensive, factor-corrected analysis is essential for accurately assessing lockdown impacts on urban air quality.

6.3.2.3 Additional Analysis in Munich: NO_2 variations measure by LP-DOAS and mobile measurements during the COVID-19 lockdown periods

To further connect this analysis with the observation of stationary measurements by LP-DOAS in Munich, we conducted additional analysis on the NO_2 variations during the COVID-19 lockdown periods. This analysis aims to analyze the impact of these lockdowns on NO_2 levels measured by LP-DOAS and mobile measurements. The lockdowns in Germany, which started in March 2020, significantly reduced traffic volume and other activities, which formed a natural experiment ground to study the impact of traffic on NO_2 levels. The first lockdown started on 21 March 2020, and the second one occurred on 15 December 2020. The NO_2 mixing ratios measured by LP-DOAS at background level during these periods were compared with those from the other years to assess the impact of the lockdowns on NO_2 levels, and the mobile measurements were used to validate the findings at the street level.

6.3.2.3.1 Comparison under similar meteorological conditions using the GAM regression result

To isolate the impact of traffic volume, we applied the findings from the GAM regression to identify suitable time periods for comparison with the lockdown period. By quantifying the different influences, we searched for periods in past years with similar meteorological conditions, ensuring that the confounding influence of weather variability was kept as small as possible. While it is impossible to completely remove the influence of meteorological factors, analyzing their effects provides information into how they shape NO_2 variability. This approach ensured that the NO_2 trends were primarily influenced by traffic volume.

The initial week of the first lockdown in Munich (21-27 March 2020), was selected as the reference period ($t_{r,2020}$) due to its significant impact on NO_2 levels. A direct comparison of the lockdown period with the same time of the year (21-27 March) in 2019 ($t_{s,2019}$) might be confounded by other meteorological factors that could offset the effects of reduced traffic. To enable meaningful comparisons, similar periods (t_m) in the past couple of years were identified, ensuring that the start date of each period aligned with the same day of the week to preserve the weekly NO_2 cycle. One t_m was determined for each year based on closely matching meteorological parameters, as shown in Fig. 6.44. The selected periods were 02-08 March 2019

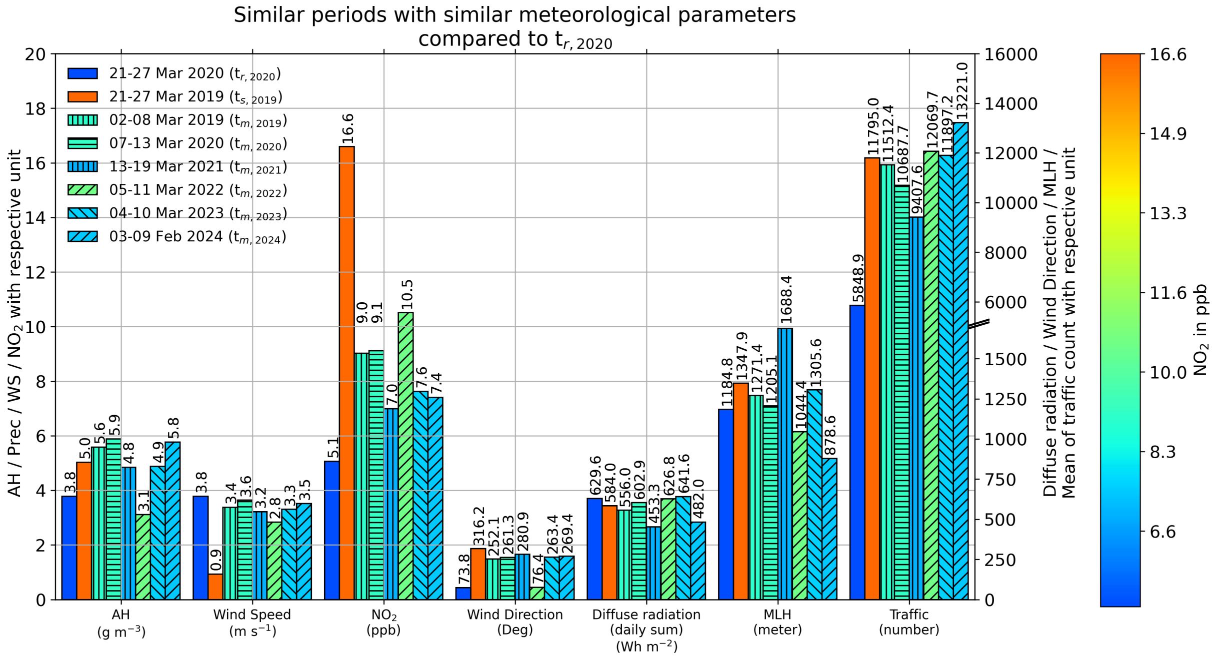

Figure 6.44: Periods t_s and t_m in the past couple of years compared to $t_{r,2020}$. (The bar chart is color-coded to represent the NO_2 mixing ratio during the different periods.)

($t_{m,2019}$), 07-13 March 2020 ($t_{m,2020}$), 13-19 March 2021 ($t_{m,2021}$), 05-11 March 2022 ($t_{m,2022}$), 04-10 March 2023 ($t_{m,2023}$), and 03-09 February 2024 ($t_{m,2024}$).

The data presented in Table 6.2 indicate that the lowest NO_2 mixing ratio (5.00 ppb) was observed during $t_{r,2020}$ with the minimal traffic volume. NO_2 levels in t_m in past years were higher than in $t_{r,2020}$, with increases of 23.41 % in $t_{m,2019}$, 18.75 % in $t_{m,2020}$, 17.03 % in $t_{m,2021}$, 50.09 % in $t_{m,2022}$, 32.82 % in $t_{m,2023}$, and 36.11 % in $t_{m,2024}$. A direct comparison of $t_{r,2020}$ with $t_{s,2019}$ reveals the significant influence of wind speed, which contributed 30.53 % to NO_2 reduction. The GAM regression analysis identified traffic volume as the primary driver of NO_2 variability. Meteorological factors, while influenced NO_2 dispersion, chemical transformation, and transport, thereby affecting observed mixing ratios directly. Among these, wind speed was the most significant factor in shaping NO_2 distribution and variability.

These findings indicate that the observed decline in NO_2 mixing ratios in $t_{r,2020}$ was primarily driven by reduced traffic volume, with meteorological conditions acting as key roles of how NO_2 levels were distributed and transformed in the atmosphere. This underscores the importance of analyzing both traffic volume as emission sources and meteorological influences in air quality assessments.

Table 6.2: Percentage change ($\frac{c_{NO_2,tr}-c_{NO_2,tm}}{c_{NO_2,tm}}$ or $\frac{c_{NO_2,tr}-c_{NO_2,ts}}{c_{NO_2,ts}}$) of NO_2 mixing ratio in Munich-LPDOAS caused by variations in key factors in t_s and t_m compared to the reference date range ($t_{r,2020}$), as determined by Equation (6.1).

	Period	$t_{r,2020}$	$t_{s,2019}$	$t_{m,2019}$	$t_{m,2020}$	$t_{m,2021}$	$t_{m,2022}$	$t_{m,2023}$	$t_{m,2024}$
NO_2 measured by LP-DOAS	ppb	5.00	16.59	9.02	9.02	6.98	10.53	7.69	7.32
NO_2 predicted by GAM	ppb	6.59	12.37	8.60	8.11	7.94	13.20	9.81	10.31
Percentage change of NO_2 mixing ratio (based on GAM)									
AH	%	-	11.38	19.39	20.01	11.02	-4.68	10.39	18.72
WS	%	-	-30.53	-2.94	-4.20	-11.19	-16.78	-10.94	-3.74
WD	%	-	2.14	-2.14	-2.88	5.9	-0.82	-0.97	-0.71
DDR	%	-	2.09	0.34	-0.28	7.28	-3.38	3.27	-4.43
MLH	%	-	-2.18	-3.26	-1.55	-5.38	-0.95	0.05	-3.89
Traffic volume	%	-	-32.91	-30.49	-27.50	-20.04	-32.68	-33.08	-38.03
All factors	%	-	-46.76	-23.41	-18.75	-17.03	-50.09	-32.82	-36.11

6.3.2.3.2 Analysis for the lockdown periods (21 March 2020 and 16 December 2020)

Building upon the identification of meteorological comparable periods using the GAM approach, we now examine how NO_2 levels evolved during the actual lockdown periods isolating the meteorological factors. This section provides a more detailed temporal analysis of the NO_2 variations observed by LP-DOAS and spatial analysis based on mobile measurements during the first and second lockdowns in Munich. By focusing on key episodes and policy interventions, we assess the immediate response of NO_2 to changes in traffic volume under constrained conditions.

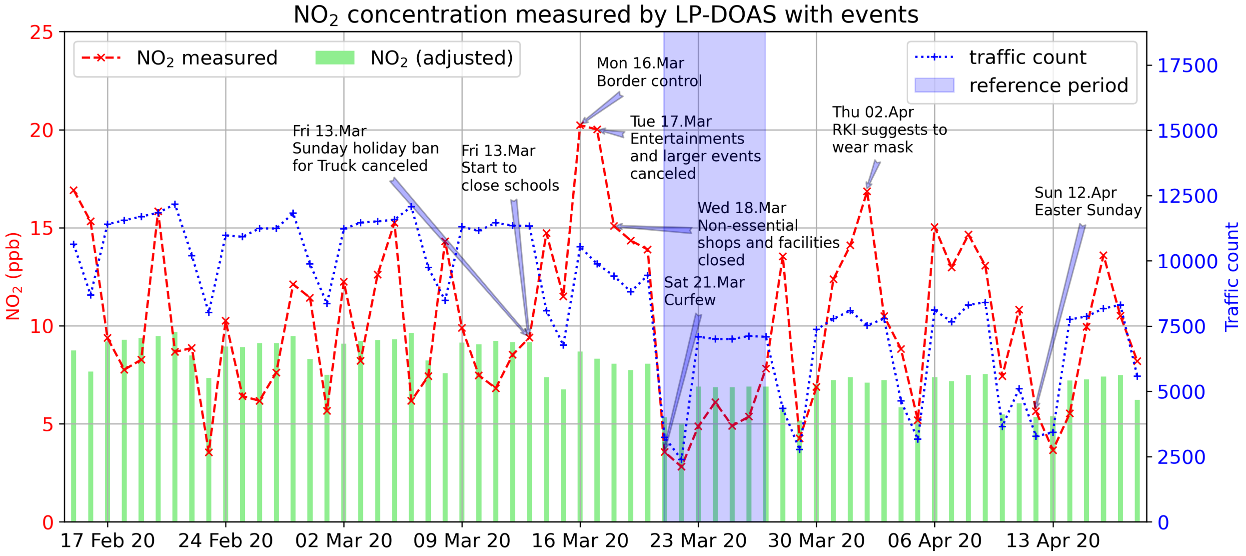

Figure 6.45: Daily NO_2 mixing ratios measured by LP-DOAS from 17 February 2020 to 19 April 2020 with traffic volume data (right axis) and government regulations/episodes. The adjusted NO_2 mixing ratio isolating traffic impact from other factors based on GAM regression is shown as green bars.

Figure 6.45 illustrates key episodes and major government restrictions related to COVID-19 before and after the first lockdown (Bayerisches Staatsministerium des Innern). Following the implementation of a set of restrictions from 13 March 2020, NO_2 mixing ratio increased noticeably one week before the lockdown. The anticipation of lockdown led to stockpiling during the pre-lockdown week, with the highest NO_2 level observed on Tuesday 17 March 2020. This peak occurred one day before the shutdown of the non-essential shops and facilities, driven by increased anthropogenic activities, particularly increased vehicle usage. A significant drop in NO_2 was noted on 21 March 2020, the first day of the lockdown. This reduction was short-lived, and NO_2 levels began to rise again by the end of March. From 28 March 2020, NO_2 levels began to rise, despite the traffic volume remaining low. This increase might be attributed to other anthropogenic activities, such as industrial and residential emissions, these were not considered in this study.

Figure 6.46 displays the daily NO_2 mixing ratio from 01 October 2020 to 28 February 2021

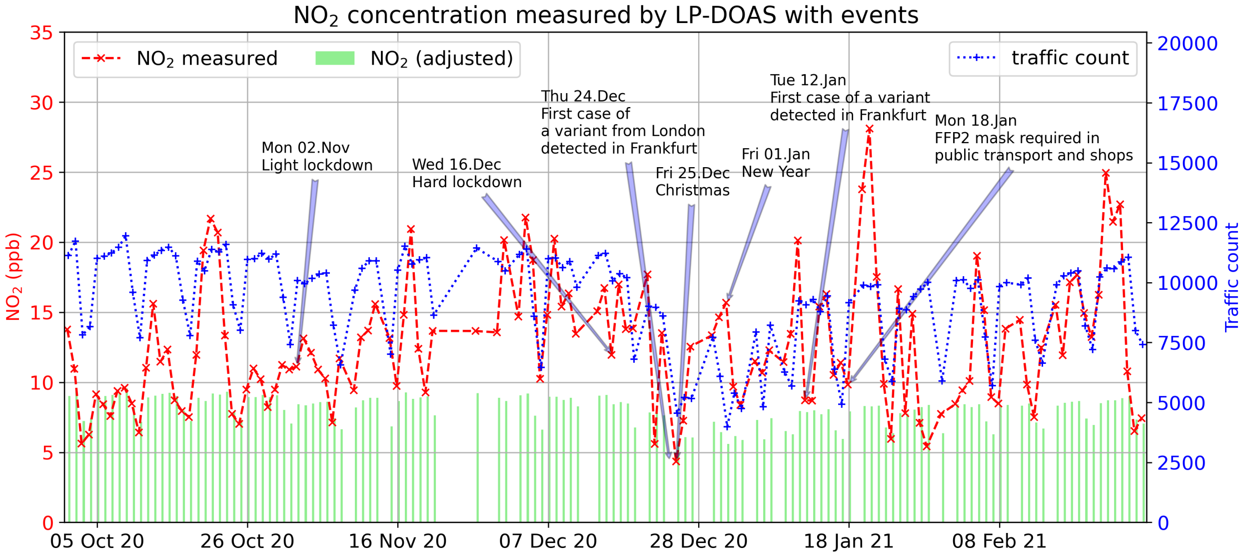

Figure 6.46: Daily NO$_2$ mixing ratios measured by LP-DOAS from 01 October 2020 to 28 February 2021

covering the second lockdown period, highlighting key events during this period. Unlike the first lockdown, the NO$_2$ levels measured by LP-DOAS showed a slight decline in the two consecutive days before and after the second hard lockdown, which began on Wednesday, 16 December 2020. During these two days, meteorological conditions were similar. However, no significant variation was observed immediately after the lockdown as traffic volume did not significantly decrease.

While stationary measurements offer insights into broader atmospheric trends, mobile measurements provide a more localized perspective. Compared to stationary LP-DOAS measurement, roadside and on-road NO$_2$ mixing ratios are more directly influenced by traffic emissions. Figure 6.47a and b represent NO$_2$ maps from two mobile measurement campaigns, which are measured by CE-DOAS (19-25 July 2019), and measured by AIRQUIX (24-29 March 2020). To ensure a fair comparison between these periods, which are significantly affected by seasonal variation, weekly patterns, and diurnal cycles of NO$_2$, we applied a normalization method to the NO$_2$ mixing ratios developed by Zhu et al. (2020) for weekly and diurnal cycles. The seasonal variation was adjusted by applying a weighting factor to Fig. 6.47e based on the long-term NO$_2$ mixing ratios measured by LP-DOAS during these two periods. This adjustment was based on the long term NO$_2$ mixing ratios measured by LP-DOAS. Figure 6.47c clearly shows a significant reduction in NO$_2$ levels, indicating a significant decrease in NO$_2$ emissions across most areas of Munich, which is consistent with the initial decrease seen in stationary measurement.

Similar with the results drawn from the study in Berlin conducted by Schatke et al. (2022), significant reduction in NO$_2$ could not be observed during the second lock down period. Mobile measurements were carried out with AIRQUIX in two consecutive days before and after the second lockdown. Both Fig. 6.47d and Fig. 6.47e show lower NO$_2$ mixing ratios compared to the mobile measurement in 2019. However, there was no significant variation observed before

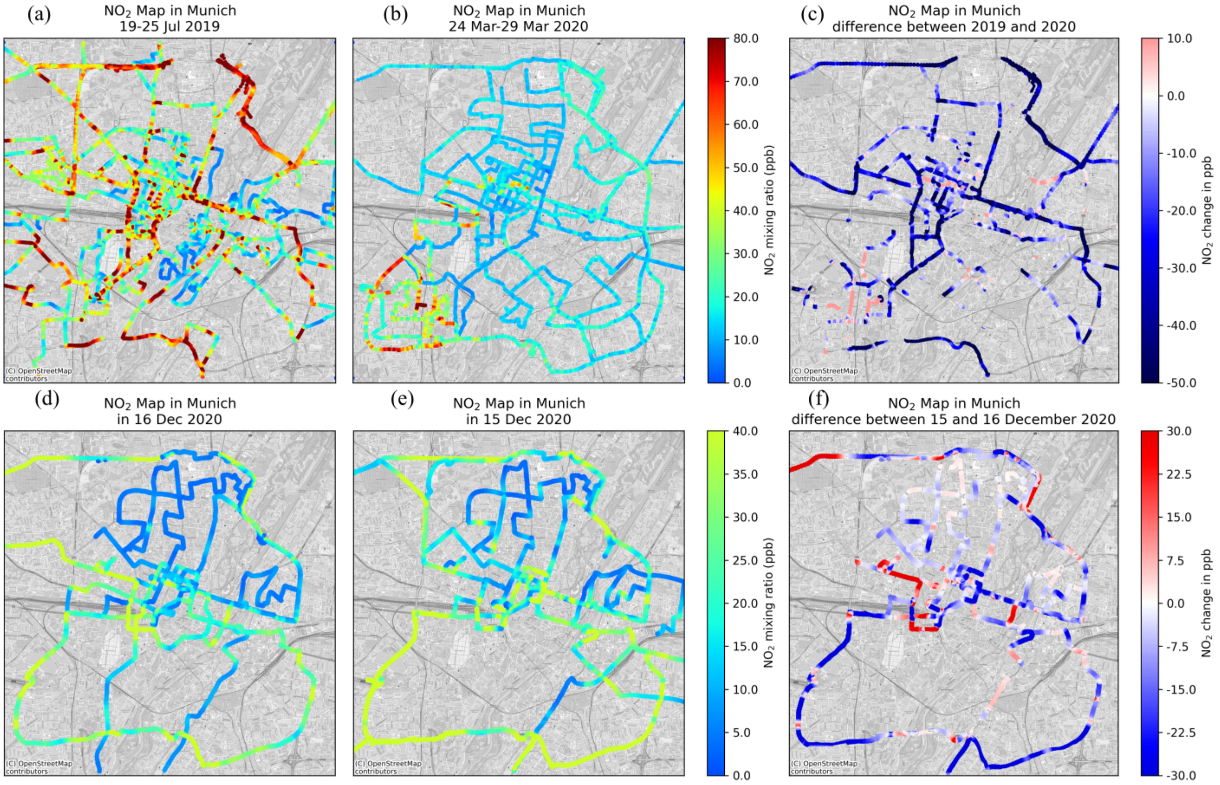

Figure 6.47: NO$_2$ mixing ratios from mobile measurements (adjusted for seasonal variation, weekly and diurnal cycles using the long-term LP-DOAS measurements) in Munich. The colorbar scale highlights the magnitude of NO$_2$ or NO$_2$ differences, while consistent color schemes are maintained across panels: shared between (a), (b), (d), (e), and separately between (c) and (f). (a) NO$_2$ map measured by CE-DOAS (19-25 July 2019). (b) NO$_2$ measured by AIRQUIX from 24 March 2020 to 29 March 2020. (c) NO$_2$ difference map $(b)-(a)$ where overlap exists. (d) NO$_2$ map measured by AIRQUIX on 15 December 2020. (e) NO$_2$ map measured by AIRQUIX on 16 December 2020. (f) NO$_2$ difference map $(e)-(d)$ where overlap exists. (Map data copyrighted OpenStreetMap contributors)

and after the second hard lockdown, as indicated by Fig. 6.47f. This lack of change mirrors the findings from both stationary and mobile observations, suggesting that the second lockdown restrictions were insufficient to significantly impact NO_2 emissions. Burns et al. (2021) pointed out the effect became more pronounced as additional measures were implemented. These are consistent with our findings, which show that the NO_2 levels were significantly reduced during the first lockdown period.

6.4 Case IV: Personal Exposure to AiR poLlution (PEARL)

Building on the mobile monitoring approaches, personal exposure devices track the pollutant levels individuals actually encounter throughout their daily activities. Personal exposure monitoring represents a critical advancement in understanding individual-level air pollution impacts and developing targeted health protection strategies. Unlike stationary monitoring networks that measure ambient pollutant levels, personal exposure devices capture the actual pollutant levels that individuals encounter during their daily activities, including variations due to location, behavior, and microenvironmental conditions. This approach is particularly important for vulnerable populations such as children, elderly individuals, and those with pre-existing health conditions, who may experience disproportionate exposure risks.

The development of wearable exposure monitoring devices requires careful consideration of several key factors: sensor miniaturization while maintaining accuracy, power efficiency for extended operation, user comfort and acceptance, and robust data logging and communication capabilities. These devices must be capable of operating reliably across diverse environments, from indoor settings to busy urban streets, while withstanding the physical demands of daily wear. Additionally, the data collected must be of sufficient quality to support epidemiological studies, detailed time–activity analyses, and comprehensive risk assessments.

Within the PEARL framework, AIRQUIX and AIRQUIXMini form the core hardware platforms for personal exposure monitoring. They integrate electrochemical sensors for reactive gases (e.g. NO_2, NO, O_3), optical particle counters for PM, and environmental sensors (T/RH/p), complemented by GPS and onboard storage or wireless transmission. These units can be configured as fully portable boxes (e.g. APPLE lifestyle campaign) or embedded into specialized wearables (e.g. the VADER mask), enabling both generic and highly application-specific exposure assessments.

Personal exposure studies using such devices provide insights into exposure patterns that cannot be captured through ambient monitoring alone. They reveal how individual behaviors, commuting choices, occupational activities, and residential characteristics influence actual exposure levels. The resulting datasets help identify high-exposure scenarios, evaluate the effectiveness of exposure reduction strategies (e.g. masks, filters, route choices), and inform public health recommendations. Furthermore, personal monitoring enables the development and validation of more accurate exposure models for health risk assessments, potentially leading to more effective air quality standards and protection measures.

This section details both the core device development process and the exposure assessment applications (VADER and APPLE), illustrating how technological innovation in sensor miniaturization and integration can enable new approaches to personal environmental health monitoring.

6.4.1 Project VADER: Development of a fan-assisted, acoustically optimized (+10 dB(A)) respiratory protection mask with a calibration box that filters inhaled air (H13) and accurately measures pollutant mixing ratios below 5 ppm to warn in the event of a threshold exceedance

The VADER project represents a specialized adaptation of the AIRQUIX framework, miniaturizing the sensor technology for integration into a smart respiratory protection mask. The VADER mask is designed in collaboration with LMD GmbH as a specialized wearable device which can meanwhile detect the pollutant levels. The device features a fan-assisted filtration system designed to remove aerosols. It incorporates a multi-chamber sensor array (NO_2, aerosols, T, RH, p) to monitor ambient air quality and verify filter performance. Breathing assistance is provided by a micro-fan. By leveraging the calibration strategies developed for standalone AIRQUIX units, this wearable node provides real-time warnings for pollutant threshold exceedances, demonstrating the potential for high-accuracy personal exposure monitoring and protection.

6.4.1.1 Methodology

6.4.1.1.1 Sensor and Software Adaptation

The software infrastructure is directly adapted from the AIRQUIX platform described in Chapter 5. Due to the strict size and weight constraints of a wearable mask, the compact AIRQUIXMini configuration is utilized. This includes the MICS-6814 for NO_2 pollutants and the PMSA003 for particulate matter, selected for their small footprint.

6.4.1.1.2 MO_x Sensor Evaluation

To evaluate the sensor data, a conversion formula is needed to convert the sensor outputs from all available sensors into the desired mixing ratios. In our case, the desired mixing ratios are aerosol particles and nitrogen dioxide, as both pollutants can have adverse health effects. Because this conversion formula also depends on temperature, pressure, and humidity signals, cross-sensitivities must be examined. At the same time, the formula or model must not be too complex or computationally intensive, as it needs to be implemented on an onboard single board computer.

The chosen sensor for measuring NO_2, the MICS-6814, has three output voltages. According to the sensor manufacturer, the first output voltage is for converting into nitrogen dioxide (NO_2) mixing ratios, the second for ammonia (NH3), and the third for carbon monoxide (CO). Additionally, the output voltages from temperature, pressure, and humidity sensors are available. After examining the cross-sensitivities of all these input data on NO_2 mixing ratio, various formulas and models could be tested to maximize sensor accuracy. The method developed was applied for nitrogen dioxide measurements because a high-quality CE-DOAS NO_2 instrument was available for testing.

GLM was used to examine cross-sensitivities. Six input parameters were used: the three sensor output voltages, temperature (T), pressure (p), and relative humidity (RH). It was evident that there was a linear relationship between NO_2 mixing ratio and the NO_2 sensor's output voltage, as expected, albeit with a negative slope. Interestingly, a similarly strong relationship was observed with the second output voltage, which, according to the manufacturer, should primarily respond to NH3. This correlation should be taken into account in the calibration. The sensitivity of the third output voltage to NO_2 mixing ratio was low, as was the sensitivity to air pressure. However, temperature and relative humidity had a significant impact on the results, indicating that these cross-sensitivities must also be considered in the analysis.

6.4.1.2 Results and Discussion

6.4.1.2.1 Calibration of MO_x sensor

A mini version of the Air Quality Inspection boX (AIRQUIXMini) was made with MICS-6814 (a MO_x sensor from SGX Sensortech) and PMSA003 (an optical particle counter from Plantower Technology) and was created and placed at the calibration station (Fig. 4.1) for 102 days. It was calibrated using a Generalized Linear Model (GLM). Calibration was performed at a 5-second sampling rate with 30 days of data, and then applied to the remaining days. The results are presented at a 5-second sampling rate (Fig. 6.48) and resampled to a 60-minute rate for improved visualization (Fig. 6.49). The model shows good accuracy in predicting NO_2 mixing ratios for ambient air quality monitoring at the 60-minute sampling rate. However, it was unable to accurately capture the rapidly fluctuating NO_2 mixing ratios characteristic of on-road environments. The RMSE is, as expected, rising over time (Fig. 6.50). The model performs well within one year, but it is obvious that recalibration is still necessary depending on the application.

Since the MO_x sensor is not the key focus in this thesis, the three parallel devices test was not performed for the calculation of MNB and CV (Chapter 4). The model is not able to capture the rapid fluctuations of NO_2 mixing ratios in on-road environments, but it performs well for ambient air quality monitoring at a lower sampling rate. The model's performance is limited by the sensor's response time and the inherent noise in the data, which can lead to inaccuracies in rapidly changing environments.

Based on these findings, the MO_x sensor appears to be more appropriate for ambient or lower temporal resolution monitoring (on the order of minutes) rather than for on-road applications that require high temporal resolution for frequently changing environments.

6.4.1.2.2 Air Pollution Personal Lifestyle Exposure (APPLE) study

We conducted a study utilizing portable units in real-life settings to show how personal monitoring reveals hidden exposure patterns and informs health risk assessments (Ye et al., 2023). The unit was calibrated against the CE-DOAS before and after the campaign, and was carried by participants during daily activities, including indoor/outdoor environments, different commuting methods, shopping, and cooking. The data collected were analyzed to identify exposure patterns and assess health risks associated with NO_2 exposure. The study aimed to provide insights into individual exposure levels and inform strategies for reducing exposure.

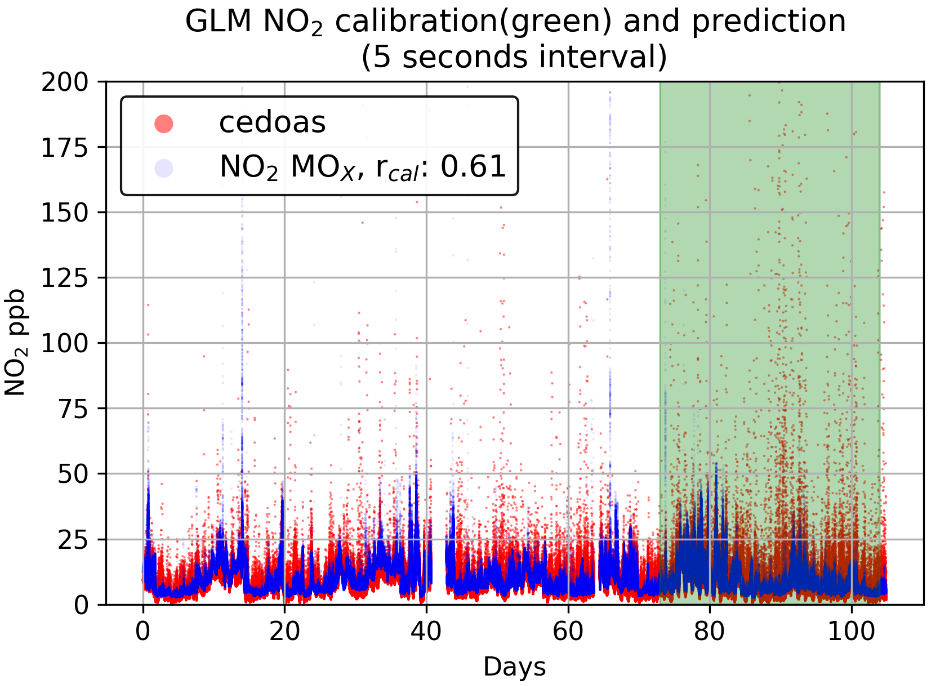

Figure 6.48: Time series comparison of NO_2 mixing ratios derived from the MO_x sensor using a GLM calibration (blue) versus the reference instrument (orange) at a 5-second temporal resolution.

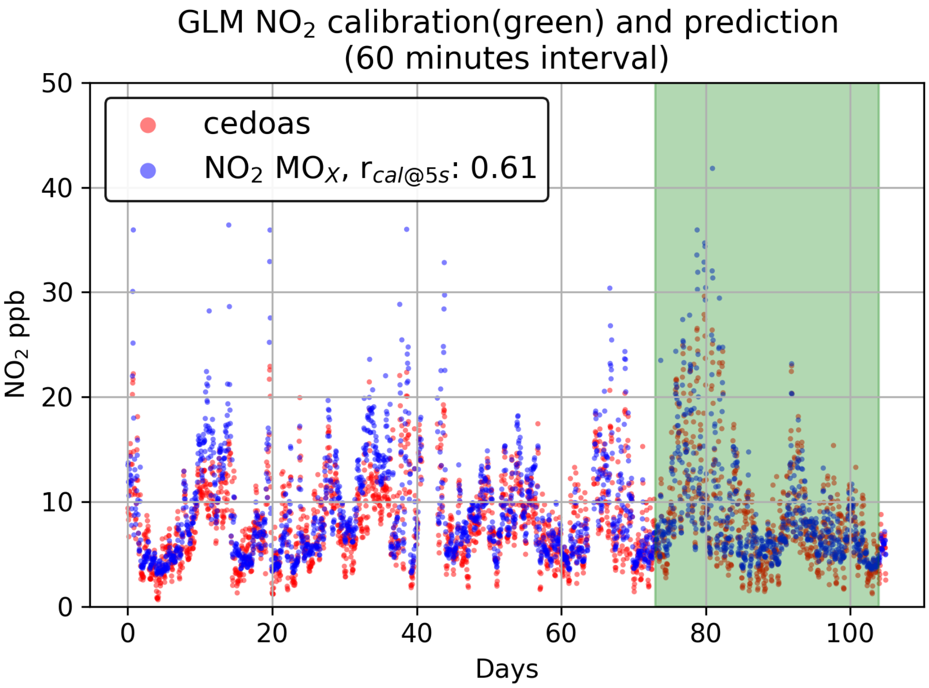

Figure 6.49: Time series comparison of NO$_2$ mixing ratios resampled to a 60-minute resolution. The resampling smooths out rapid fluctuations that the MO$_x$ sensor fails to capture, resulting in improved agreement between the sensor model (blue) and reference data (orange).

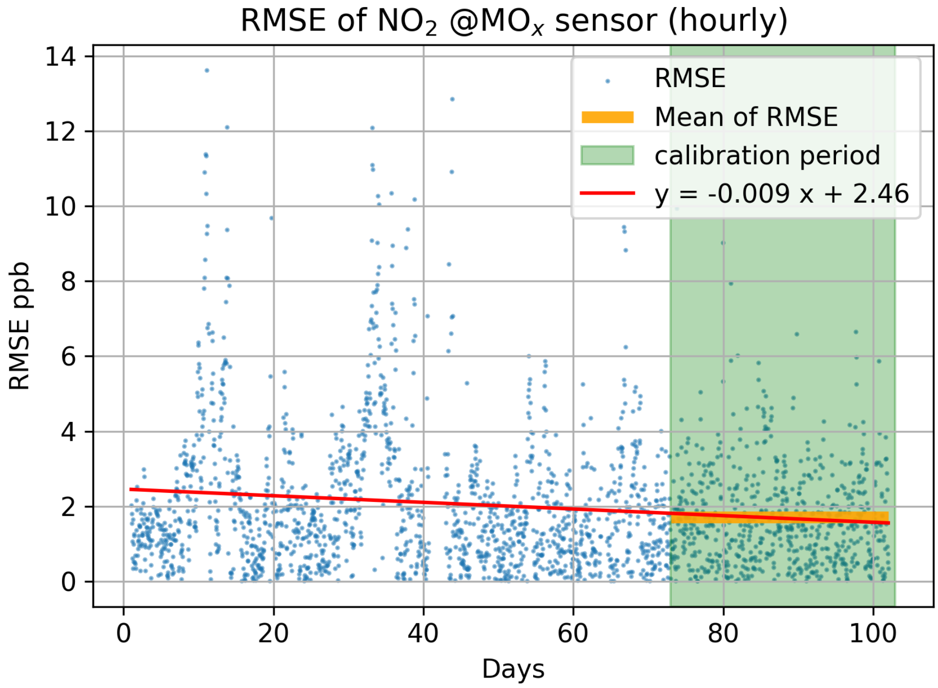

Figure 6.50: RMSE of the model

Figure 6.51 presents the NO_2 exposure patterns across different environments. The most pronounced fluctuations in NO_2 levels were observed in the underground walkway environment, primarily attributed to the ventilation dynamics between underground and surface air masses. NO_2 infiltration from surface sources accumulates in underground spaces, creating variable mixing ratio patterns influenced by ventilation rates and air exchange mechanisms.

In enclosed transportation environments such as subways, buses, and trams, NO_2 levels remained relatively stable due to controlled cabin environments. However, notable changes occurred during station stops when doors opened, allowing ambient air infiltration into the cabin space. Indoor environments exhibited distinct NO_2 exposure patterns depending on their characteristics and connected systems. Office environments showed considerable fluctuations, likely associated with ventilation systems connected to parking areas where vehicle emissions could infiltrate the indoor air supply. In contrast, residential environments maintained relatively stable NO_2 levels, with notable exceptions during specific activities such as cooking and moxibustion treatments, which generated localized emission sources. PM2.5 exposure patterns are illustrated in Fig. 6.52. Elevated PM2.5 concentrations were consistently observed in subway systems and stations, attributed to particle generation from train operations, including braking, wheel-rail friction, and re-suspension of accumulated dust particles. Cooking activities demonstrated substantial PM2.5 elevation, particularly during high-temperature food preparation such as pan-frying steak, where combustion processes and oil heating generate significant particulate emissions. Similarly, moxibustion treatments contributed measurably to PM2.5 levels through

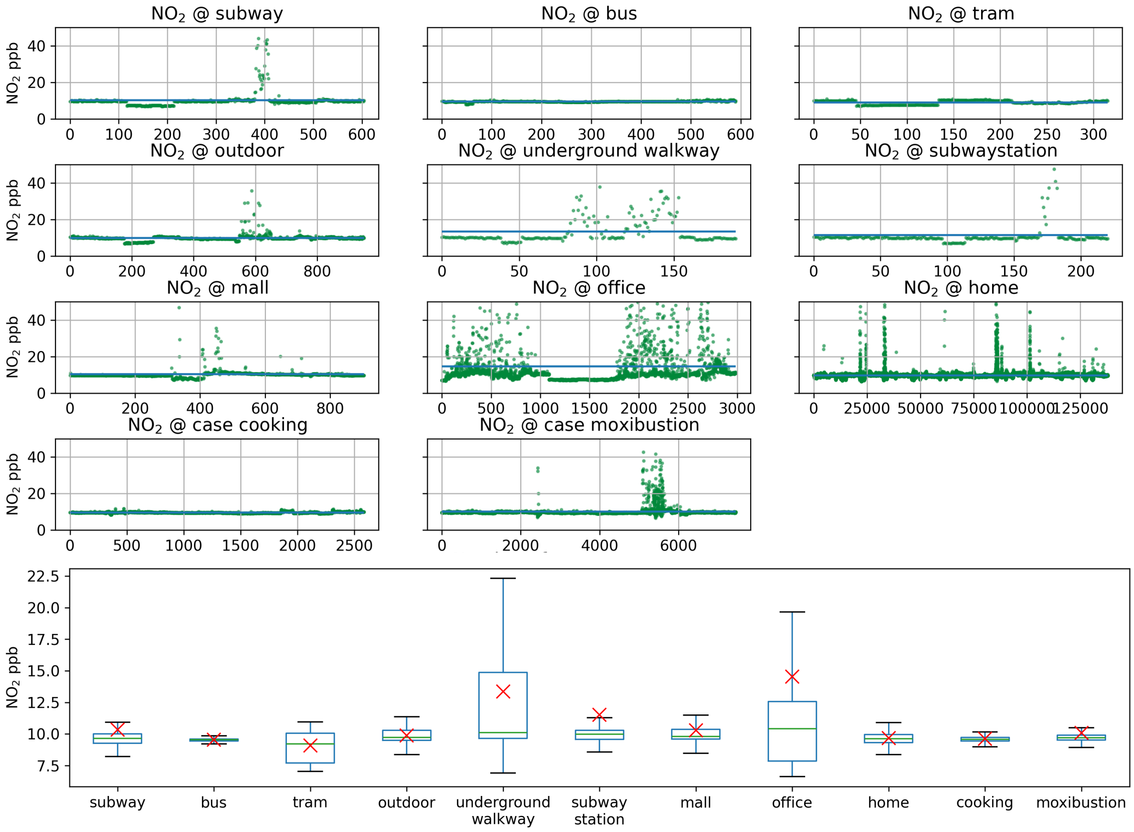

Figure 6.51: Personal exposure plots for NO_2 levels in different environments during the study period.

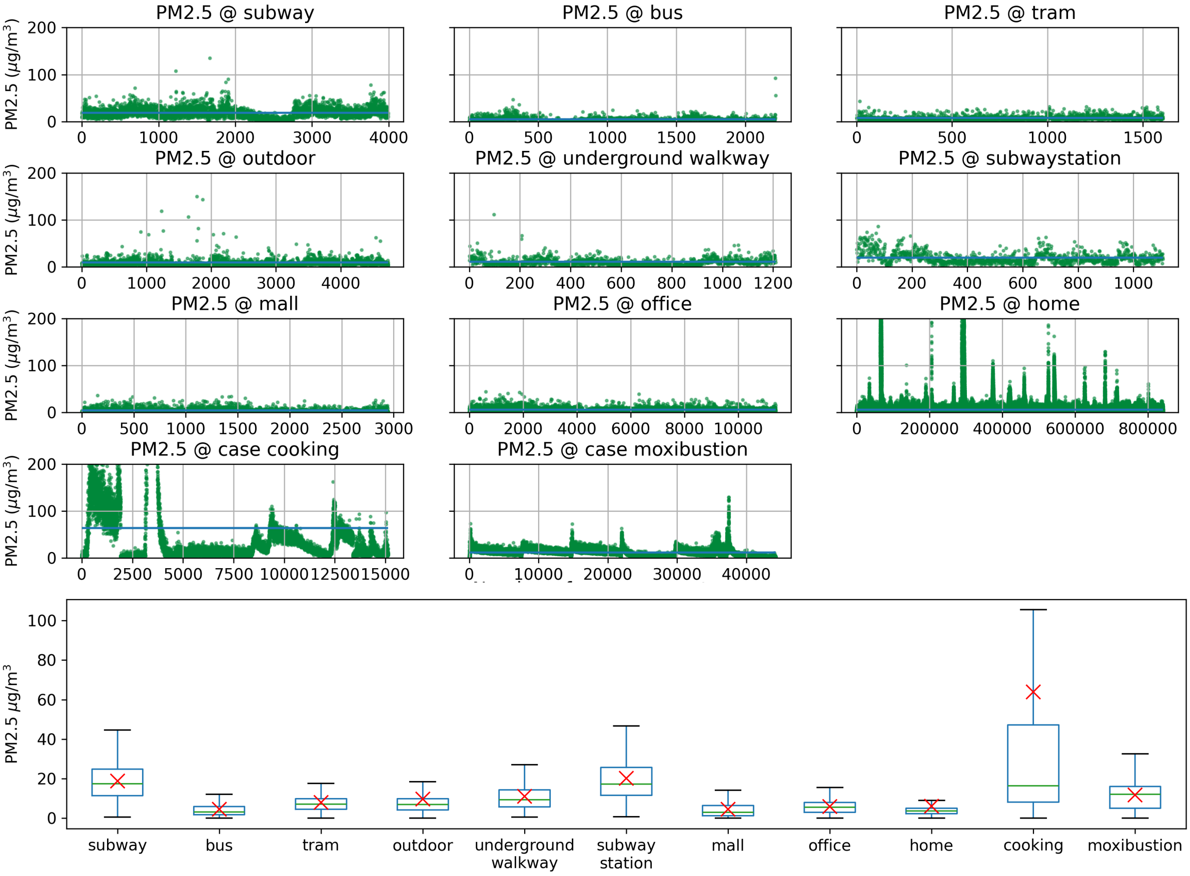

Figure 6.52: Personal exposure plots for PM2.5 levels in different environments during the study period.

controlled combustion of moxa sticks, demonstrating how traditional practices can influence personal exposure levels.

Other monitored environments maintained relatively stable PM2.5 concentrations, with occasional fluctuations corresponding to specific activities such as cleaning operations or window opening events that altered indoor-outdoor air exchange rates.

6.5 Case V: WOod-burning stOve impact on Domestic air qualitY (WOODY)

The previous sections focused on mobile and portable applications. The WOODY case study demonstrates the use of AIRQUIX in stationary settings to assess the impact of wood burning stoves on indoor and outdoor air quality.

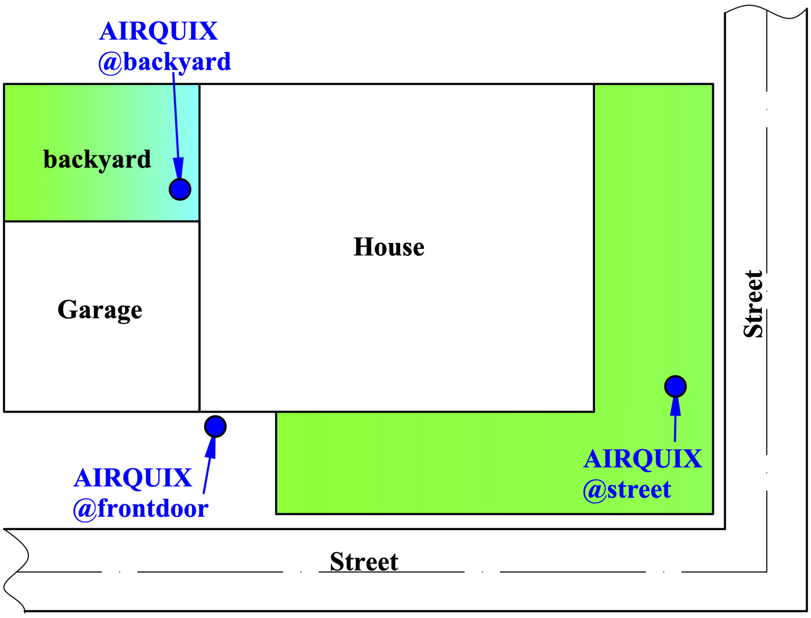

Figure 6.53: AIRQUIXs deployed in/out a house with wood burning stove.

Since 2022, wood burning stoves have gained popularity as an energy conservation measure in response to the European energy crisis. However, the combustion process releases harmful pollutants into the air, which can have serious health consequences, particularly for indoor air quality.

6.5.1 Methodology

To investigate the impact of wood burning stoves on local air quality and assess associated health risks (Simon Plentinger et al., 2022), this pilot study employed a spatial gradient monitoring approach. Three AIRQUIX units were strategically deployed in and around a residential property equipped with an active wood burning stove (Fig. 6.53). The study focused primarily on particulate matter (PM), the primary pollutant of concern from wood combustion, while also monitoring NO_2 levels to distinguish between sources. The sensor placement was designed to capture different pollution dynamics: one unit was positioned at street level to monitor traffic-related background emissions, a second at the front door to measure concentrations near the building envelope, and a third in the backyard to assess dispersion and accumulation within the residential microenvironment.

The measurement campaign was conducted over a five-day period from 4 November 2022 to 8 November 2022. To isolate the impact of the wood stove, specific operational windows were defined where the stove was active between 15:00 and 20:00 on selected days (Friday through Sunday), allowing for a comparative analysis between burning and non-burning periods.

6.5.2 Results and Discussion

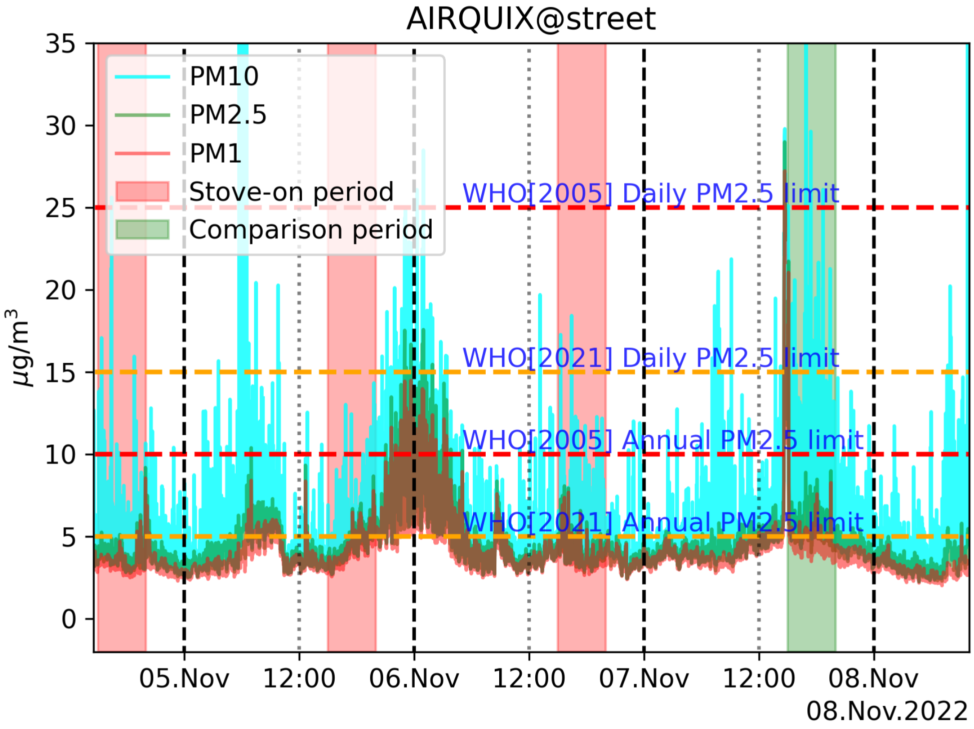

Figure 6.54: PM levels measured by OPC at the street.

The PM levels measured by the OPC at the street (Fig. 6.54) were generally higher than the PM levels at the other locations. However, the street sensor could not effectively capture the PM levels from the wood burning stove during the shaded operational periods. The intensive PM levels at midnight on 6 November 2022 might be attributed to the broader community using wood burning stoves for heating during the cold night.

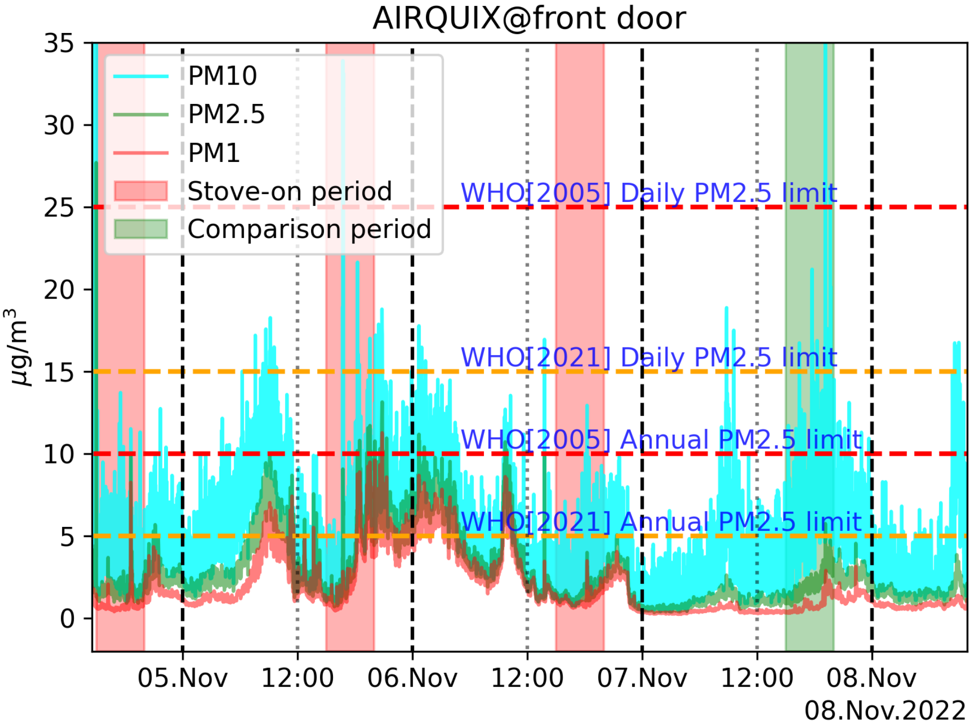

Figure 6.55: PM levels measured by OPC at the front door.

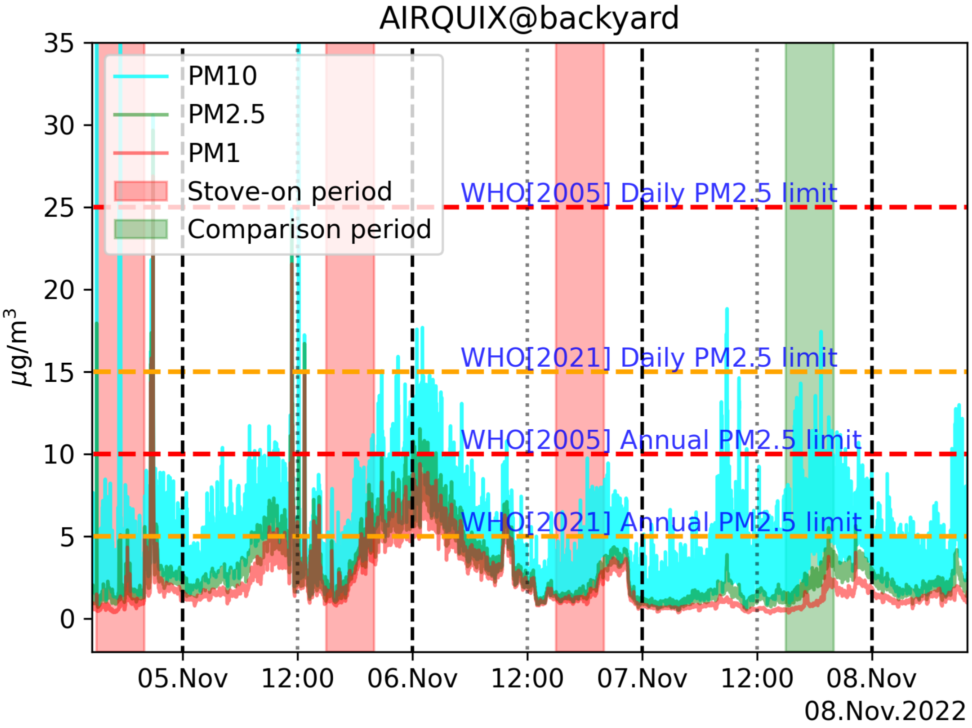

Figure 6.56: PM levels measured by OPC at the backyard.

The PM levels at the front door (Fig. 6.55) and backyard (Fig. 6.56) were both elevated during the period when the wood burning stove was in use. The PM levels continued to rise even after the stove was extinguished, which can be attributed to several factors. First, the residual heat in the stove and chimney likely continued to generate emissions as the system gradually cooled. Second, the cooling process within the stove may have triggered incomplete combustion of remaining fuel, temporarily increasing particulate emissions. Third, the limited air exchange rate in residential buildings allowed the accumulated particles to persist and even increase in concentration before eventual dispersion. Additionally, previously deposited particles on indoor surfaces may have been re-suspended into the air due to household activities. These observations highlight the complex dynamics of indoor air pollution from wood combustion, where exposure risks extend beyond the active burning period.

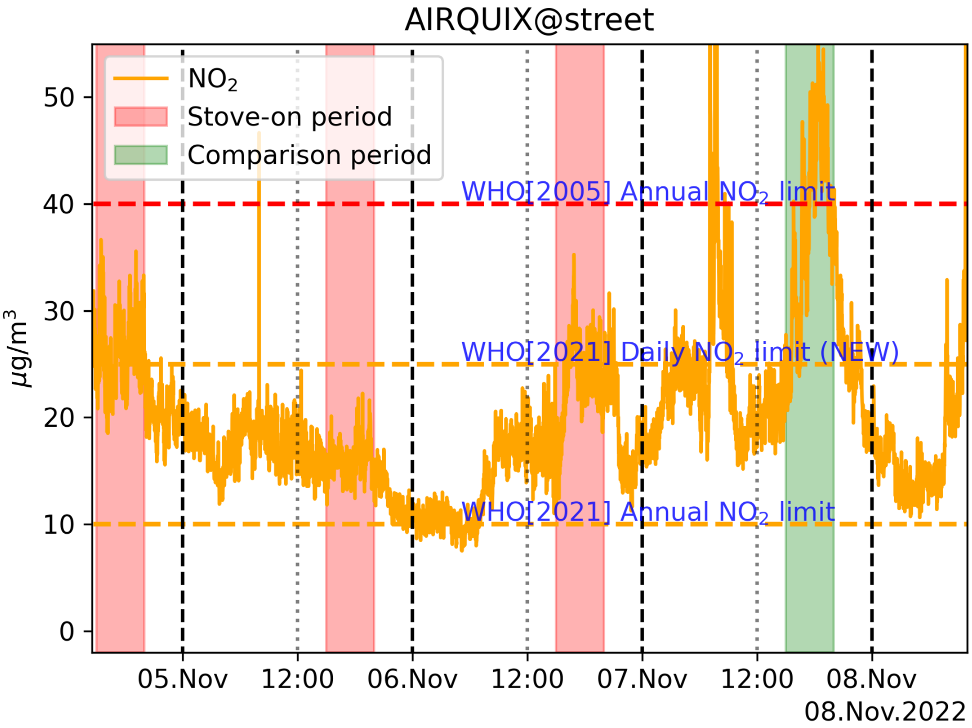

Figure 6.57: NO_2 levels measured by AIRQUIX at the street.

The NO_2 mixing ratios measured by AIRQUIX at the street (Fig. 6.57), front door (Fig. 6.58), and backyard (Fig. 6.59) exhibited distinct temporal patterns driven by different source contributions. The street-level sensor consistently recorded the highest NO_2 values, with peaks correlating to traffic rush hours, confirming vehicular emissions as the dominant local source for nitrogen oxides. In contrast, measurements at the front door and backyard remained generally lower and did not show a clear correlation with the wood stove operation periods. While minor fluctuations were observed at the residential locations, they lacked the sharp, sustained increases seen in the PM data during burning events. This divergence between PM and NO_2 trends aligns with combustion physics; residential wood burning is a primary source of particulate matter but

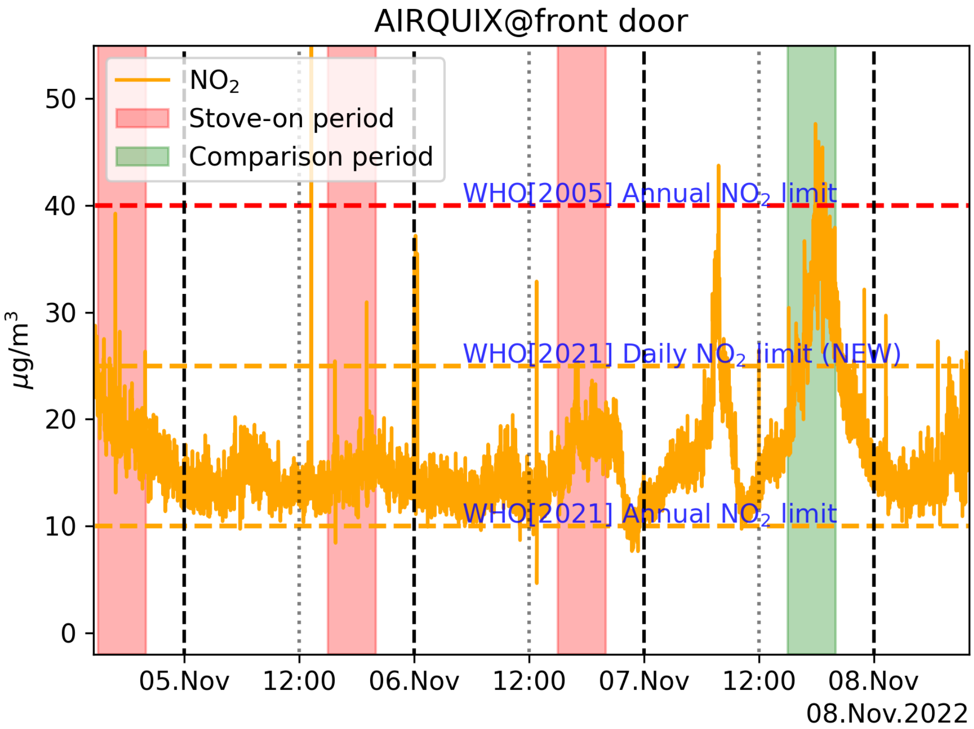

Figure 6.58: NO$_2$ levels measured by AIRQUIX at the front door.

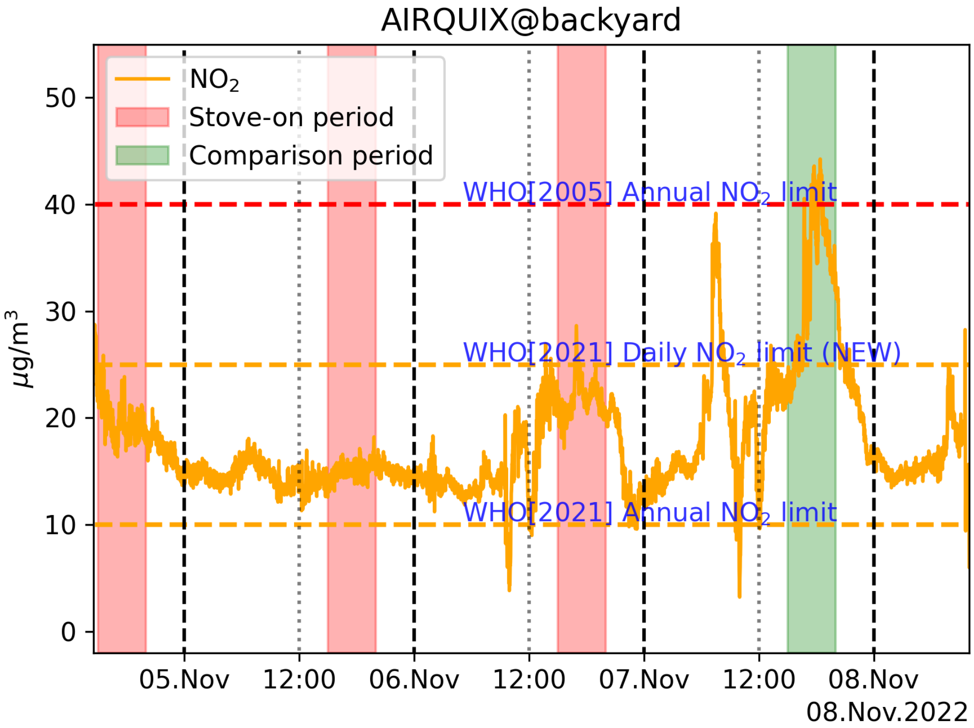

Figure 6.59: NO$_2$ levels measured by AIRQUIX at the backyard.

emits comparatively lower levels of NO_x relative to the high-temperature combustion found in internal combustion engines. Consequently, while the stove significantly degraded local air quality regarding particulates, its contribution to the local NO2 budget was lower compared to the traffic background.

6.6 Case VI: Carbon-based Localized Evaluation of Air purification Near ROADsides (CLEANROAD)

Another stationary application it CLEANROAD which involves evaluating infrastructure interventions. This study evaluates the effectiveness of a roadside air filtering system based on activated carbon technology, developed in collaboration with an industrial partner, for reducing nitrogen dioxide (NO_2) concentrations in urban environments. Driven by increasing concerns over urban air quality and the adverse health effects of vehicular NO_2 emissions, the primary objectives were to assess the system's performance in removing NO_2 along a 30-meter section of roadway and to investigate its potential contribution to urban air quality management strategies. The evaluation was conducted at Tegernseer Landstraße in Munich, Germany, providing insights for broader applications of air filtering technologies in urban settings.

In this study, we use concentration (μg·m^{-3}) as the unit for NO_2 levels instead of mixing ratio (ppb), following common practice in air quality monitoring, as concentration values are more directly relevant to health effects and regulatory standards. The conversion between concentration and mixing ratio can be performed using the ideal gas law using the measured ambient temperature and pressure.

$$c_{mass,NO_2} = \frac{c_{vol,NO_2} \times M \times P}{R \times (273.15 + T)} \times 0.1 \tag{6.5}$$

where:

- c_{mass,NO_2} is the concentration in μg·m^{-3},
- c_{vol,NO_2} is the mixing ratio in ppb,
- M is the molar mass of NO_2 (46.0055 g·mol^{-1}),
- P is the ambient pressure in hPa,
- T is the ambient temperature in °C,
- R is the ideal gas constant (8.314 J·K^{-1}·mol^{-1}).

6.6.1 Evaluation Methodology

The air filtering system and the evaluation system were installed at Tegernseer Landstraße (see Fig. 6.60). The system features air inlet ducts running along a 30-meter stretch of the street to

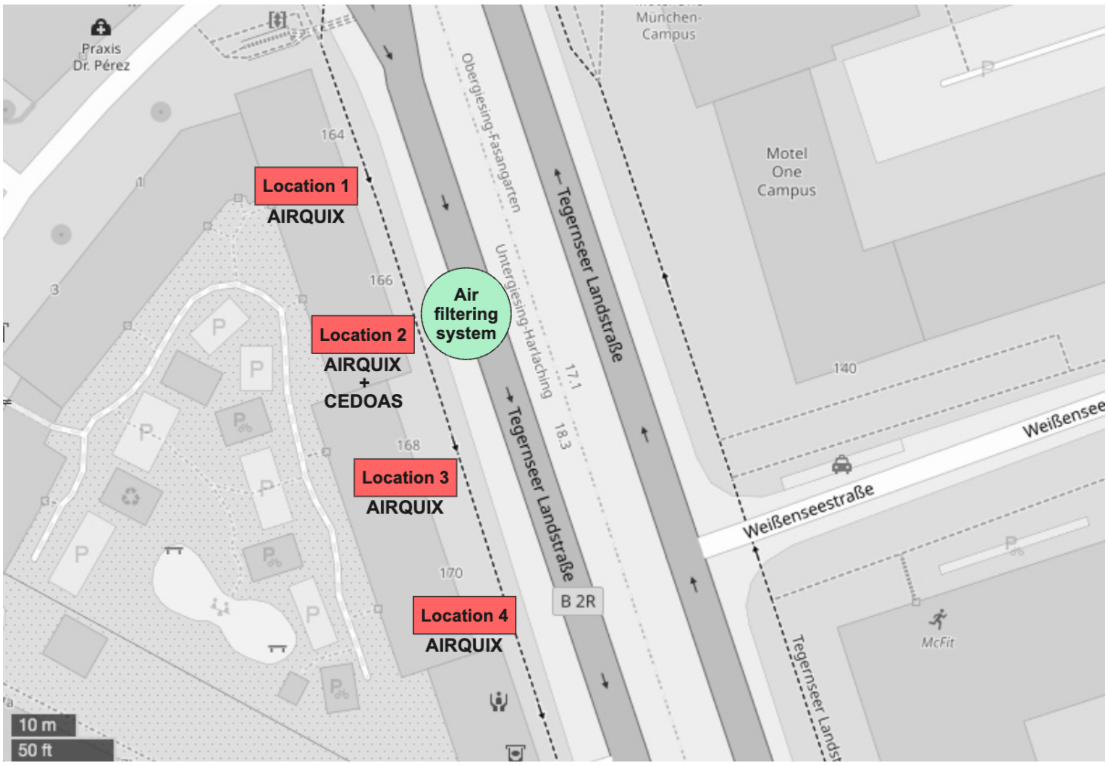

Figure 6.60: Location of the roadside air filtering system. Map data © OpenStreetMap.

separate the urban road from adjacent bicycle and pedestrian paths—serving as an alternative to traditional green belts. The outlets, positioned at a height of 5 meters in the center, are equipped with activated carbon designed to capture NO_2 emitted by passing vehicles.

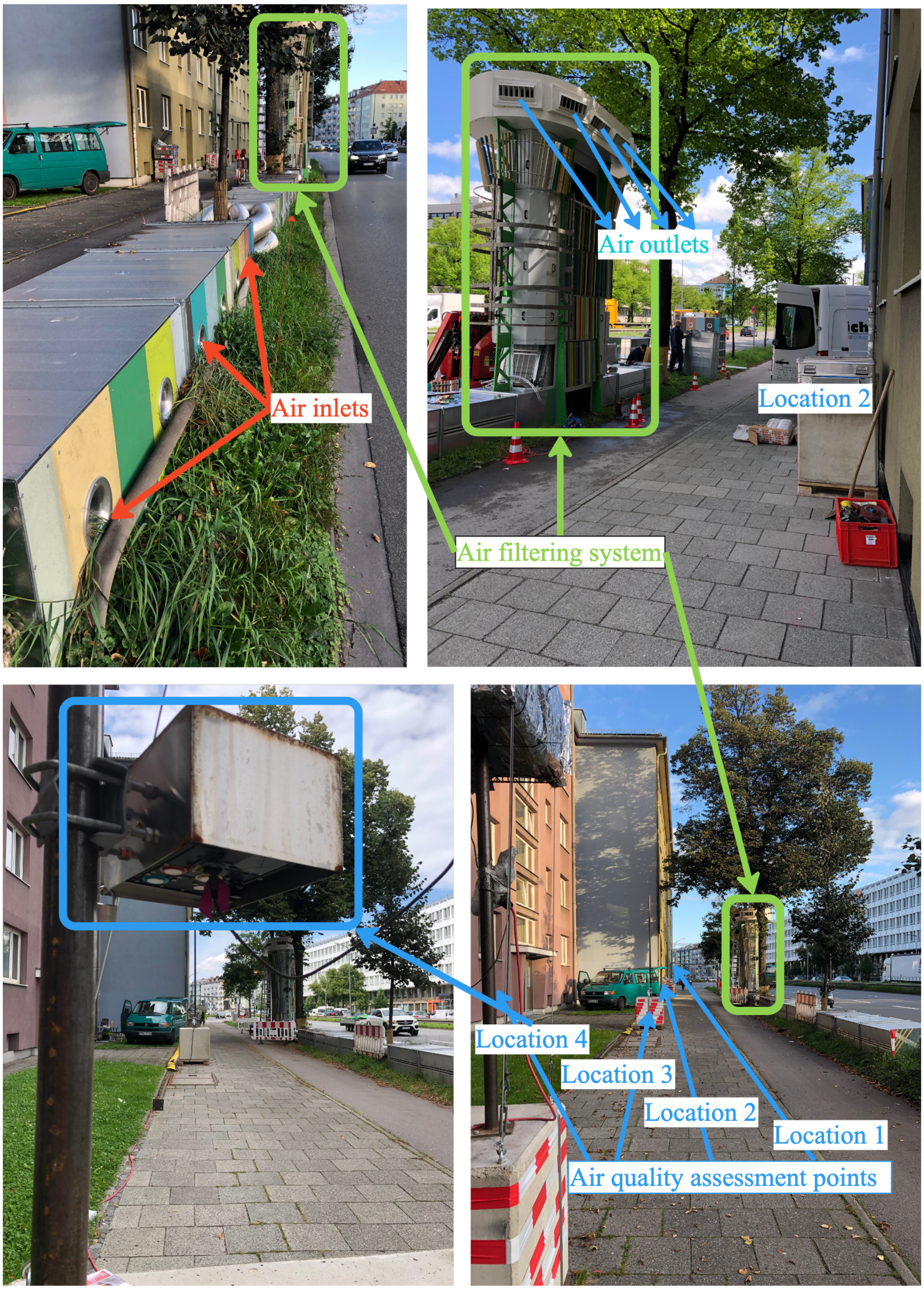

Figure 6.61: Roadside air filtering system installed at Tegernseer Landstraße.

The evaluation system utilizes low-cost sensors to measure NO_2 concentrations at approximately 1.5 meters above street level. It comprises four air quality assessment points, including a calibration box (location 2) positioned directly below the filtering system outlet (refer to Fig. 4.1). Three AIRQUIXs are deployed at intervals of 10 meters along the street to monitor NO_2 levels, and additional AIRQUIXs are cycled through the calibration box weekly to ensure measurement accuracy (see Fig. 6.61).

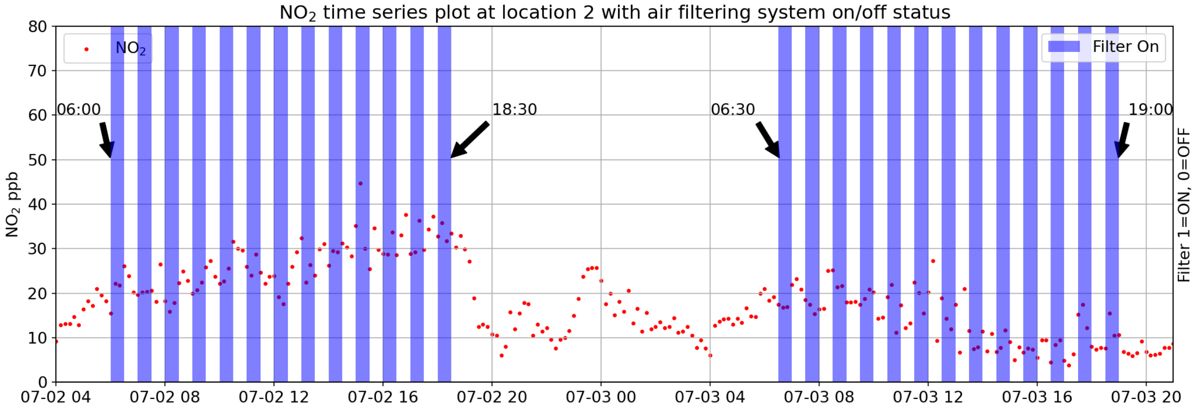

Figure 6.62: Instruction for turning on and off the air filtering system.

To assess the performance of the air filtering system, the device was programmed to alternate between the "on" and "off" states every 30 minutes. To avoid systematic timing effects, the system's starting time was shifted by 30 minutes on different days (Fig. 6.62). Data collected during the alternating periods were then analyzed to determine the filtering efficiency.

6.6.2 Results and Discussion

Direct measurements at the filtering system outlet demonstrated substantial NO_2 removal efficiency. An AIRQUIX recorded average concentrations of 47.9 $\mu g \cdot m^{-3}$ when the system was deactivated compared to 20.5 $\mu g \cdot m^{-3}$ during operation, representing a 57.1 % reduction (Fig. 6.63). This result confirms the activated carbon system's high capture efficiency at the point of emission control.

Table 6.3: All Air Quality Measurement Data.

Location	$\frac{c_{NO_2,\text{Filter On}} - c_{NO_2,\text{Filter Off}}}{c_{NO_2,\text{Filter On}}}$	$c_{NO_2,FilterOn}$-$c_{NO_2,FilterOff}$	$c_{NO_2,FilterOn}$	$c_{NO_2,FilterOff}$	Days
Location1	-1.05	-0.28	26.87	27.16	33
Location2	-5.18	-2.01	38.77	40.78	36
Location3	-5.01	-1.62	32.35	33.97	14
Location4	-1.26	-0.48	38.19	38.67	33

However, the filtering effectiveness diminished considerably at street level, showing a clear distance-dependent relationship. The spatial analysis revealed that the greatest reductions oc-

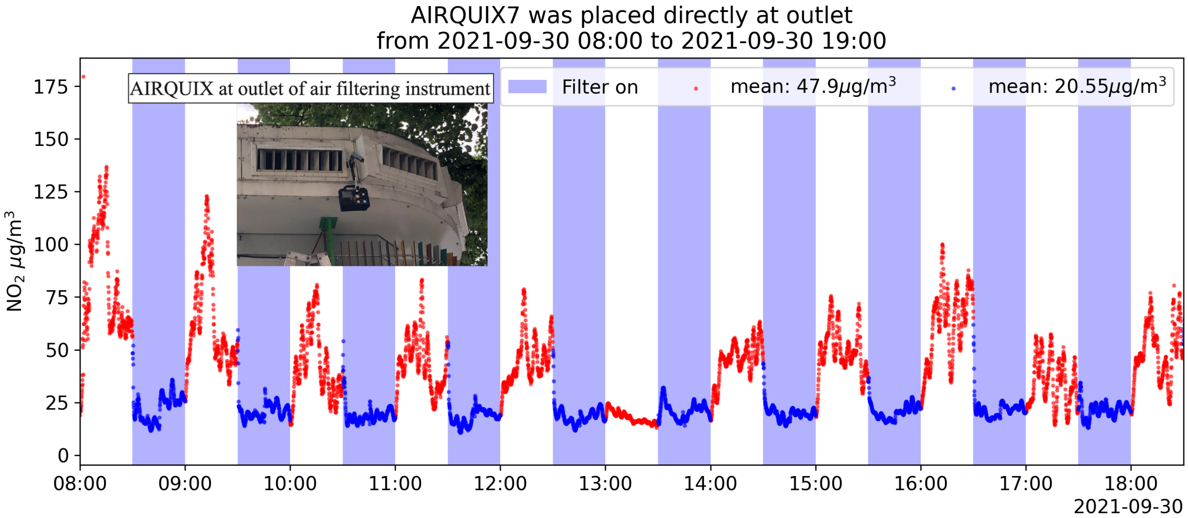

Figure 6.63: NO$_2$ levels at the filtering system outlet with 57.1 % reduction.

Table 6.4: Centre (Low wind condition) Air Quality Measurement Data.

Location	$\frac{c_{NO_2,\text{Filter On}} - c_{NO_2,\text{Filter Off}}}{c_{NO_2,\text{Filter On}}}$ (%)	$c_{NO_2,FilterOn}$-$c_{NO_2,FilterOff}$ (μg·m^{-3})	$c_{NO_2,FilterOn}$ (μg·m^{-3})	$c_{NO_2,FilterOff}$ (μg·m^{-3})	Days
Location1	-2.61	-0.77	29.43	30.19	33
Location2	-7.60	-3.05	40.17	43.22	36
Location3	-1.14	-0.38	33.67	34.06	14
Location4	-1.87	-0.75	40.07	40.82	33

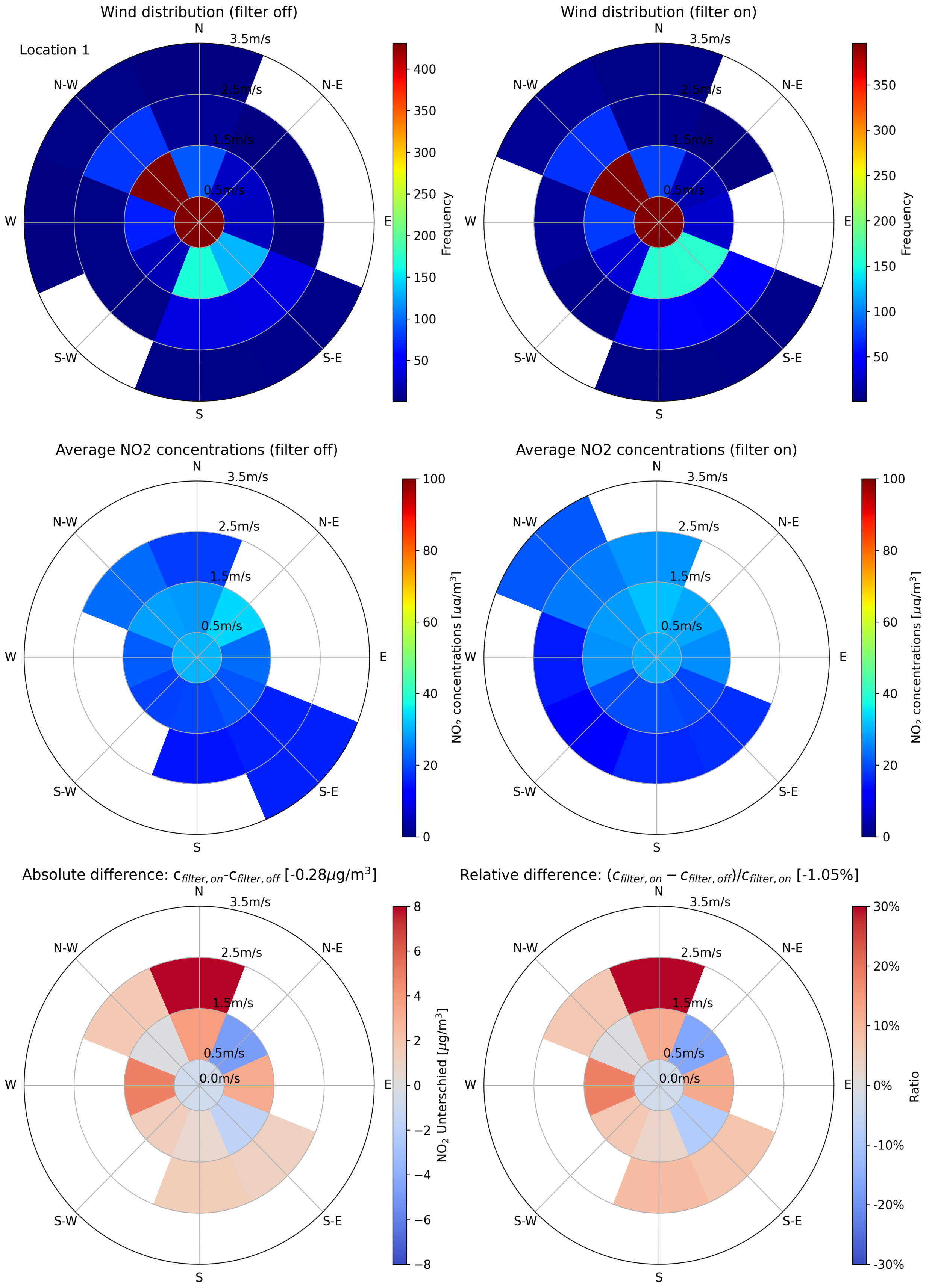

Figure 6.64: NO$_2$ levels when the air filtering system is turned on and off at Location 1.

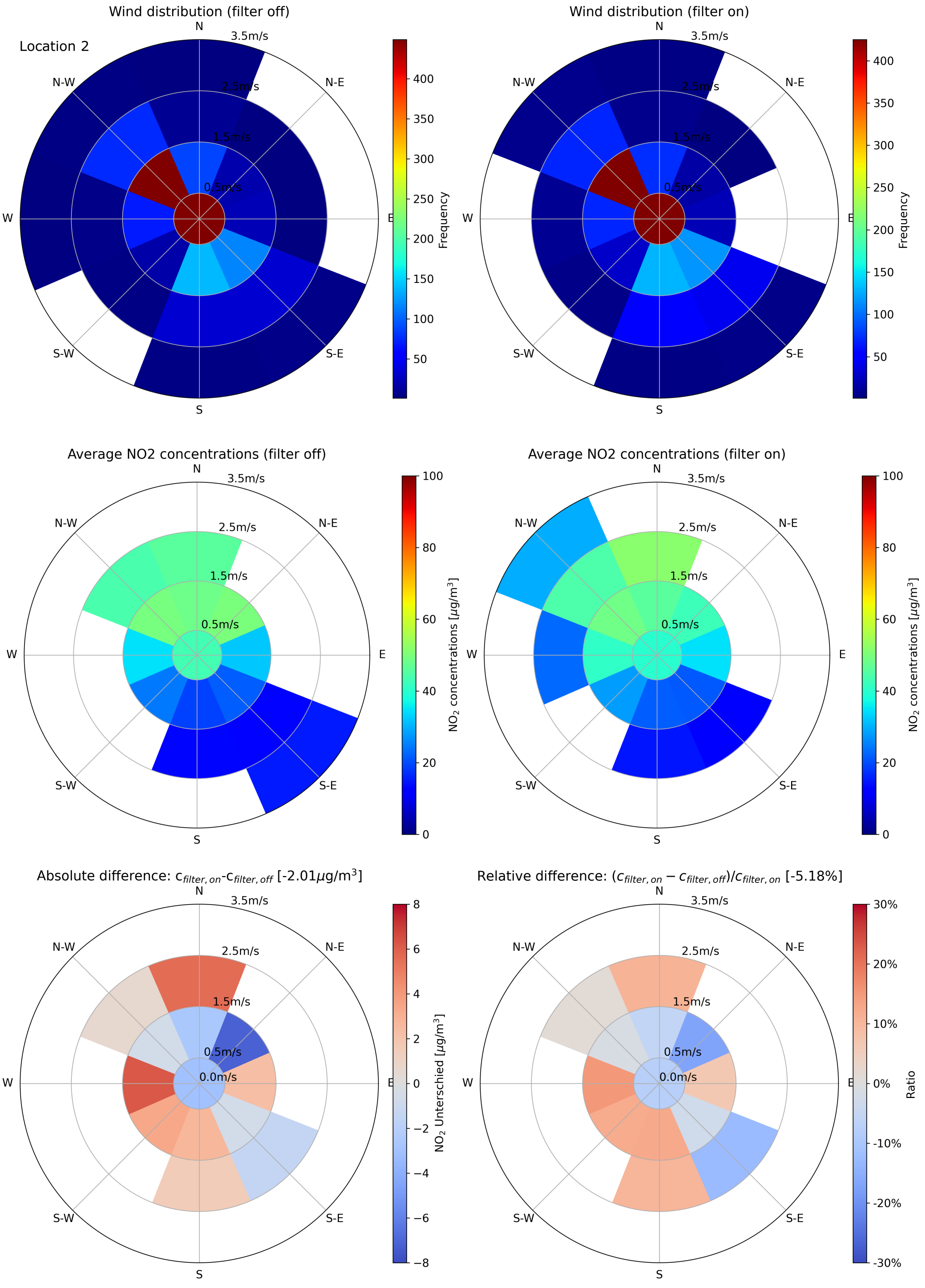

Figure 6.65: NO_2 levels when the air filtering system is turned on and off at Location 2.

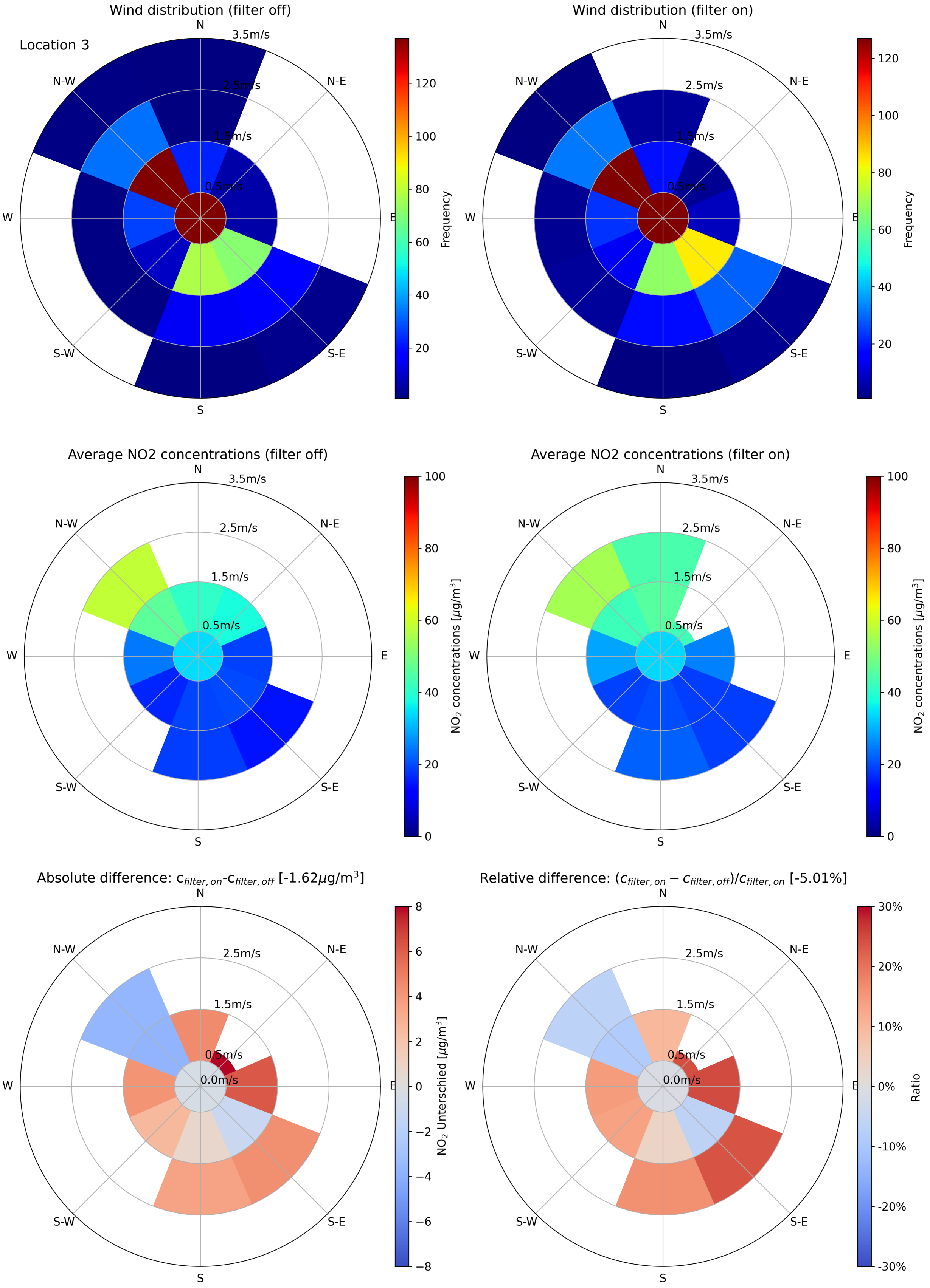

Figure 6.66: NO_2 levels when the air filtering system is turned on and off at Location 3.

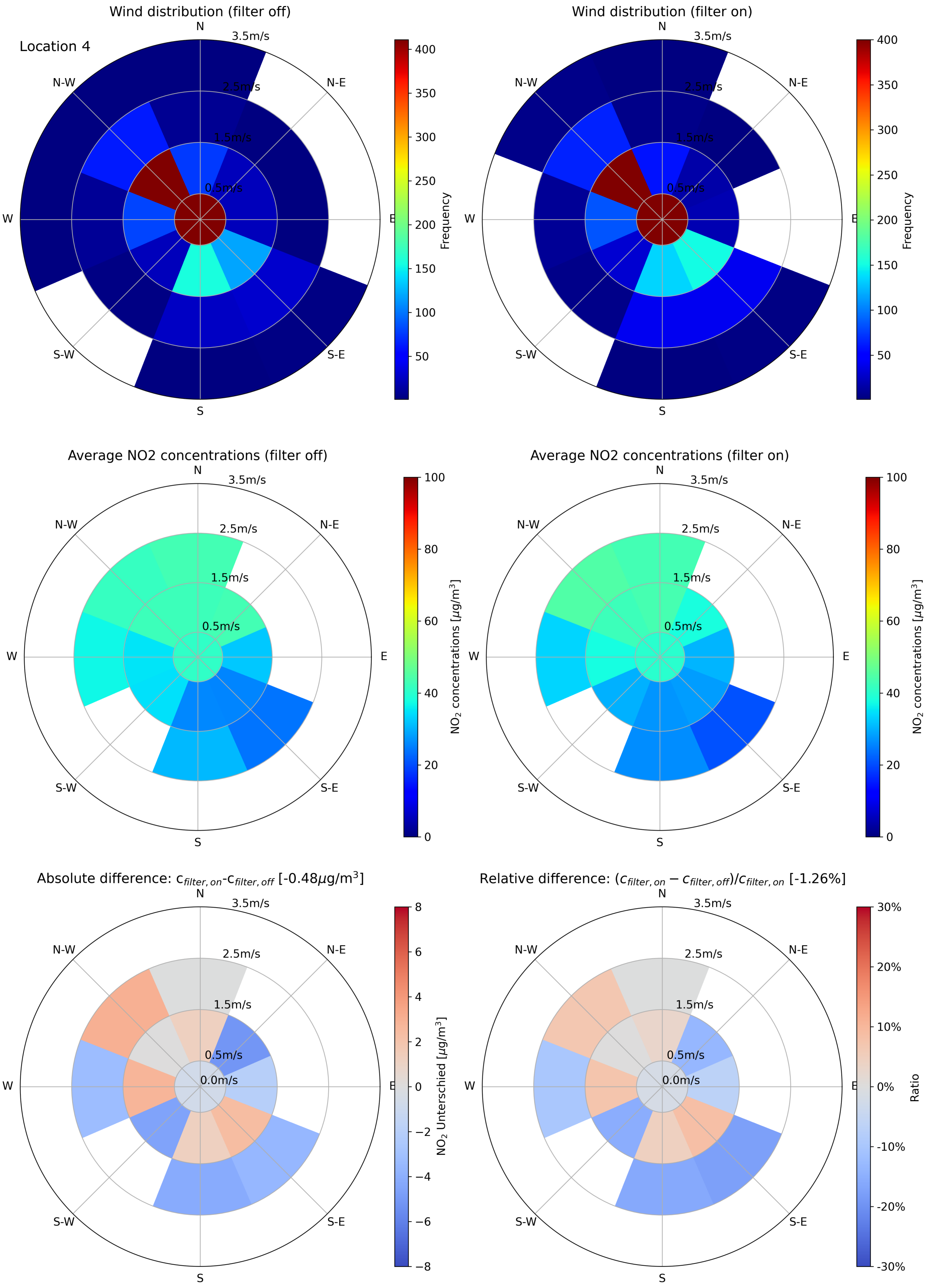

Figure 6.67: NO$_2$ levels when the air filtering system is turned on and off at Location 4.

curred directly beneath the outlet at location 2 (-5.18 %), while more distant monitoring points showed minimal effects (Table 6.3). Locations 1 and 4, positioned further from the outlet, demonstrated only modest reductions of -1.05 % and -1.26 %, respectively. Location 3 showed an intermediate reduction of -5.01 %, likely due to its downwind position relative to the outlet.

Meteorological conditions, particularly wind speed, significantly influenced system performance. Under low wind conditions (<0.5 m/s), when atmospheric dispersion was limited, the filtering effect became more pronounced at all locations (Table 6.4). Location 2 showed the highest reduction of 7.60 %, while locations 1, 3, and 4 demonstrated reductions of 2.61 %, 1.14 %, and 1.87 %, respectively. These calm conditions allowed the filtered air to remain in the immediate vicinity longer, enhancing the system's observable impact.

Conversely, higher wind speeds reduced system effectiveness by promoting rapid atmospheric mixing and entrainment of unfiltered air from surrounding areas. The wind rose analysis (Figs. 6.64-6.67) illustrates this relationship between wind conditions, NO_2 levels, and system performance. Under turbulent conditions, both filtered and unfiltered air masses were rapidly dispersed, minimizing detectable differences between operational and non-operational periods.

An interesting observation emerged at location 3, which showed only 1.14 % reduction under calm conditions but 5.01 % average reduction for all wind conditions. This enhanced performance under variable wind conditions may be attributed to its downwind positioning (see wind distribution in Figs. 6.64-6.67), where specific wind patterns occasionally direct filtered air toward the monitoring point. This pattern was not observed at location 4, which remained too distant from the outlet to benefit significantly from the filtering system.

These findings highlight both the potential and limitations of current roadside air filtering technologies. While the system demonstrates clear effectiveness at the emission control point, its ambient air quality impact remains highly localized and meteorologically dependent. The robust evaluation methodology, employing alternating operational schedules with time-shifted starting periods and multi-point monitoring, successfully controlled for temporal confounding factors and provided reliable performance assessment.

6.7 Summary and Discussion of Applications

The case studies presented in this chapter demonstrate the adaptability of the AIRQUIX in addressing complex air quality monitoring applications. Building upon the overview provided in Table 6.1, these applications validate the system's performance across mobile, personal, and stationary domains. A summary of the key findings and specific outcomes for each case study is presented in Table 6.5.

Collectively, these applications highlight the AIRQUIX's ability to provide high-resolution spatial and temporal data that complements traditional monitoring networks. The mobile and personal monitoring applications (AIRQMORE, AIRIDE, PEARL) successfully captured dynamic exposure patterns and local hotspots, while stationary deployments (WOODY, CLEANROAD) enabled targeted evaluations of specific sources and interventions.

These studies also underscore the importance of rigorous data processing and calibration. The successful interpretation of mobile data required advanced normalization techniques to account

Table 6.5: Summary of key findings and outcomes from AIRQUIX application case studies.

Case Study	Key Findings and Outcomes
AIRQMORE	Demonstrated the feasibility of city-wide NO_2 mapping using public transport. Identified pollution hotspots and spatial gradients not captured by static stations. Highlighted the importance of temporal normalization for mobile data interpretation.
AIRIDE	Revealed significant discrepancies between ambient and in-vehicle air quality. Showed that in-vehicle exposure is strongly influenced by ventilation settings, vehicle age, and filtration efficiency, emphasizing the need for microenvironmental monitoring.
METROUNO2	Validated the GAM-based calibration approach across multiple cities. Disentangled meteorological influences from emission changes, providing robust assessments of traffic-related NO_2 trends and COVID-19 lockdown effects.
PEARL	Characterized distinct personal exposure patterns across daily activities. Identified high PM exposure risks in subway systems and during cooking/moxibustion. Demonstrated the utility of wearable sensors for capturing high-resolution exposure dynamics.
WOODY	Quantified the impact of residential wood burning on local air quality. Detected elevated PM levels in both indoor and outdoor environments during stove operation, while NO_2 levels remained relatively unaffected.
CLEANROAD	Evaluated the effectiveness of roadside air filtration infrastructure. Measured high removal efficiency at the outlet ($\sim$57%) but found limited, meteorology-dependent reductions at street level, suggesting the need for source control over end-of-pipe solutions.

for temporal variability, and the evaluation of infrastructure interventions necessitated careful consideration of meteorological confounding factors. These findings reinforce the conclusion that while low-cost sensors offer powerful new capabilities, their effective deployment requires robust methodological frameworks to ensure data reliability and meaningful interpretation.

Chapter 7

Conclusions and Outlook

This thesis addressed challenges in air quality monitoring by developing and validating a calibration approach for low-cost NO_2 sensors and deploying them in diverse scenarios. The research focused on improving sensor accuracy through statistical modeling and evaluating the system's performance in real-world applications.

7.1 Conclusions

The investigation of low-cost electrochemical sensors led to the development of a new calibration algorithm. As a white-box model, this approach effectively addressed environmental dependencies as well as cross-sensitivities, while preserving interpretability. Comparative analysis indicated that this algorithm offered improved long-term stability and accuracy compared to traditional linear and black-box machine learning models, particularly when evaluated against reference CE-DOAS measurements.

A key methodological finding was the importance of a multi-metric evaluation framework. Relying solely on correlation coefficients proved insufficient for characterizing sensor performance. The use of additional metrics, including RMSE, Mean Normalized Bias, and Relative Expanded Uncertainty, provided a more comprehensive assessment of sensor reliability and compliance with data quality objectives.

The development and deployment of the AIRQUIX monitoring system demonstrated the feasibility of using calibrated low-cost sensors for high-resolution air quality assessment. Field studies across urban, in-vehicle, and indoor environments revealed spatial and temporal pollution patterns that are difficult to capture with static monitoring networks alone. Specifically, mobile monitoring campaigns identified local variations in NO_2 concentrations, while in-vehicle measurements highlighted the discrepancy between ambient air quality and personal exposure.

Furthermore, the research highlighted the significance of feature selection in calibration algorithms. Including environmental transients and co-located pollutant measurements was found to be essential for maintaining accuracy during mobile measurements, where rapid changes in environmental conditions occur.

7.2 Outlook

Despite the progress made, several limitations remain. Low-cost sensors continue to exhibit higher measurement uncertainties compared to reference instruments, and their performance is subject to sensor drift over time. The dependence on periodic re-calibration against reference standards currently limits deployment in areas lacking reference infrastructure. Additionally, while electrochemical sensors performed well for NO_2, the study noted limitations in other sensor types, such as metal oxide sensors, for high-temporal-resolution monitoring.

Future research should focus on advancing calibration methodologies to reduce reliance on frequent reference measurements. Potential avenues include the development of self-calibrating networks and the integration of advanced machine learning techniques to model non-linear sensor responses more effectively. Improving sensor hardware to enhance selectivity and durability would also address current stability issues.

On a broader scale, the integration of low-cost sensor networks with existing monitoring infrastructure and meteorological models offers potential for more detailed urban air quality mapping. Such networks could support epidemiological studies by providing higher-resolution exposure data. Finally, the wider adoption of these technologies will require the establishment of standardized protocols for calibration and data quality assurance to ensure comparability and reliability in regulatory and scientific contexts.

Appendix A

AIRQUIX framework Layout

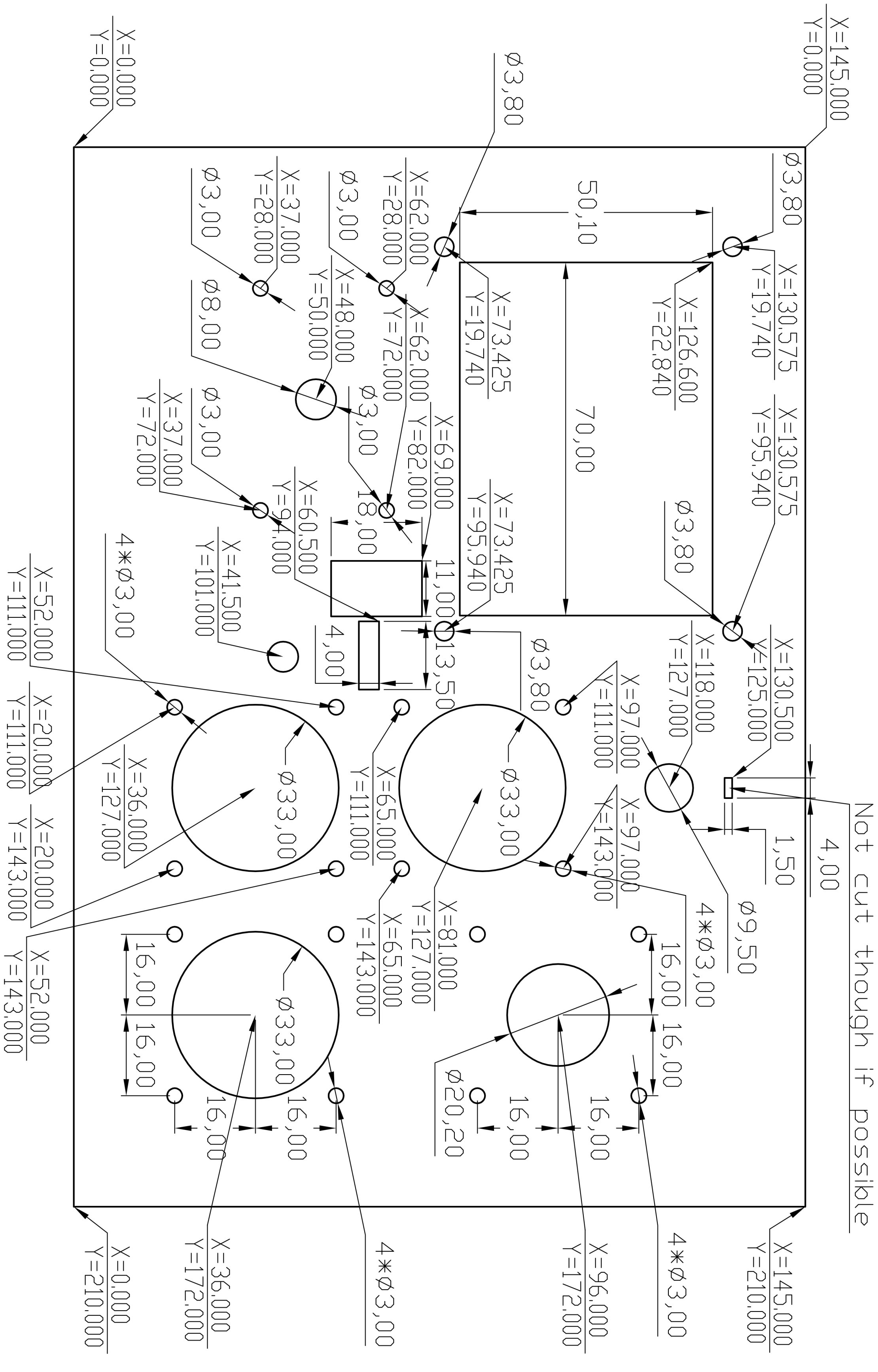
X=0.000 Y=0.000
X=145.000 Y=0.000
ø3,80
ø3,80
50,10
70,00
X=130.575 Y=19.740
X=126.600 Y=22.840
X=73.425 Y=19.740
X=62.000 Y=28.000
ø3,00
X=37.000 Y=28.000
ø3,00
X=62.000 Y=72.000
X=48.000 Y=50.000
ø8,00
ø3,00
X=69.000 Y=82.000
X=37.000 Y=72.000
ø3,00
X=60.500 Y=94.000
X=73.425 Y=95.940
X=130.575 Y=95.940
ø3,80
18,00
11,00
13,50
4,00
ø3,80
X=41.500 Y=101.000
4*ø3,00
X=52.000 Y=111.000
X=20.000 Y=111.000
X=36.000 Y=127.000
X=65.000 Y=111.000
ø33,00
ø33,00
ø33,00
X=97.000 Y=111.000
X=118.000 Y=127.000
X=130.500 Y=125.000
ø9,50
1,50
4,00
Not cut though if possible
4*ø3,00
X=97.000 Y=143.000
X=81.000 Y=127.000
X=65.000 Y=143.000
X=20.000 Y=143.000
X=52.000 Y=143.000
16,00
16,00
16,00
16,00
16,00
16,00
16,00
16,00
ø20,20
X=0.000 Y=210.000
X=36.000 Y=172.000
4*ø3,00
X=96.000 Y=172.000
4*ø3,00
X=145.000 Y=210.000

Appendix B

AIRQUIX PCB design

B.1 Main board

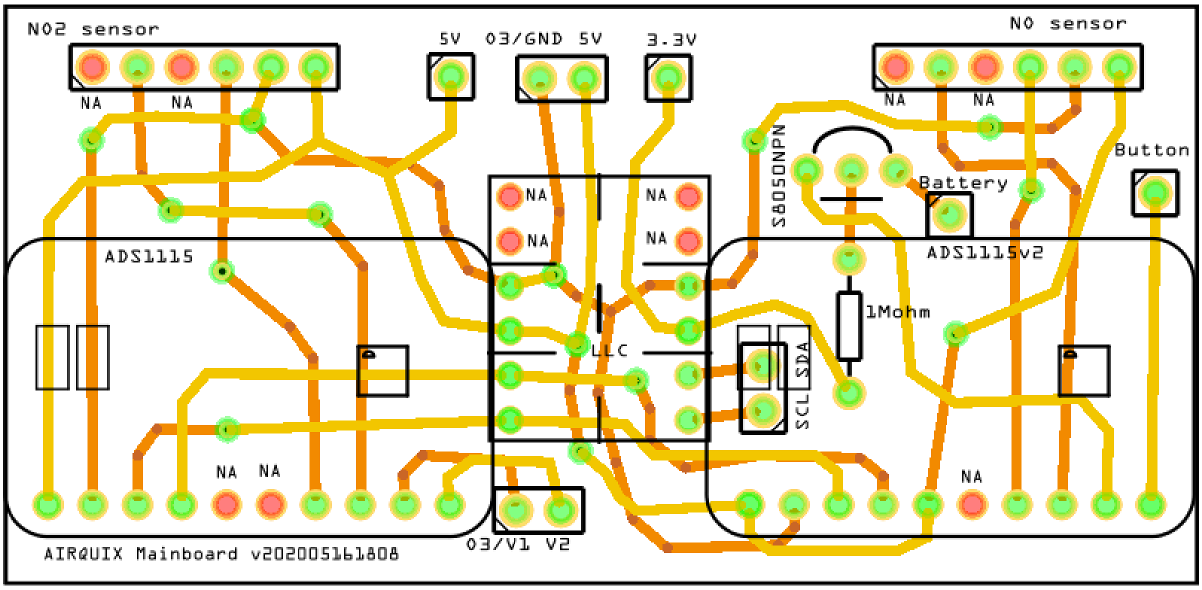

B.2 Battery connector

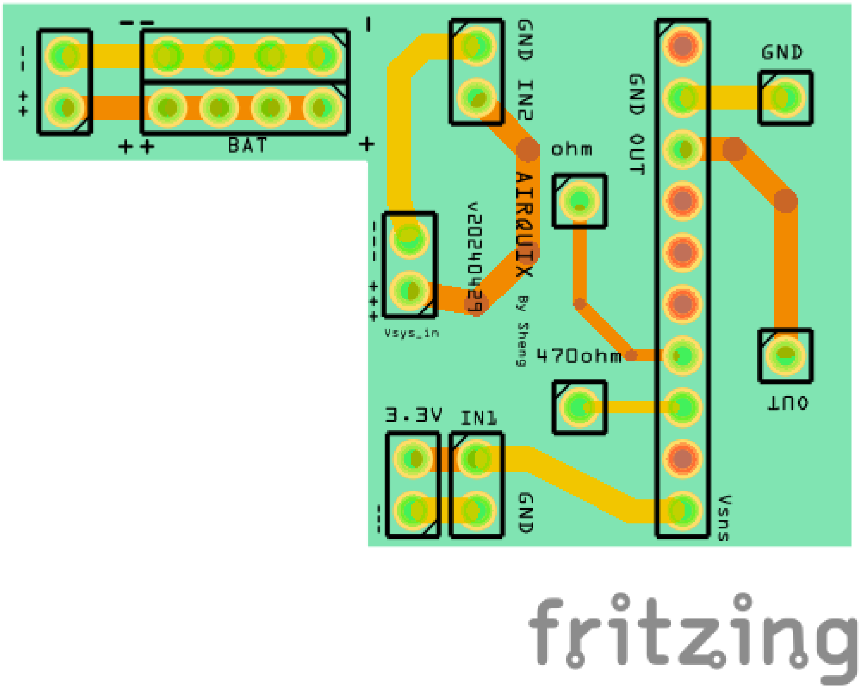

Appendix C

Server/Client diagram

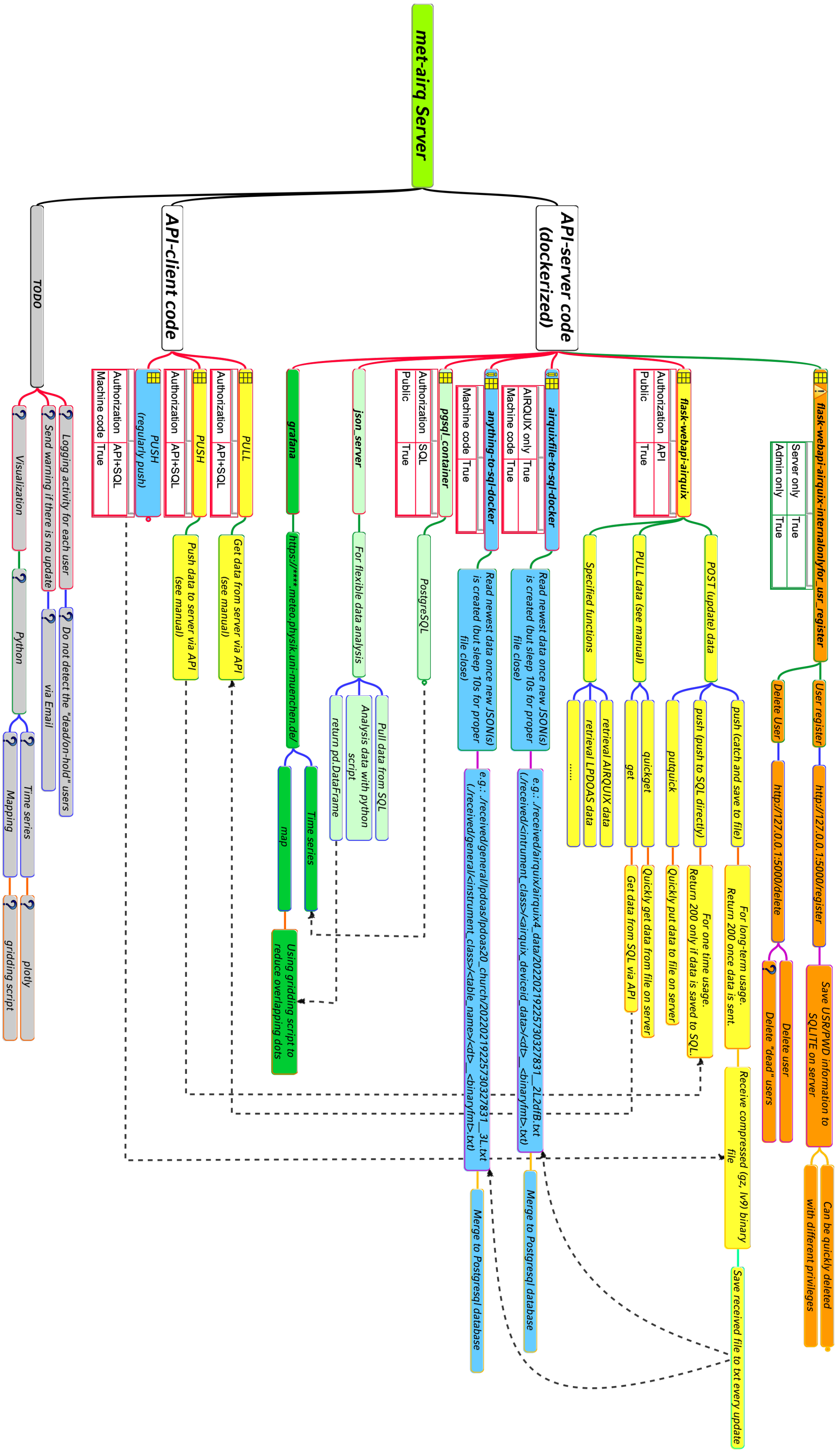
met-airq Server
API-server code (dockerized)
API-client code
TODO
flask-webapi-airquix-internalonlyfor_usr_register
Server only True
Admin only True
User register
http://127.0.0.1:5000/register
Save USR/PWD information to SQLITE on server
Can be quickly deleted
with different privileges
Delete User
http://127.0.0.1:5000/delete
Delete user
Delete "dead" users
flask-webapi-airquix
Authorization API
Public True
POST (update) data
push (catch and save to file)
For long-term usage. Return 200 once data is sent.
Receive compressed (gz, lv9) binary file
Save received file to txt every update
push (push to SQL directly)
For one time usage. Return 200 only if data is saved to SQL.
putquick
Quickly put data to file on server
PULL data (see manual)
quickget
Quickly get data from file on server
get
Get data from SQL via API
Specified functions
retrieval AIRQUIX data
retrieval LPDOAS data
......
airquixfile-to-sql-docker
AIRQUIX only True
Machine code True
Read newest data once new JSON(s) is created (but sleep 10s for proper file close)
e.g.: ./received/airquix/airquix4_data/20220219225730327831__2L2dfB.txt (./received/<intrument_class>/<airquix_deviceid_data>/<dt>__<binaryfmt>.txt)
Merge to Postgresql database
anything-to-sql-docker
Machine code True
Read newest data once new JSON(s) is created (but sleep 10s for proper file close)
e.g.: ./received/general/lpdoas/lpdoas20_church/20220219225730327831__3L.txt (./received/general/<instrument_class>/<table_name>/<dt>__<binaryfmt>.txt)
Merge to Postgresql database
pgsql_container
Authorization SQL
Public True
PostgreSQL
json_server
For flexible data analysis
Pull data from SQL
Analysis data with python script
return pd.DataFrame
grafana
https://****.meteo.physik.uni-muenchen.de/
Time series
map
Using gridding script to reduce overlapping dots
PULL
Authorization API+SQL
Get data from server via API (see manual)
PUSH
Authorization API+SQL
Push data to server via API (see manual)
PUSH (regularly push)
Authorization API+SQL
Machine code True
Logging activity for each user
Do not detect the "dead/on-hold" users
Send warning if there is no update
via Email
Visualization
Python
Time series
plotly
Mapping
gridding script

List of Figures

List of Tables

LIST OF ABBREVIATIONS

Main System and Technology

AIRQUIX	AIR Quality Inspection boX
CE-DOAS	Cavity-Enhanced Differential Optical Absorption Spectroscopy
CLD	Chemiluminescence Detector
DOAS	Differential Optical Absorption Spectroscopy
ECS	ElectroChemical Sensor
ICAD	Iterative Cavity-enhanced Absorption Detector
LP-DOAS	Long-Path Differential Optical Absorption Spectroscopy
MO_x	Metal Oxide sensor
NDIR	Non-Dispersive Infrared
OPC	Optical Particle Counter

Chemical Compounds and Pollutants

CO	Carbon Monoxide
CO_2	Carbon Dioxide
N_2O_5	Dinitrogen Pentoxide
NH_3	Ammonia
NO	Nitric Oxide
NO_2	Nitrogen Dioxide
NO_3	Nitrate Radical

NO_x	Nitrogen Oxides
NO_y	Odd Nitrogen Species
O_3	Ozone
PM	Particulate Matter
PM1	Particulate Matter with a diameter of 1 micrometer or less
PM2.5	Particulate Matter with a diameter of 2.5 micrometers or less
PM10	Particulate Matter with a diameter of 10 micrometers or less
SO_2	Sulfur Dioxide
VOC	Volatile Organic Compound
TVOC	Total Volatile Organic Compounds

Statistical and Evaluation Methods

AU	Absolute Uncertainty
CNN	Convolutional Neural Network
CV	Coefficient of Variation
DQO	Data Quality Objectives
GAM	Generalized Additive Model
GLM	Generalized Linear Model
MNB	Mean Normalized Bias
MLR	Multiple Linear Regression
OLS	Ordinary Least Squares
REU	Relative Expanded Uncertainty
RF	Random Forest
RMSE	Root Mean Square Error
RSS	Residual Sum of Squares

Organizations and Standards

ASHRAE	American Society of Heating, Refrigerating, and Air-Conditioning Engineers
EPA	Environmental Protection Agency
EU	European Union
WHO	World Health Organization

Technical and Computing

AE	Auxiliary Electrode
API	Application Programming Interface
DC	Direct Current
GPS	Global Positioning System
IAQ	Indoor Air Quality
LED	Light-Emitting Diode
LMU	Ludwig-Maximilians-Universität München
PCB	Printed Circuit Board
RH	Relative Humidity
SQL	Structured Query Language
UPS	Uninterruptible Power Supply
WE	Working Electrode

Units

ppb	parts per billion
ppm	parts per million

Projects and Studies

AIRIDE	Assessment of In-vehicle Reactive gases and Indoor air during Driving Environments
AIRQMORE	Pilot study of Air Quality Mobile Observation and Research with an Electric bus in Munich

CLEANROAD	Carbon-based Localized Evaluation of Air purification Near ROADsides
METROUNO2	Multi-city Evaluation of Traffic Related Urban NO_2 levels in Germany
PEARL	Personal Exposure to AiR poLlution
WOODY	WOod-burning stOve impact on Domestic air qualitY

Bibliography

2B Technologies: Model 205 Dual Beam Ozone Monitor | 2B Tech, `https://2btech.io/items/ambient-ozone-monitors/model-205-ozone-monitor/`, last access: 14 March 2025.

Alameddine, I., Esber, L. A., Zeid, E. B., Hatzopoulou, M., and El-Fadel, M.: Operational and environmental determinants of in-vehicle CO and PM2. 5 exposure, Sci. Total Environ., 551, 42–50, 2016.

Aldrin, M. and Haff, I. H.: Generalised additive modelling of air pollution, traffic volume and meteorology, Atmos. Environ., 39, 2145–2155, https://doi.org/10.1016/j.atmosenv.2004.12.020, 2005.

Ali, S., Alam, F., Arif, K. M., and Potgieter, J.: Low-Cost CO Sensor Calibration Using One Dimensional Convolutional Neural Network, Sens., 23, 854, https://doi.org/10.3390/s23020854, 2023.

Alphasense Limited: AAN 106 Humidity Extremes: Drying Out and Water Absorption, a.

Alphasense Limited: AAN 110 Environmental Changes: Temperature, Pressure, Humidity, b.

Alphasense Limited: AAN 803-01 CORRECTING FOR BACKGROUND CURRENTS IN FOUR ELECTRODE TOXIC GAS SENSORS, c.

Alphasense Limited: AAN 803-05 CORRECTING FOR BACKGROUND CURRENTS IN FOUR ELECTRODE TOXIC GAS SENSORS, d.

Ao, C. and Lee, S.: Enhancement effect of TiO2 immobilized on activated carbon filter for the photodegradation of pollutants at typical indoor air level, Applied Catalysis B: Environmental, 44, 191–205, https://doi.org/10.1016/s0926-3373(03)00054-7, 2003.

Apostolopoulos, I. D., Fouskas, G., and Pandis, S. N.: Field Calibration of a Low-Cost Air Quality Monitoring Device in an Urban Background Site Using Machine Learning Models, 14, 368, https://doi.org/10.3390/atmos14020368, 2023.

Apostolopoulos, I. D., Androulakis, S., Kalkavouras, P., Fouskas, G., and Pandis, S. N.: Calibration and Inter-Unit Consistency Assessment of an Electrochemical Sensor System Using Machine Learning, Sens., 24, 4110, https://doi.org/10.3390/s24134110, 2024.

ASHRAE Standards Committee: ANSI/ASHRAE addendum p to ANSI/ASHRAE standard 62.1-2013, 2013.

Ayvaz, C., Şahin, Ü. A., Kumar, P., and Gelir, A.: Low-cost sensors for atmospheric NO2 measurement: A review, Environ. Pollut., 377, 126 418, https://doi.org/10.1016/j.envpol.2025.126418, 2025.

Baden-Württemberg, R.: Luftreinhaltepläne - Regierungspräsidium Stuttgart, `https://rp.baden-wuerttemberg.de/rps/abt5/ref541/seiten/luftreinhalteplaene/`, last access: 22 July 2025.

Bagkis, E., Hassani, A., Schneider, P., DeSouza, P., Shetty, S., Kassandros, T., Salamalikis, V., Castell, N., Karatzas, K., Ahlawat, A., and Khan, J.: Evolving trends in application of low-cost air quality sensor networks: challenges and future directions, npj Clim. Atmos. Sci., 8, 335, https://doi.org/10.1038/s41612-025-01216-4, 2025.

Ball, S. M., Langridge, J. M., and Jones, R. L.: Broadband cavity enhanced absorption spectroscopy using light emitting diodes, Chem. Phys. Lett., 398, 68–74, https://doi.org/10.1016/j.cplett.2004.08.144, 2004.

Barnes, N., Ng, T., Ma, K., and Lai, K.: In-cabin air quality during driving and engine idling in air-conditioned private vehicles in hong kong, Int. J. Environ. Res. Public. Health, 15, 611, 2018.

Bayerischen Landesamtes für Umwelt: Air hygiene monitoring system Bavaria, LÜB [data set], `https://www.lfu.bayern.de/luft/immissionsmessungen/index.htm`.

Bayerisches Staatsministerium des Innern: Alle Newsletter - Bayerisches Staatsministerium des Innern, für Sport und Integration, `https://www.stmi.bayern.de/miniwebs/coronavirus/lage/index.php`, last access: 6 December 2020.

Behörde für Umwelt, Klima, Energie und Agrarwirtschaft: Data from the Hamburg air monitoring network, Hamburger Luftmessnetz [data set], `https://luft.hamburg.de/`.

Behörde für Verkehr und Mobilitätswende Hamburg: Verkehrsstärken, Entwicklung und Echtzeitdaten des Kfz-Verkehrs, Geoportal Hamburg [data set], `https://www.hamburg.de/politik-und-verwaltung/behoerden/bvm/verkehrsstaerken-kfz-193324`.

Bell, M. L., McDermott, A., Zeger, S. L., Samet, J. M., and Dominici, F.: Ozone and short-term mortality in 95 US urban communities, 1987-2000, 292, 2372–2378, 2004.

Bosch Sensortec: BME280 Combined humidity and pressure sensor, 2024.

Breiman, L.: Bagging predictors, Mach. Learn., 24, 123–140, https://doi.org/10.1007/BF00058655, 1996.

Breiman, L.: Random Forests, Mach. Learn., 45, 5–32, https://doi.org/10.1023/A:1010933404324, 2001.

Brodzik, K., Faber, J., Łomankiewicz, D., and Gołda-Kopek, A.: In-vehicle VOCs composition of unconditioned, newly produced cars, J. Environ. Sci., 26, 1052–1061, https://doi.org/10.1016/s1001-0742(13)60459-3, 2014.

Brown, S. S.: Absorption Spectroscopy in High-Finesse Cavities for Atmospheric Studies, Chem. Rev., 103, 5219–5238, https://doi.org/10.1021/cr020645c, 2003.

Brunekreef, B. and Holgate, S. T.: Air pollution and health, 360, 1233–1242, https://doi.org/10.1016/S0140-6736(02)11274-8, 2002.

Buck, A., Roberts, M. I., and Overfelt, R.: Transient Response Characteristics of Electrochemical Carbon Monoxide Sensors, 43rd Int. Conf. Environ. Syst., https://doi.org/10.2514/6.2013-3343, 2013.

Burns, J., Hoffmann, S., Kurz, C., Laxy, M., Polus, S., and Rehfuess, E.: COVID-19 mitigation measures and nitrogen dioxide – A quasi-experimental study of air quality in Munich, Germany, Atmos. Environ., 246, 118 089, https://doi.org/10.1016/j.atmosenv.2020.118089, 2021.

Campagnolo, D., Cattaneo, A., Corbella, L., Borghi, F., Del Buono, L., Rovelli, S., Spinazzé, A., and Cavallo, D. M.: In-vehicle airborne fine and ultra-fine particulate matter exposure: the impact of leading vehicle emissions, Environ. Int., 123, 407–416, 2019.

Carl Malings, Kofi Amegah, Colleen Marciel F. Rosales, Sara Basart, Naomi Zimmerman, and Sebastián Diez: Integrating Low-cost Sensor Systems and Networks to Enhance Air Quality Applications, Tech. Rep. 293, World Meteorological Organization, 2024.

Chan, A.: Indoor–outdoor air quality relationships in vehicle: effect of driving environment and ventilation modes, Atmos. Environ., 37, 3795–3808, https://doi.org/10.1016/s1352-2310(03)00466-7, 2003.

Chan, C. C., Ozkaynak, H., Spengler, J. D., and Sheldon, L.: Driver exposure to volatile organic compounds, carbon monoxide, ozone and nitrogen dioxide under different driving conditions, Environ. Sci. Technol., 25, 964–972, 1991.

Chan, L. Y., Lau, W. L., Zou, S. C., Cao, Z. X., and Lai, S. C.: Exposure level of carbon monoxide and respirable suspended particulate in public transportation modes while commuting in urban area of guangzhou, china, Atmos. Environ., 36, 5831–5840, 2002.

Chauhan, A. J., Krishna, M. T., Frew, A. J., and Holgate, S. T.: Exposure to nitrogen dioxide (NO2) and respiratory disease risk, Rev. Environ. Health, 13, 73–90, 1998.

Chen, X., Feng, L., Luo, H., and Cheng, H.: Analyses on influencing factors of airborne VOCS pollution in taxi cabins, Environ. Sci. Pollut. Res., 21, 12 868–12 882, https://doi.org/10.1007/s11356-014-3223-y, 2014.

Cichowicz, R., Wielgosiński, G., and Fetter, W.: Dispersion of atmospheric air pollution in summer and winter season, Environ. Monit. Assess., 189, 605, https://doi.org/10.1007/s10661-017-6319-2, 2017.

Clements, A., Duvall, R., Greene, D., and Dye, T.: The Enhanced Air Sensor Guidebook, 2022.

Cooper, M. J., Martin, R. V., Hammer, M. S., Levelt, P. F., Veefkind, P., Lamsal, L. N., Krotkov, N. A., Brook, J. R., and McLinden, C. A.: Global fine-scale changes in ambient NO2 during COVID-19 lockdowns, Nature, 601, 380–387, https://doi.org/10.1038/s41586-021-04229-0, 2022.

Copernicus Climate Change Service: ERA5 post-processed daily statistics on single levels from 1940 to present, Climate Data Store [data set], https://doi.org/10.24381/cds.4991cf48, 2024.

Cordero, J. M., Borge, R., and Narros, A.: Using statistical methods to carry out in field calibrations of low cost air quality sensors, Sens. Actuators, B, 267, 245–254, https://doi.org/10.1016/j.snb.2018.04.021, 2018.

Deutscher Bundestag: Deutscher Bundestag - AfD stellt sich gegen Diesel-Fahrverbote in Innenstädten, `https://www.bundestag.de/dokumente/textarchiv/2020/kw25-de-diesel-fahrverbote-698656`, last access: 31 March 2022, 2020.

Deutscher Wetterdienst: Wetter und Klima - Deutscher Wetterdienst - Our services - Climate data for direct download, DWD [data set], `https://www.dwd.de/EN/ourservices/cdc/cdc_ueberblick-klimadaten_en.html`.

Diao, L., Bi, X., Zhang, W., Liu, B., Wang, X., Li, L., Dai, Q., Zhang, Y., Wu, J., and Feng, Y.: The Characteristics of Heavy Ozone Pollution Episodes and Identification of the Primary Driving Factors Using a Generalized Additive Model (GAM) in an Industrial Megacity of Northern China, Atmosphere, 12, 1517, https://doi.org/10.3390/atmos12111517, 2021.

Diez, S., Lacy, S. E., Bannan, T. J., Flynn, M., Gardiner, T., Harrison, D., Marsden, N., Martin, N. A., Read, K., and Edwards, P. M.: Air pollution measurement errors: is your data fit for purpose?, Atmos. Meas. Tech., 15, 4091–4105, https://doi.org/10.5194/amt-15-4091-2022, 2022.

Diez, S., Lacy, S., Coe, H., Urquiza, J., Priestman, M., Flynn, M., Marsden, N., Martin, N. A., Gillott, S., Bannan, T., and Edwards, P. M.: Long-term evaluation of commercial air quality sensors: an overview from the QUANT (Quantification of Utility of Atmospheric Network Technologies) study, Atmos. Meas. Tech., 17, 3809–3827, https://doi.org/10.5194/amt-17-3809-2024, 2024.

Dunlea, E. J., Herndon, S. C., Nelson, D. D., Volkamer, R. M., San Martini, F., Sheehy, P. M., Zahniser, M. S., Shorter, J. H., Wormhoudt, J. C., Lamb, B. K., Allwine, E. J., Gaffney, J. S., Marley, N. A., Grutter, M., Marquez, C., Blanco, S., Cardenas, B., Retama, A., Ramos Villegas, C. R., Kolb, C. E., Molina, L. T., and Molina, M. J.: Evaluation of nitrogen dioxide chemiluminescence monitors in a polluted urban environment, Atmos. Chem. Phys., 7, 2691–2704, https://doi.org/10.5194/acp-7-2691-2007, 2007.

European Centre for Medium-Range Weather Forecasts: Parameter detail - Boundary layer height, https://codes.ecmwf.int/grib/param-db/159, last access: 8 July 2025.

European Commission: Guide to the demonstration of equivalence of ambient air monitoring methods, 2010.

European Parliament and Council of the European Union: Directive 2008/50/EC of the European Parliament and of the Council of 21 May 2008 on ambient air quality and cleaner air for Europe, 2008.

European Parliament and Council of the European Union: Directive (EU) 2024/2881 of the European Parliament and of the Council of 23 October 2024 on ambient air quality and cleaner air for Europe (recast), 2024.

Faber, J., Brodzik, K., Łomankiewicz, D., Gołda-Kopek, A., Nowak, J., and Świątek, A.: Temperature influence on air quality inside cabin of conditioned car, Silniki Spalinowe, 51, 49–56, 2012.

Faber, J., Brodzik, K., Gołda-Kopek, A., and Łomankiewicz, D.: Benzene, toluene and xylenes levels in new and used vehicles of the same model, J. Environ. Sci., 25, 2324–2330, https://doi.org/10.1016/s1001-0742(12)60333-7, 2013.

FAZ: Neuer pendler-rekord, 2019.

Fedoruk, M. J. and Kerger, B. D.: Measurement of volatile organic compounds inside automobiles, J. Expo. Anal. Environ. Epidemiol., 13, 31–41, https://doi.org/10.1038/sj.jea.7500250, 2003.

Geiß, A.: Automated calibration of ceilometer data and its applicability for quantitative aerosol monitoring, Ph.D. thesis, Ludwig-Maximilians-Universität München, 2016.

Geiß, A., Wiegner, M., Bonn, B., Schäfer, K., Forkel, R., von Schneidemesser, E., Münkel, C., Chan, K. L., and Nothard, R.: Mixing layer height as an indicator for urban air quality?, Atmos. Meas. Tech., 10, 2969–2988, https://doi.org/10.5194/amt-10-2969-2017, 2017.

German Institute of Development and Sustainability (IDOS): Policy Brief: Combustion engine phase-out by 2035 will strengthen the German car industry, https://www.idos-research.de/en/press/press-releases/policy-brief-combustion-engine-phase-out-by-2035-will-strengthen-the-german-car-industry/, last access: 28 May 2025.

Ghio, A. J. and Huang, Y.-C. T.: Exposure to concentrated ambient particles (CAPs): a review, Inhal. Toxicol., 16, 53–59, 2004.

Grabbs, J. S., Corsi, R. L., and Torres, V. M.: Volatile organic compounds in new automobiles: screening assessment, J. Environ. Eng., 126, 974–977, 2000.

Gu, J., Deffner, V., Küchenhoff, H., Pickford, R., Breitner, S., Schneider, A., Kowalski, M., Peters, A., Lutz, M., Kerschbaumer, A., Slama, R., Morelli, X., Wichmann, H.-E., and Cyrys, J.: Low emission zones reduced PM10 but not NO2 concentrations in Berlin and Munich, Germany, J. Environ. Manage., 302, 114 048, https://doi.org/10.1016/j.jenvman.2021.114048, 2022.

Hagler, G. S. W., Williams, R., Papapostolou, V., and Polidori, A.: Air Quality Sensors and Data Adjustment Algorithms: When Is It No Longer a Measurement?, Environ. Sci. Technol., 52, 5530–5531, https://doi.org/10.1021/acs.est.8b01826, 2018.

Hastie, T.: Generalized additive models, Chapman and Hall, London, ISBN 978-0-412-34390-2, 1990.

Hastie, T. and Tibshirani, R.: Generalized Additive Models, Stat. Sci., 1, 297–310, https://doi.org/10.1214/ss/1177013604, 1986.

Horbanski, M., Pöhler, D., Lampel, J., and Platt, U.: The ICAD (iterative cavity-enhanced DOAS) method, Atmos. Meas. Tech., 12, 3365–3381, https://doi.org/10.5194/amt-12-3365-2019, 2019.

Ionascu, M.-E., Castell, N., Boncalo, O., Schneider, P., Darie, M., and Marcu, M.: Calibration of CO, NO2, and O3 Using Airify: A Low-Cost Sensor Cluster for Air Quality Monitoring, Sens., 21, 7977, https://doi.org/10.3390/s21237977, 2021.

ISO: Part 1: Whole vehicle test chamber — Specification and method for the determination of volatile organic compounds in cabin interiors (ISO 12219-1:2021), 2021.

Jiao, W., Hagler, G., Williams, R., Sharpe, R., Brown, R., Garver, D., Judge, R., Caudill, M., Rickard, J., Davis, M., Weinstock, L., Zimmer-Dauphinee, S., and Buckley, K.: Community Air Sensor Network (CAIRSENSE) project: evaluation of low-cost sensor performance in a suburban environment in the southeastern United States, Atmos. Meas. Tech., 9, 5281–5292, https://doi.org/10.5194/amt-9-5281-2016, 2016.

Johnson, T. R.: Recent advances in the estimation of population exposure to mobile source pollutants, J. Expo. Anal. Environ. Epidemiol., 5, 551–571, 1995.

Jones, A. M., Harrison, R. M., and Baker, J.: The wind speed dependence of the concentrations of airborne particulate matter and NOx, Atmos. Environ., 44, 1682–1690, https://doi.org/10.1016/j.atmosenv.2010.01.007, 2010.

Kagawa, J.: Evaluation of biological significance of nitrogen oxides exposure, Tokai J. Exp. Clin. Med., 10, 348–353, 1985.

Karagulian, F., Belis, C. A., Dora, C. F. C., Prüss-Ustün, A. M., Bonjour, S., Adair-Rohani, H., and Amann, M.: Contributions to cities' ambient particulate matter (PM): a systematic review of local source contributions at global level, Atmos. Environ., 120, 475–483, 2015.

Karagulian, F., Barbiere, M., Kotsev, A., Spinelle, L., Gerboles, M., Lagler, F., Redon, N., Crunaire, S., and Borowiak, A.: Review of the Performance of Low-Cost Sensors for Air Quality Monitoring, 10, 506, https://doi.org/10.3390/atmos10090506, 2019a.

Karagulian, F., Gerboles, M., Barbiere, M., Kotsev, A., Lagler, F., and Borowiak, A.: Review of sensors for air quality monitoring, Publications Office of the European Union, ISBN 978-92-76-09255-1, 2019b.

Kerr, G. H., Goldberg, D. L., Emma Knowland, K., Keller, C. A., Oladini, D., Kheirbek, I., Mahoney, L., Lu, Z., and Anenberg, S. C.: Diesel passenger vehicle shares influenced COVID-19 changes in urban nitrogen dioxide pollution, Environ. Res. Lett., 17, 74 010, https://doi.org/10.1088/1748-9326/ac7659, 2022.

Kim, H., Müller, M., Henne, S., and Hüglin, C.: Long-term behavior and stability of calibration models for NO and NO_2 low-cost sensors, Atmos. Meas. Tech., 15, 2979–2992, https://doi.org/10.5194/amt-15-2979-2022, 2022.

Kim, Y.-J. and Gu, C.: Smoothing Spline Gaussian Regression: More Scalable Computation via Efficient Approximation, J. R. Stat. Soc. B, 66, 337–356, https://doi.org/10.1046/j.1369-7412.2003.05316.x, 2004.

Komulainen, H.: The opinion on risk assessment on indoor air quality by SCHER, Proc. Indoor Air Cph., 2008.

Kunkel, C.: Weniger Verkehr sorgt für bessere Luftqualität, `https://www.sueddeutsche.de/wissen/luftschadstoffe-coronavirus-covid-19-verkehr-stickoxide-1.4905056`, last access: 4 January 2023, 2020.

Künzli, N. and Tager, I. B.: Air pollution: from lung to heart, Swiss Med Wkly, 135, 697–702, 2005.

Landesanstalt für Umwelt Baden-Württemberg: Air quality monitoring in Baden-Württemberg, LUBW [data set], `https://www.lubw.baden-wuerttemberg.de`.

Landeshauptstadt München: Exemption authorisations for driving in the low emission zone, `https://stadt.muenchen.de/service/en-GB/info/hauptabteilung-ii-fahrzeugzulassungs-und-fahrerlaubnisbehoerde-ausnahmegenehmigung-umweltzone/10422459/`, last access: 26 May 2025.

Landeshauptstadt München Mobilitätsreferat: Über das Mobilitätsreferat, Mobilithek [data set], https://stadt.muenchen.de/infos/portrait-mobilitaetsreferat.html.

LeCun, Y., Boser, B., Denker, J. S., Henderson, D., Howard, R. E., Hubbard, W., and Jackel, L. D.: Backpropagation Applied to Handwritten Zip Code Recognition, Neural Comput., 1, 541–551, https://doi.org/10.1162/neco.1989.1.4.541, 1989.

Lee, E. S. and Zhu, Y.: Application of a high-efficiency cabin air filter for simultaneous mitigation of ultrafine particle and carbon dioxide exposures inside passenger vehicles, Environ. Sci. Technol., 48, 2328–2335, 2014.

Lee, E. S., Fung, C.-C. D., and Zhu, Y.: Evaluation of a high efficiency cabin air (HECA) filtration system for reducing particulate pollutants inside school buses, Environ. Sci. Technol., 49, 3358–3365, 2015.

Leibinger, A., Rehfuess, E., and Burns, J.: Munich's selective diesel vehicle ban and its impact on nitrogen dioxide concentrations: A quasi-experimental study, Environ. Int., 193, 109 067, https://doi.org/10.1016/j.envint.2024.109067, 2024.

Leighton, P.: Photochemistry of air pollution, 2012.

Li, N., Hao, M., Phalen, R. F., Hinds, W. C., and Nel, A. E.: Particulate air pollutants and asthma: a paradigm for the role of oxidative stress in PM-induced adverse health effects, Clin. Immunol., 109, 250–265, 2003.

LI-COR Environmental: LI-840A | Specifications, https://www.licor.com/support/LI-840A/topics/specifications.html, last access: 14 March 2025.

Lian, X., Huang, J., Huang, R., Liu, C., Wang, L., and Zhang, T.: Impact of city lockdown on the air quality of COVID-19-hit of Wuhan city, Sci. Total Environ., 742, 140 556, https://doi.org/10.1016/j.scitotenv.2020.140556, 2020.

Liang, L., Daniels, J., Bailey, C., Hu, L., Phillips, R., and South, J.: Integrating low-cost sensor monitoring, satellite mapping, and geospatial artificial intelligence for intra-urban air pollution predictions, Environ. Pollut., 331, 121 832, https://doi.org/10.1016/j.envpol.2023.121832, 2023.

Liang, Y., Wu, C., Jiang, S., Li, Y. J., Wu, D., Li, M., Cheng, P., Yang, W., Cheng, C., Li, L., Deng, T., Sun, J. Y., He, G., Liu, B., Yao, T., Wu, M., and Zhou, Z.: Field comparison of electrochemical gas sensor data correction algorithms for ambient air measurements, Sensors and Actuators B: Chemical, 327, 128 897, https://doi.org/10.1016/j.snb.2020.128897, 2021.

Lindsey, R. and Miller, J.: Climate change: atmospheric carbon dioxide | NOAA Climate.gov, https://www.climate.gov/news-features/understanding-climate/climate-change-atmospheric-carbon-dioxide, last access: 13 June 2025, 2025.

Maag, B., Saukh, O., Hasenfratz, D., and Thiele, L.: Pre-Deployment Testing, Augmentation and Calibration of Cross-Sensitive Sensors, in: Proc. 2016 Int. Conf. Embed. Wirel. Syst. Netw., EWSN '16, pp. 169–180, Junction Publishing, USA, ISBN 978-0-9949886-0-7, 2016.

Maag, B., Zhou, Z., and Thiele, L.: W-Air: Enabling Personal Air Pollution Monitoring on Wearables, Proc. ACM Interact. Mob. Wearable Ubiquitous Technol., 2, 24:1–24:25, https://doi.org/10.1145/3191756, 2018.

Margaritis, D., Keramydas, C., Papachristos, I., and Lambropoulou, D.: Calibration of Low-cost Gas Sensors for Air Quality Monitoring, Aerosol Air Qual. Res., 21, 210 073, https://doi.org/10.4209/aaqr.210073, 2021.

Massagué, J., Carnerero, C., Escudero, M., Baldasano, J. M., Alastuey, A., and Querol, X.: 2005–2017 ozone trends and potential benefits of local measures as deduced from air quality measurements in the north of the Barcelona metropolitan area, Atmos. Chem. Phys., 19, 7445–7465, https://doi.org/10.5194/acp-19-7445-2019, 2019.

McConnell, R., Berhane, K., Gilliland, F., London, S. J., Islam, T., Gauderman, W. J., Avol, E., Margolis, H. G., and Peters, J. M.: Asthma in exercising children exposed to ozone: a cohort study, The lancet, 359, 386–391, 2002.

McDonnell, W. F., Abbey, D. E., Nishino, N., and Lebowitz, M. D.: Long-term ambient ozone concentration and the incidence of asthma in nonsmoking adults: the AHSMOG study, Environ. Res., 80, 110–121, 1999.

Meinen, J., Thieser, J., Platt, U., and Leisner, T.: Technical Note: Using a high finesse optical resonator to provide a long light path for differential optical absorption spectroscopy: CE-DOAS, Atmos. Chem. Phys., 10, 3901–3914, https://doi.org/10.5194/acp-10-3901-2010, 2010.

Ministerium für Verkehr Baden-Württemberg: Mobilität & Verkehr, Baden-Württemberg [data set], `https://vm.baden-wuerttemberg.de/de/mobilitaet-verkehr`.

Morillas, C., Alvarez, S., Pires, J. C., Garcia, A. J., and Martinez, S.: Impact of the implementation of Madrid's low emission zone on NO2 concentration using Sentinel-5P/TROPOMI data, Atmos. Environ., 320, 120 326, https://doi.org/10.1016/j.atmosenv.2024.120326, 2024.

Orak, N. H.: Effect of ambient air pollution and meteorological factors on the potential transmission of COVID-19 in Turkey, Environ. Res., 212, 113 646, https://doi.org/10.1016/j.envres.2022.113646, 2022.

Othman, M., Théron, C., Bendahan, M., Caillat, L., Rivron, C., Bernardini, S., Le Chevallier, G., Chevallier, E., Som, M. P., Aguir, K., and Tran-Thi, T. H.: Efficiency of new ozone filters for NO2 sensing and air depollution, Sens. Actuators B Chem., 265, 591–599, https://doi.org/10.1016/j.snb.2018.03.019, 2018.

Pedregosa, F., Varoquaux, G., Gramfort, A., Michel, V., Thirion, B., Grisel, O., Blondel, M., Prettenhofer, P., Weiss, R., Dubourg, V., Vanderplas, J., Passos, A., Cournapeau, D., Brucher, M., Perrot, M., and Duchesnay, É.: Scikit-learn: Machine Learning in Python, J. Mach. Learn. Res., 12, 2825–2830, 2011.

Piedrahita, R., Xiang, Y., Masson, N., Ortega, J., Collier, A., Jiang, Y., Li, K., Dick, R. P., Lv, Q., Hannigan, M., and Shang, L.: The next generation of low-cost personal air quality sensors for quantitative exposure monitoring, Atmos. Meas. Tech., 7, 3325–3336, https://doi.org/10.5194/amt-7-3325-2014, 2014.

Plantower Technology: PMSA003—Laser PM2.5 Sensor-Plantower Technology, https://www.plantower.com/en/products_33/77.html, last access: 6 April 2025.

Platt, U. and Stutz, J.: Differential Optical Absorption Spectroscopy, ISBN 978-3-540-21193-8, 2008.

Pültz, J., Thürkow, M., Banzhaf, S., and Schaap, M.: Nitrogen Dioxide Source Attribution for Urban and Regional Background Locations Across Germany, 16, 312, https://doi.org/10.3390/atmos16030312, 2025.

Qi, C., Stanley, N., Pui, D. Y., and Kuehn, T. H.: Laboratory and on-road evaluations of cabin air filters using number and surface area concentration monitors, Environ. Sci. Technol., 42, 4128–4132, 2008.

Riediker, M., Cascio, W. E., Griggs, T. R., Herbst, M. C., Bromberg, P. A., Neas, L., Williams, R. W., and Devlin, R. B.: Particulate matter exposure in cars is associated with cardiovascular effects in healthy young men, Am. J. Respir. Crit. Care Med., 169, 934–940, 2004.

Satish, U., Mendell, M. J., Shekhar, K., Hotchi, T., Sullivan, D., Streufert, S., and Fisk, W. J.: Is CO2 an indoor pollutant? Direct effects of low-to-moderate CO2 concentrations on human decision-making performance, Environ. Health Perspect., 120, 1671–1677, 2012.

Schatke, M., Meier, F., Schröder, B., and Weber, S.: Impact of the 2020 COVID-19 lockdown on NO2 and PM10 concentrations in Berlin, Germany, Atmos. Environ., 290, 119 372, https://doi.org/10.1016/j.atmosenv.2022.119372, 2022.

Schwitalla, T., Bauer, H.-S., Warrach-Sagi, K., Bönisch, T., and Wulfmeyer, V.: Turbulence-permitting air pollution simulation for the Stuttgart metropolitan area, Atmos. Chem. Phys., 21, 4575–4597, https://doi.org/10.5194/acp-21-4575-2021, 2021.

Senatsverwaltung für Mobilität, Verkehr, Klimaschutz und Umwelt: Berlin Air Quality Monitoring Network (BLUME), BLUME [data set], https://luftdaten.berlin.de/lqi.

SGX Sensortech: SGX - SGX Sensortech Sensor, https://www.sgxsensortech.com/sensor/mics-6814, last access: 6 April 2025.

Simon Plentinger, Helene Köck, Hermann Scholz, and Susanne Delonge: Feinstaub: Droht der dreckigste Winter seit Jahrzehnten?, 2022.

Spinelle, L., Gerboles, M., Villani, M. G., Aleixandre, M., and Bonavitacola, F.: Field calibration of a cluster of low-cost available sensors for air quality monitoring. Part A: Ozone and nitrogen dioxide, Sens. Actuators, B, 215, 249–257, https://doi.org/10.1016/j.snb.2015.03.031, 2015.

Stein, T.: No sign of greenhouse gases increases slowing in 2023, `https://research.noaa.gov/no-sign-of-greenhouse-gases-increases-slowing-in-2023/`, last access: 9 March 2025, 2024.

Sullivan, J., Sheppard, L., Schreuder, A., Ishikawa, N., Siscovick, D., and Kaufman, J.: Relation between short-term fine-particulate matter exposure and onset of myocardial infarction, pp. 41–48, 2005.

Tager, I. B., Balmes, J., Lurmann, F., Ngo, L., Alcorn, S., and Künzli, N.: Chronic exposure to ambient ozone and lung function in young adults, pp. 751–759, 2005.

Tartakovsky, L., Baibikov, V., Czerwinski, J., Gutman, M., Kasper, M., Popescu, D., Veinblat, M., and Zvirin, Y.: In-vehicle particle air pollution and its mitigation, Atmos. Environ., 64, 320–328, 2013.

Urbansky, F.: Corona, Immissionen und der Verbrennungsmotor, MTZ - Motortechnische Zeitschrift, 81, 8–13, https://doi.org/10.1007/s35146-020-0298-5, 2020.

Uysal, N. and Schapira, R. M.: Effects of ozone on lung function and lung diseases, Curr. Opin. Pulm. Med., 9, 144–150, 2003.

van Zoest, V., Osei, F. B., Stein, A., and Hoek, G.: Calibration of low-cost NO2 sensors in an urban air quality network, Atmos. Environ., 210, 66–75, https://doi.org/10.1016/j.atmosenv.2019.04.048, 2019.

Vande Hey, J. D., Sonderfeld, H., Jeanjean, A. P., Panchal, R., Leigh, R. J., Allen, M. A., Dawson, M., and Monks, P. S.: Experimental and modeling assessment of a novel automotive cabin PM2. 5 removal system, Aerosol Sci. Technol., 52, 1249–1265, 2018.

Varga, G., Csávics, A., Szeberényi, J., and Gresina, F.: Non-uniform tropospheric NO2 level changes in European Union caused by governmental COVID-19 restrictions and geography, City Environ. Interact., 22, 100 145, https://doi.org/10.1016/j.cacint.2024.100145, 2024.

Verkehrsinformationszentrale Berlin: Aktuelle Informationen für alle Verkehrsmittel, VIZ [data set], `https://viz.berlin.de/`.

Viehmann, S.: Stuttgart schafft seinen Feinstaub-Alarm ab - Kritik an Diesel-Verboten wächst, `https://www.focus.de/auto/news/diesel-drama-stuttgart-schafft-seinen-feinstaub-alarm-ab-fahrverbote-bleiben-trotzdem_id_11888497.html`, last access: 28 June 2025, 2020.

Villena, G., Bejan, I., Kurtenbach, R., Wiesen, P., and Kleffmann, J.: Interferences of commercial NO2 instruments in the urban atmosphere and in a smog chamber, Atmos. Meas. Tech., 5, 149–159, https://doi.org/10.5194/amt-5-149-2012, 2012.

Virtanen, P., Gommers, R., Oliphant, T. E., Haberland, M., Reddy, T., Cournapeau, D., Burovski, E., Peterson, P., Weckesser, W., Bright, J., Van Der Walt, S. J., Brett, M., Wilson, J., Millman, K. J., Mayorov, N., Nelson, A. R. J., Jones, E., Kern, R., Larson, E., Carey, C. J., Polat, İ., Feng, Y., Moore, E. W., VanderPlas, J., Laxalde, D., Perktold, J., Cimrman, R., Henriksen, I., Quintero, E. A., Harris, C. R., Archibald, A. M., Ribeiro, A. H., Pedregosa, F., Van Mulbregt, P., SciPy 1.0 Contributors, Vijaykumar, A., Bardelli, A. P., Rothberg, A., Hilboll, A., Kloeckner, A., Scopatz, A., Lee, A., Rokem, A., Woods, C. N., Fulton, C., Masson, C., Häggström, C., Fitzgerald, C., Nicholson, D. A., Hagen, D. R., Pasechnik, D. V., Olivetti, E., Martin, E., Wieser, E., Silva, F., Lenders, F., Wilhelm, F., Young, G., Price, G. A., Ingold, G.-L., Allen, G. E., Lee, G. R., Audren, H., Probst, I., Dietrich, J. P., Silterra, J., Webber, J. T., Slavič, J., Nothman, J., Buchner, J., Kulick, J., Schönberger, J. L., De Miranda Cardoso, J. V., Reimer, J., Harrington, J., Rodríguez, J. L. C., Nunez-Iglesias, J., Kuczynski, J., Tritz, K., Thoma, M., Newville, M., Kümmerer, M., Bolingbroke, M., Tartre, M., Pak, M., Smith, N. J., Nowaczyk, N., Shebanov, N., Pavlyk, O., Brodtkorb, P. A., Lee, P., McGibbon, R. T., Feldbauer, R., Lewis, S., Tygier, S., Sievert, S., Vigna, S., Peterson, S., More, S., Pudlik, T., Oshima, T., Pingel, T. J., Robitaille, T. P., Spura, T., Jones, T. R., Cera, T., Leslie, T., Zito, T., Krauss, T., Upadhyay, U., Halchenko, Y. O., and Vázquez-Baeza, Y.: SciPy 1.0: fundamental algorithms for scientific computing in Python, Nat. Methods, 17, 261–272, https://doi.org/10.1038/s41592-019-0686-2, 2020.

von Schneidemesser, E., Sibiya, B., Caseiro, A., Butler, T., Lawrence, M. G., Leitao, J., Lupascu, A., and Salvador, P.: Learning from the COVID-19 lockdown in berlin: Observations and modelling to support understanding policies to reduce NO2., Atmos. Environ.: X, 12, 100 122, https://doi.org/10.1016/j.aeaoa.2021.100122, 2021.

Wallace, J. M. and Hobbs, P. V.: Atmospheric Science: An Introductory Survey, ISBN 978-0-08-049953-6, 2006.

Wenig, M., Jähne, B., and Platt, U.: Operator representation as a new differential optical absorption spectroscopy formalism, Appl. Opt., 44, 3246–3253, https://doi.org/10.1364/AO.44.003246, 2005.

Westfälische Nachrichten: Luftqualität nicht besser geworden, `https://www.wn.de/muenster/luftqualitat-nicht-besser-geworden-863004`, last access: 11 August 2024, 2020.

Wood, S.: mgcv: Mixed GAM Computation Vehicle with Automatic Smoothness Estimation, CRAN [software], https://doi.org/10.32614/CRAN.package.mgcv, 2023.

Wood, S. N.: Generalized Additive Models, Taylor & Francis Group, ISBN 978-1-4987-2834-8, https://doi.org/10.1201/9781315370279, 2017.

World Health Organization: Billions of people still breathe unhealthy air: new WHO data, `https://www.who.int/news/item/04-04-2022-billions-of-people-still-breathe-unhealthy-air-new-who-data`, last access: 4 January 2025, a.

World Health Organization: Health community calls for urgent action for clean air ahead of WHO conference, `https://www.who.int/news/item/27-01-2025-health-community-calls-for-urgent-action-for-clean-air-ahead-of-who-conference`, last access: 6 March 2025, b.

World Health Organization: WHO global air quality guidelines: particulate matter (PM2.5 and PM10), ozone, nitrogen dioxide, sulfur dioxide and carbon monoxide, World Health Organization, ISBN 978-92-4-003422-8, 2021.

World Health Organization: Ambient (outdoor) air pollution, `https://www.who.int/news-room/fact-sheets/detail/ambient-(outdoor)-air-quality-and-health`, last access: 6 March 2025, 2024.

Xiao, Q., Zheng, Y., Geng, G., Chen, C., Huang, X., Che, H., Zhang, X., He, K., and Zhang, Q.: Separating emission and meteorological contributions to long-term PM2.5 trends over eastern China during 2000–2018, Atmos. Chem. Phys., 21, 9475–9496, https://doi.org/10.5194/acp-21-9475-2021, 2021.

Xu, B., Chen, X., and Xiong, J.: Air quality inside motor vehicles' cabins: A review, Indoor Built Environ., 27, 452–465, https://doi.org/10.1177/1420326X16679217, 2018.

Xu, X., Zhang, T., and Su, Y.: Temporal variations and trend of ground-level ozone based on long-term measurements in Windsor, Canada, Atmos. Chem. Phys., 19, 7335–7345, https://doi.org/10.5194/acp-19-7335-2019, 2019.

Yan, Y., Pozzer, A., Ojha, N., Lin, J., and Lelieveld, J.: Analysis of European ozone trends in the period 1995–2014, Atmos. Chem. Phys., 18, 5589–5605, https://doi.org/10.5194/acp-18-5589-2018, 2018.

Yan, Y., Ren, P., and Meng, Q.: Quantitative evaluation of the synergistic effects of multiple meteorological parameters on air pollutants based on generalized additive models, Urban Clim., 55, 101 965, https://doi.org/10.1016/j.uclim.2024.101965, 2024.

Yang, S.-S. and Pan, C.-J.: Climatology of the Atmospheric Boundary Layer Height Using ERA5: Spatio-Temporal Variations and Controlling Factors, Atmosphere, 16, 573, https://doi.org/10.3390/atmos16050573, 2025.

Yassin, M. F., Al-Shatti, L. A., and Al Rashidi, M. S.: Assessment of the atmospheric mixing layer height and its effects on pollutant dispersion, Environ. Monit. Assess., 190, 372, https://doi.org/10.1007/s10661-018-6737-9, 2018.

Ye, S., Ziemann, M., and Wenig, M.: Personal air pollution exposure assessment using wearable sensors, Tech. Rep. EGU23-11085, Copernicus Meetings, https://doi.org/10.5194/egusphere-egu23-11085, 2023.

Yoshida, T. and Matsunaga, I.: A case study on identification of airborne organic compounds and time courses of their concentrations in the cabin of a new car for private use, Environ. Int., 32, 58–79, 2006.

Yoshida, T., Matsunaga, I., Tomioka, K., and Kumagai, S.: Interior Air Pollution in Automotive Cabins by Volatile Organic Compounds Diffusing from Interior Materials: I. Survey of 101 Types of Japanese Domestically Produced Cars for Private Use, Indoor Built Environ., 15, 425–444, https://doi.org/10.1177/1420326X06069395, 2006.

You, K.-w., GE, Y.-s., Bin, H. U., NING, Z.-w., ZHAO, S.-t., ZHANG, Y.-n., and Peng, X. I. E.: Measurement of in-vehicle volatile organic compounds under static conditions, J. Environ. Sci., 19, 1208–1213, 2007.

Yu, C. M., Chin, M., Tan, Q., Bian, H., Colarco, P. R., and Yu, H.: Assessing COVID-19 Lockdowns' Impacts on Global Urban $PM_{2.5}$ Air Quality with Observations and Modeling, pp. 1–40, https://doi.org/10.5194/egusphere-2025-1750, 2025.

Yu, N., Shu, S., Lin, Y., She, J., Ip, H. S. S., Qiu, X., and Zhu, Y.: High efficiency cabin air filter in vehicles reduces drivers' roadway particulate matter exposures and associated lipid peroxidation, PLoS ONE, 12, e0188 498, https://doi.org/10.1371/journal.pone.0188498, 2017.

Żak, M., Melaniuk-Wolny, E., and Widziewicz, K.: The exposure of pedestrians, drivers and road transport passengers to nitrogen dioxide, Atmospheric Pollut. Res., 8, 781–790, https://doi.org/10.1016/j.apr.2016.10.011, 2017.

Zalicki, P. and Zare, R. N.: Cavity ring-down spectroscopy for quantitative absorption measurements, J. Chem. Phys., 102, 2708–2717, https://doi.org/10.1063/1.468647, 1995.

Zhao, P. and Lai, L.: Minimax Rate Optimal Adaptive Nearest Neighbor Classification and Regression, IEEE Trans. Inf. Theory, 67, 3155–3182, https://doi.org/10.1109/TIT.2021.3062078, 2021.

Zhu, Y.: Citywide measurements of nitrogen dioxide (NO2) using a combination of remote sensing and in-situ measurement techniques, Ph.D. thesis, Ludwig-Maximilians-Universität München, 2018.

Zhu, Y., Chen, J., Bi, X., Kuhlmann, G., Chan, K. L., Dietrich, F., Brunner, D., Ye, S., and Wenig, M.: Spatial and temporal representativeness of point measurements for nitrogen dioxide pollution levels in cities, Atmos. Chem. Phys., 20, 13 241–13 251, https://doi.org/10.5194/acp-20-13241-2020, 2020.

Danksagung/Acknowledgment

It would not have been possible to complete this thesis without the help and support of many wonderful people around me, to only some of whom I can give particular mention here.

First and foremost, I express my sincerest gratitude to my supervisor Prof. Dr. Mark Wenig for his guidance and support throughout my Ph.D. journey. His expertise, insights, and constructive feedback have been invaluable in shaping my research and helping me develop as a scientist. The ideas and suggestions he provided have been instrumental in the development of my work, and I am grateful for his patience and encouragement throughout this process. I especially appreciate his openness to new ideas, his readiness to discuss challenges in detail, and the freedom he gave me to pursue my own research interests. His continuous support, both academically and personally, created an inspiring and motivating environment for my scientific growth, for which I am deeply thankful.

I would also like to express my sincerest gratitude to Prof. Dr. Christoph Haisch for kindly accepting the appointment as co-supervisor for this thesis and for providing me with the valuable opportunity to work within his group. His insightful comments, constructive criticism, and continuous encouragement have greatly contributed to not only the quality of this thesis but also my personal and professional growth. I am deeply grateful for his support and guidance throughout this journey.

I thank all members of the Meteorological Institute, especially the Air Quality Research group at LMU and the Lasers and Particles group at TUM, for the open discussions and their valuable feedback.

I would also like to thank Heinz Lösslein and Dr. Robert Redl for their kindness and IT support. These services are essential for my work, and I am grateful for their patience and assistance in resolving IT issues and providing the necessary resources for my research.

I am grateful to Anton Lex[†], who helped me greatly in the workshop and provided valuable insights on mechanical design. I wish I had learned better German to communicate with him more effectively, not only about mechanical design but also about life in Germany. I am thankful for his patience and kindness, even when I occasionally approached him with urgent tasks and questions.

Special thanks to Markus Garhammer for his invaluable suggestions and help as an all-rounder, including measurement campaigns, equipment design, and accessories purchase. He is always there to help me (and everyone) out. It was always a pleasure to work with him, and his sense of humor and positive attitude made the work atmosphere enjoyable.

Special thanks to our secretary, Ms. Barbara Baumann, for her patience and kindness in help-

ing me with administrative tasks and paperwork. Her support has been invaluable in navigating the administrative aspects of my journey.

I thank Prof. Dr. ret. Klaus Schäfer for his insights and suggestions on low-cost sensor development in the scientific community and for open discussions on sensor development.

I acknowledge the financial support provided by the China Scholarship Council and extend my gratitude to LMU and TUM for their comprehensive support throughout my Ph.D. studies, including access to various essential resources.

I appreciate Prof. Dr. Jörg Schreiber, Prof. Dr. Lode Pollet, Prof. Dr. Tim Liedl, and Prof. Dr. Stefan Hofmann for joining my committee to evaluate my Ph.D. work.

Special thanks to X. Wang, for her patience and understanding during the long hours I spent working on my experiments and thesis. Her support in listening and providing feedback was invaluable, and kept me motivated throughout this journey.

Special thanks to Birkin and Xenia, my cats, for being my loyal companions during the long hours of writing and research. Their presence provided comfort and joy, helping me stay focused and motivated throughout this journey.

I owe my deepest gratitude to my parents for their unconditional love, support, and sacrifices throughout my entire academic journey. Their encouragement and belief in my abilities have been the foundation of my success. Despite the physical distance, their emotional support has been a constant source of strength, and I am forever grateful for the opportunities they provided me to pursue my dreams and education.

Last but not least, I would like to thank my family and friends for their constant support, encouragement, and endless love, even when I disappeared from their sights from time to time. Their belief in me and my abilities has been a constant source of strength and motivation, and I am grateful for their unwavering support.

It has been a long and challenging journey, but I am grateful for the opportunity to pursue my Ph.D. and to work with so many wonderful people along the way. I have finally achieved my goals: first, to have "Dr." as title when filling out forms or applications, and second, to be able to call myself a scientist and contribute to the scientific community.

I hope that this thesis will contribute to the scientific community and inspire future research in this field. More importantly, I hope this work will advance environmental protection efforts by promoting the development and application of low-cost sensors for air quality monitoring, ultimately helping to create a healthier environment for current and future generations.